Visualization of Brain Tumors with Intraoperative Confocal Laser Endomicroscopy

by

Evgenii Belykh

A Dissertation Presented in Partial Fulfillment
of the Requirements for the Degree
Doctor of Philosophy

Approved April 2020 by the
Graduate Supervisory Committee:

Mark C. Preul, Co-Chair
Brent Vernon, Co-Chair
Peter Nakaji
Sarah E. Stabenfeldt

ARIZONA STATE UNIVERSITY

May 2020

ABSTRACT

Intraoperative diagnosis in neurosurgery has traditionally relied on frozen and formalin-fixed, paraffin-embedded section analysis of biopsied tissue samples. Although this technique is considered to be the “gold standard” for establishing a histopathologic diagnosis, it entails a number of significant limitations such as invasiveness and the time required for processing and interpreting the tissue. Rapid intraoperative diagnosis has become possible with a handheld confocal laser endomicroscopy (CLE) system. Combined with appropriate fluorescent stains or labels, CLE provides an imaging technique for real-time intraoperative visualization of histopathologic features of the suspected tumor and healthy tissues.

This thesis scrutinizes CLE technology for its ability to provide real-time intraoperative in vivo and ex vivo visualization of histopathological features of the normal and tumor brain tissues. First, the optimal settings for CLE imaging are studied in an animal model along with a generational comparison of CLE performance. Second, the ability of CLE to discriminate uninjured normal brain, injured normal brain and tumor tissues is demonstrated. Third, CLE was used to investigate cerebral microvasculature and blood flow in normal and pathological conditions. Fourth, the feasibility of CLE for providing optical biopsies of brain tumors was established during the fluorescence-guided neurosurgical procedures. This study established the optimal workflow and confirmed the high specificity of the CLE optical biopsies. Fifth, the feasibility of CLE was established for endoscopic endonasal approaches and interrogation of pituitary tumor tissue. Finally,

improved and prolonged near wide-field fluorescent visualization of brain tumor margins was demonstrated with a scanning fiber endoscopy and 5-aminolevulinic acid.

These studies suggested a novel paradigm for neurosurgery-pathology workflow when the noninvasive intraoperative optical biopsies are used to interrogate the tissue and augment intraoperative decision making. Such optical biopsies could shorten the time for obtaining preliminary information on the histological composition of the tissue of interest and may lead to improved diagnostics and tumor resection. This work establishes a basis for future in vivo optical biopsy use in neurosurgery and planning of patient-related outcome studies. Future studies would lead to refinement and development of new confocal scanning technologies making noninvasive optical biopsy faster, convenient and more accurate.

DEDICATION

To my parents Olga and Georgiy, who raised me in kindness and love, and whom I owe everything I have. To my wife Liudmila for being a constant source of encouragement, inspiration, happiness and support to me. To my mentor, Dr. Mark C. Preul, who immensely supported my path as a physician-scientist.

ACKNOWLEDGMENTS

I am indebted to my mentors Dr. Mark C. Preul and Dr. Peter Nakaji for guiding me and supervising the research with confocal endomicroscopy and beyond, and for supporting my career path. Without their excellent mentorship this work would not have be possible. I am indebted to Dr. Vadim Byvaltsev who opened incredible opportunities for me and supported my endeavors on the path to being physician-scientist.

I would like to thank graduate committee Dr. Stabenfeldt, Dr. Vernon, Dr. Nakaji, and Dr. Preul for helping me navigate through the graduate curriculum and take the maximum benefits provided by the program.

I would like to thank all the members of the Neuropathology Department at the Barrow Neurological Institute, and Dr. Jennifer M. Eschbacher for providing priceless long hours of expert support and sharing her knowledge.

I wish to express my deepest gratitude to Drs. Leonard Y. Nelson and Eric J. Seibel, for incredible scientific collaboration, friendship and support.

I would like to thank medical students for valuable help with the projects resulted in this work: Arpan Patel, Eric J. Miller, Alessandro Carotenuto, Dara S. Farhadi, Brandon Ngo, Kurt V. Shaffer. Thank you for helping me become better in team work and teaching. I would also like to thank Debbie R. Healey for incredible help with animal models.

I wish to acknowledge the support of my colleagues Drs. Xiaochun Zhao, Irakliy Abramov, Kaan Yagmurlu, Daniel Vali, Claudio Cavallo, Sirin Gandhi, Mohammadhassan Izady Yazdanabadi. You are my teachers and friends. I am grateful to

Nikolay L. Martirosyan for being an example of hard work and dedication. I want to thank Joseph F. Georges for introducing me to the quantitative confocal microscopy.

I wish to express my deepest gratitude to ASU professors Dr. Janete Neisewander and Dr. Jason Newbern for creating a unique collaborative, supportive atmosphere among multiple institutions and for cultivating the spirit of innovation at the Interdisciplinary Graduate Program in Neurosciences (IGPN). I would like to pay special regards to Dr. Rita Sattler, co-director of the ASU-BNI IGPN for her active involvement in the program development, and for strong standing and support for the BNI students.

A big thank you to the BNI physicians, staff, residents and especially former director Dr. Robert F. Spetzler and current director Dr. Michael T. Lawton, for including me and for being great sources of wisdom and inspiration to me.

I am grateful to the staff of the Neuropublication office at BNI and to Dr. Danielle Golub for their excellent editorial support.

Finally, I would like to express especial gratitude to the Barrow Neurological Foundation and the Newsome Chair in Neurosurgery Research for their funding support to the part of the work presented in this dissertation.

TABLE OF CONTENTS

LIST OF TABLES

LIST OF FIGURES

Figure Page

Figure Page

CHAPTER 1

INTRODUCTION

Significance

Glioblastoma multiforme is the most common malignant brain tumor found in adults. The prognosis, even for early stage, is poor, with median patient survival spanning about 1 year (Koc et al. 2008, Zhao et al. 2013, Stummer et al. 2006, Chen et al. 2012). Current treatment strategies consist of surgical resection with adjuvant radiation and chemotherapy. Studies over the past 20 years have demonstrated that the extent of tumor resection (EOTR) is strongly correlated to average survival time and overall prognosis (Koc et al. 2008, Zhao et al. 2013, Stummer et al. 2006, Stummer et al. 1998, Stummer et al. 2000, Okuda, Yoshioka, and Kato 2012, Shinoda et al. 2003). In an attempt to optimize EOTR, visualization techniques utilizing fluorescent agents have been trialed against standard surgical resection under white light.

The first documented tumor visualization using fluorescence dates back to 1948 (Moore, Peyton, and et al. 1948). By utilizing fluorescein sodium (FNa) (>20mg/kg), a sensitivity >95% for identifying brain tumor was achieved at that time, noting that brain tumor tissue invariably glowed a brilliant yellow to the naked eye. However, this approach was not accepted as normal brain tissue had also accumulated FNa decreasing specificity of the method. FNa leaks extravascularly at the areas of compromised blood brain barrier, which is a characteristic hallmark of certain aggressive brain tumors (Okuda, Yoshioka, and Kato 2012, Shinoda et al. 2003). This quality of FNa allows for its selective accumulation in tumor tissue, while it remains minimally detectable in the

normal brain. At lower doses, special microscope filters (Yellow560) are required to visualize fluorescence of FNa (Shinoda et al. 2003). It was previously shown that combination of FNa with a Yellow560 wide field surgical microscopy improves the reliability of glioma identification during resection (Okuda, Yoshioka, and Kato 2012).

Another increasingly used drug for fluoresce-guided surgery that received FDA approval in 2017 is 5-Aminolevulinic acid (5-ALA), a non-fluorescent prodrug metabolite of heme synthesis that causes accumulation of fluorescent protoporphyrin IX (PpIX) in highly metabolically active tumor tissue (Zhao et al. 2013, Stummer et al. 1998). PpIX visualization requires ~405 nm excitation light and operating microscopes with special BLUE400 optical filters for visualization. In 1998, Randomized study demonstrated 85% sensitivity, 100% specificity, and 90% accuracy in detecting malignant tissue using 5-ALA (Stummer et al. 1998). 5-ALA guided glioma resection not only increased rates of EOTR, but was also correlated to significant increases in 6 month survival rates (Stummer et al. 2006). In a recent study, 5-ALA was claimed to be better than FNa for detecting tumor cells in boundary zones (Yano et al. 2017). However, described fluorescence imaging techniques were all based on the wide field microscopy which resolution does not allow to put fluorescence signal in the context of histological features of tissue with cellular resolution. Visualization of tissue architecture on the cellular level has been possible only with standard, microtome sliced and stained frozen sections. The limitations of current standard of care frozen section technique include the time required for transferring, processing and interpreting the tissue (Martirosyan, Eschbacher, et al. 2016), the presence of artifacts and sampling errors (Martirosyan,

Eschbacher, et al. 2016, Ackerman and Ramirez 1959, Novis and Zarbo 1997) as well as the differences present when comparing frozen and permanent section that may lead to misdiagnosis (Martirosyan, Eschbacher, et al. 2016, Plesec and Prayson 2007).

Previous studies from our group have showed that a blinded review of first generation CLE imaging by a neuropathologist yielded an accuracy rate of 92.9% (Eschbacher et al. 2012) similar to those previously reported with either frozen-section analysis or H&E staining (Eschbacher et al. 2012, Plesec and Prayson 2007, Roessler, Dietrich, and Kitz 2002, Rao et al. 2009). Therefore, CLE may give a significant aid in the intraoperative tumor identification at the tumor margin. In this way CLE may be used as a diagnostic tool, but it also has a potential to aid in EOTR, a strategy that has a positive impact in long-term patient's survival (Ammirati et al. 1987, Devaux, O'Fallon, and Kelly 1993, Lacroix et al. 2001, Nitta and Sato 1995, Rostomily et al. 1994, Wood, Green, and Shapiro 1988). One of the drawbacks of the previous generation of CLE technology is that it required sterilization of CLE probe after each patient which limited it's practical use. In this work, novel design of CLE probe that includes exchangeable single-use plastic sheaths that enable aseptic use has been analyzed. Moreover, a detailed comparison of CLE generations and in-depth analysis of histological features detectable with CLE is performed in this work. Overall, accumulated evidence for CLE application in neurosurgery will provide the basis for significant improvements in intraoperative histopathology and surgical workflow. Furthermore, an analysis of near-view scanning fiber endoscope has been performed to assess opportunities for improved detection of tumor border with red-emitting PpIX fluorophore.

Aim of work

In this work, the new confocal laser endomicroscopy (CLE) technology is scrutinized for its ability to provide real-time intraoperative in-vivo and ex-vivo visualization of histopathological features of the normal and tumor brain tissues.

Gaps in the literature

Although CLE use in vivo has been documented in the broad range of human brain tumors (Martirosyan, Eschbacher, et al. 2016, Eschbacher et al. 2012), there has been no focused analysis on the multiple biopsy spots per patient. This is especially relevant for gliomas, which have invasive growth and extensive border region. Even in small size ($0.5cm^3$) biopsy sample the neuropathologist often could identify areas representative of normal brain and glioma tissues. Prior studies lack rigorous approaches to address this limitation. Previous literature on biopsy-based studies was reporting high numbers of positive (tumor) biopsies and low numbers of negative (no tumor) biopsies (Eschbacher et al. 2012, Martirosyan, Eschbacher, et al. 2016). While positive predictive value and concordance with standard histology is high, the tumor core is usually obvious to the unaided surgeon's eye and does not require additional tests. It is the margin area, which can retain residual tumor tissue during resection and which gains the most surgical attention and is the most questionable. Therefore, the validity of the negative predictive value of confocal surgical biopsy has been largely unknown.

There was no investigation on the feasibility of visualization of pituitary tumor microstructure with the CLE.

There was no detailed investigation of normal and pathological cerebral microvasculature with the CLE and clinically-relevant fluorescent contrast.

Furthermore, there was no imaging technology that could demonstrate visualization of low-level PpIX signal on a cellular and tissue levels simultaneously.

Composition of the Thesis

This dissertation is composed of eight chapters: Chapter 1 serves as an introduction, Chapter 8 is a discussion and the core six chapters together examine the central thesis of the work. Chapter 2 is dedicated to the detailed assessment of the operation characteristics of the CLE and direct side-by side comparison of the previous generation with a novel generation CLE. In this chapter, the optimal practices for brain tumor imaging are determined in a preclinical animal model. Chapter 3 the diagnostic accuracy of in vivo confocal laser endomicroscopy (CLE) after FNa administration is assessed to differentiate normal brain, injured normal brain, and tumor brain tissue in an animal glioma model. Chapter 4 is dedicated to the qualitative and quantitative investigation of the brain and spinal cord microvasculature and blood flow in normal and pathologic conditions using the CLE. Chapter 5 describes results of the ex vivo imaging performance of a new generation CLE in human brain lesions, mostly aimed at invasive brain tumors. In chapter 6, for the first time, the feasibility of diagnosing unprocessed pituitary adenoma tissue using intraoperative digital optical biopsy with CLE is evaluated on multiple ex vivio biopsies. Chapter 7 describes investigation of tumor border highlighted by fluorescent agent 5-aminolevulenic acid with a novel near-view scanning fiber endoscope. Finally, chapter 8 summarizes the results and discusses limitations,

implications and potential future work related to the intraoperative brain tumor visualization using the confocal microscopy techniques.

Publications

A complete list of peer-reviewed manuscripts describing the work performed on this dissertation project is presented in appendix A.

CHAPTER 2

The following chapter has been published in the Journal Frontiers in Oncology, Cancer Imaging and Image Guided Interventions.

(DOI: 10.3389/fonc.2019.00554)

CHAPTER 2

PROGRESS IN CONFOCAL LASER ENDOMICROSCOPY FOR NEUROSURGERY AND TECHNICAL NUANCES FOR BRAIN TUMOR IMAGING WITH FLUORESCEIN

Belykh E., Miller E.J., Carotenuto A., Patel, A.A., Cavallo C., Healey D.R., Byvaltsev V.A., Scheck A.C., Eschbacher J.M., Nakaji P., Preul M.C.

Abstract

Background: Previous studies showed that confocal laser endomicroscopy (CLE) images of brain tumors acquired by a first generation (Gen1) CLE system using fluorescein sodium (FNa) contrast yielded a diagnostic accuracy similar to frozen surgical sections and histologic analysis. We investigated performance improvements of a second generation (Gen2) CLE system designed specifically for neurosurgical use.

Methods: Rodent glioma models were used for in vivo and rapid ex vivo CLE imaging. FNa and 5-aminolevulinic acid were used as contrast agents. Gen1 and Gen2 CLE images were compared to distinguish cytoarchitectural features of tumor mass and margin and surrounding and normal brain regions. We assessed imaging parameters (gain, laser power, brightness, scanning speed, imaging depth, and Z-stack [3D image acquisition]) and evaluated optimal values for better neurosurgical imaging performance with Gen2.

Results: Efficacy of Gen1 and Gen2 was similar in identifying normal brain tissue, vasculature, and tumor cells in masses or at margins. Gen2 had smaller field of view, but higher image resolution, and sharper, clearer images. Other advantages of the

Gen2 were auto-brightness correction, user interface, image metadata handling, and image transfer. CLE imaging with FNa allowed identification of nuclear and cytoplasmic contours in tumor cells. Injection of higher dosages of FNa (20 and 40 mg/kg vs. 0.1-8 mg/kg) resulted in better image clarity and structural identification. When used with 5-aminolevulinic acid, CLE was not able to detect individual glioma cells labeled with protoporphyrin IX, but overall fluorescence intensity was higher ($p<0.01$) than in the normal hemisphere. Gen2 Z-stack imaging allowed a unique 3D image volume presentation through the focal depth.

Conclusion: Compared with Gen1, advantages of Gen2 CLE included a more responsive and intuitive user interface, collection of metadata with each image, automatic Z-stack imaging, sharper images, and a sterile sheath. Shortcomings of Gen2 were a slightly slower maximal imaging speed and smaller field of view. Optimal Gen2 imaging parameters to visualize brain tumor cytoarchitecture with FNa as a fluorescent contrast were defined to aid further neurosurgical clinical in vivo and rapid ex vivo use. Further validation of the Gen2 CLE for microscopic visualization and diagnosis of brain tumors is ongoing.

Introduction

Intraoperative diagnosis in neurosurgery has traditionally relied on frozen and formalin-fixed, paraffin-embedded section analysis of biopsied tissue samples. Although this technique is considered to be the “gold standard” for establishing a histopathologic diagnosis, it entails a number of significant limitations. These limitations include the time required for transferring, processing, and interpreting the tissue (Martirosyan,

Eschbacher, et al. 2016); the presence of artifacts and sampling errors (Martirosyan, Eschbacher, et al. 2016, Ackerman and Ramirez 1959, Novis and Zarbo 1997); as well as the differences present when comparing frozen and permanent sections that may lead to misdiagnosis (Martirosyan, Eschbacher, et al. 2016, Plesec and Prayson 2007). Rapid intraoperative diagnosis has become possible with refinement and miniaturization of the research-type confocal laser scanning microscope into a handheld confocal laser endomicroscopy (CLE) system (Osman et al. 2018, Belykh et al. 2016). Combined with appropriate fluorescent stains or labels, CLE provides an imaging technique for real-time intraoperative in vivo visualization of histopathologic features of suspected tumor and healthy tissues.

Previous studies using a CLE system originally designed for nonneurosurgical use (e.g., gastrointestinal luminal examination) showed that a blinded review of CLE imaging of brain gliomas and meningiomas by a neuropathologist yielded an accuracy rate of 92.9%, similar to those previously reported with frozen-section analysis (Eschbacher et al. 2012, Plesec and Prayson 2007, Roessler, Dietrich, and Kitz 2002, Rao et al. 2009). In terms of analysis of tumor margins, CLE has not yet been thoroughly investigated in human brain tumors; however, in experimental animals, CLE was able to visualize border regions of glioma (Martirosyan et al. 2014, Foersch et al. 2012). In humans, CLE was shown to increase accuracy of delineation of margins in early gastric cancer (Park et al. 2017). CLE may be used as a diagnostic tool, but also has a potential to aid in optimizing surgical resection of brain tumors, including maximal safe tumor resection, which is a strategy that would be expected to have a positive impact on long-term neurosurgical

patient survival, especially among patients with invasive malignant tumors (Martirosyan et al. 2014, Ammirati et al. 1987, Devaux, O'Fallon, and Kelly 1993, Lacroix et al. 2001, Nitta and Sato 1995, Rostomily et al. 1994, Wood, Green, and Shapiro 1988).

Various CLE devices have been developed; the proximal scanning fiber optic CLE (Pavlov et al. 2016, Charalampaki et al. 2015) and distal scanning CLE (Martirosyan, Eschbacher, et al. 2016) systems are the most advanced in terms of potential for becoming adopted into wide clinical use (Belykh, Cavallo, Gandhi, et al. 2018a). Importantly, each CLE system has different pre-set, mostly unchangeable, imaging parameters that may result in unique and different diagnostic performance; therefore, meticulous independent assessment of each microscope system is required. We previously evaluated the diagnostic performance and other application parameters of a handheld scanning CLE system (Optiscan Pty., Ltd., Mulgrave, Australia), referred to in this report as the first generation (Gen1) device and designed for gastrointestinal use. This system has recently served as the imaging platform for development of a second generation (Gen2) CLE system specifically aimed at neurosurgery.

The Gen2 CLE device was designed to function specifically for intraoperative application in neurosurgery and to integrate with the robotic operating microscope visualization platform for neurosurgery (Belykh, Zhao, et al. 2018). The goals for this device in neurosurgery are ultimately to increase the positive yield of biopsies and to serve as a tool to microscopically explore, in portable and rapid fashion, for tumor cells beyond the obvious margin of infiltrating tumors, such as cells in and around the surgical resection bed, or to define suspected tumor invasion within eloquent cortex. Previous

studies regarding in vivo investigation of distal scanning CLE in human and animal model brain tumors were conducted using the Gen1 device, which had several performance characteristics that limited its use in neurosurgery. These included lack of a sterile attachment cover sheath for the imaging probe, a different design and function of the handheld probe that was not optimal for the neurosurgeon's usual hand position, and nonoptimal imaging processing and display (Martirosyan et al. 2014, Fenton et al. 2014, Sankar et al. 2010, Sanai, Snyder, et al. 2011, Martirosyan, Eschbacher, et al. 2016, Eschbacher et al. 2012). Therefore, this study was designed to assess performance of the Gen2 CLE system, assess differences in image quality or diagnostic accuracy of the Gen1 and Gen2 systems, and provide additional information on the probe conformation, and optimal handling practices that were designed to produce high-quality confocal intraoperative images for neurosurgery on-the-fly.

Gen1 and Gen2 functionalities were compared using fluorescein sodium (FNa), the primary fluorophore with which they were designed to work, and with 5-aminolevulinic acid (5-ALA)-induced protoporphyrin IX (PpIX) fluorescence. Although the fluorescence signal from PpIX is not within the optimal detection range for these CLE systems, 5-ALA is also of interest in brain tumor surgery, especially for use in invasive gliomas, and our preliminary studies suggested that the PpIX signal may be faintly detected with the CLE systems. This study aimed to expand on the current literature related to CLE for brain tumor imaging, including further investigating the relationship between FNa dosage and image quality, the ability to differentiate cellular structures with

CLE and FNa, and the utility of both generations of CLE with 5-ALA for the detection of tumor tissue.

Methods

Ethics Approval

All animal investigations were performed according to the guidelines outlined by the National Institutes of Health *Guide for the Care and Use of Laboratory Animals* and with approval from the Institutional Animal Care and Use Committee of the Barrow Neurological Institute and St. Joseph's Hospital and Medical Center, Phoenix, Arizona. Animals were maintained under approved veterinary care in the vivarium of St. Joseph's Hospital and Medical Center.

Patient tissues used for this project were acquired from a prospective ongoing brain tumor clinical study. Patients with preoperative diagnoses of brain masses requiring surgical removal and for whom the decision was to use the assistance of fluorescence surgical guidance with FNa were prospectively enrolled. Extra biopsies from tumor tissue that would have to be safely removed during the normal course of the surgery were used. De-identified samples were placed on a wet telfa and submitted for immediate ex vivo CLE analysis. The same samples were then sent for routine histologic processing and review by a neuropathologist. All patients gave voluntary informed consent as a part of a study protocol approved by the Institutional Review Board of the Barrow Neurological Institute, St. Joseph's Hospital and Medical Center, Phoenix, Arizona. A flowchart describing the study protocol is presented in Figure 2.1.

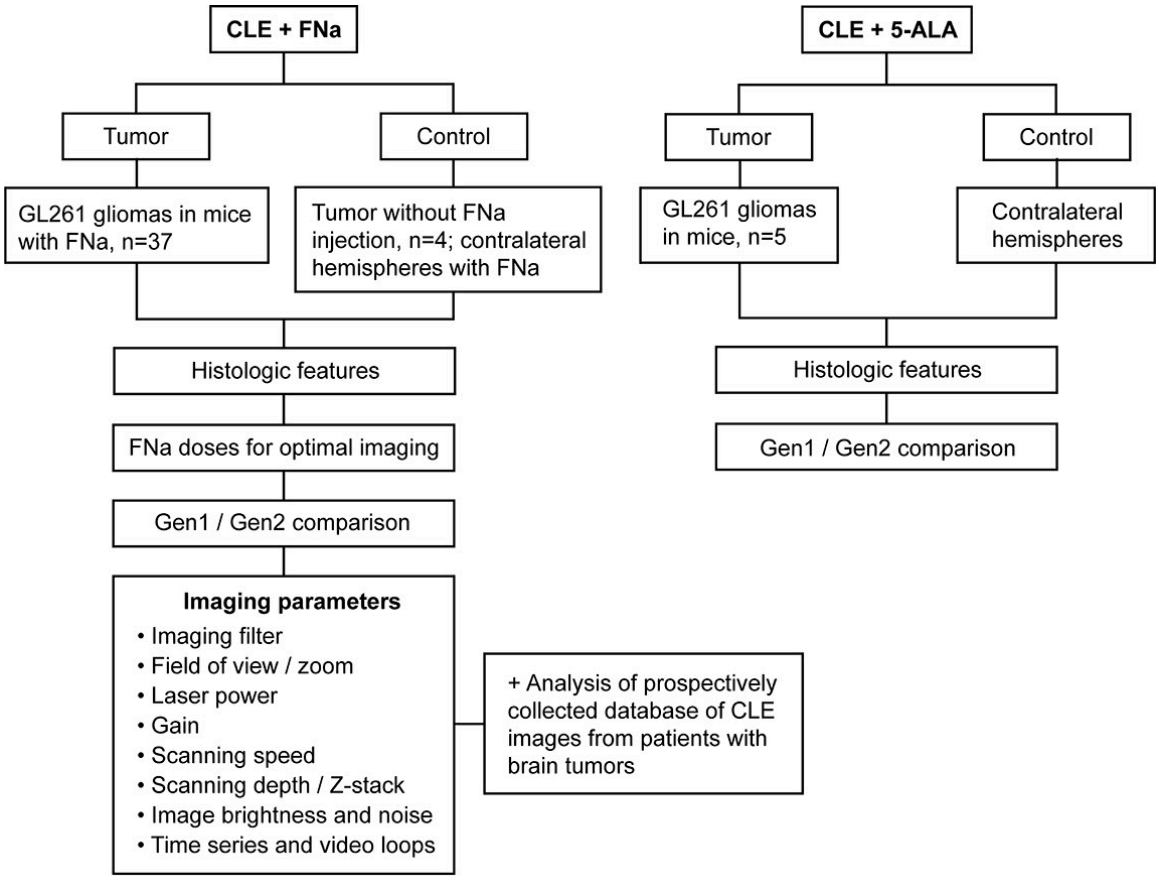

Figure 2.1. Study design flowchart. CLE, confocal laser endomicroscope; FNa, fluorescein sodium; Gen2, generation 1; Gen2, generation 2; 5-ALA, 5-aminolevulinic acid. Used with permission from Barrow Neurological Institute, Phoenix, Arizona.

Mouse Glioma Model

Ten-week-old female B6(Cg)-Tyr$^{c\text{-}2J}$/J mice (albino variant C57BL/6J, The Jackson Laboratory, Bar Harbor, ME) weighing 20 g (mean) were anesthetized and placed in a small-animal stereotactic headframe. Glioma models were created according to the previously described protocol (Abdelwahab et al. 2011). Briefly, 2 µL of GL261-luc tumor cells (1.45×10^7 cells/mL; Division of Cancer Treatment and Diagnosis,

National Cancer Institute, Bethesda, MD) were infused 2 mm lateral and 2 mm posterior to bregma at a depth of 2.5 mm from the brain surface through a bur hole at the targeted brain location after the syringe needle was withdrawn 0.5 mm to a total depth of 2 mm below the surface of the brain to create a 0.5 mm pocket for the cells. The 2-μL cell suspension was infused using a controllable microinjector (0.67 μL/min × 3 minutes with the needle in place for 2 minutes afterward) (Martirosyan et al. 2014).

A week prior to surgery, the mice were injected with 15 μg/kg of luciferin (PerkinElmer, Waltham, MA), anesthetized using isoflurane in a 37°C chamber, and glioma growth was confirmed using bioluminescence detection in the IVIS Spectrum in vivo imaging system (PerkinElmer). Bioluminescence images were examined and quantified in Living Image 4.3 software (PerkinElmer) (Abdelwahab et al. 2011).

Drug Administration

CLE imaging was performed within the first 2 hours after FNa injection. We used escalating dosages of FNa: 0.1 (n=4), 1 (n=7), 2 (n=2), 5 (n=7), 8 (n=5), 20 (n=6), and 40 (n=6) mg/kg. These doses approximate the doses of FNa that can be used in humans, as we have previously used 5 mg/kg IV in clinical study. The 5-ALA (Clinical grade, NIOPIK, Moscow, Russia) was injected intraperitoneally 2 hours before surgery at a dose of 5 mg dissolved in 200 μL of normal saline (n=5). Chosen dosages are similar to those previously used in comparable animal studies with 5-ALA (Swanson et al. 2015, Cho et al. 2014, Fisher et al. 2017) and FNa (Diaz et al. 2015, Folaron et al. 2018a, Belykh,

Miller, Patel, et al. 2018, Martirosyan et al. 2014) studies and are similar to or higher than those used in humans to compensate for differences in metabolism.

Intraoperative CLE Imaging

After confirmation of tumor growth and size, on average 21 days after implantation, the mice underwent craniectomy. The animals were anesthetized, and their oxygen supply and body temperature were maintained throughout the procedure. An operating microscope (Pentero 900, Carl Zeiss AG, Oberkochen, Germany) was used to visualize exposed surfaces of both cerebral hemispheres. Brain tumors were identified macroscopically in the right hemisphere of all mice, and the CLE scanning was performed. After imaging was performed, the anesthetized animals were euthanized according to protocol guidelines. Brains were extracted, sliced fresh coronally (1 mm in thickness) through the center of the tumor in a mouse brain slicer matrix (ZIVIC Instruments, Pittsburgh, PA), and imaged rapidly ex vivo with CLE again.

Gen1 (Optiscan 5.1, Carl Zeiss AG) and Gen2 CLE (Convivo, Carl Zeiss AG) were compared in terms of intraoperative fluorescence visualization using either FNa (n=37), 5-ALA (n=5), or no dye injection (n=4 control). This comparison was completed initially using the Gen1 CLE at a designated area. Once adequate images were acquired, the Gen2 CLE was used to take further images at the same area. All scanning was performed in vivo and then ex vivo within the 2-hour interval alternating Gen1 and Gen2 confocal microscopes targeting multiple regions of interest. Further testing included evaluation of Gen2 imaging with different available filters (green bandpass or green

longpass and red longpass) and with various gain, laser intensity, brightness, acquisition speed, and zoom settings controlling for image quality and noise levels. In 2 animals, topical acridine orange was used for nuclear staining as described elsewhere (Martirosyan et al. 2014).

Operating Microscopy Fluorescence Imaging

Gross FNa and protoporphyrin IX fluorescence in the brain was assessed with the operating microscopes equipped with the Yellow 560 and Blue 400 filters, respectively (Pentero 900 and Kinevo 900, Carl Zeiss AG).

Benchtop Confocal Laser Microscopy

The benchtop laser scanning microscopy (LSM) imaging (LSM 710 DUO, Carl Zeiss AG) was performed with a C-Apochromat 40×/1.20 W Korr M27 objective. Sliced fresh brain samples were imaged on 35-mm glass-bottom Petri dishes (MatTek, Ashland, MA). For PpIX visualization, the excitation and detection wavelengths used were 405 nm and 635–750 nm, respectively. Additionally, topical staining was performed with acridine orange (AO), acriflavine (AF), Hoechst 33342 (ThermoFisher Scientific, Waltham, MA), and 4′6-diamidino-2-phenylindole (DAPI). The excitation wavelength was 488 nm for AO, AF, or FNa, and 405 nm for DAPI and Hoechst; and the detection wavelength was 493–625 nm for AO, AF, or FNa, and 410-585 nm for DAPI and Hoechst. Examples of imaging modalities are shown in Figure 2.2.

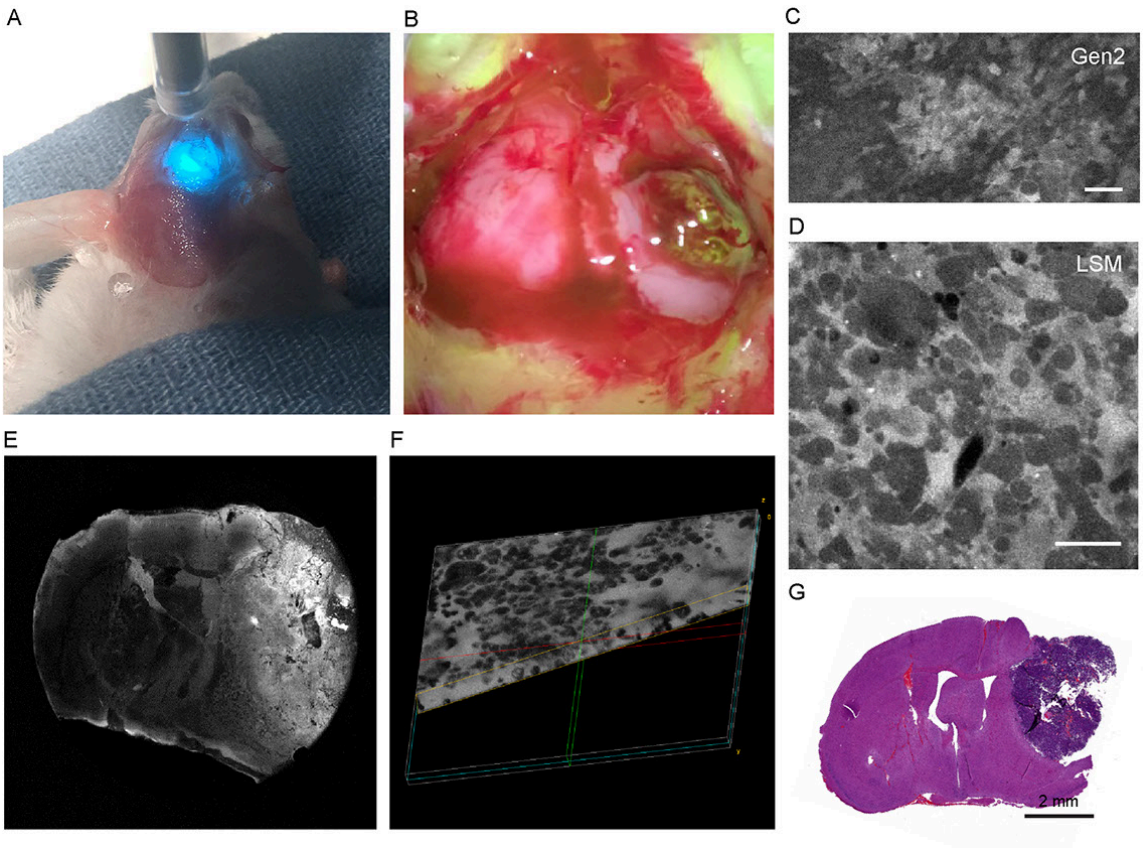

Figure 2.2. Overview of the study methods. (A) In vivo and rapid ex vivo confocal laser endomicroscopy (CLE) imaging. (B) Pentero 900 imaging with Yellow 560 filter. (C) Generation 2 (Gen2) CLE image acquisition. Scale bar is 50 µm. (D, E) Benchtop laser scanning microscopy. Scale bar is 50 µm. (F) Z-stack volumetric reconstruction sliced obliquely to demonstrate the thickness of the stack. (G) Hematoxylin and eosin stained coronal brain slice. Used with permission from Barrow Neurological Institute, Phoenix, Arizona.

Image Assessment and Statistical Analysis

Imaging analysis and cell and nuclei size measurements were performed in FIJI software (open source software) (Schindelin et al. 2012). Statistical analysis was

completed in Excel (Microsoft, Redmond, WA). Quality of CLE imaging was scored independently by 5 respondents trained in interpreting CLE images as bad (1), average (2), good (3), or excellent (4), based on the ability to visualize characteristic GL261 tumor histologic characteristics and patterns. Grading was performed based on the assessment of the best confocal images from each animal. Student *t* test, Mann-Whitney U test, and Kruskal-Wallis analysis of variance (ANOVA) with significance set at $p < 0.05$ were used to establish whether differences were statistically significant, and the Spearman R value was used to assess correlations.

RESULTS

Assessment of CLE Imaging Parameters

To produce clear images, several parameters were controlled in both systems: gain, brightness level, laser power, scanning speed, imaging depth, and Z-stack thickness (Gen2 only). Because many imaging parameters were similar between Gen1 and Gen2 CLE, salient results are presented of observations for Gen2, and are specifically mentioned when differences were observed with Gen1. Gen2 imaging parameters are summarized in Table 2.1 (APPENDIX B).

Field of View

The field of view (FOV) of the Gen2 (475 × 267 μm, 1980 pixels/line) was half the size of the Gen1 image (475 × 475 μm, 1080 pixels/line). Gen2 images were essentially twice the resolution. Gen2 images appear sharper, but upon magnification they have a grainier appearance compared with Gen1 images. This graininess is due to

the raw image TIFF format of Gen2 images, compared to compressed and smoothing JPG formatting of Gen1 images.

Gain

Specimens with grossly average fluorescence brightness produced clear CLE images on Gen2 gain setting of 2400 (Table 2.1, APPENDIX B). When the brain tumor appeared grossly intensely bright yellow, lowering the gain allowed imaging with a CLE brightness level within a 20 to 60% range, which produced optimal quality images without oversaturated pixels and with low noise. However, in specimens with low gross fluorescence intensity, the quality and resolution of CLE images did not improve regardless of the changes in imaging parameters. The increased level of black noise with increase of brightness level and laser power only lowered image quality in dark images.

Scanning Speed

Scanning speed was critically important for time series imaging. Comparison of imaging speed recorded for both generations of CLEs is presented in Table 2.2. Scanning speed of Gen1 was 0.8 seconds per frame for a 1024 × 512-pixel image and 1.2 seconds per frame for a 1024 × 1024-pixel image. The scanning speed for Gen2 ranged from 1.3 seconds per frame for the highest quality imaging to 0.27 seconds per frame for the lowest quality imaging. Despite the difference in scanning speed, all images were recorded and stored as 1920 × 1080-pixel red, green, blue (RGB) TIFF files.

Table 2.2. Comparison of image acquisition speed.

Image size, pixels	Gen1	Gen2
1920 × 1080	N/A	1.29 spf
	N/A	0.78 fps
1024 × 1024	1.2 spf	N/A
	0.83 fps	N/A
1920 × 540	N/A	0.71 spf
	N/A	1.41 fps
1024 × 512	0.8 spf	N/A
	1.25 fps	N/A
1920 × 270	N/A	0.44 spf
	N/A	2.27 fps
1920 × 135	N/A	0.26 spf
	N/A	3.79 fps

Abbreviations: fps, frames per second; N/A, not available; spf, seconds per frame.

Scanning Depth

Optimal imaging depth with FNa was within the first few microns in depth from the surface of the imaged tissue. The CLE Z-stack function (Gen2 only) resulted in a series of images, the first of which was a central image from the current position on the Z axis. A series of images was acquired starting from the surface and ending at the deepest position, with the Z-step image thickness selection to be between 3 and 20 μm. The interval of the scanning depth could be chosen by selecting two offset positions. The maximal range was obtained at the offsets from -47 to +50, which resulted in a 97-μm thick Z-stack. The number of images per Z-stack was limited by the size of the Z-step (3 μm minimum), which for the 97-μm Z-stack resulted in 35 images. Higher ranges are not practically necessary, so the available CLE Z-stack range is sufficient for use in human brain tissue. Previous experiments have shown that the maximal depth of brain tumor

tissue (using FNa) for interrogation through Z-stack imaging is 36 μm in animal and 28 μm in human brain tissue (Belykh, Patel, Miller, Bozkurt, Yağmurlu, et al. 2018).

Probe movements during image capturing produced similar artifacts in both Gen1 and Gen2 CLEs. Although free-hand probe positioning yielded informative images, remaining in a steady position for an optimal Z-stack was difficult for image series acquisition. A semiflexible surgical probe holder was used to decrease movement artifacts.

Time Series and Video Loops

Time series imaging (in both Gen1 and Gen2) allowed observation of blood cell movements inside and outside the vessels (Figure 2.3). Tumor cell movements seen with tissue squeezing under the CLE lens were also noted during in vivo imaging, which is not possible on fixed tissues. In contrast to the static hematoxylin and eosin (H&E) slide, in vivo CLE revealed histologic features of the living tumor cells and their behavior. In animal gliomas, many tumor cells were actually moving independently, squeezing and pushing each other, captivated by the stream of oozing blood. Such tumor cells were flowing independent of the tumor core, especially when they were at the border of the brain slice. When imaged in vivo, GL261 glioma cells were actually not tightly connected to each other, as they appear on H&E slides, although they grow as relatively solid tumors. CLE imaging revealed pericellular spaces that were filled with FNa, which were not previously visualized well on H&E stained slides.

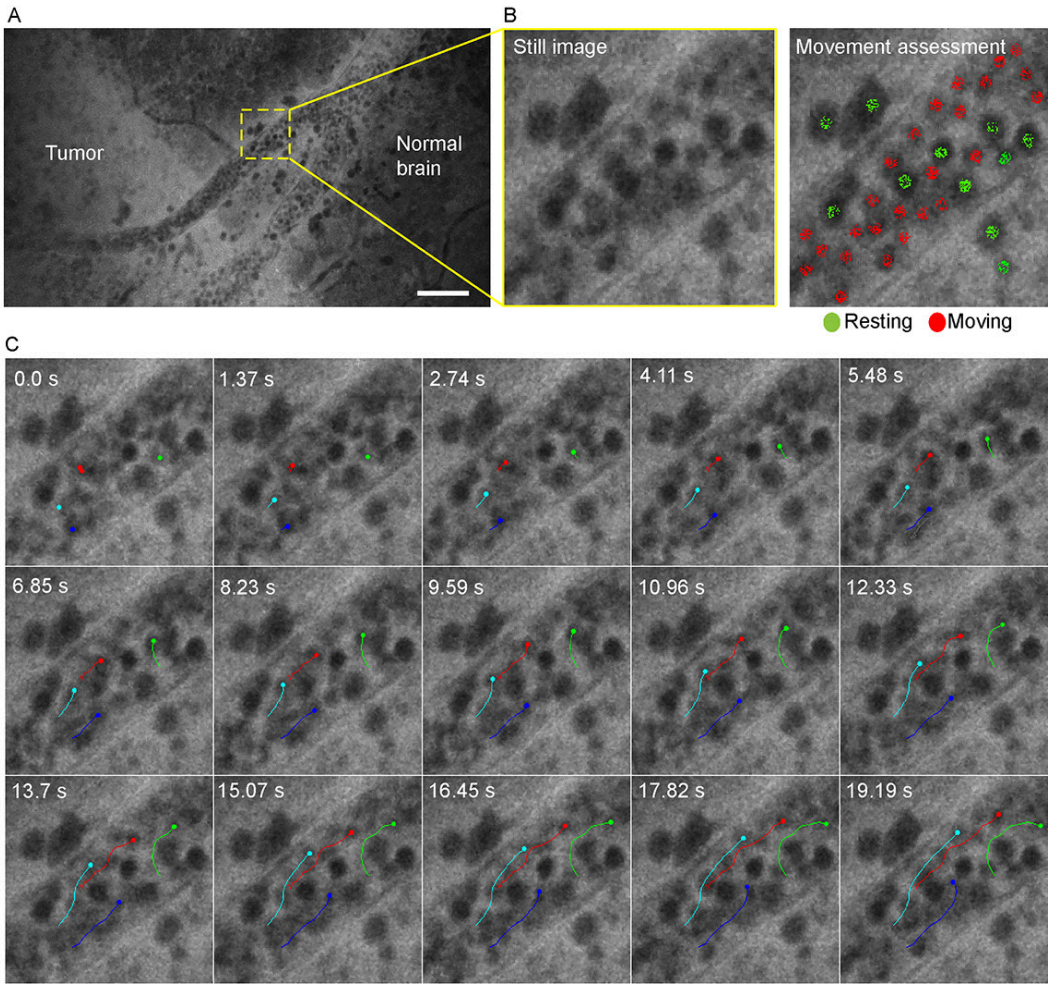

Figure 2.3. Time series imaging to differentiate stationary and mobile cells using a Gen2 confocal laser endomicroscope. (A) Single frame from time-lapse image. (B) Enlarged view of the vessel (left) and same image with moving cells labeled red and stationary cells labeled green (right). (C) Tracking of the selected cells shows intravascular movement of individual blood cells. Particle tracking performed in FIJI. Scale bar is 50 µm. Used with permission from Barrow Neurological Institute, Phoenix, Arizona.

Histologic Features During CLE Imaging with FNa (Gen1 and Gen2)

In no case was the tumor location uncertain based on CLE images after successful intravenous FNa injection. When imaging normal brain without tumor using CLE, FNa could be seen inside blood vessels, and occasionally leaking from vessels because of damage from surgery. Red blood cells could be visualized in these vessels as dark moving objects. No FNa was seen in other areas of the normal brain, other than intravascularly, except for sparse autofluorescent cells. Ultimately, the area of brain away from the vessels appeared similar to the brain when FNa had not been injected, with both generally lacking fluorescence, except for rare autofluorescent cells and with limited fluorescence (Figure 2.4). After FNa injection, tumor cells were seen as nonfluorescent cells on a highlighted fluorescent background.

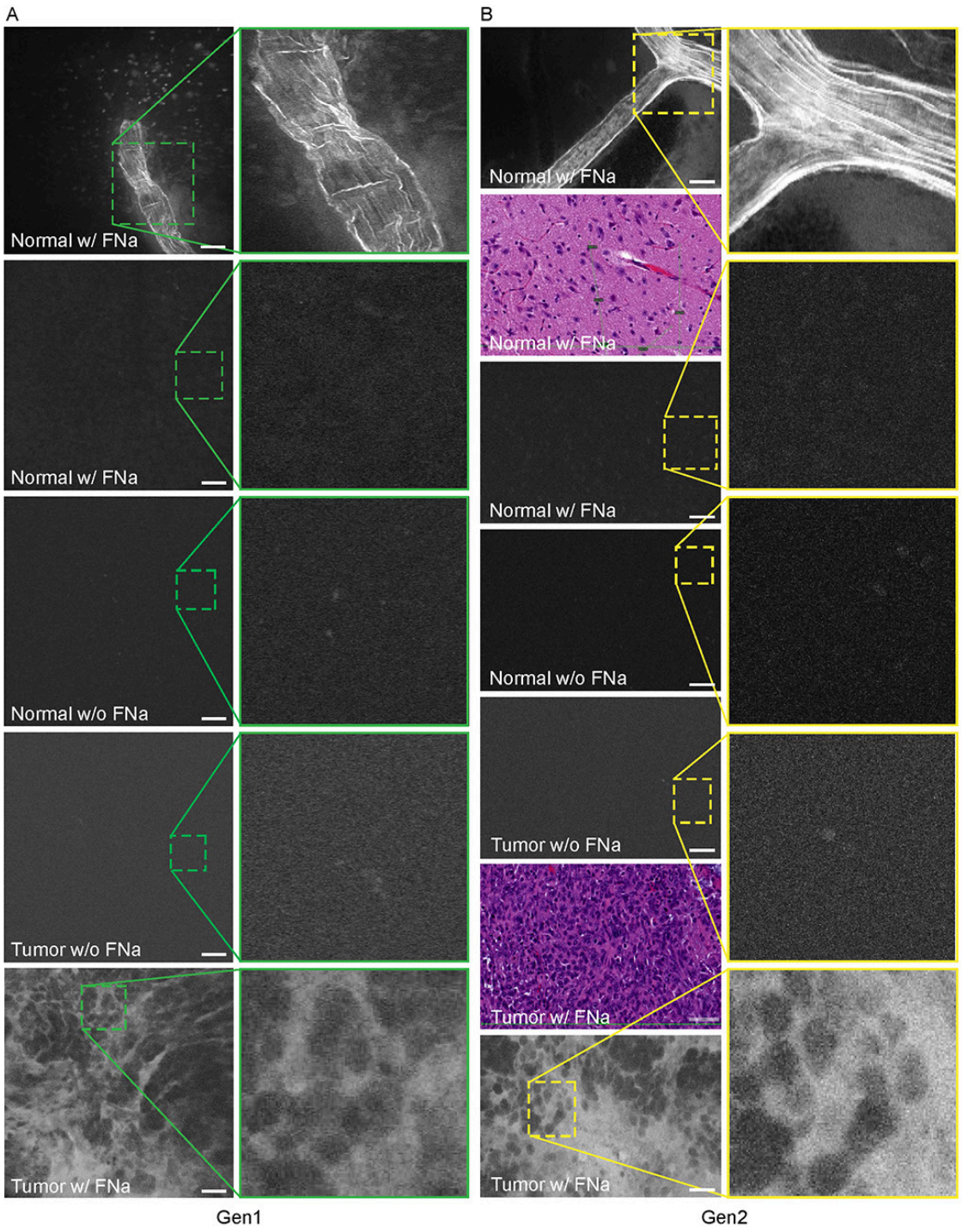

Figure 2.4. Confocal laser endomicroscopy (CLE) images of normal mouse brain, GL261 brain glioma, visualized with and without fluorescein sodium (FNa), using (A) generation 1 (Gen1) and (B) generation 2 (Gen2) CLE. Brain vasculature, brain parenchyma, and

tumor staining patterns were observed with similar quality between Gen1 and Gen2 systems. The insets show similarly magnified views from Gen1 and Gen2 systems. Additional hematoxylin and eosin (H&E) images are provided from the regions of interest of normal brain and glioma areas scanned with Gen1 and Gen2 CLE. Scale bars are 50 μm. Used with permission from Barrow Neurological Institute, Phoenix, Arizona.

Abnormal tumor vasculature was seen in several tumor biopsy spots (Figure 2.5). A gradient of FNa in the tumor was observed on images and may suggest proximity to the tumor vessels (Figure 2.6).

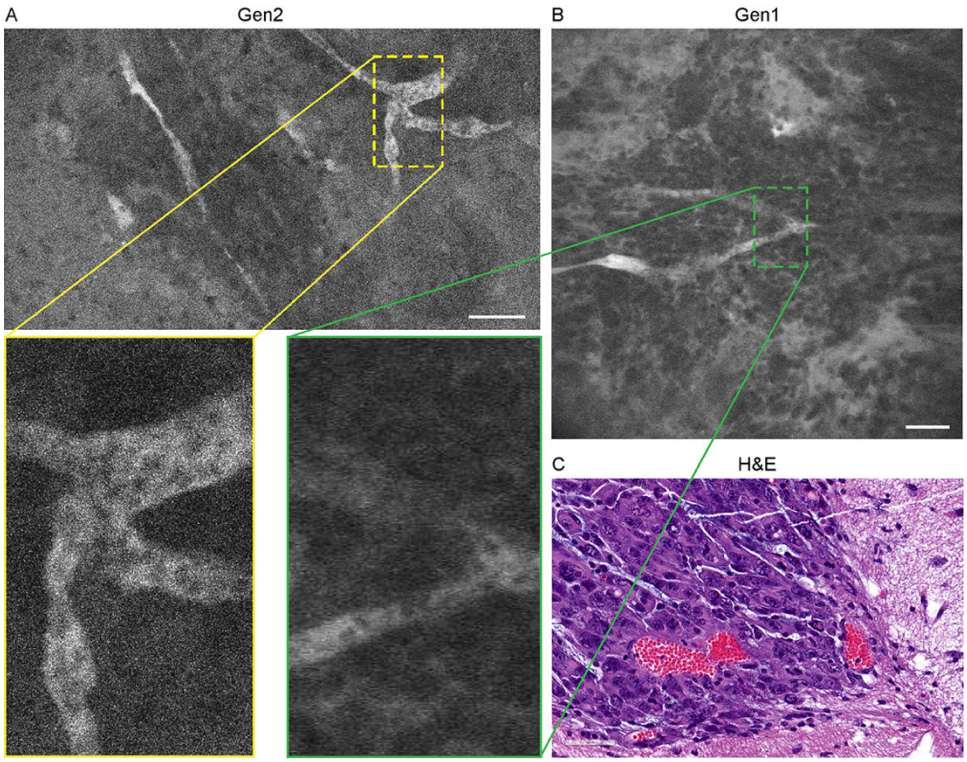

Figure 2.5. Abnormal tumor vessels visualized with (A) generation 2 (Gen2) and (B) generation 1 (Gen1) confocal laser endoscopes (CLE) after fluorescein sodium injection. CLE images show similar tissue architecture pattern. (C) Hematoxylin and eosin (H&E)-

stained tumor tissue shows tumor vasculature. Scale bar is 50 µm. Used with permission from Barrow Neurological Institute, Phoenix, Arizona.

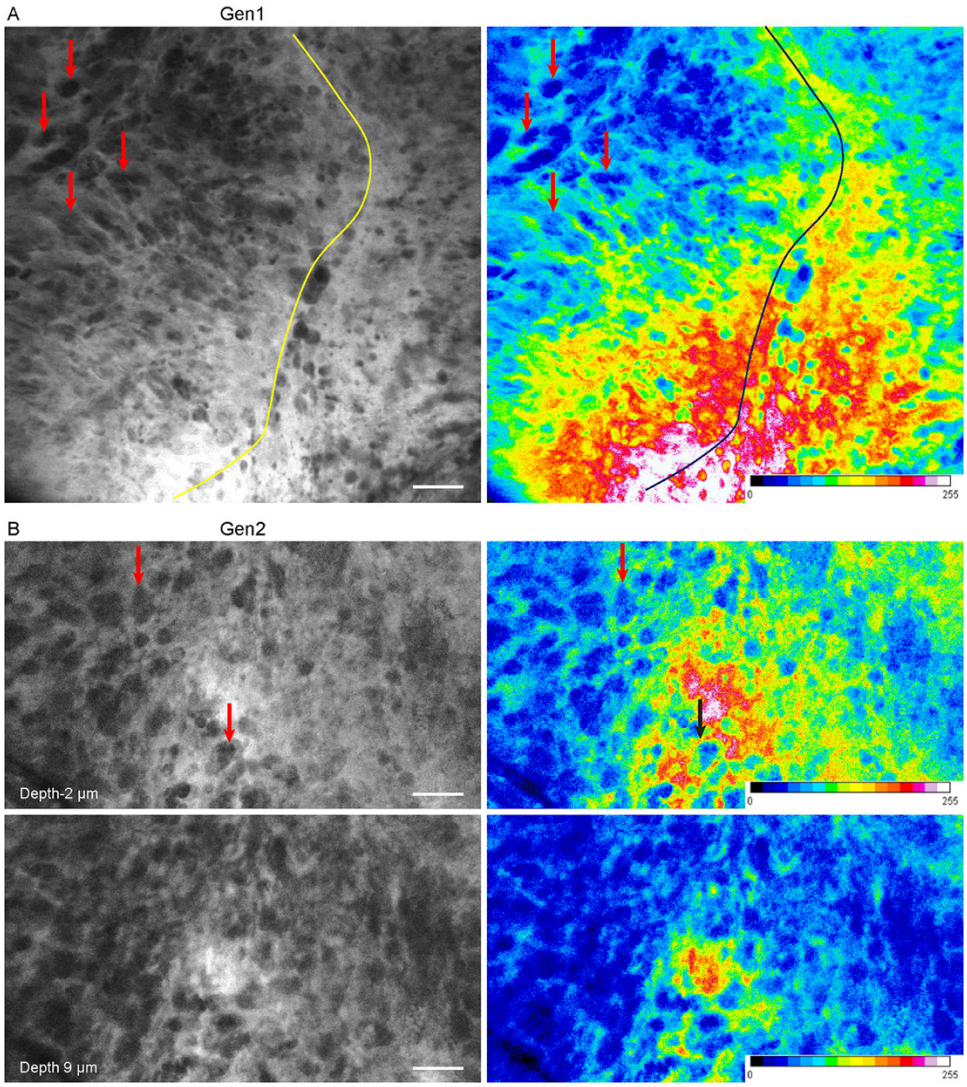

Figure 2.6. Fluorescein sodium diffusion gradient from the vessel into the tumor. Images acquired with (A) generation 1 (Gen1) and (B) generation 2 (Gen2) confocal laser endomicroscopes. Arrows point to the individual tumor cells. The bright area shown in red represents the area close to the vessel. Dotted line shows tumor border, with tumor

located to the left. Scale bar is 50 µm. Used with permission from Barrow Neurological Institute, Phoenix, Arizona.

Average nuclei sizes measured on AO-stained tumor images (11.9 ± 2.5 µm) were not different (p=0.10) to those measured on FNa-contrasted CLE brain tumor images (11.6 ± 2.5 µm), suggesting validity of identification of nuclei on the FNa-based confocal images. The average nuclei size was significantly smaller (p<0.01) than the cell sizes (20.8 ± 3.9 µm) (Figure 2.7). Benchtop confocal LSM of fresh samples stained with FNa (in vivo, intravenous) and Hoechst (rapid ex vivo, topical live cell nuclear stain) showed images similar to CLE grayscale images and provided additional confirmation regarding the dimensions of nuclei and cells observed with CLE (Figure 2.8).

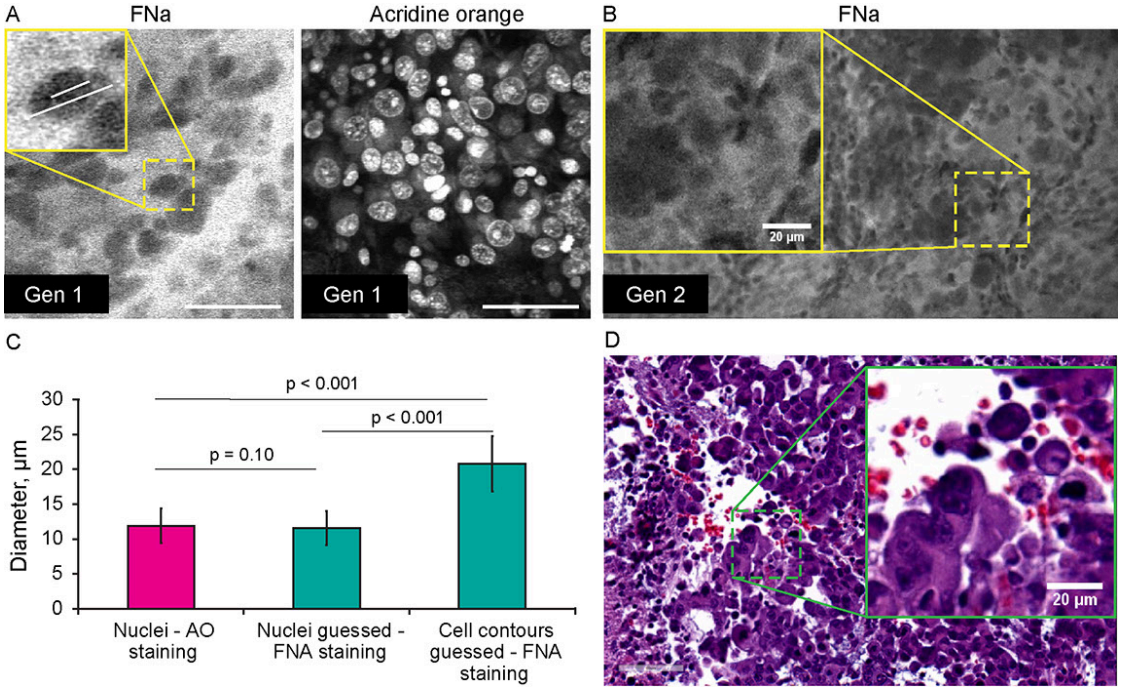

Figure 2.7. Identified cellular features. (A and B) Comparison of the tumor cellular features visible on confocal laser endomicroscopy images with fluorescein sodium (FNa) and acridine orange (AO). AO staining of the same specimen shows true nuclei size.

Gradient of FNa distribution delineates cell contours with bright gray, while cell nuclei may be visible in some of the cells in a darker gray. (C) Comparison of the nuclei size measured on the images with AO staining to the nuclei size measured on the images with the FNa staining (n = 106 cells measured with AO stain; n=53 nuclei and n = 52 cell diameters were measured with FNa stain). The average nucleus size determined on the FNa images was similar to the true average nucleus size based on the AO staining. Generation (Gen) 2 CLE image (B) shows anisocytosis, similar to (D) histologic findings. Scale bar in A is 50 μm. Used with permission from Barrow Neurological Institute, Phoenix, Arizona.

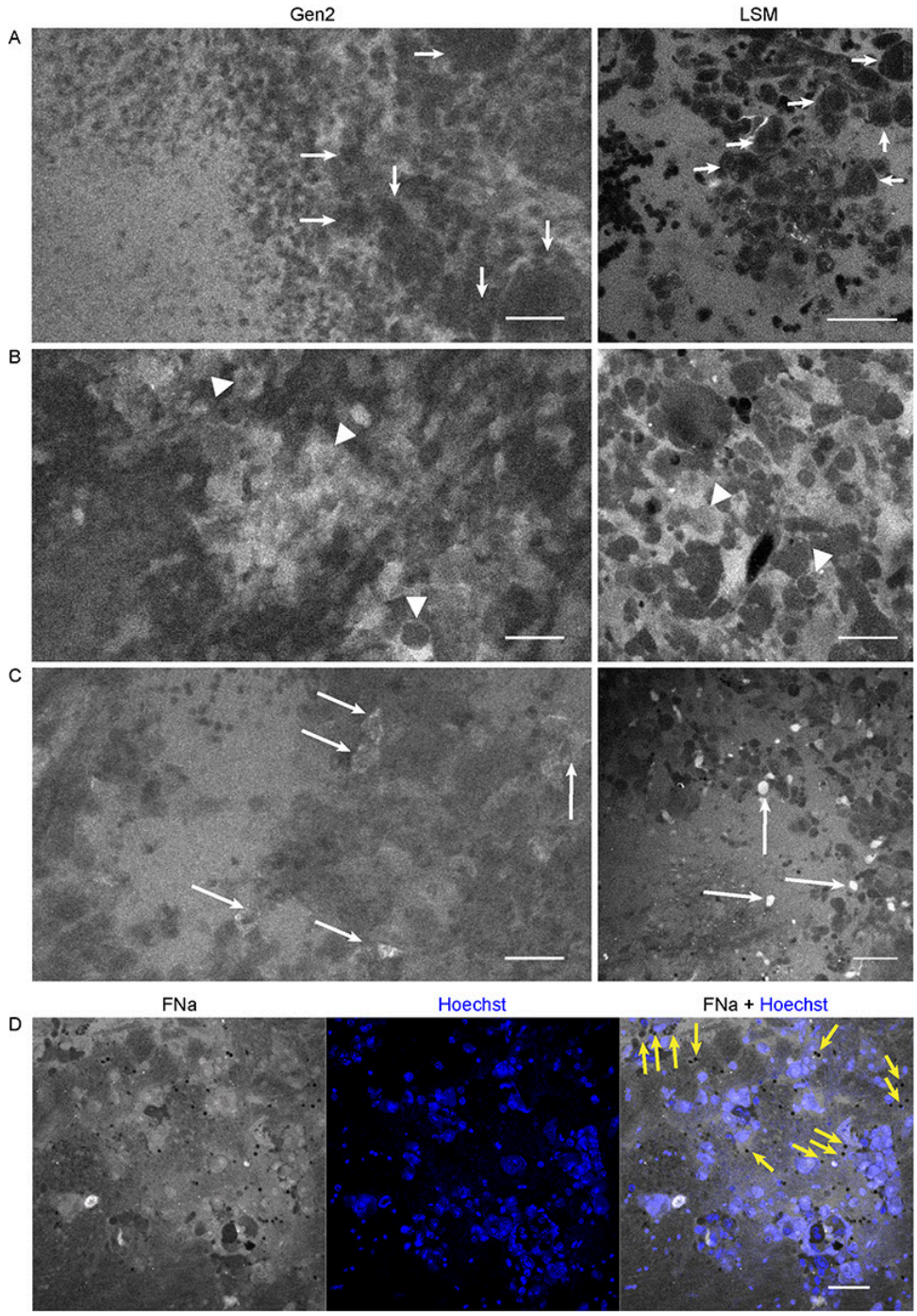

Figure 2.8. Confocal laser endomicroscopy (CLE) patterns of GL261 glioma core. In vivo Gen2 CLE and rapid ex vivo laser scanning microscopy (LSM) images show higher fluorescein sodium (FNa) signal in the tumor area and visible contours of the tumor cells.

Overall tissue architecture presents similarly in CLE and LSM images. (A) Most often tumor cells appeared darker than the background (arrows), while in some areas (B and C) tumor cells absorbed FNa and appeared bright. (D) Red blood cells, which were not stained by the Hoechst dye, are visible on a bright FNa background (yellow arrows). Scale bars are 50 μm. Used with permission from Barrow Neurological Institute, Phoenix, Arizona.

The tumor margin was visible in the GL261 model with both CLEs. The tumor border region appeared as a non-uniform delineation between the area with low FNa signal that did not contain atypical cellular features (normal brain) and an area with high FNa signal containing silhouettes of the abnormal tumor cells (Figure 2.9). Benchtop confocal microscopy of samples stained with FNa in vivo and rapidly counterstained ex vivo with Hoechst suggested that FNa signal "followed" invasions of the tumor cells in the normal brain. It confirmed that many small cell contours visible with FNa are actually anuclear red blood cells. A gradient of FNa distribution from the tumor into the normal brain was also visible with the higher FOV confocal microscopy.

When normal brain tissue was injured, leaking FNa signal was visible. Brain regions of injury without tumor could be differentiated from regions of brain with tumor on CLE images by small and non-variable red blood cells being present, rather than large, numerous, and variable tumor cells (Belykh, Miller, Patel, et al. 2018).

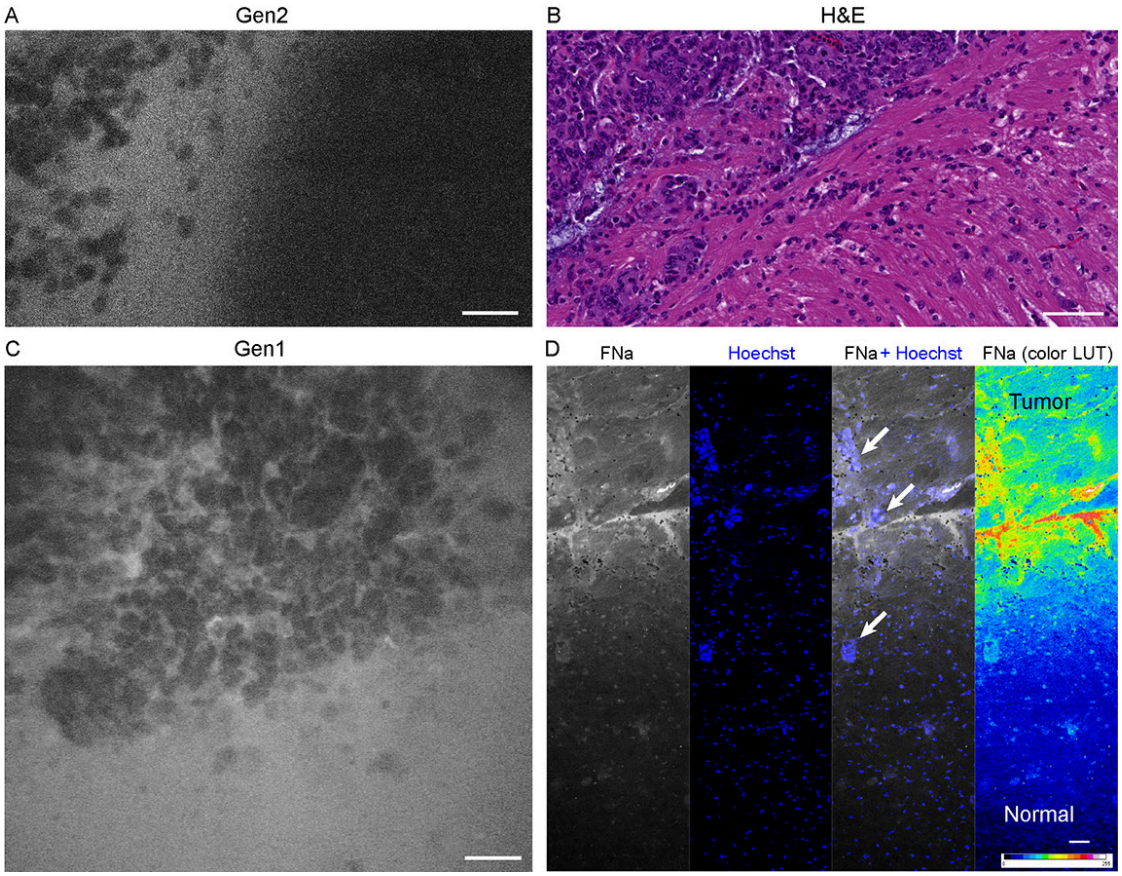

Figure 2.9. Tumor border 1 hour after intravenous fluorescein sodium (FNa) injection. (A) Generation 2 (Gen2) and (C) generation 1 (Gen1) confocal laser endomicroscopy images show a similar cellular architecture pattern of the GL261 glioma border region. (B) Hematoxylin and eosin (H&E) image of the tumor border from a matched sample. (D) Larger field of view ex vivo benchtop confocal image shows gradient of fluorescein diffusion from the tumor to the normal brain. LUT = look-up table. Scale bars are 50 μm. Used with permission from Barrow Neurological Institute, Phoenix, Arizona.

FNa Doses for Optimal CLE Imaging

Different concentrations of intravenous FNa as a contrast for CLE imaging yielded variations in image appearance. Bolus injections of higher concentrations of FNa resulted in brighter images of tumors with less noise, and an overall increase in the fraction of diagnostic frames, compared to lower FNa concentrations ($R = 0.5$, $p<0.05$) (Figure 2.10). The best working dosages were 20 mg/kg and 40 mg/kg and are in accordance with previous publications (100 mg/kg (Foersch et al. 2012); 8 mg/kg (Sankar et al. 2010); 7.7 mg/kg (Diaz et al. 2015)). Based on our experience, imaging closer to the time of FNa injection produced images with greater contrast and overall higher quality compared with images obtained longer after the injection.

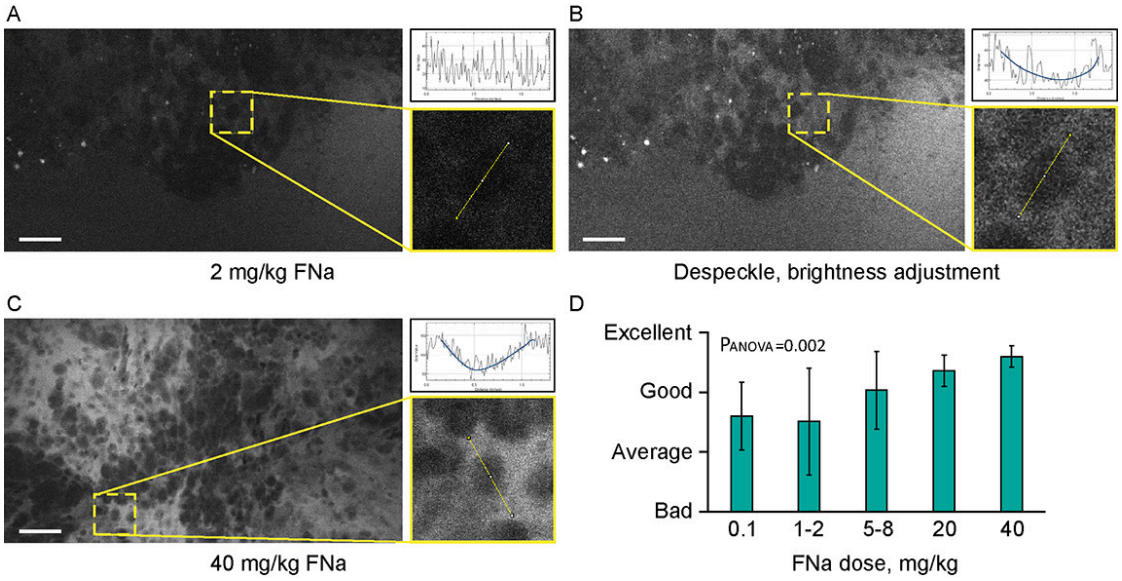

Figure 2.10. Higher concentrations of fluorescein sodium (FNa) produces images with less noise on a generation 2 confocal laser endomicroscope. Images acquired with a low dose of FNa **(A)** could be postprocessed to improve brightness **(B)**, so they appear similar to higher FNa dose images **(C)**. Comparison of the enlarged regions in A, B, and C shows

that cell contours are distinguished on all images; however, noise level (diagrams in A, B, and C) is less with a higher FNa concentration. **(D)** Subjective grading of overall CLE imaging quality is presented as a mean of all grades from 5 independent raters. The image quality is significantly better with higher FNa dosages (P_{ANOVA}=0.002). Scale bars are 50 μm. *Used with permission from Barrow Neurological Institute, Phoenix, Arizona.*

Histologic Features During CLE Imaging with 5-ALA (Gen1 and Gen2)

Neither Gen1 nor Gen2 CLE were reliably able to detect PpIX fluorescence in experimental tumors after 5-ALA administration. At the same time, Pentero 900 imaging with a dedicated Blue 400 filter showed very bright red PpIX fluorescence with all tumor masses. Gen2 CLE detected some signal in several tumor areas; however, this signal was not consistent in different locations imaged over the tumor area. Most imaging of the tumor showed dark images without visible signal. In all 5 animals interrogated with both Gen1 and Gen2, reliable histologic features of tumor or normal brain were not discernible with PpIX fluorescence. However, sparse fluorescent spots were observed in normal brain and tumor in experimental animals and were likely autofluorescence. (Croce and Bottiroli 2014) Overall image intensities when comparing the normal brain and tumor areas, and acquired with the similar parameters, showed significant differences ($p<0.01$) (Figure 2.11).

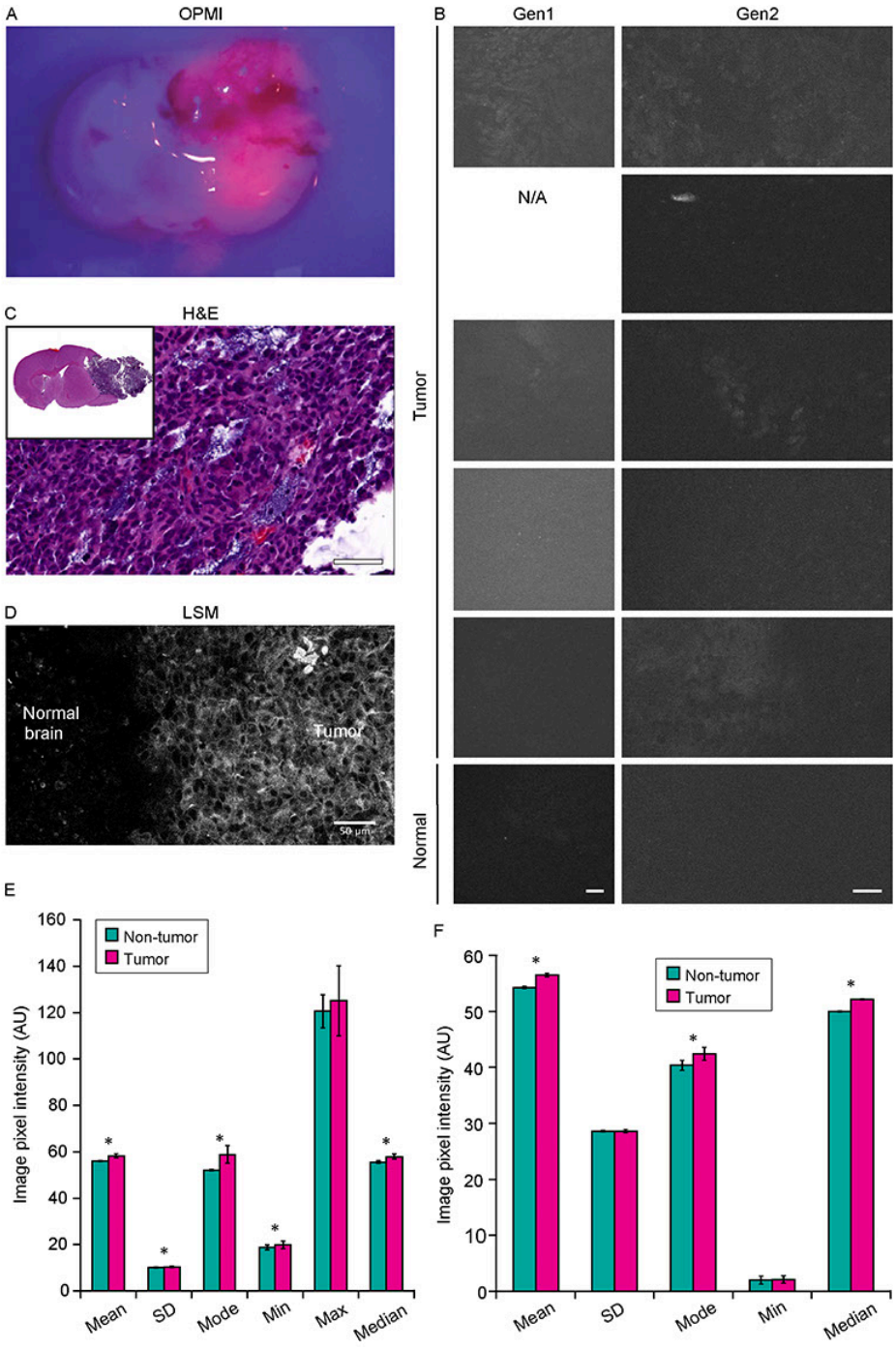

Figure 2.11. Confocal laser endomicroscopy (CLE) imaging of GL261 glioma with 5-aminolevulenic acid (5-ALA). (A) Representative image of a coronal brain slice with a tumor viewed through the Pentero 900 operative microscope in Blue 400 mode shows

bright red fluorescence from the tumor. (B) The best representative generation 1 (Gen1) and generation 2 (Gen2) CLE images of tumor (rows are 5 separate animals) and normal brain 2 hours after intraperitoneal 5-ALA administration. Normal brain shows no fluorescent signal in any of the cases. Fluorescent signal from tumor is very low, visible only from a few areas and is not consistent across the biopsy locations and across the animals imaged. (C) Hematoxylin and eosin (H&E) coronal slice of the brain with a tumor shows hypercellular tumor in the areas from which CLE imaging was performed. (D) Laser scanning microscopy (LSM) image at the tumor margin shows the protoporphyrin signal localized to tumor cell cytoplasm. The image displayed in grey scale and size is similar to Gen2 CLE. (Image acquired with 40× 1.2 W objective; 405 nm excitation; 598-740 nm detection range.) (E) Gen1 CLE imaging of GL261 gliomas and contralateral normal brain as a control with 5-ALA. Quantification of the images (n=54 control; n=59 tumor images from 5 animals) showed minimal, but yet significant difference in the overall pixel intensities of the images taken from the tumor vs. normal brain. Groups were compared using t tests; an asterisk indicates $p<0.01$. (F) Quantification of the Gen2 CLE images (n=5 control; n=4 tumor) showed minimal, yet significant differences in the overall pixel intensities of the selected best images taken from the tumor and normal brain. Groups were compared using t tests; an asterisk indicates $p<0.01$. Selected images were acquired with similar CLE settings. Scale bars are 50 μm. AU = arbitrary unit. Used with permission from Barrow Neurological Institute, Phoenix, Arizona.

Influence of Imaging Parameters on the Image Quality (Gen2 System)

Imaging Filter

Imaging using green bandpass or green longpass filters was compared on both systems to visualize FNa in mouse glioma models. Images acquired with the longpass filter appeared brighter. At the same time, quantitative analysis showed that the bandpass filter resulted in significantly better contrasted images (Figure 2.12). With autobrightness function on, some Gen2 images (using FNa or AO as a contrast) appeared subjectively dark. However, adjusting the brightness during postprocessing resulted in significantly better contrasted images than when using the longpass filter. The red longpass filter was not useful for FNa imaging; however, scant cells and structures emitted light in the red spectrum within normal brain and tumor areas.

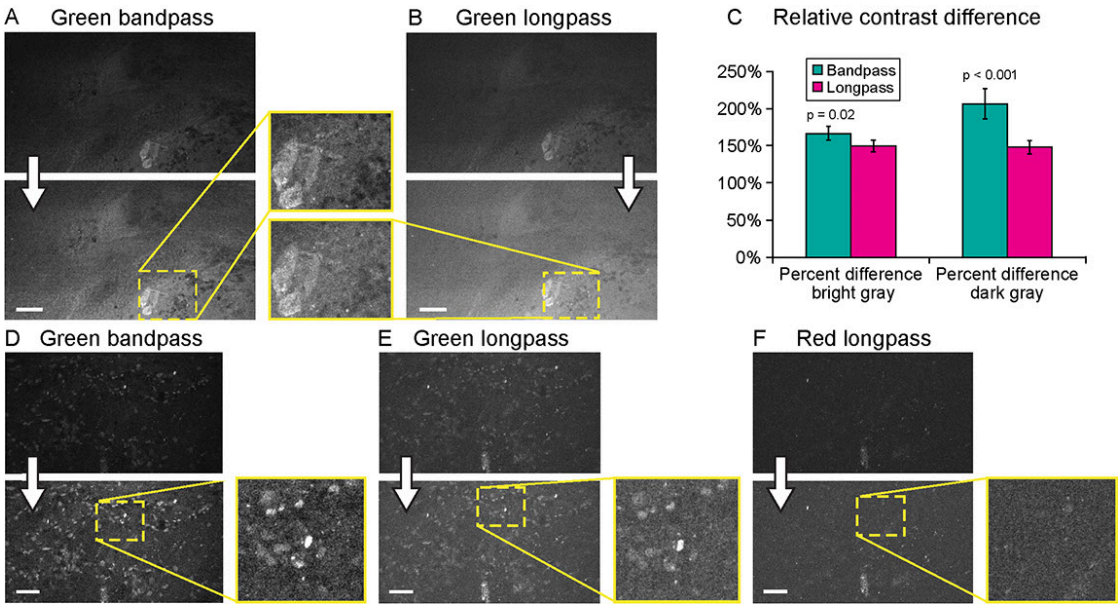

Figure 2.12. Generation 2 confocal laser endomicroscope (CLE) imaging with various filters. Comparison of the CLE images taken from the same regions of interest with green bandpass (A, D), green longpass (B, E), and red (F) optical filters. Human glioma

samples (patients were injected with FNa intraoperatively) were used for analysis and illustration. Thick arrows signify postprocessing in FIJI, which includes despeckling and maximum brightness adjustment. (C) Matching regions of interest (ROI) were selected in FIJI to compare contrast between various structures in longpass and bandpass filters. ROIs were manually drawn over the brightest structures (n=5), over the surrounding gray background (n=3), and on the dark round structures (n=5). Paired t tests were used for comparison. D, E, and F images are taken at the same location. Scale bars are 50 μm. Used with permission from Barrow Neurological Institute, Phoenix, Arizona.

Detector Gain

When FNa was used, images were acquired mainly with a gain at the mid-position (2400). Very bright fluorescent specimens (10-40 mg/kg FNa) required gain adjustments on only rare occasions, as control was usually possible for oversaturated pixels and image quality by lowering the laser power and brightness (Figure 2.13).

Laser Power

For FNa imaging, laser power was usually at 50% (500 mW). In locations that produced dark images (low FNa or bleached areas), increasing the laser intensity improved image quality and brightness to some extent, but further increases in laser power did not result in quality improvement. The functioning of laser power control was not different between Gen1 and Gen2 systems. Overall, grossly bright fluorescent samples resulted in excellent contrast and quality at 50% laser power and gain position at the midpoint range (2400) (Figure 2.14).

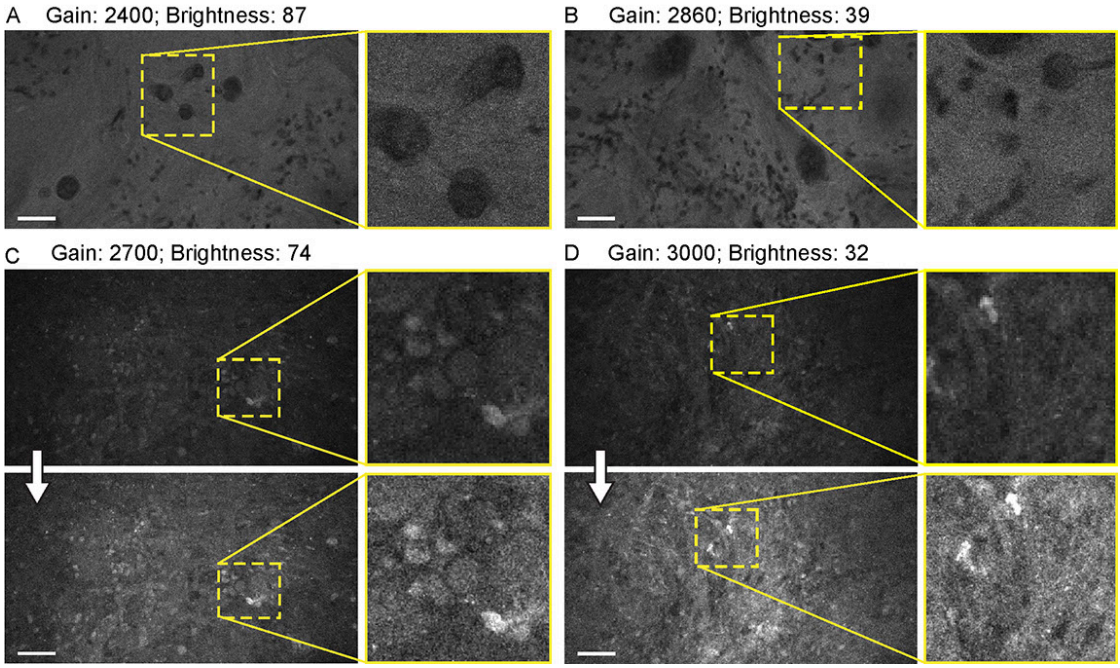

Figure 2.13. Balanced generation 2 (Gen2) confocal laser endomicroscope (CLE) images with different gain results in comparable image quality. (A-D) Comparison of the CLE images taken with various gain setup. Human meningioma (A, B) and glioblastoma (C, D) samples scanned ex vivo 2 hours after fluorescein sodium (2-mg/kg) injection are used for analysis and illustration. Increase in the gain requires reciprocal adjustments in the brightness. Overall, the resulting images have comparable quality. Images (A) and (B) are visualized from one patient, while images (C) and (D) are visualized from a different patient. Thick arrows signify postprocessing in FIJI, which includes despeckling and maximum brightness adjustment. Scale bars are 50 μm. Used with permission from Barrow Neurological Institute, Phoenix, Arizona.

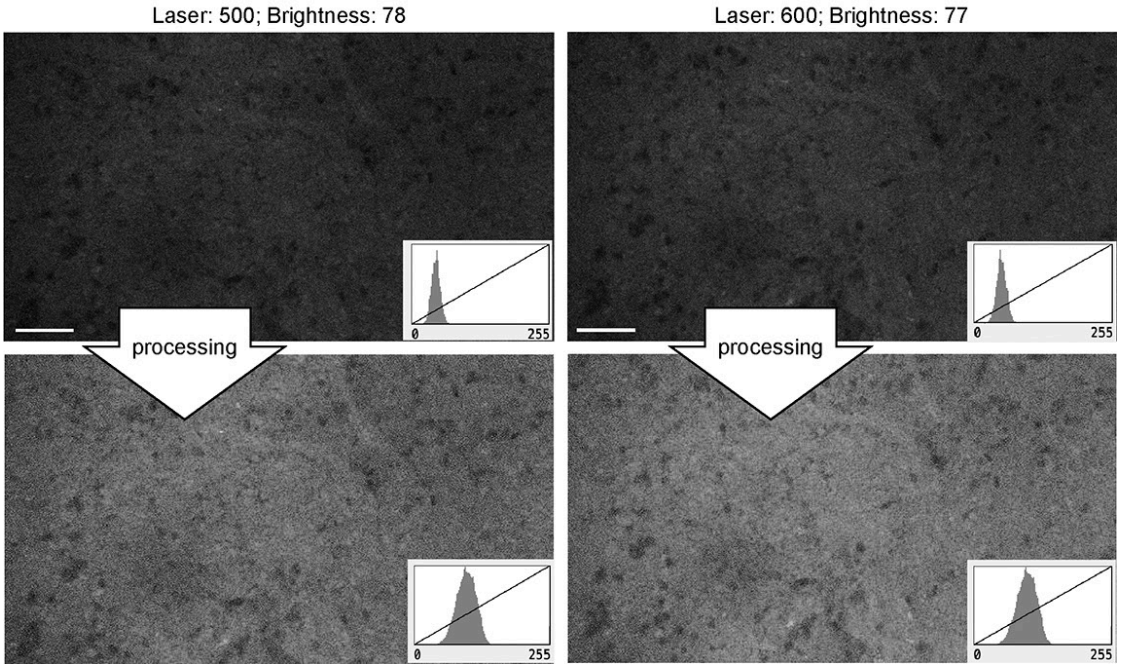

Figure 2.14. Generation 2 confocal laser endomicroscope images taken at different laser intensity values. A human meningioma sample is used for analysis and illustration. Brightness was kept at a similar level during image acquisition. Increase in the laser intensity from 500 mW (upper left) to 600 mW (upper right) leads to a brighter overall image. Further increase in laser power does not improve contrast. Thick arrows signify postprocessing in FIJI, which includes despeckling and maximum brightness adjustment. There are no subjective differences in images after postprocessing (lower row). Scale bars are 50 μm. Used with permission from Barrow Neurological Institute, Phoenix, Arizona.

Image Brightness and Noise

The autobrightness function auto-adjusts the brightness of the image on the fly during continuous imaging based on the brightness histogram of the precedent image,

independently from the gain and laser power settings. With one exception, the autobrightness function of the Gen2 was advantageous for rapid image and optimal brightness display, contrasting with the Gen1 that lacked this function and required frequent manual adjustments. The exception occurred when the image had abnormally bright artifacts. In such situations, the autobrightness function decreased the overall image brightness, with FNa signal in the tumor interstitium becoming low and barely detectable—this was observed both qualitatively in real time and quantitatively during postprocessing. In such situations, manual brightness setup was used to obtain better overall image quality.

When the autobrightness function was on, the increase in gain resulted in a proportional decrease in automatic brightness level. Brightness values can be indicative of noise level. Brightness levels below 80% were the most optimal with less black noise, compared to a brightness level of 80% and above. To keep the noise levels low, the brightness values were maintained at below 80% (Figure 2.15).

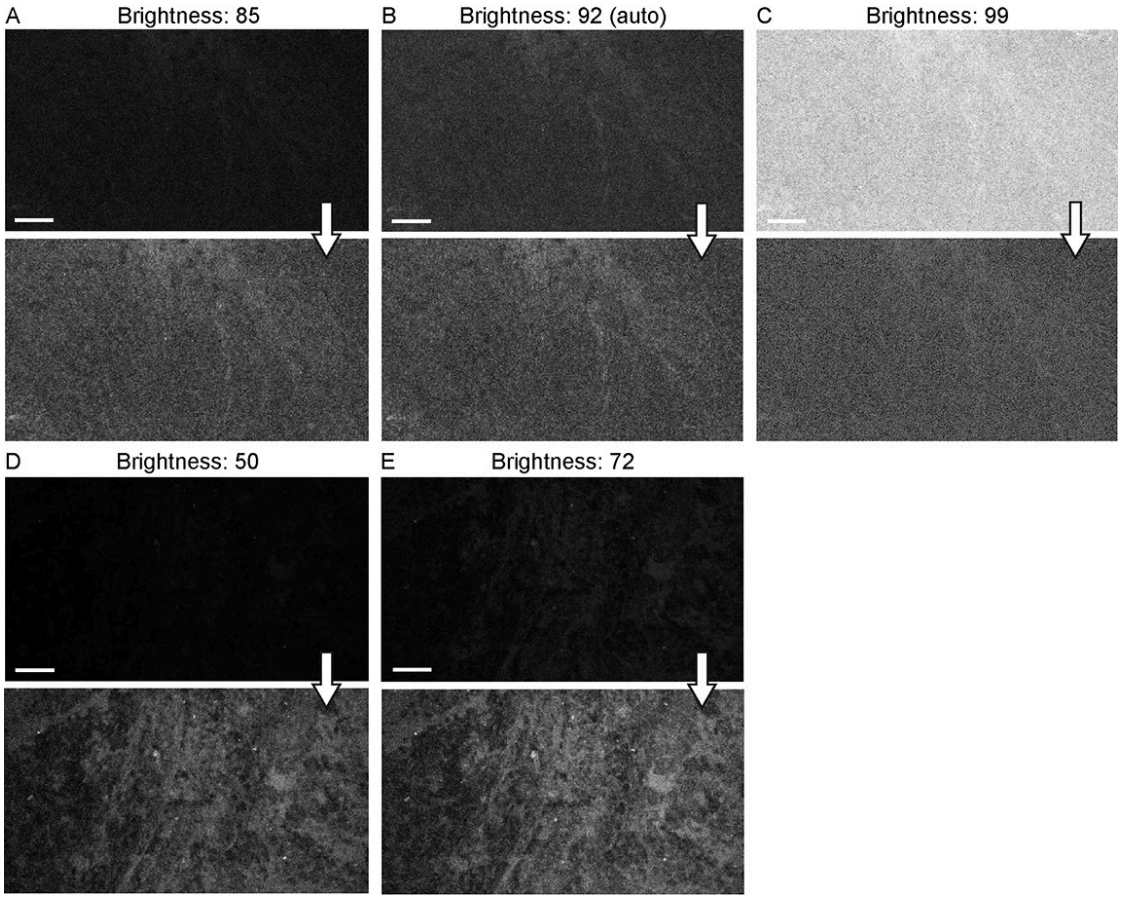

Figure 2.15. Generation 2 confocal laser endomicroscope (CLE) images taken with different brightness setup. (A-E) Comparison of the CLE images taken with various brightness settings. The same fields of view of meningioma (A, B, C) and low-grade glioma (D, E) human samples are used for analysis and illustration. Brightness is in the automatic position for figure (B); in all other figures, brightness is set manually. Increase in brightness higher than automatic position does not increase image quality quantitatively (C). Thick arrows signify postprocessing in FIJI, which includes despeckling and maximum brightness adjustment, except for figure (C) in which brightness is decreased with postprocessing. Scale bars are 50 μm. Used with permission from Barrow Neurological Institute, Phoenix, Arizona.

To further assess the effect of Gen2 imaging parameters on image quality, background noise levels were studied. Imaging of normal brain with various manually set brightness levels revealed that mean image intensity and standard deviation of the individual pixels had a positive correlation with brightness level (Figure 2.16). At 91% brightness, 50% laser power (505 mW), speed 1080 (~0.78 frames per second), and gain 2400, the average pixel intensity from a normal brain (black color) was 53.5 arbitrary units, corresponding to about 20% saturation of the 8-bit image.

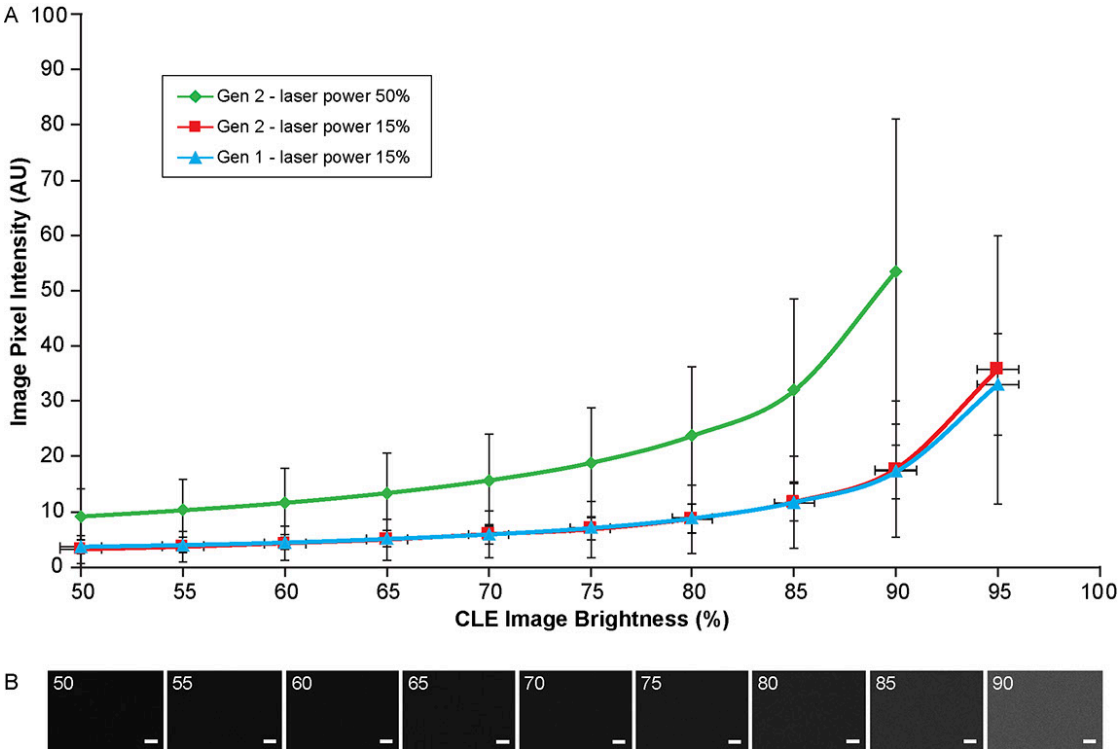

Figure 2.16. Image brightness and background noise level with the generation 1 (Gen1) and generation 2 (Gen2) confocal laser endomicroscope (CLE). Image brightness and background noise level depend on the laser power and image brightness set up of the

CLE. (A) Graph showing observed image intensity in arbitrary units (AU) (y axis) at the various brightness positions, while imaging normal brain area. This value represents "black" noise. Brightness setting above 80% results in a significant increase of black noise, which may decrease image quality. Therefore, when imaging, one should aim at getting a picture at a brightness levels below 80%. (B) Unprocessed Gen 2 CLE images taken at various indicated brightness levels (%) that are set manually. Scale bars are 50 μm. Used with permission from Barrow Neurological Institute, Phoenix, Arizona.

Image Acquisition Speed

Most images were acquired at speed 1080 (~0.78 frames per second), which allowed for the best quality (Table 2.1, APPENDIX B). Faster scanning at speed 135 (~3.8 frames per second) or speed 270 (~2.5 frames per second) was practically useful for rapid scanning of larger areas to determine presence or absence of FNa signal or for blood flow imaging (Figure 2.17). Some gross tumor tissue structures were visible at 135 or 270 speed settings but appeared overly pixelated on a CLE display. Image quality and contrast were significantly better at speed 1080, especially in areas with small vessels contrasted with FNa or when using nuclear stains (AO, AF).

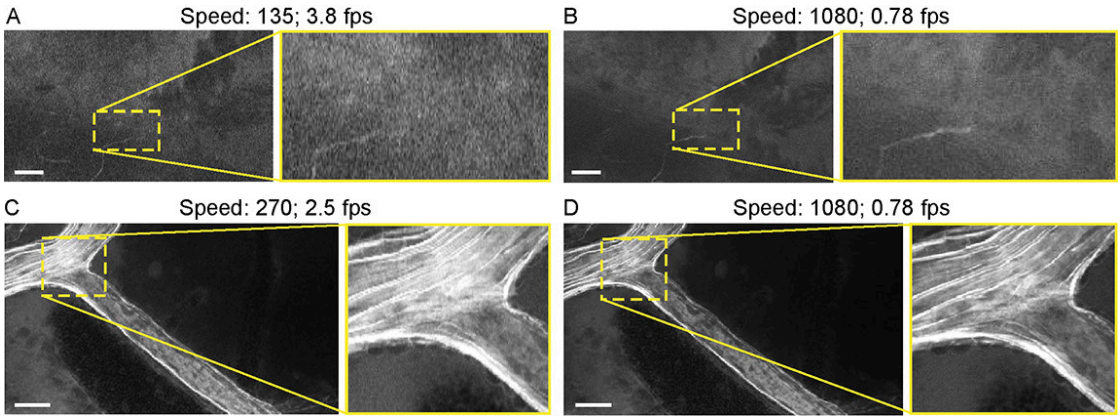

Figure 2.17. Generation 2 confocal laser endomicroscope (CLE) images taken at different speeds. Comparison of CLE images taken with 3 various acquisition speed settings: (A) 135, (B and D) 1080, and (C) 270. Images acquired at an intermediate speed setting (C) of 270 (calculated mean 2.5 frames per second) are of average quality and are able to resolve more structural details than images taken at the faster speed of 135 (A). Significant improvement in image quality at the slower speed of 1080 (B, D) is mostly apparent in the areas with high contrast, such as small vessels when fluorescein sodium is used. When viewed as smaller pictures, the differences are less pronounced. However, on a large high-definition display, the image quality at different speeds differs substantially. Scale bars are 50 μm. Used with permission from Barrow Neurological Institute, Phoenix, Arizona.

Discussion

The Gen2 CLE system is compatible with the specific demands of neurosurgical use. With the disposable sterile sheath that includes a coverslip, the Gen2 CLE can now be safely used on the human brain during surgery without the need for a complex

sterilization procedure after surgery, as was the case with the Gen1 system (Figure 2.18). The ergonomics of the probe conformation are such that it resembles a curved, lightweight neurosurgical suction device that will lie comfortably in the hand, grasped by the first few fingers, in a fashion that allows smooth, stabilized movement as a neurosurgeon is used to for surgical instruments. In this study, we performed a preclinical investigation of the Gen2 CLE, characterized its operation, capabilities, and limitations, and compared its performance to the Gen1 CLE system.

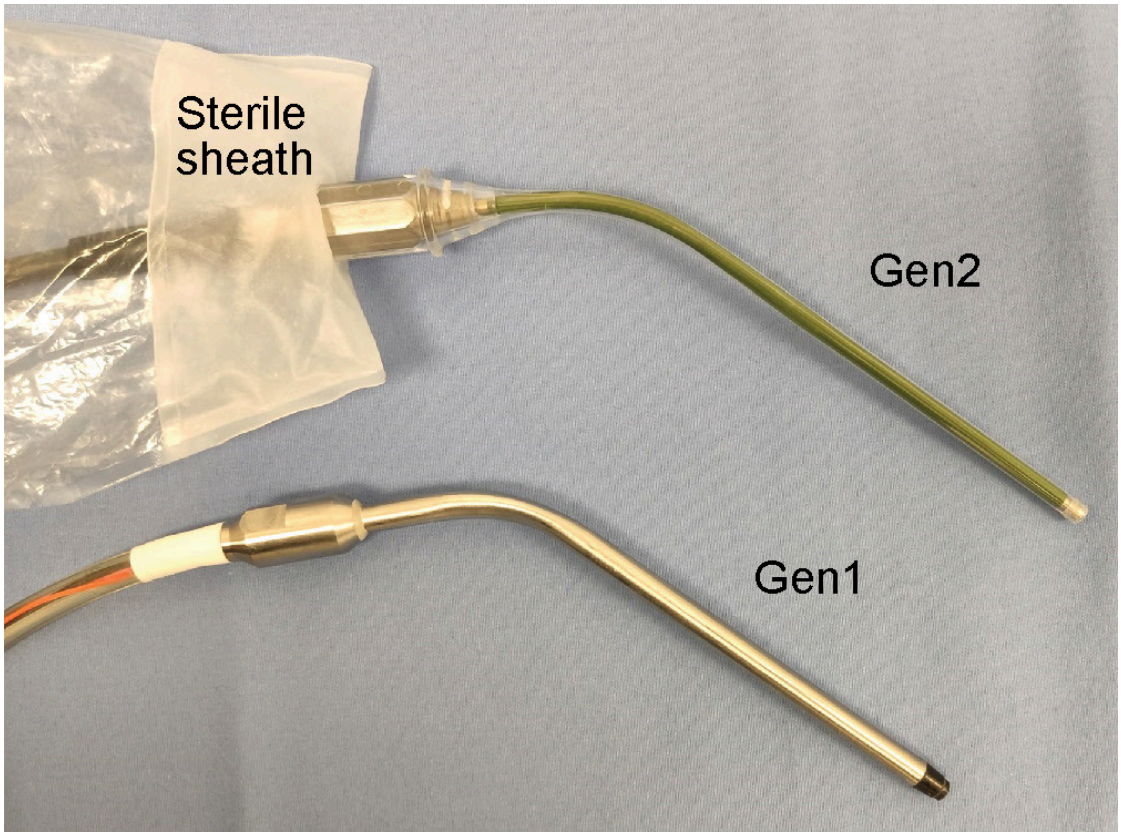

Figure 2.18. Generation 1 (Gen1) and generation 2 (Gen2) confocal laser endomicroscopes. Used with permission from Barrow Neurological Institute, Phoenix, Arizona.

Imaging Parameters (Gen1 and Gen2)

Multiple imaging parameters can be adjusted in both Gen1 and Gen2 systems making them flexible and capable of detecting a single-channel fluorescent signal over a broad range of intensity values. Gen2 is more adjustable, as it allows for changing most parameters rapidly during scanning, while with the Gen1, the user is required to create a new imaging session using the operating software interface to change the gain or filter. Another convenient advantage is that unlike the Gen1, the Gen2 imaging parameters are recorded as part of the file properties. Having access to these parameters is important for quantitative analysis and comparison among various images, especially to evaluate fluorophore signal intensity in the image, which correlates with the concentration of the fluorophore in the sample. For FNa-guided optical biopsy in brain tumors, such information may be used to assess the degree of blood-brain barrier disruption, to eliminate imaging artifacts, to identify potential causes of suboptimal images, or to improve images in postprocessing.

Still Images (Gen1 and Gen2)

While continuous imaging occurs at a chosen speed in both CLE systems, the recording options are different. Both systems have the option to record a single still image and time series, while the Gen2 can also automatically record Z-stacks. Still image recordings were used when the sample quality was perfect and when there was no concern about having only a few selected imaging frames recorded while interrogating the tissue. However, in most cases continuous recording was preferred and advantageous,

which is discussed later. Finding the exact same position again is nearly impossible with a CLE system due to the minute dimensions on the order of fractions of a millimeter (475 × 475 μm for Gen1; 475 × 267 μm for Gen2), contact probe design, and pliable nature of unfixed brain tissue. Thus, there was always a concern of not being able to return the CLE to the previous imaging plane. Therefore, still recordings were used less frequently than Z-stacks or time series. Incorporation and registration of the probe into an image-guided surgery navigation system would allow improvement in reassessing tissue imaging location.

Z-stack Function (Gen2 Only)

A Z-stack is a series of images taken in rapid succession at different depths and a constant position (Belykh, Patel, Miller, Bozkurt, Yağmurlu, et al. 2018). The "Z-step" is the depth distance between images and is a novel feature for handheld CLE imaging with the Gen2 CLE system. The range of the Z-stack can be set by the user, and the Z-step is a constant 3 μm, resulting in 2 to 35 images per stack. At least several slices (maximum 10-13) from the Z-stack were acquired at optimal Z positions that were in focus, usable, and diagnostic (Belykh, Patel, Miller, Bozkurt, Yagmurlu, et al. 2018). Informative images from a Z-stack can be easily processed into video loops or semitransparent volumetric images for detailed assessment and further interpretation.

It also worth mentioning that the size of objects becomes larger when they are imaged out of focus deeper within the tissue. This could potentially make small red blood cells look larger than they are, thus imposing a minor potential for misdiagnosing small cells as tumor cells.

Time Series Recording and Video Loops (Gen1 and Gen2)

Time series (or "cine"-series) recordings were used extensively for postprocessing and creation of video loops. Continuous nonstop recording during Gen1 or Gen2 CLE interrogation of the sample was helpful compared with "on-demand" snapshot recording because with the latter technique some locations were bleached out before the image was recorded. The gradual photobleaching was definitely observed, but with practice, minimizing the scanning time avoided this problem. We did not investigate whether laser interrogation results in tissue damage. Although tissue damage is unlikely, we are conducting an ongoing investigation of the potential phototoxicity of CLE scanning. Additionally, minute tissue shifts changed the observed image before taking a picture and the probe often could not be returned to the desirable location because of the pliable nature of unfixed brain tissue. Z-position, brightness, and laser power can be adjusted during the time series imaging to record optimal quality images.

Notably, time series imaging revealed a "movement" feature of the tissue and supplemented visual information gained from still images. This feature is useful in several aspects for tissue histologic characteristics and CLE image interpretation. Primarily, differentiation of freely moving red blood cells from other moving or stationary cells becomes much easier and thus fosters the diagnostic accuracy of image and tissue interpretation. Additionally, it becomes easier to differentiate real signal from noise. By viewing time series, differentiation is possible between what is meaningful and what is merely stochastic noise. Such judgment is usually difficult on still images because of the nature of FNa. FNa is a non-specific dye that is not bound to any structure, but

rather provides a bright background (i.e., a silhouetted appearance) on which to observe, contrast, and differentiate structures. Noise is an inherent limitation of FNa. In vivo CLE demonstrated dynamics of the glioma environment for the first time, something that is not possible in fixed brain tissue.

It should also be noted that CLE allowed for in vivo tracking of blood flow in vessels. Tracking of individual blood cells is not always possible because of fast movements that require high-speed scanning confocal imaging systems, such as spinning disk confocal microscopes (Goetz et al. 2008, Norman et al. 2008, Belykh, Cavallo, Zhao, et al. 2018).

Histologic Pictures Visualized by CLE with FNa (Gen1 and Gen2)

The use of FNa with both distal scanning CLE systems was effective to visualize brain vasculature, red blood cells, silhouettes of neoplastic cells, nuclear and cell dimensions, GL261 glioma border, and brain injury. FNa aided detection of normal and tumor vessels and did not significantly highlight normal brain tissue. Cell nuclei and cytoplasm may be distinguished in some of the cells by a gradient of FNa penetration through different biological membranes (Figure 2.19). FNa extravasation due to injury can be differentiated from the FNa diffusion in the tumor using characteristic histologic patterns on CLE (Belykh, Miller, Patel, et al. 2018). It is worth noting that individual fluorescent cells were frequently observed in both tumor and normal brain (Figure 2.20). This phenomenon had various patterns and was observed more frequently with increased imaging time after FNa injection. Singular and multiple cells were observed that took up FNa on the cut surface of the tumors. Even though such images did not represent a

characteristic CLE image of tumor, they were helpful to assess the cell morphology, tissue architecture, and cytoplasm-to-nucleus ratio. The reason for such FNa uptake by some cells is still unknown, because tumor cells do not show FNa uptake in vitro (Diaz et al. 2015). However, it might be due to cell membrane disruption caused by injury, as such findings were seen mostly in ex vivo samples. Additionally, large singular cells that took up FNa seen in the tumor may be macrophages.

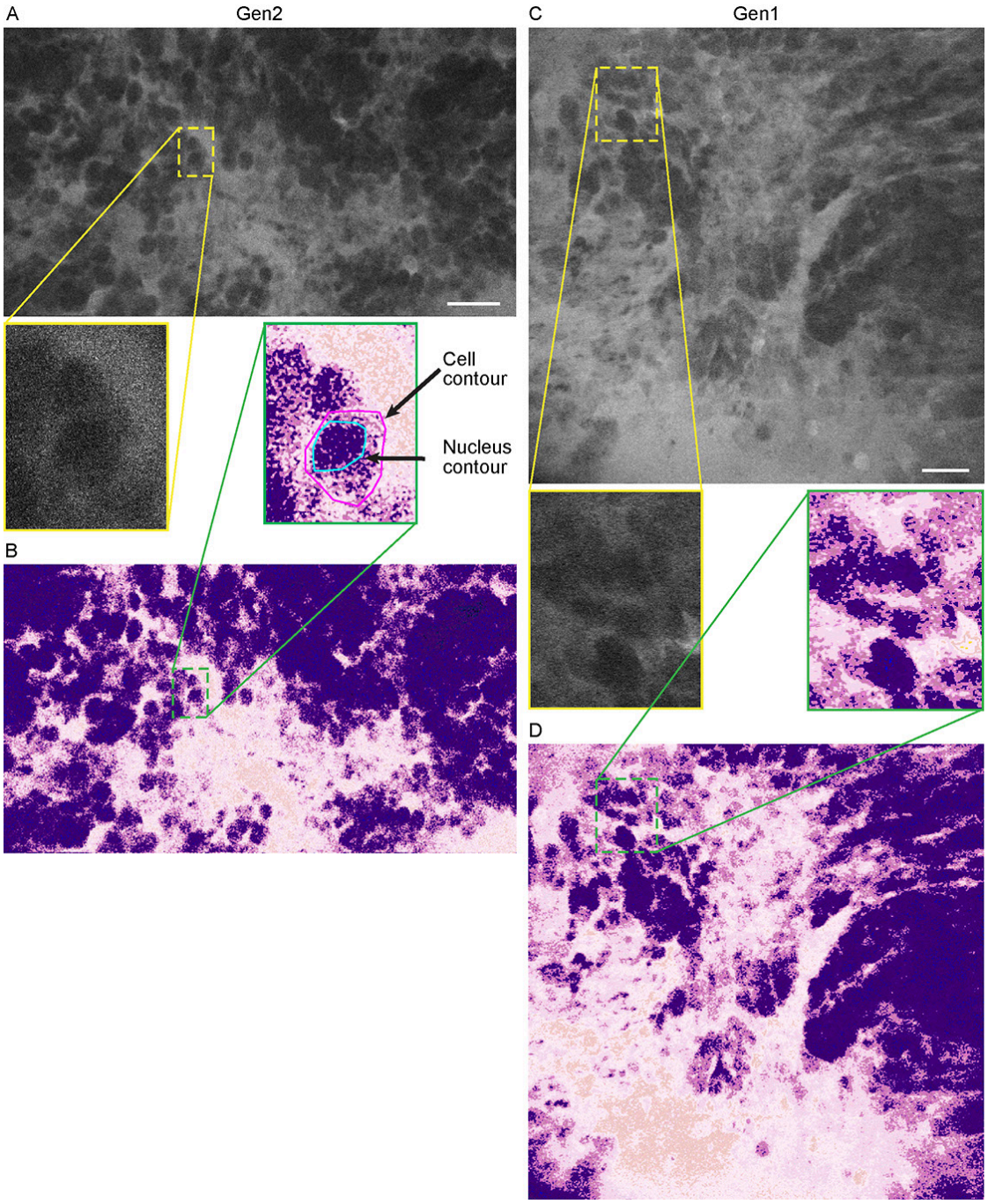

Figure 2.19. Fluorescein dye delineating nuclei and cellular silhouettes in brain tumor, as visualized by generation 1 (Gen1) and generation 2 (Gen2) confocal laser endomicroscopes (CLE). Images from (A) Gen2 and (C) Gen1 show how the gradient of fluorescein sodium penetration through the biologic membranes helps delineate nuclei

and cellular silhouettes in the animal brain tumor region. Image analysis performed in FIJI. Selected regions of interest are cropped, and filters are applied: despeckle, smooth, average 2 pixels. A custom color look-up table is applied on a grayscale image. Brightness was increased for better visualization of contrast between the gray tones. (B) and (D) are colored CLE images from Gen2 and Gen1 systems, respectively, in the style of a hematoxylin and eosin stain, to illustrate the similarity in quality between CLE imaging and histology. (A) and (B) are corresponding images. (C) and (D) are also corresponding images. Scale bar is 50 μm. Used with permission from Barrow Neurological Institute, Phoenix, Arizona.

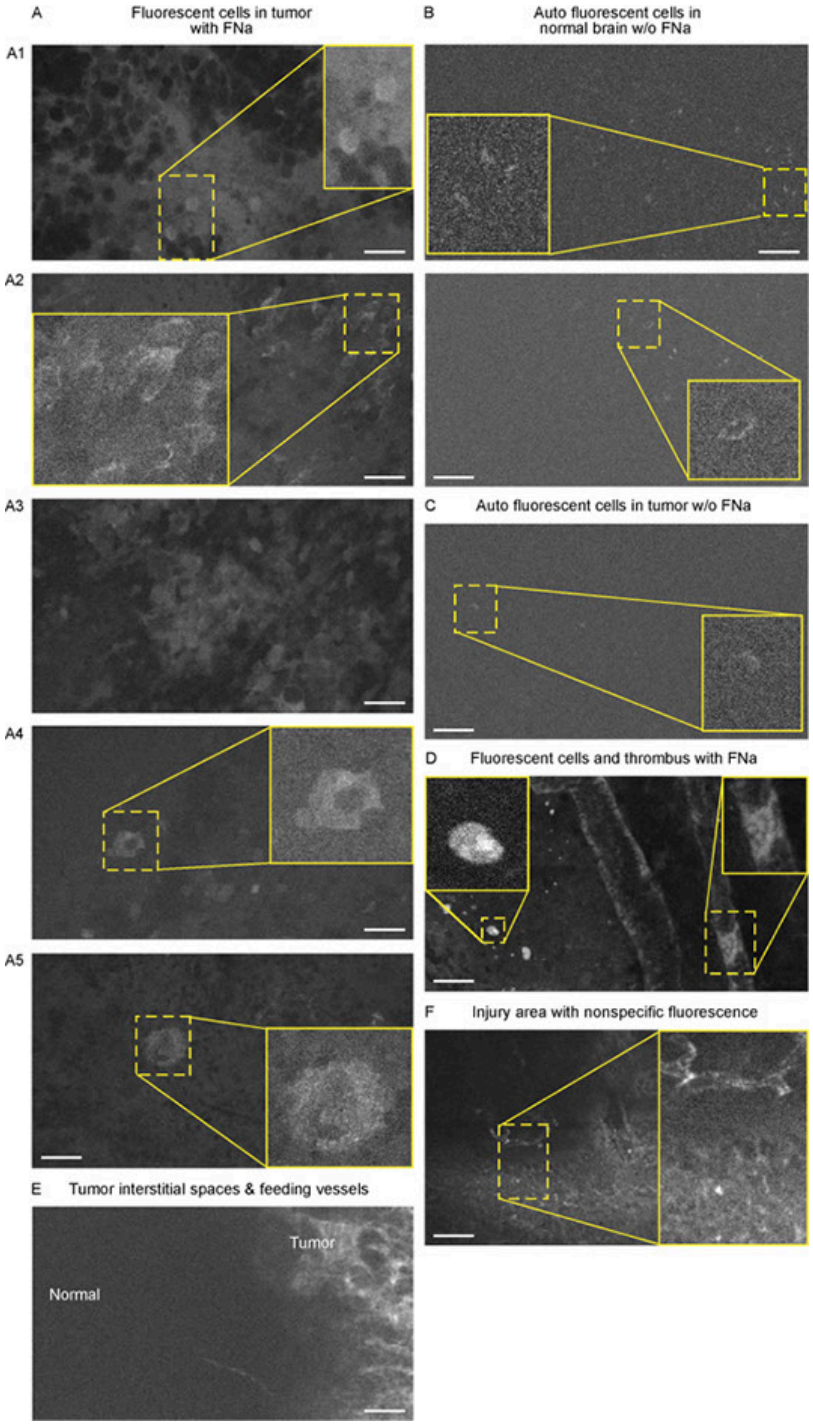

Figure 2.20. Various patterns of fluorescence visualized with generation 2 confocal laser endomicroscope. (A) Some tumor cells exhibited fluorescein sodium (FNa) fluorescence. (A1) Singular fluorescent tumor cells. (A2) Multiple tumor cells with granular

fluorescent pattern. (A3) Mix of dark nonfluorescent and bright fluorescent cells. (A4 and A5) Giant fluorescent cells with a diameter of about 50 um. (B) Examples of sparse autofluorescence. Some cells just have inclusions that are visible; in others a dark nucleus may be distinguished. Note smaller cell size. (C) Some cells from tumor also contain autofluorescent inclusions. (D) Individual parenchymal fluorescent cells and intravascular thrombus with visible fluorescent cells are visible. (E) FNa is visible in the vessels of the normal brain and in the interstitial spaces of the tumor area. (F) Injured nontumor brain tissue embedded with FNa; some normal vessels are also visible. Scale bar is 50 μm. Used with permission from Barrow Neurological Institute, Phoenix, Arizona.

When considering FNa imaging strategies, continuous cine-like time series image recordings and Z-stacks were the most useful and productive. Continuous recordings were used to identify red blood cells and better appreciate cell morphology based on cell movement while reformatted volume views of Z-stacks provided improved understanding of the 3-dimensional structure of the tissue.

Histologic Pictures Visualized by CLE with 5-ALA (Gen1 and Gen2)

The combination of metabolic dye 5-ALA with either Gen1 or Gen2 was not a reliable method for identification of tumor in our observations, as characteristic histologic features could not be identified. The laser wavelength of both systems (488 nm) is not optimally tuned for excitation of PpIX and CLE images did not show specific information. CLE images did not reproduce findings when LSM with the appropriate

excitation laser was used to image PpIX in the same mouse glioma model (Belykh, Miller, Hu, et al. 2018).

While it was possible to differentiate glioma from normal brain tissue by comparing overall average image intensity, this was not deemed useful. Similar "fluorescence intensity" sampling has been shown previously using spectrophotometric methods (Potapov et al. 2016, Potapov et al. 2013, Stummer et al. 2014). Of note, sparse fluorescent "spots" seen using the Gen2 CLE with 5-ALA were consistent with the previous intraoperative observations of patients with brain tumors with the Gen1 CLE, although the exact identification of these PpIX fluorescent signals is not confirmed (Sanai, Snyder, et al. 2011). These structures are likely autofluorescent due to lipofuscin (Croce and Bottiroli 2014). Imaging of histologic patterns created by 5-ALA-induced PpIX in brain tumors remains limited to benchtop confocal microscopes, or hand-held fluorescence microscopes specifically designed for PpIX excitation and detection, such as a dual axis confocal microscope (Wei et al. 2017) or a scanning fiber endoscope system (Belykh, Miller, Hu, et al. 2018).

CLE Parameters for Best Image Quality with FNa (Gen2 only)

Filter

The first parameter to consider during CLE imaging is the filter. Between the two types of green filters (i.e., the longpass filter and bandpass filter), the longpass filter produced brighter images. Although images with such longpass filters may look more pleasing, they include nonspecific light from the background that attenuates FNa-induced

contrast. Ultimately, the bandpass filter produced images with higher contrast and was preferable for obtaining better quality and interpretable images.

Gain

Unlike in the benchtop confocal microscope, where the gain is fine-tuned during the constant image capturing, with the Gen2 CLE the gain control is located in a separate window and is not available for rapid adjustments on the fly. However, adjustments of brightness and laser power were enough to obtain quality images in most cases without the need to adjust gain. Only in a few very bright or very dim specimens was there a need to adjust gain for optimal image quality.

Laser Power

Laser power at mid-range (50% or 500 mW) was generally optimal for imaging, with increasing intensity providing some improvements in image quality. Lack of significant improvement in image quality with increasing laser power is mainly explained by the nature of FNa, which, after extravasation, is diffused through almost all tissue thickness. Therefore, increased excitation results in increased emission in all image regions, including background and cells. Moreover, autofluorescence and noise begin to be visible at higher laser settings. This association of laser power and gain with contrast and autofluorescence is shown schematically in Figure 2.21. Compared with targeted fluorophores or reflectance imaging (Martirosyan et al. 2018a), imaging of FNa is always associated with higher levels of noise.

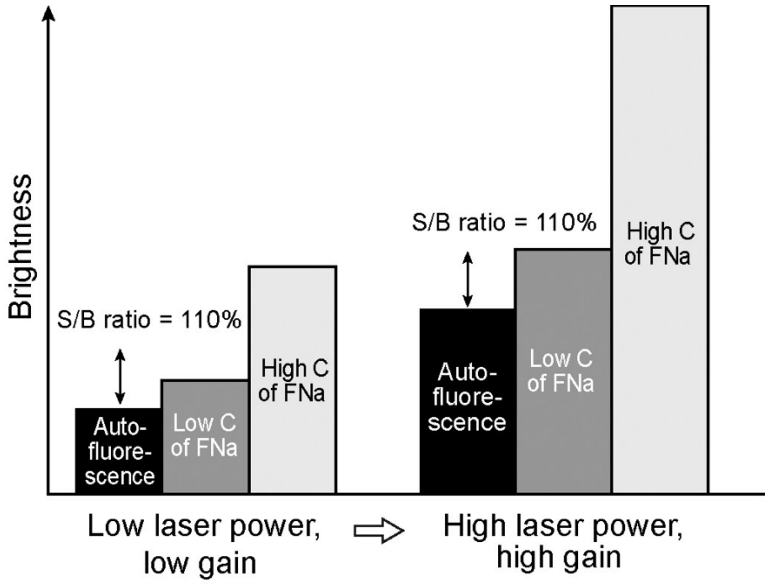

Figure 2.21. Relationship between gain, laser power, and contrast, in terms of brightness. Increase in gain or laser power has limited impact on contrast because of the proportional increase of autofluorescence and non-specific fluorescein sodium signal in the same spectral range. Therefore, relative signal to background (S/B) ratio stays constant. C = concentration; FNa = fluorescein sodium. Scale bar is 50 μm. Used with permission from Barrow Neurological Institute, Phoenix, Arizona.

Brightness

The brightness is the built-in adjustable proprietary setting parameter used during CLE imaging. It has a range of settings from 0% to 100% and, unlike the gain and laser power settings, could be adjusted during the imaging. Brightness was a primary setting of both CLE systems. Autobrightness is a new Gen2 function that saved time and made imaging process faster. Images acquired in autobrightness mode had good quality, comparable with the quality of images acquired at manually set brightness levels.

Additionally, an optimal brightness level, or even pseudocoloring, can be applied later during postprocessing (Belykh, Patel, Miller, Bozkurt, Yağmurlu, et al. 2018).

Speed

Speed of image acquisition was generally inversely correlated with image quality. This illustrated the tradeoff of convenience of using high-speed imaging to quickly locate informative structures within a large area with little detail, versus slowly looking at areas and imaging resulting in higher detail. For areas of high contrast, such as intact vessels with FNa within the normal brain, or pronounced hypercellular tumor areas with bright FNa nearby, high-speed imaging was able to nicely resolve structures. However, in most cases fast scanning was not able to resolve red blood cells and finer cellular details.

Zoom

Although the FOV of the Gen2 is about half the size of Gen1 images, it was sufficient to obtain similar image interpretation for corresponding histological structures. Subjective image quality appraisal between the systems is dependent on the display size. The Gen2 is capable of increasing optical zoom twice, but this results in a corresponding decrease of FOV size, which is not particularly helpful for the identification of cell or tissue architecture using FNa imaging. However, a zoom function might be advantageous for dyes such as AO or AF (Figure 2.22). Unlike benchtop confocal scanning microscope systems, where zoom can be adjusted in real time (Eschbacher et al. 2017, Martirosyan et al. 2018a), handheld CLE systems are limited to a preset zoom because of limitations in miniature design and construction.

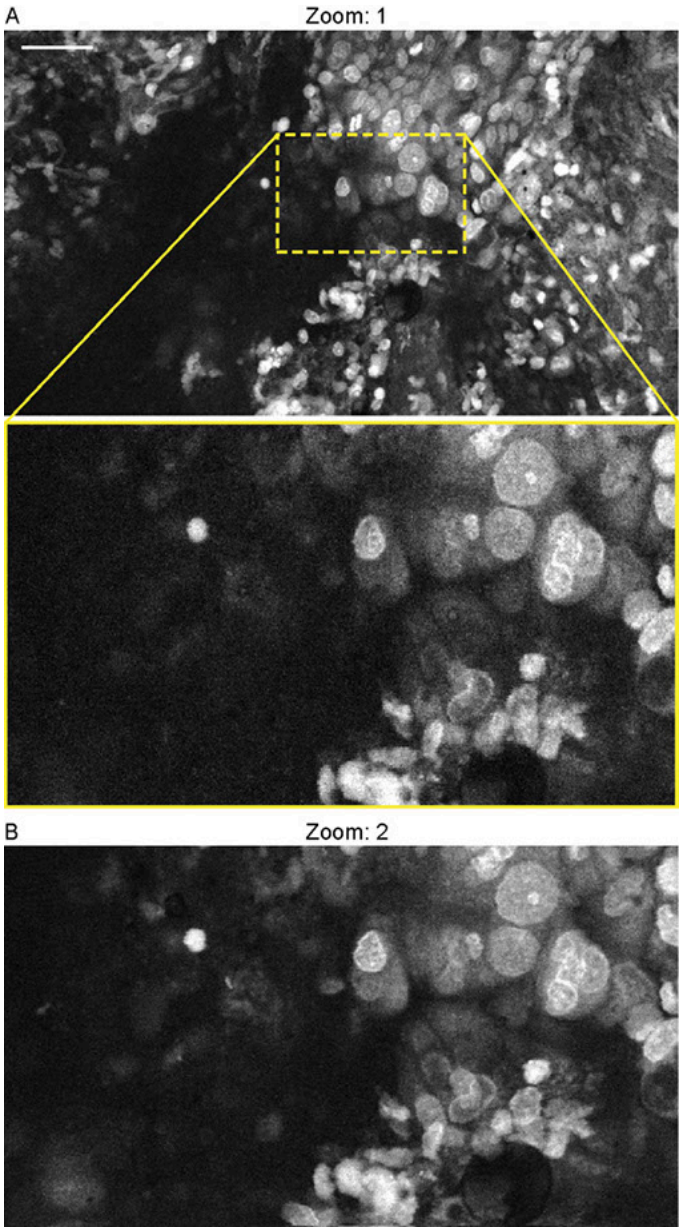

Figure 2.22. Comparison of generation 2 confocal laser endomicroscope images taken with various zoom levels. Human samples stained with acridine orange are used for analysis and illustration. (A) 1× zoom provides similar image quality to (B) 2× zoom. Higher zoom shows smaller field of view enlarged on the screen. Scale bar is 50 µm. *Used with permission from Barrow Neurological Institute, Phoenix, Arizona.*

Because of the inherent cellular composition of different tumor types, including cellular and regional tissue architectural heterogeneity, CLE system functionality may benefit the surgeon or pathologist by use of a lower resolution and larger FOV image assessment. This would allow a closer match to the lower power magnification of a conventional pathology microscope, which would allow the surgeon a larger FOV for scanning the tissue surface (Belykh, Miller, Hu, et al. 2018). However, the portability and capability to move the CLE probe compensate for the smaller FOV, along with Z-stack functionality. Combining multiple small FOV frames together using mosaicking computational algorithms has been shown as a means to yield a larger reconstructed FOV (Becker et al. 2007).

Different Concentrations and Timing of FNa Administration

FNa doses in animals are higher than human doses used in brain tumor surgery either with epifluorescence guidance using the operating microscope with a dedicated filter (2-20 mg/kg (Schebesch et al. 2016)) or previously used with CLE (5 mg/kg (Martirosyan, Eschbacher, et al. 2016)), which most likely is due to faster metabolism of such fluorophores in rodents. CLE imaging likely requires similar or higher, but not lower, dosages than epifluorescent imaging to obtain informative images. CLE imaging was performed within a period of 5 minutes to 2 hours after FNa injection. This timing was chosen to approximate the duration of tumor surgery in humans and complements the previous data on the biodistribution of FNa in a rodent model (Diaz et al. 2015).

Overall, the shorter time periods produced a higher number of diagnostic frames, while imaging at longer time periods produced less contrasted images, which corresponds to the findings by Folaron et al (Folaron et al. 2018b).

Limitations

The current study was performed using a mouse GL261 glioma model. Histologic patterns and the feasibility of FNa imaging with CLE in other experimental tumor models were not addressed in this project. However, clinical experience (Martirosyan, Eschbacher, et al. 2016, Eschbacher et al. 2012) and available literature indicate the general feasibility of such an approach for intraoperative brain tumor imaging. Limitations that have not been addressed in this discussion include the need for the development of remote access to the system by another surgeon or neuropathologist or the ability to push images out to cellular devices for rapid assessment or consultation. In addition, the number of images acquired during a case can be very high—in the thousands—and number of images with artifact caused by motion or other distortions causing them to be unusable is high. Thus, image stabilization control and software built into system would be beneficial for quick informative image selection, identification, review and/or optimization (Kamen et al. 2016, Izadyyazdanabadi, Belykh, Mooney, et al. 2018, Izadyyazdanabadi, Belykh, Cavallo, et al. 2018).

Conclusions

Functionality and parameters were assessed for a CLE system (Gen2) designed specifically to perform to the demands and progress of neurosurgery to potentially assist in managing invasive brain tumors in a preclinical setting. Experimental brain tumor models (in vivo) and human tumor samples (ex vivo) were employed to discern and describe optimal imaging parameters for microscopic histologic visualization with a clinical-grade CLE system and intravenous FNa as a contrast fluorophore. Visualized histologic patterns and pixel intensity values were of comparable quality on Gen1 and Gen2 systems, if not improved with the Gen2 system. The Gen2 had a limitation of a smaller FOV, while having higher resolution, clearer images, and a more responsive user interface including an autobrightness function and volumetric Z-stack image acquisition that enrich diagnostic possibilities and imaging functionality.

Such portable CLE systems are designed ultimately for in vivo use. CLE systems cannot replace the wide functionality of benchtop confocal scanning microscopes, and they are not designed to accomplish such tasks. CLE systems depend on their specificity, rapid applicability and portability; their functions, ergonomics, and employment will depend on the demand of the surgical or diagnostic specialty. Additionally, the properties of the emitted and detected light range and concomitant fluorophores will have critical impact on use and efficacy.

CLE provides the neurosurgeon with real-time intraoperative cellular resolution imaging that is a critical basis of the potential for cell-precision surgery (although neurosurgical instrumentation does not yet provide for precision maneuvers at the cellular

level). Although CLE has been used routinely in other medical and surgical specialties, such as for gastrointestinal diagnosis, neurosurgery is in its infancy with respect to CLE use. CLE technology does appear to be responding to the demands of neurosurgeons and neuropathologists for practical introduction into the operating room as an aid in surgery for invasive brain tumors after nearly a decade of developmental exploration and testing.

Concepts for CLE use that must be considered are those that will make the system meaningful in a surgical setting. CLE usefulness to neurosurgery must be proven by being shown to provide a measurable ability to discriminate and guide removal of tumor invasion, thereby extending or optimizing the resection. As much as CLE may provide precise information on where to biopsy or remove tissue, it may be just as crucially used to inform the neurosurgeon where to stop the resection. Further clinical investigation of the diagnostic value of the Gen2 CLE system in fluorescence-guided brain tumor surgery is ongoing.

References

Abdelwahab, M. G., T. Sankar, M. C. Preul, and A. C. Scheck. 2011. "Intracranial implantation with subsequent 3D in vivo bioluminescent imaging of murine gliomas." J Vis Exp (57):e3403. doi: 10.3791/3403.

Ackerman, L. V., and G. A. Ramirez. 1959. "The indications for and limitations of frozen section diagnosis; a review of 1269 consecutive frozen section diagnoses." Br J Surg 46 (198):336-50.

Ammirati, M., N. Vick, Y. L. Liao, I. Ciric, and M. Mikhael. 1987. "Effect of the extent of surgical resection on survival and quality of life in patients with supratentorial glioblastomas and anaplastic astrocytomas." Neurosurgery 21 (2):201-6.

Becker, V., T. Vercauteren, C. H. von Weyhern, C. Prinz, R. M. Schmid, and A. Meining. 2007. "High-resolution miniprobe-based confocal microscopy in

combination with video mosaicing (with video)." Gastrointest Endosc 66 (5):1001-7. doi: 10.1016/j.gie.2007.04.015.

Belykh, E., C. Cavallo, S. Gandhi, X. Zhao, D. Veljanoski, M. Izady Yazdanabadi, N. L. Martirosyan, V. A. Byvaltsev, J. Eschbacher, M. C. Preul, and P. Nakaji. 2018. "Utilization of intraoperative confocal laser endomicroscopy in brain tumor surgery." J Neurosurg Sci. doi: 10.23736/S0390-5616.18.04553-8.

Belykh, E., N. L. Martirosyan, K. Yagmurlu, E. J. Miller, J. M. Eschbacher, M. Izadyyazdanabadi, L. A. Bardonova, V. A. Byvaltsev, P. Nakaji, and M. C. Preul. 2016. "Intraoperative Fluorescence Imaging for Personalized Brain Tumor Resection: Current State and Future Directions." Front Surg 3:55. doi: 10.3389/fsurg.2016.00055.

Belykh, E., E. J. Miller, D. Hu, N. L. Martirosyan, E. C. Woolf, A. C. Scheck, V. A. Byvaltsev, P. Nakaji, L. Y. Nelson, E. J. Seibel, and M. C. Preul. 2018. "Scanning Fiber Endoscope Improves Detection of 5-Aminolevulinic Acid-Induced Protoporphyrin IX Fluorescence at the Boundary of Infiltrative Glioma." World Neurosurg 113:e51-e69. doi: 10.1016/j.wneu.2018.01.151.

Belykh, E., E. J. Miller, A. A. Patel, M. I. Yazdanabadi, N. L. Martirosyan, K. Yagmurlu, B. Bozkurt, V. A. Byvaltsev, J. M. Eschbacher, P. Nakaji, and M. C. Preul. 2018. "Diagnostic Accuracy of a Confocal Laser Endomicroscope for In Vivo Differentiation Between Normal Injured And Tumor Tissue During Fluorescein-Guided Glioma Resection: Laboratory Investigation." World Neurosurg 115:e337-e348. doi: 10.1016/j.wneu.2018.04.048.

Belykh, E., A. A. Patel, E. J. Miller, B. Bozkurt, K. Yagmurlu, E. C. Woolf, A. C. Scheck, J. M. Eschbacher, P. Nakaji, and M. C. Preul. 2018. "Probe-based three-dimensional confocal laser endomicroscopy of brain tumors: technical note." Cancer Manag Res 10:3109-3123. doi: 10.2147/CMAR.S165980.

Belykh, Evgenii, Claudio Cavallo, Xiaochun Zhao, Michael T. Lawton, Peter Nakaji, and Mark C. Preul. 2018. "312 Intraoperative Imaging of Cerebral Vasculature and Blood Flow Using Confocal Laser Endomicroscopy: New Perspectives in Precise Real-Time Brain Fluorescence Microimaging." Neurosurgery 65 (CN_suppl_1):126-127. doi: 10.1093/neuros/nyy303.312.

Belykh, Evgenii G., Xiaochun Zhao, Claudio Cavallo, Michael A. Bohl, Kaan Yagmurlu, Joseph L. Aklinski, Vadim A. Byvaltsev, Nader Sanai, Robert F. Spetzler, Michael T. Lawton, Peter Nakaji, and Mark C. Preul. 2018. "Laboratory Evaluation of a Robotic Operative Microscope - Visualization Platform for Neurosurgery." Cureus. doi: 10.7759/cureus.3072.

Belykh, Evgenii, Arpan A. Patel, Eric J. Miller, Baran Bozkurt, Kaan Yağmurlu, Eric C. Woolf, Adrienne C. Scheck, Jennifer M. Eschbacher, Peter Nakaji, and Mark C.

Preul. 2018. "Probe-based three-dimensional confocal laser endomicroscopy of brain tumors: technical note." Cancer Management and Research Volume 10:3109-3123. doi: 10.2147/cmar.s165980.

Charalampaki, P., M. Javed, S. Daali, H. J. Heiroth, A. Igressa, and F. Weber. 2015. "Confocal Laser Endomicroscopy for Real-time Histomorphological Diagnosis: Our Clinical Experience With 150 Brain and Spinal Tumor Cases." Neurosurgery 62 Suppl 1:171-6. doi: 10.1227/NEU.0000000000000805.

Cho, H. R., D. H. Kim, D. Kim, P. Doble, D. Bishop, D. Hare, C. K. Park, W. K. Moon, M. H. Han, and S. H. Choi. 2014. "Malignant glioma: MR imaging by using 5-aminolevulinic acid in an animal model." Radiology 272 (3):720-30. doi: 10.1148/radiol.14131459.

Croce, A. C., and G. Bottiroli. 2014. "Autofluorescence spectroscopy and imaging: a tool for biomedical research and diagnosis." Eur J Histochem 58 (4):2461. doi: 10.4081/ejh.2014.2461.

Devaux, B. C., J. R. O'Fallon, and P. J. Kelly. 1993. "Resection, biopsy, and survival in malignant glial neoplasms. A retrospective study of clinical parameters, therapy, and outcome." J Neurosurg 78 (5):767-75. doi: 10.3171/jns.1993.78.5.0767.

Diaz, R. J., R. R. Dios, E. M. Hattab, K. Burrell, P. Rakopoulos, N. Sabha, C. Hawkins, G. Zadeh, J. T. Rutka, and A. A. Cohen-Gadol. 2015. "Study of the biodistribution of fluorescein in glioma-infiltrated mouse brain and histopathological correlation of intraoperative findings in high-grade gliomas resected under fluorescein fluorescence guidance." J Neurosurg 122 (6):1360-9. doi: 10.3171/2015.2.JNS132507.

Eschbacher, J. M., J. F. Georges, E. Belykh, M. I. Yazdanabadi, N. L. Martirosyan, E. Szeto, C. Y. Seiler, M. A. Mooney, J. K. Daniels, K. Y. Goehring, K. R. Van Keuren-Jensen, M. C. Preul, S. W. Coons, S. Mehta, and P. Nakaji. 2017. "Immediate Label-Free Ex Vivo Evaluation of Human Brain Tumor Biopsies With Confocal Reflectance Microscopy." J Neuropathol Exp Neurol 76 (12):1008-1022. doi: 10.1093/jnen/nlx089.

Eschbacher, J., N. L. Martirosyan, P. Nakaji, N. Sanai, M. C. Preul, K. A. Smith, S. W. Coons, and R. F. Spetzler. 2012. "In vivo intraoperative confocal microscopy for real-time histopathological imaging of brain tumors." J Neurosurg 116 (4):854-60. doi: 10.3171/2011.12.JNS11696.

Fenton, K. E., N. L. Martirosyan, M. G. Abdelwahab, S. W. Coons, M. C. Preul, and A. C. Scheck. 2014. "In vivo visualization of GL261-luc2 mouse glioma cells by use of Alexa Fluor-labeled TRP-2 antibodies." Neurosurg Focus 36 (2):E12. doi: 10.3171/2013.12.FOCUS13488.

Fisher, C. J., C. Niu, W. Foltz, Y. Chen, E. Sidorova-Darmos, J. H. Eubanks, and L. Lilge. 2017. "ALA-PpIX mediated photodynamic therapy of malignant gliomas augmented by hypothermia." PLoS One 12 (7):e0181654. doi: 10.1371/journal.pone.0181654.

Foersch, S., A. Heimann, A. Ayyad, G. A. Spoden, L. Florin, K. Mpoukouvalas, R. Kiesslich, O. Kempski, M. Goetz, and P. Charalampaki. 2012. "Confocal laser endomicroscopy for diagnosis and histomorphologic imaging of brain tumors in vivo." PLoS One 7 (7):e41760. doi: 10.1371/journal.pone.0041760.

Folaron, M., R. Strawbridge, K. S. Samkoe, C. Filan, D. W. Roberts, and S. C. Davis. 2018a. "Elucidating the kinetics of sodium fluorescein for fluorescence-guided surgery of glioma." J Neurosurg:1-11. doi: 10.3171/2018.4.JNS172644.

Folaron, Margaret, Rendall Strawbridge, Kimberley S. Samkoe, Caroline Filan, David W. Roberts, and Scott C. Davis. 2018b. "Elucidating the kinetics of sodium fluorescein for fluorescence-guided surgery of glioma." Journal of Neurosurgery:1-11. doi: 10.3171/2018.4.jns172644.

Goetz, M., S. Thomas, A. Heimann, P. Delaney, C. Schneider, M. Relle, A. Schwarting, P. R. Galle, O. Kempski, M. F. Neurath, and R. Kiesslich. 2008. "Dynamic in vivo imaging of microvasculature and perfusion by miniaturized confocal laser microscopy." Eur Surg Res 41 (3):290-7. doi: 10.1159/000148242.

Izadyyazdanabadi, M., E. Belykh, M. A. Mooney, J. M. Eschbacher, P. Nakaji, Y. Yang, and M. C. Preul. 2018. "Prospects for Theranostics in Neurosurgical Imaging: Empowering Confocal Laser Endomicroscopy Diagnostics via Deep Learning." Front Oncol 8:240. doi: 10.3389/fonc.2018.00240.

Izadyyazdanabadi, Mohammadhassan, Evgenii Belykh, Claudio Cavallo, Xiaochun Zhao, Sirin Gandhi, Leandro Borba Moreira, Jennifer Eschbacher, Peter Nakaji, Mark C. Preul, and Yezhou Yang. 2018. "Weakly-Supervised Learning-Based Feature Localization for Confocal Laser Endomicroscopy Glioma Images." 11071:300-308. doi: 10.1007/978-3-030-00934-2_34.

Kamen, A., S. Sun, S. Wan, S. Kluckner, T. Chen, A. M. Gigler, E. Simon, M. Fleischer, M. Javed, S. Daali, A. Igressa, and P. Charalampaki. 2016. "Automatic Tissue Differentiation Based on Confocal Endomicroscopic Images for Intraoperative Guidance in Neurosurgery." Biomed Res Int 2016:6183218. doi: 10.1155/2016/6183218.

Lacroix, M., D. Abi-Said, D. R. Fourney, Z. L. Gokaslan, W. Shi, F. DeMonte, F. F. Lang, I. E. McCutcheon, S. J. Hassenbusch, E. Holland, K. Hess, C. Michael, D. Miller, and R. Sawaya. 2001. "A multivariate analysis of 416 patients with glioblastoma multiforme: prognosis, extent of resection, and survival." J Neurosurg 95 (2):190-8. doi: 10.3171/jns.2001.95.2.0190.

Martirosyan, N. L., J. M. Eschbacher, M. Y. Kalani, J. D. Turner, E. Belykh, R. F. Spetzler, P. Nakaji, and M. C. Preul. 2016. "Prospective evaluation of the utility of intraoperative confocal laser endomicroscopy in patients with brain neoplasms using fluorescein sodium: experience with 74 cases." Neurosurg Focus 40 (3):E11. doi: 10.3171/2016.1.FOCUS15559.

Martirosyan, N. L., J. Georges, J. M. Eschbacher, E. Belykh, A. Carotenuto, R. F. Spetzler, P. Nakaji, and M. C. Preul. 2018. "Confocal scanning microscopy provides rapid, detailed intraoperative histological assessment of brain neoplasms: Experience with 106 cases." Clin Neurol Neurosurg 169:21-28. doi: 10.1016/j.clineuro.2018.03.015.

Martirosyan, N. L., J. Georges, J. M. Eschbacher, D. D. Cavalcanti, A. M. Elhadi, M. G. Abdelwahab, A. C. Scheck, P. Nakaji, R. F. Spetzler, and M. C. Preul. 2014. "Potential application of a handheld confocal endomicroscope imaging system using a variety of fluorophores in experimental gliomas and normal brain." Neurosurg Focus 36 (2):E16. doi: 10.3171/2013.11.FOCUS13486.

Nitta, T., and K. Sato. 1995. "Prognostic implications of the extent of surgical resection in patients with intracranial malignant gliomas." Cancer 75 (11):2727-31.

Norman, M. U., S. Hulliger, P. Colarusso, and P. Kubes. 2008. "Multichannel fluorescence spinning disk microscopy reveals early endogenous CD4 T cell recruitment in contact sensitivity via complement." J Immunol 180 (1):510-21.

Novis, D. A., and R. J. Zarbo. 1997. "Interinstitutional comparison of frozen section turnaround time. A College of American Pathologists Q-Probes study of 32868 frozen sections in 700 hospitals." Arch Pathol Lab Med 121 (6):559-67.

Osman, H., J. Georges, D. Elsahy, E. M. Hattab, S. Yocom, and A. A. Cohen-Gadol. 2018. "In Vivo Microscopy in Neurosurgical Oncology." World Neurosurg 115:110-127. doi: 10.1016/j.wneu.2018.03.218.

Park, J. C., Y. Park, H. K. Kim, J. H. Jo, C. H. Park, E. H. Kim, D. H. Jung, H. Chung, S. K. Shin, S. K. Lee, and Y. C. Lee. 2017. "Probe-based confocal laser endomicroscopy in the margin delineation of early gastric cancer for endoscopic submucosal dissection." J Gastroenterol Hepatol 32 (5):1046-1054. doi: 10.1111/jgh.13635.

Pavlov, V., D. Meyronet, V. Meyer-Bisch, X. Armoiry, B. Pikul, C. Dumot, P. A. Beuriat, F. Signorelli, and J. Guyotat. 2016. "Intraoperative Probe-Based Confocal Laser Endomicroscopy in Surgery and Stereotactic Biopsy of Low-Grade and High-Grade Gliomas: A Feasibility Study in Humans." Neurosurgery 79 (4):604-12. doi: 10.1227/NEU.0000000000001365.

Plesec, T. P., and R. A. Prayson. 2007. "Frozen section discrepancy in the evaluation of central nervous system tumors." Arch Pathol Lab Med 131 (10):1532-40. doi: 10.1043/1543-2165(2007)131[1532:fsdite]2.0.co;2.

Potapov, A. A., S. A. Goriainov, V. B. Loshchenov, T. A. Savel'eva, A. G. Gavrilov, V. A. Okhlopkov, VIu Zhukov, P. V. Zelenkov, D. A. Gol'bin, V. A. Shurkhai, L. V. Shishkina, P. V. Grachev, M. N. Kholodtsova, S. G. Kuz'min, G. N. Vorozhtsov, and A. P. Chumakova. 2013. "[Intraoperative combined spectroscopy (optical biopsy) of cerebral gliomas]." Zh Vopr Neirokhir Im N N Burdenko 77 (2):3-10.

Potapov, A. A., S. A. Goryaynov, V. A. Okhlopkov, L. V. Shishkina, V. B. Loschenov, T. A. Savelieva, D. A. Golbin, A. P. Chumakova, M. F. Goldberg, M. D. Varyukhina, and A. Spallone. 2016. "Laser biospectroscopy and 5-ALA fluorescence navigation as a helpful tool in the meningioma resection." Neurosurg Rev 39 (3):437-47. doi: 10.1007/s10143-015-0697-0.

Rao, S., A. Rajkumar, M. D. Ehtesham, and P. Duvuru. 2009. "Challenges in neurosurgical intraoperative consultation." Neurol India 57 (4):464-8. doi: 10.4103/0028-3886.55598.

Roessler, K., W. Dietrich, and K. Kitz. 2002. "High diagnostic accuracy of cytologic smears of central nervous system tumors. A 15-year experience based on 4,172 patients." Acta Cytol 46 (4):667-74.

Rostomily, R. C., A. M. Spence, D. Duong, K. McCormick, M. Bland, and M. S. Berger. 1994. "Multimodality management of recurrent adult malignant gliomas: results of a phase II multiagent chemotherapy study and analysis of cytoreductive surgery." Neurosurgery 35 (3):378-88; discussion 388.

Sanai, N., L. A. Snyder, N. J. Honea, S. W. Coons, J. M. Eschbacher, K. A. Smith, and R. F. Spetzler. 2011. "Intraoperative confocal microscopy in the visualization of 5-aminolevulinic acid fluorescence in low-grade gliomas." J Neurosurg 115 (4):740-8. doi: 10.3171/2011.6.JNS11252.

Sankar, T., P. M. Delaney, R. W. Ryan, J. Eschbacher, M. Abdelwahab, P. Nakaji, S. W. Coons, A. C. Scheck, K. A. Smith, R. F. Spetzler, and M. C. Preul. 2010. "Miniaturized handheld confocal microscopy for neurosurgery: results in an experimental glioblastoma model." Neurosurgery 66 (2):410-7; discussion 417-8. doi: 10.1227/01.NEU.0000365772.66324.6F.

Schebesch, K. M., A. Brawanski, C. Hohenberger, and J. Hohne. 2016. "Fluorescein Sodium-Guided Surgery of Malignant Brain Tumors: History, Current Concepts, and Future Project." Turk Neurosurg 26 (2):185-94. doi: 10.5137/1019-5149.JTN.16952-16.0.

Schindelin, J., I. Arganda-Carreras, E. Frise, V. Kaynig, M. Longair, T. Pietzsch, S. Preibisch, C. Rueden, S. Saalfeld, B. Schmid, J. Y. Tinevez, D. J. White, V. Hartenstein, K. Eliceiri, P. Tomancak, and A. Cardona. 2012. "Fiji: an open-source platform for biological-image analysis." Nat Methods 9 (7):676-82. doi: 10.1038/nmeth.2019.

Stummer, W., J. C. Tonn, C. Goetz, W. Ullrich, H. Stepp, A. Bink, T. Pietsch, and U. Pichlmeier. 2014. "5-Aminolevulinic acid-derived tumor fluorescence: the diagnostic accuracy of visible fluorescence qualities as corroborated by spectrometry and histology and postoperative imaging." Neurosurgery 74 (3):310-9; discussion 319-20. doi: 10.1227/NEU.0000000000000267.

Swanson, K. I., P. A. Clark, R. R. Zhang, I. K. Kandela, M. Farhoud, J. P. Weichert, and J. S. Kuo. 2015. "Fluorescent cancer-selective alkylphosphocholine analogs for intraoperative glioma detection." Neurosurgery 76 (2):115-23; discussion 123-4. doi: 10.1227/NEU.0000000000000622.

Wei, L., Y. Chen, C. Yin, S. Borwege, N. Sanai, and J. T. C. Liu. 2017. "Optical-sectioning microscopy of protoporphyrin IX fluorescence in human gliomas: standardization and quantitative comparison with histology." J Biomed Opt 22 (4):46005. doi: 10.1117/1.JBO.22.4.046005.

Wood, J. R., S. B. Green, and W. R. Shapiro. 1988. "The prognostic importance of tumor size in malignant gliomas: a computed tomographic scan study by the Brain Tumor Cooperative Group." J Clin Oncol 6 (2):338-43. doi: 10.1200/jco.1988.6.2.338.

CHAPTER 3

The following chapter has been published in the Journal World Neurosurgery

(DOI: 10.1016/j.wneu.2018.04.048)

CHAPTER 3

DIAGNOSTIC ACCURACY OF A CONFOCAL LASER ENDOMICROSCOPE FOR IN VIVO DIFFERENTIATION BETWEEN NORMAL AND TUMOR TISSUE DURING FLUORESCEIN-GUIDED GLIOMA RESECTION: LABORATORY INVESTIGATION

Abstract

Objective: Glioma resection with fluorescein sodium (FNa) guidance has a potential drawback of nonspecific leakage of FNa from non-tumor areas with a compromised blood-brain barrier. We investigated the diagnostic accuracy of in vivo confocal laser endomicroscopy (CLE) after FNa administration to differentiate normal brain, injured normal brain, and tumor brain tissue in an animal glioma model.

Methods: GL261-Luc2 gliomas in C57BL/6 mice were used as a brain tumor model. CLE images of normal, injured normal, and tumor brain tissues were collected after intravenous FNa administration. Correlative hematoxylin-and-eosin–stained sections were taken at the same sites. A set of 40 CLE images was given to 1 neuropathologist and 3 neurosurgeons to assess diagnostic accuracy and rate image quality (1–10 scale). Additionally, we developed a deep convolution neural network (DCNN) model for automatic image classification.

Results: The mean observer accuracy for correct diagnosis of glioma compared to either injured or uninjured brain using CLE images was 85%, and the DCNN model accuracy was 80%. For differentiation of tumor from non-tumor tissue, the experts' mean accuracy, specificity, and sensitivity were 90%, 86%, and 96%, respectively, with high

interobserver agreement overall (Cohen's kappa=0.74). The percentage of correctly identified images was significantly higher for images with a quality rating >5 (104/116, 90%) than for images with a quality rating ≤5 (32/44, 73%) (p=0.007).

Conclusion: With sufficient FNa present in tissues, CLE was an effective tool for intraoperative differentiation among normal, injured normal, and tumor brain tissue. Clinical studies are warranted to confirm these findings.

Introduction

Current evidence indicates that patient survival is improved with maximum resection of glioblastoma multiforme along with other treatment modalities (Chan et al. 2017, Sanai and Berger 2018). The effectiveness of tumor resection can be improved by using fluorescent dyes to enhance the visibility of tumor tissue during surgery (Diaz et al. 2015). Fluorescein sodium (FNa), a U.S. Food and Drug Administration–approved drug, is administered off-label to patients in fluorescence-guided resection of brain tumors using intraoperative imaging technology that can detect its emitted fluorescence. The use of FNa dates back to 1948 (Moore and Peyton 1948); since then, its use in brain (Acerbi 2016, Catapano et al. 2017, Acerbi et al. 2018, Acerbi, Broggi, et al. 2014, Neira et al. 2017, Francaviglia et al. 2017, Minkin et al. 2016, Hamamcioglu et al. 2016, Hohne et al. 2017, Akcakaya et al. 2017, Roberts and Olson 2017) and spinal cord (Acerbi et al. 2017) tumor surgery, brain abscesses (Hohne, Brawanski, and Schebesch 2016, 2017), cerebrospinal fluid leaks (Emanuelli et al. 2015, Banu et al. 2014) and for cerebrovascular angiography application (Kakucs et al. 2017, Misra, Samantray, and

Churi 2017, Narducci et al. 2018b, Ito et al. 2017, Hashimoto et al. 2017) has been investigated and reviewed in multiple studies (Belykh et al. 2016, Acerbi, Cavallo, et al. 2014, D'Amico et al. 2017, Schebesch et al. 2016).

For tumor application, FNa is administered intravenously at dosages of 2–20 mg/kg and accumulates in and around tumor tissue because of the disruption of the blood-brain barrier in this tissue (Diaz et al. 2015). FNa can be visualized intraoperatively using a wide-field operative microscope equipped with a special filter set (YELLOW 560, Carl Zeiss AG, Oberkochen, Germany), low-cost in-house devices (Gollapudi et al. 2018, Lovato, Vitorino Araujo, and Esteves Veiga 2017, Bongetta et al. 2016, Thien et al. 2017) as well as by using confocal laser endomicroscopy (CLE) (Sankar et al. 2010, Sanai, Eschbacher, et al. 2011). The latter technique involves the use of a handheld CLE probe with a 488-nm excitation laser light that allows the surgeon to visualize tumor cytoarchitecture with FNa contrast on the intraoperative display (Martirosyan, Eschbacher, et al. 2016). CLE is aimed to provide the surgeon with real-time cell-resolution digital images during surgery allowing interrogation of the tumor removal interface or border region of the tumor (i.e., an “optical biopsy”).

A limitation of FNa is that it potentially accumulates in areas of blood-brain barrier disruption outside or independent of the tumor location. Such situations, when located near the tumor, may confuse histologic interpretation. For example, iatrogenic trauma to normal brain tissue that occurs during surgery may result in FNa accumulation in the injured area (Schwake et al. 2015). Various strategies being investigated to overcome this limitation include proper injection timing and lower dosages of FNa

(Acerbi et al. 2015); however, this strategy can leave the wide field of fluorescent visualization vulnerable to misdiagnosis. In this study, we investigated whether tissue visualization on a cellular level, with a commercially available intraoperative CLE, could further assist in differentiating fluorescence from tumor tissue from fluorescence in other injuries related to blood-brain barrier damage.

This study is critical to the ability to discriminate tumor tissue fluorescence using FNa, versus that for injury-related tissue or other non-tumor brain tissue where FNa may also extravasate because of the blood-brain barrier breakdown. Although the use of fluorescence-guided techniques is gaining acceptance for intrinsic brain tumor surgery to facilitate more extensive tumor removal, such techniques have not taken into consideration the various appearances of tissue in which fluorophores such as FNa (a non-specific fluorophore) collect, especially at the margin of a malignant glioma. The tumor margin is the region most applicable and critical for such technology to operate and provide a biopsy yield advantage.

Although, previous studies confirmed that CLE can visualize tumor tissue, these were done on patients without detailed assessment of multiple biopsies at the tumor border that would include at least some surrounding non-tumorous brain tissue (Martirosyan, Eschbacher, et al. 2016). Furthermore, animal and human studies have not scrutinized normal and injured brain tissue using CLE in the setting of a concurrent tumor. This study using FNa fluorescence imaging technology is thus central to the problem of discriminating tissue at the border or margin region of the tumor where it transitions to non-tumorous or compromised tissue and to more normal brain tissue.

Furthermore, animal and human studies have not scrutinized normal and injured brain tissue using CLE in the setting of a concurrent tumor. This study using FNa fluorescence imaging technology is thus central to the problem of discriminating tissue at the border or margin region of the tumor where it transitions to non-tumorous or compromised tissue and to more normal brain tissue. Furthermore, animal and human studies have not scrutinized normal and injured brain tissue using CLE in the setting of a concurrent tumor. This study using FNa fluorescence imaging technology is thus central to the problem of discriminating tissue at the border or margin region of the tumor where it transitions to non-tumorous or compromised tissue and to more normal brain tissue. Furthermore, animal and human studies have not scrutinized normal and injured brain tissue using CLE in the setting of a concurrent tumor. This study using FNa fluorescence imaging technology is thus central to the problem of discriminating tissue at the border or margin region of the tumor where it transitions to non-tumorous or compromised tissue and to more normal brain tissue.

The primary objective of this study was to investigate the diagnostic accuracy of in vivo use of CLE along with FNa dye in differentiating tumor tissue, injured tissue, and normal brain tissue. We hypothesized that trained neuropathologists and neurosurgeons would be able to identify 3 tissue classes (normal, injured, and tumor) with a high rate of accuracy based on CLE images. We also developed a computer algorithm using a deep convolutional neural network (DCNN) for automatic classification of the CLE images into the same 3 tissue classes. To achieve this goal, we used a GL261 mouse glioma model, which is a commonly used and standardized glioblastoma multiforme model

(Ciezka et al. 2016). Features of this model reflect the real-life characteristics of glioblastoma multiforme, such as brain tissue invasiveness; lack of metastasis; and similar molecular alterations including p53, K-ras, and c-myc (Szatmari et al. 2006).

METHODS

Study Design

The study consisted of 2 arms. In the experimental group of animals (n=7), after FNa administration, CLE images were collected from normal uninjured, normal injured, and tumor brain tissue. In the control group (n=3), animals did not receive an FNa injection and images were acquired from the same anatomic locations. Animal brain sections were taken at the same sites used for CLE imaging, stained with hematoxylin and eosin (H&E), and used as a reference. This study was performed according to STARD (Bossuyt et al. 2015b) and ARRIVE (Kilkenny et al. 2010) guidelines and in accordance with preliminary recommendations for reporting intraoperative fluorescence tumor imaging studies (Stummer 2017).

Animal Model for Fluorescein-Guided Resection of Brain Tumor

Ethics Statement

The study was approved by the Institutional Animal Care and Use Committee for St. Joseph's Hospital and Medical Center and Barrow Neurological Institute, Phoenix, Arizona, and was conducted in accordance with the *Guide for the Care and Use of Laboratory Animals* provided by the National Institutes of Health. The mice were kept in

an institutional veterinarian-supervised vivarium with standard 12-hour day/night cycle and free access to food and water. All efforts were attempted to minimize animal pain and suffering and to reduce the number of animals sacrificed.

Animal Tumor Model

Ten female, 10-week-old, type B6 (Cg)-Tyrc-23/J (albino C57BL/6) mice with a mean weight of 20 g were purchased from The Jackson Laboratory (Bar Harbor, ME). Glioma models were established according to a previously described protocol by injecting 2 μL of GL261-Luc2 mouse glioma cells (1.45×10^7 cells/mL) into the mouse brain (Abdelwahab et al. 2011, Martirosyan et al. 2014).

Animal Surgery

All surgeries performed after administration of xylazine-ketamine anesthetic were conducted 24-30 days after tumor implantation. Mice were injected with 1 mg/mL FNa (n=3) or 0.1 mg/mL FNa (n=4), or they were administered no FNa injection (n=3). Random assignment was used to create the experimental (n=7) and control (n=3) groups. After craniotomy, part of the contralateral hemisphere was injured via 9 stabbing passes of a 26-G needle. Each hemisphere of the brain was then thoroughly investigated using CLE.

CLE Imaging and Data Collection

Location

FNa signal was visible intraoperatively as bright yellow fluorescence in tumor and injured areas with a Pentero microscope with a YELLOW 560 filter (Carl Zeiss AG,

Oberkochen, Germany). In vivo and rapid ex vivo CLE imaging was performed using a Convivo CLE (Carl Zeiss AG, Oberkochen, Germany). Known locations of (1) tumor, (2) injured areas in the experimental animals, and (3) normal brain tissue from control and experimental animals were imaged. Image locations were recorded, and brains were processed for correlative H&E staining.

Timing

Image acquisition was performed 15–60 min after FNa administration and 10–30 min after injury to the normal brain. The timing of FNa administration was meant to imitate the timing that would potentially be encountered during human fluorescein-guided glioma surgery.

Setup

The CLE probe (4 mm in diameter) was covered with a detachable sterile plastic sheath with a coverslip at the tip end. The probe was attached to a Greenberg retractor and was hand-positioned to contact the desired location at the tissue surface (Figure 3.1). This setup is representative of clinical (Martirosyan, Eschbacher, et al. 2016) and research settings reported previously (Martirosyan et al. 2014).

Imaging Parameters

The imaging depth (z-position) was adjusted with a foot pedal. The 488 nm laser intensity was set to 50% (about 0.5 mW), and the gain was set to 2400 (range, 1800–3000). A green long-pass filter was used for signal detection (505–720 nm). The zoom was set at 1×, resulting in 237×475 μm field-of-view images with 8-bit 1920×1080 pixel resolution. Images were recorded as a time series, z-stacks, or single frames during the

constant scanning process, aiming for probe positions with optimal picture quality. Imaging time was 1.28 seconds per frame. The CLE produced both high-quality diagnostic images and other superfluous nondiagnostic images. The diagnostic images were later manually selected from the database for further analysis.

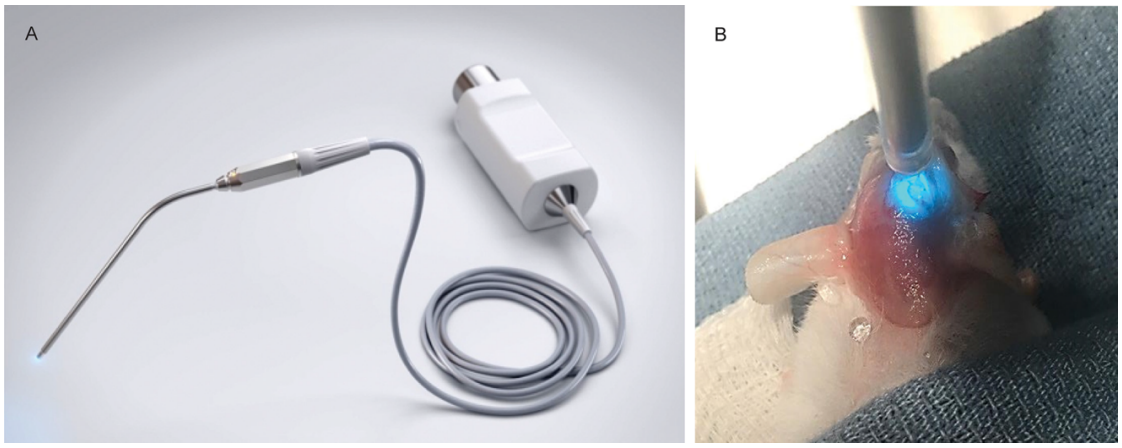

Figure 3.1. Confocal laser endomicroscope (A) scanning handle and (B) imaging setup. Figure 3.1A is used with permission from Carl Zeiss AG. Figure 3.1B is used with permission from Barrow Neurological Institute, Phoenix, Arizona.

Personnel

Image acquisition and diagnostic image selection were performed by a neurosurgeon trained to interpret FNa confocal endomicroscopy images (E.B.). These images were interpreted and analyzed by a board-certified neuropathologist and 3 neurosurgeons who were masked to the image-acquisition process, place of biopsy, and histological verification. Before grading, all 4 evaluators received and reviewed a training module containing model CLE images from various biopsy sites with explanations. Images used in the training module were not repeated in the assessment.

Image Interpretation Analysis

The evaluators were given a set of 40 CLE images in the form of an online Google-form test. The evaluators were asked to select the type of the images displayed as tumor, injured, or normal brain tissue and to rate the image quality on a 10-point scale. According to the accuracy of their identification, as compared to the reference H&E images, the sensitivity and specificity of the CLE system were calculated (Martirosyan, Eschbacher, et al. 2016).

Statistics and Data Analysis

The total number of animals included in the study (n=10) was determined to provide sufficient power for statistical calculations while minimizing the number of animals used. Multiple biopsy sites per animal decreased the total number of animals sacrificed. Only biopsy locations from known tumor locations (including known tumor border region), known injury location and known normal uninjured brain were used. Certainty about the tissue being tumor was established by the contours of positive fluorescence under the operative microscope in YELLOW 560 mode and by H&E stained slices from the same brain surface location that was imaged with CLE.

Image brightness was measured from the region of interest drawn on the whole raw CLE image representative of a particular biopsy site. Image analysis was performed in Fiji (National Institutes of Health, Bethesda, MD) (Schindelin et al. 2012).

Statistical analysis was performed in Statistica (Dell, Inc., Round Rock, TX) and Excel (Microsoft Corp., Redmond, WA). Data were presented as mean ± standard

deviation for parametric data and median (lower quartile; upper quartile) for nonparametric data. $P<0.05$ was selected as a threshold for statistical significance. Nonparametric tests (Mann-Whitney, χ^2) were used to assess differences among the groups. Interobserver agreement was calculated using Cohen's kappa and Kendall's coefficient of concordance.

Automatic Image Classification

We used inception multilayer DCNNs (Szegedy et al. 2015) that extract local and global features to differentiate image classes. Because of the small size of the data set (663 diagnostic images selected from 1130 images acquired), we used fine-tuning to train the model with a learning rate of 0.001. We used a nested left-out validation method to estimate the model performance on images from new biopsies. Images were divided into 3 data sets based on biopsy level: training (n=446), validation (n=217), and test set (same 40 images presented to evaluators). The training set was used to train various models, and the validation set was used only to choose the best model. We report the performance of the trained model on test and validation + test data sets to evaluate its performance on images from new biopsies. Using the best-trained model, we assessed accuracy, sensitivity, specificity, and the area under the receiver operating characteristic (ROC) curve.

RESULTS

Image Analysis

We obtained 1130 confocal images from the 7 experimental animals. The total of unique biopsy sites was 90; 60 were a known location of glioma, 25 sites were an injury to normal brain tissue, and 5 biopsy sites were normal brain tissue. The overall total of 1130 images comprised 814 images of tumor biopsy sites, 255 images of injury to normal brain tissue, and 61 images of control sites (Table 3.1). The mean number of unique biopsy sites per mouse was 12.8, with a mean of 12.5 images acquired per location. The mean number of images acquired per mouse was 161. No adverse events occurred during the collection of these images.

Table 3.1. Counts of biopsy sites and images acquired per experimental animal by tissue type

	Tumor		Injury		Normal brain		
Animal No.	Sites	Images	Sites	Images	Sites	Images	Total Images
1	6	81	11	61	0	0	142
2	11	138	2	30	2	21	189
3	4	40	2	30	0	0	70
4	8	72	2	30	1	15	117
5	7	89	4	44	1	15	148
6	9	121	4	60	0	0	181
7	15	273	0	0	1	10	283
Total	60	814	25	255	5	61	1130

The z-stack or time series of images for each unique biopsy site was compiled into a GIF image to create a short digital cine representation of the biopsy location. All 1130 images were reviewed to identify the highest quality images for use in the diagnostic test. The final test included 26 tumor, 9 injury, and 5 normal tissue GIF cines (Figure 3.2).

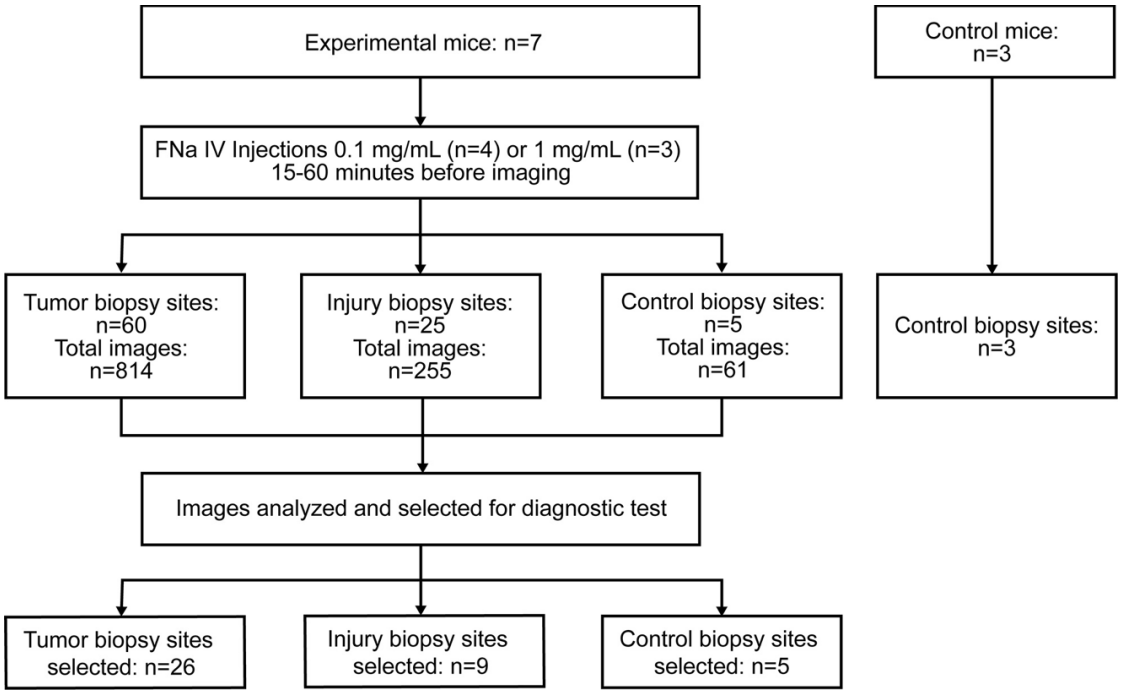

Figure 3.2. Flowchart of the study. Used with permission from Barrow Neurological Institute, Phoenix, Arizona.

Confocal Endomicroscopy Images of Fluorescein-Stained Tissue

High-resolution CLE images obtained allowed identification of tissue architecture and fluorescence staining patterns. Images that represented brain tumor, brain injury, and normal tissue showed unique and distinguishing characteristics.

Tumor

CLE images taken from tumor areas revealed a unique pattern of large nonuniform dark circular shadows on a white background, which represented neoplastic cells. The fluorescent dye leaked into tumor tissue creating linear tracks of fluorescence and highlighted silhouettes of neoplastic cells (Figure 3.3).

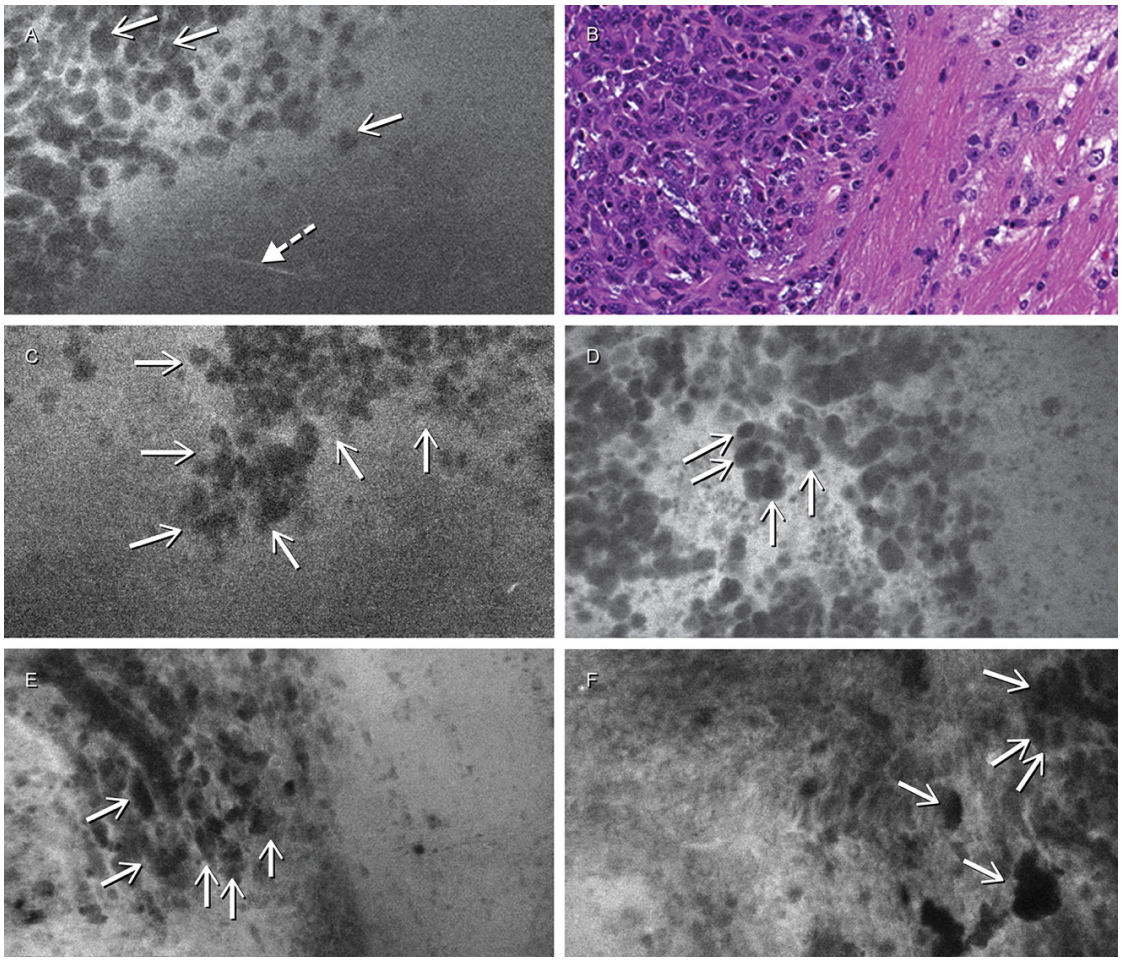

Figure 3.3. Characteristic confocal laser endomicroscopy images of Gl261 glioma. (A) Confocal endomicroscopy image at the tumor border shows darker cells (arrows) on the bright background created by fluorescein in the upper left one-half of the image. Some cells are migrating toward the normal brain. Normal brain appears dark without

apparently visible cells on the lower right one-half of the image. Some normal vessels containing bright fluorescein are visible in the normal brain (arrowhead) of fluorescein-stained tissue at the tumor border. (B) Corresponding image of H&E–stained tissue shows tumor-brain interface with some tumor cells migrating into the normal brain. (C-F) Examples of tumor cells (arrows) visualized on a bright fluorescein background. Used with permission from Barrow Neurological Institute, Phoenix, Arizona.

Injury to Normal Brain Tissue

Images of injury to normal brain tissue showed the presence of a diffuse FNa signal. The key differential features compared to the tumor tissue were the absence of large, abnormal, nonuniform, densely arranged cell silhouettes and the presence of extravasated erythrocytes. These extravasated erythrocytes appeared smaller and more uniform than the dark neoplastic cells. GIF images were useful in identifying erythrocytes by their movement (Figure 3.4).

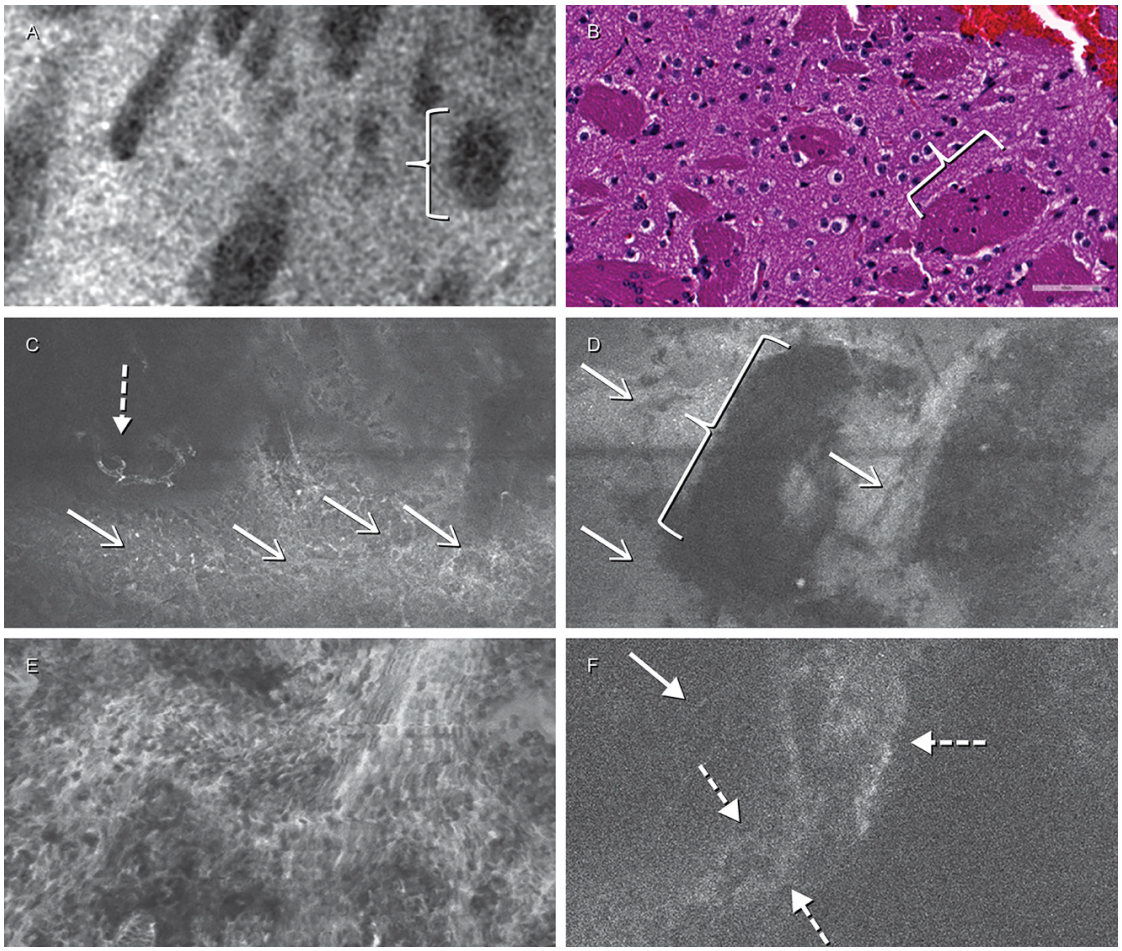

Figure 3.4. Confocal endomicroscopy images of fluorescein-stained injured brain tissue. (A) Confocal image shows presence of myelinated tracts (brackets) that are not stained with fluorescein sodium (FNa) and the relatively even distribution of FNa across the remaining image. (B) Corresponding image of hematoxylin-and-eosin (H&E)-stained tissue shows a similar pattern of myelinated white matter tracts (brackets). (C) Extravasated fluorescein-embedded brain parenchyma shows fibrillary structures (solid arrows), normal capillary is identified (dashed arrow). (D) Extravasated fluorescein-embedded brain parenchyma (arrows) and possible unstained dark myelinated tract (brackets). (E) Confocal laser endomicroscope image filled with small (smaller than

tumor cells shown in Fig. 3) uniform cells. Traces visible as dark lines are due to cell movements. This image is typical of a bleeding vessel. The bleeding point can be identified in the top right one-half of the image. (F) Thick vessel with wall stained by fluorescein is visible traversing the image in a down-to-up direction. Traces of fluorescein diffusing out of the vessel into the tissue create a fuzzy appearance and indicate edema, most likely due to trauma. (Vessel walls are indicated by dashed arrows.) Normal branching capillary is barely visible in the upper-left area (solid arrow). No structures with abnormal tumor-like cellular features could be identified on the images. Used with permission from Barrow Neurological Institute, Phoenix, Arizona.

Normal Brain Tissue

CLE images of normal brain displayed FNa dye that was contained within the vessels. In certain cases, small amounts of leaking fluorescent dye were visualized. Small round moving shadows could be seen within the blood vessels that represent erythrocytes. Areas away from the vessels were not fluorescent and were dark. Sparse fluorescent cells were occasionally seen (Figure 3.5). There were no apparent differences between images of normal brain tissue in the experimental animals or in images obtained from the control group.

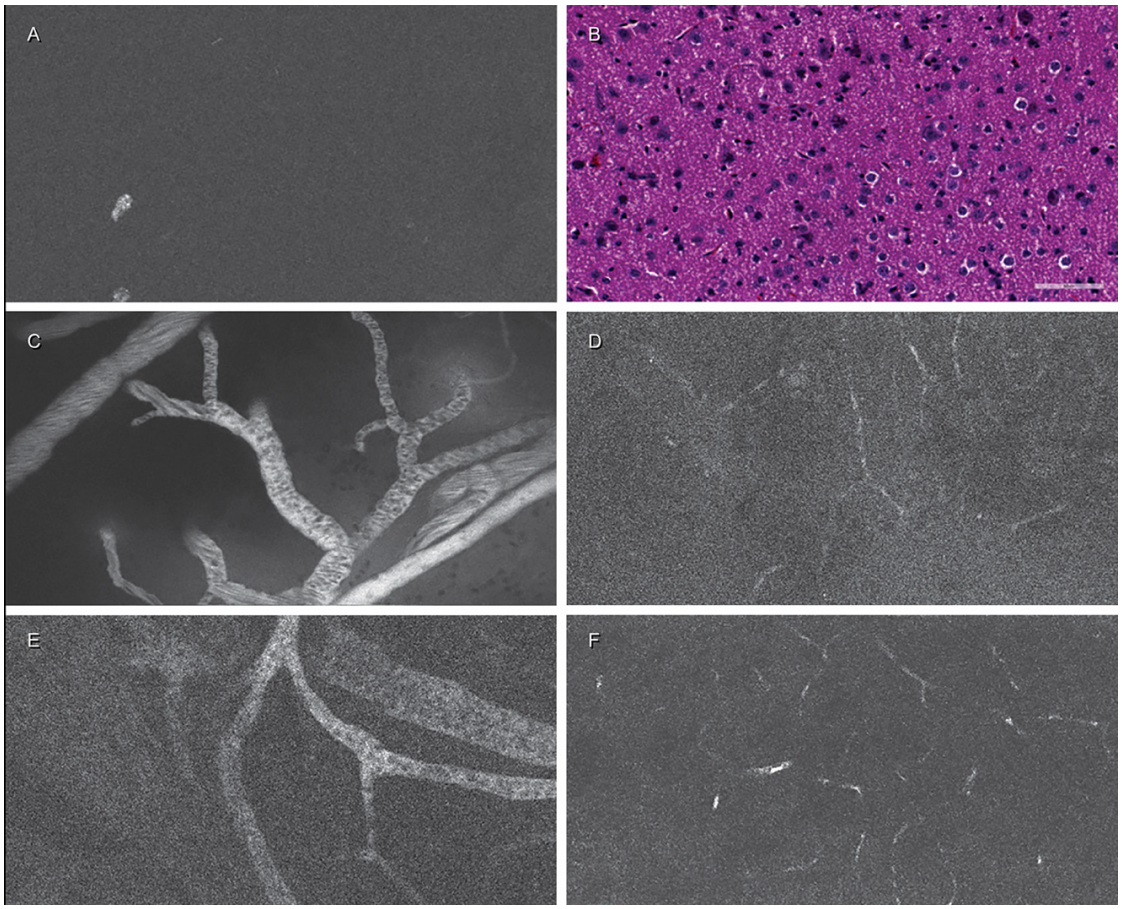

Figure 3.5. Confocal endomicroscopy image of normal brain tissue after fluorescein injection. (A) Most of the normal brain has negative staining. (B) Corresponding image of hematoxylin-and-eosin–stained tissue at the same location. (C, D, E, and F) Normal-appearing capillaries and vessels. Fluorescein highlights the content of the vessels and does not leak outside. Circulating cells (primarily uniform red blood cells) could be identified inside the vessels. Used with permission from Barrow Neurological Institute, Phoenix, Arizona.

Comparison of Tissue Types

Image quality did not differ in the subgroups of the 2 FNa concentrations, resulting in a median image quality score of 7 (5; 9) for the 0.1 mg/mL group images and 8 (6; 8) for the 1 mg/mL group images among the chosen 40 test images ($p = 0.80$). Although the 0.1 mg/mL concentration of FNa produced adequate CLE images (mean, 58.8 ± 8.4 arbitrary units), the 1 mg/mL concentration resulted in brighter images overall (74.5 ± 19.3 arbitrary units) ($p = 0.047$) that provided more pronounced, clear, and consistent FNa staining patterns (Figure 3.6).

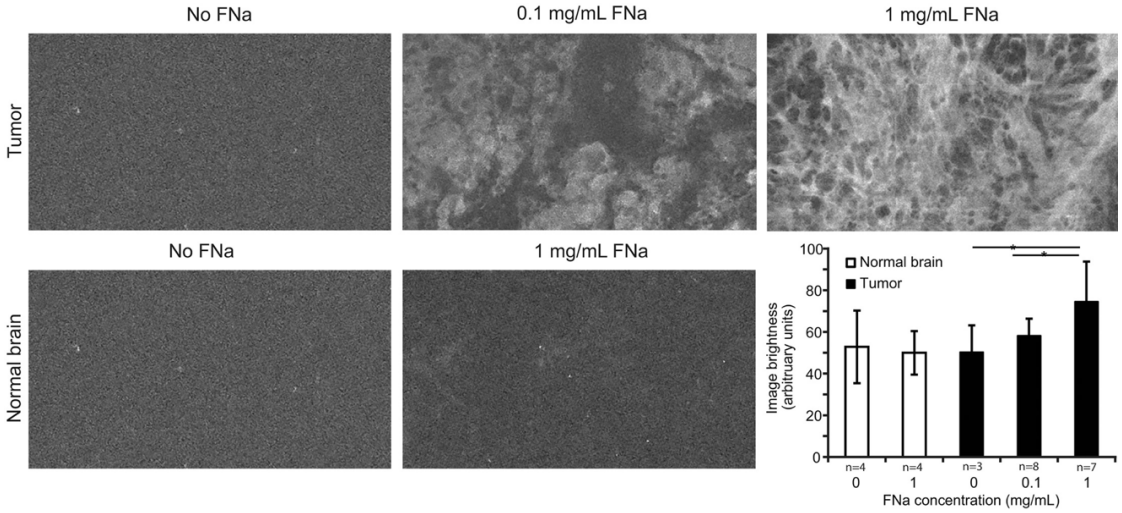

Figure 3.6. Comparison of fluorescein concentrations. Representative confocal laser endomicroscope (CLE) images of tumor region without fluorescein sodium (FNa) (top left), after 0.1 mg/mL FNa (top center), and after 1 mg/mL FNa administration (top right). CLE images of normal brain without FNa (bottom left) and with FNa (middle) and quantification (bottom right) of mean image brightness from representative images for tumors after 0.1 mg/mL, 1 mg/mL, or no FNa and normal brain with and without 1

mg/mL FNa (*p <0.05). Used with permission from Barrow Neurological Institute, Phoenix, Arizona.

Diagnostic Accuracy

Expert Performance

Overall, the neuropathologist and neurosurgeons correctly identified the diagnosis on 85% ± 7.1% of images. Moreover, when injured and non-injured normal brain images were combined as a single "no tumor" category, then the ability of evaluators to correctly differentiate the presence of tumor from no tumor at the CLE biopsy sites increased to 90.2% ± 3.6% (Table 3.2).

Table 3.2. Percent correctly identified tumor, injury, and normal brain tissue samples using CLE images and using validation and test sets developed based on DCNN model.

Tissue type and statistic	NP	NS #1	NS #2	NS #3	Mean (all evaluators)	DCNN model (test set)	DCNN model (validation + test set)
Tumor vs injury vs normal							
Accuracy	90%	75%	90%	85%	85%	80%	80%
Tumor / non-tumor							
Accuracy	90%	86%	95%	88%	90%	87.5%	89%
Sensitivity	85%	79%	96%	85%	86%	78%	78%
Specificity	100%	100%	93%	93%	96%	100%	93%
PPV	100%	100%	96%	96%	98%	100%	83%
NPV	78%	71%	93%	76%	79%	77%	91%
Tumor / injury							
Accuracy	89%	84%	94%	86%	88%	85%	83%
Sensitivity	85%	79%	92%	85%	85%	78%	78%
Specificity	100%	100%	100%	89%	97%	100%	87%

PPV	100%	100%	100%	96%	99%	100%	83%
NPV	69%	58%	82%	67%	69%	67%	83%

Abbreviations: NP, neuropathologist; NS, neurosurgeon; DCNN, deep convoluted neural network PPV, positive predictive value; NPV, negative predictive value.

The sensitivity of CLE to correctly identify tumor and non-tumor regions was 86%, the specificity was 96%, the positive predictive value (PPV) was 98%, and the negative predictive value (NPV) was 79%. Subgroup analysis, excluding normal brain regions, showed that tumor and injury CLE images could be distinguished with 85% sensitivity and 97% specificity and with a PPV of 99% and an NPV of 69%. The study showed a relatively high level of interrater agreement among the 4 appraisers (Table 3.3).

Table 3.3. Interrater agreement statistics

Tissue type	Cohen's kappa statistics	Agreement,%	Kendall's coefficient of concordance
Tumor	0.76		
Normal	0.87		
Injury	0.68		
Overall	0.74	26/40, 65%	0.749209

Image quality is likely to have influenced the ability of the appraisers to identify CLE images correctly. CLE images with a subjective quality score of 6 or greater were significantly more likely to be identified correctly (104/116, 90%) than images with subjective quality scores of 5 or less (32/44, 73%) ($p_{\chi 2} = 0.007$; Figure 3.7).

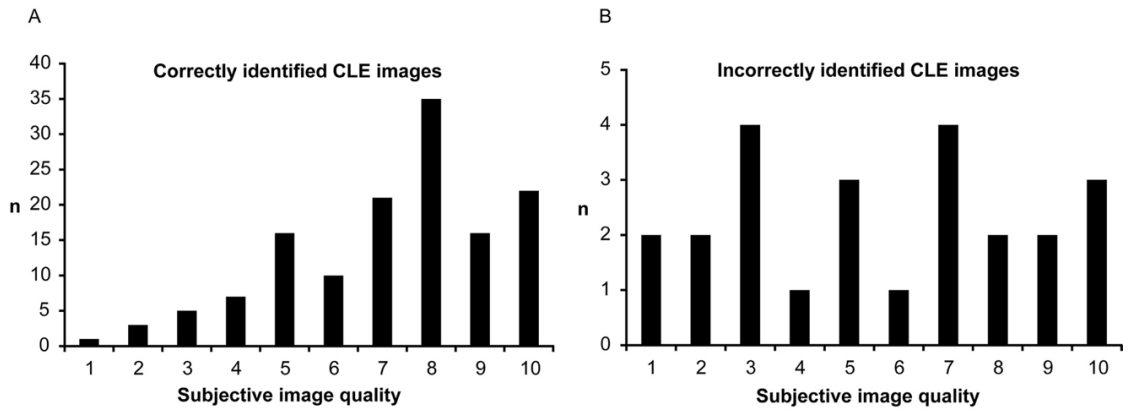

Figure 3.7. Distribution of the subjective image grading of (A) correctly and (B) incorrectly identified confocal laser endomicroscope images. Used with permission from Barrow Neurological Institute, Phoenix, Arizona.

DCNN-based Model Performance

The trained model correctly classified 80% of new images from the validation and test sets into 3 classes: tumor, injured brain, and normal brain. Performance increased to 89% when images were classified using 2 classes only (tumor or non-tumor) in the validation + test data set. The sensitivity and specificity of the model in discriminating a tumor region from non-tumor were 78% and 100%, with a PPV of 100% and an NPV of 77% on the test data set. The area under the ROC curve value for tumor/non-tumor classification was 93% (Figure 3.8). Subgroup analysis showed that the model could differentiate CLE images from tumor and injury with 78% sensitivity and 100% specificity, with a PPV of 100% and an NPV of 67% (Table 3.2).

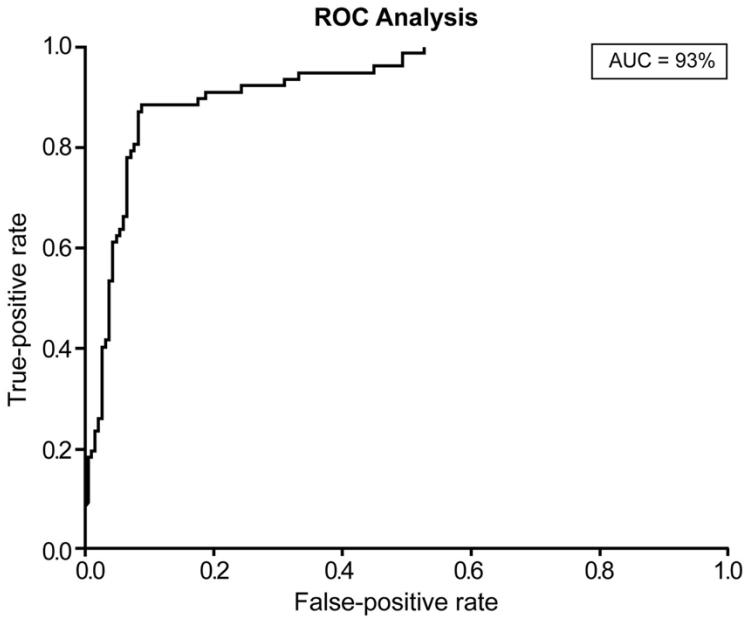

Figure 3.8. The receiver operating characteristic curve. The receiver operating characteristic curve for the deep convoluted neural network–based model for classification of confocal laser endomicroscope images into tumor and non-tumor classes after fluorescein sodium administration in the validation + test image set. Used with permission from Barrow Neurological Institute, Phoenix, Arizona.

Discussion

Fluorescence guidance to improve the resection of invasive brain tumors is an active subject of study with two fluorophores, 5-aminolevulenic acid (5-ALA) and FNa, being the most tested so far (Belykh et al. 2016). 5-ALA is a FDA-approved non-fluorescent drug that is given orally and then becomes metabolized into protoporphyrin IX, which produces red fluorescence upon exposure to 405 nm blue light projected from the surgical microscope with appropriate illumination module, helping to identify the tumor (Lau et al. 2016). FNa is a highly fluorescent drug itself, which is given

intravenously and leaks within the tumor yielding an intense yellow fluorescence stain under the exposure of 488 nm light of the surgical microscope. FNa extravasates from leaky tumor blood vessels (Xiang et al. 2018) or damaged or abnormal blood vessels in the brain and is a non-specific fluorophore collecting in the extracellular background and does not appear to regularly stain individual cells. It is seen to leak in other extracerebral locations and in other organs, however, the blood-brain barrier contains it.

The objective of this study was to investigate the feasibility and effectiveness of CLE for discrimination of malignant and normal brain tissue from areas of non-tumor tissue, specifically related to the appearance of FNa extravasation (Figure 3.9). The ability of CLE to produce high-quality diagnostic images was evaluated by a neuropathologist and 3 neurosurgeons expert with the use of CLE. All evaluators were masked to the acquisition process. We hypothesized that these qualified professionals would be able to differentiate among images of tumor tissue, injury to brain tissue, and normal brain architecture with high accuracy. This measure was evaluated through a 40-question assessment comprising diagnostic images of tumor, injured, and normal brain tissue. The assessment included still images and GIF files that contained z-stack or time-lapse confocal images. Rapidly obtained sequential time-lapse images transformed into a digital cine image loop were representative and comparable to the real-time images previously generated intraoperatively with the CLE (Martirosyan, Eschbacher, et al. 2016). We believe that cine-like CLE images often have more diagnostic value than the single CLE frame because they provide information on cell movement trajectories and

velocity of movement. This aspect of videos subjectively aids differentiation of erythrocytes from tumor cells.

Figure 3.9. Image of coronal brain slice taken in the YELLOW 560 mode of the operative microscope showing tumor in the left hemisphere and stabbing injury in the right hemisphere, both with increased fluorescein signals. Used with permission from Barrow Neurological Institute, Phoenix, Arizona.

Analysis of the data from the assessment suggested that the 3 neurosurgeons and the neuropathologist were able to correctly identify brain pathology with CLE with high sensitivity (86%) and specificity (96%). These promising data suggest that CLE may provide an adjunct tool for intraoperative decision-making regarding tumor margins. Moreover, image interpretation could be rapidly accomplished with an automatic image classification system, particularly with a DCNN-based model. Analogous to automatic detection of lesions from gastrointestinal endoscopy images (Yuana et al. 2017), diagnostic features could also be potentially identified in CLE images of the brain to

augment decision-making and is highly useful because of the high number of CLE images collected during patient use. This study offers additional validation for the use of intraoperative CLE to guide tumor resection. Analysis of the data reveals that images graded as higher quality were correctly identified significantly more often than images of lower quality (Figure 3.7). These data suggest that higher-quality CLE images can significantly improve intraoperative diagnostic capability.

Study Design Considerations

Limitations of this study include the potential source of variation among individual mice, which may arise from the differences in completeness of the tail vein injection of FNa. Although we used a xenograft brain tumor model, this syngeneic model shows invasion along the tracts and vessels that mimics human glioblastomas. Lower concentrations of FNa than those reported in our study may reduce CLE image quality. The selected imaging time window (10-30 minutes) provided consistent CLE pictures and was deemed sufficient as it fit the potential time window for CLE use during surgery or at the final stages of tumor removal. However, optimal clinical dosage and timing of FNa injection suitable for wide-field imaging and CLE should be tested in a clinical study. It may be the case that doses and timing would not be optimal for simultaneous use of the operative microscope and CLE in the same excitation-detection wavelengths. Our experience with CLE (unpublished data, ongoing studies) suggests that a combination (Suero Molina et al. 2018, Yano et al. 2017) of 5-ALA and FNa could be the solution,

with 5-ALA used to guide resection on the operative microscope level and FNa used to obtain an optical biopsy and investigate histological features.

Another potential bias for this study is that biopsy image locations for diagnostic testing were preselected from all biopsies. This preselection was done to narrow down the number of questions for the diagnostic test. Thus, similar-appearing biopsy sites from tumor and injury areas or imaging artifacts were excluded by trained personnel. Moreover, we believe that automatic recognition and deletion or hiding of nondiagnostic and distorted images should be automated, as it optimizes surgical-pathology workflow, especially given the high number of images potentially generated with the use of CLE (Kamen et al. 2016). Diagnostic testing was performed so that the imaging location was blinded for reviewing pathologists and neurosurgeons. As a result, diagnostic testing was performed post hoc. Digital images acquired rapidly in sequence in the same location and presented as cine-like GIF images created impression of real-time live CLE imaging and removed potential bias regarding knowledge of the probe position.

The images selected for diagnostic testing were from normal, injured, and known tumor tissue brain locations. The doubtful images were not selected, as they were deemed to be uninformative. This reasoning is similar to standard pathology practice where frozen sections are not infrequently called uninformative and more sections or different biopsy locations are required to make a final determination. Furthermore, the frozen tissue slice is usually at least 4 mm wide, resulting in more than a 16 mm^2 surface square available for visual analysis by a pathologist, and only part of this surface may contain diagnostic features. The actual tissue surface imaged by a CLE is 0.11 mm^2.

Hypothetically, it would require at least 145 images to cover the same surface area in a tiled fashion by CLE. Multiplied by 1.29 seconds per image on the highest resolution mode in the system used for this study, this would require more than 187 seconds (3+ minutes). In practice, it is possible to cover large tissue surfaces by moving the CLE probe and halting at the point of interest to achieve a better quality image. It was possible to gently move the probe over the surface of the brain and visualize invading tumor border, an example of which is depicted in Figure 3.3A, C, and E.

Tumor biopsy sites selected for diagnostic testing contained images taken at the center or border area where only few groups of tumor cells were visible, suggesting that CLE can detect areas with sparsely distributed tumor cells. We had few clinical cases with a questionable tumor-free border area that was scanned with CLE and showed tumor cells, later confirmed with matched H&E. While this pilot study answers basic questions of the ability of CLE to distinguish tumor and non-tumor tissue, it also exposes questions regarding precise correlation of CLE and H&E findings, and it emphasizes the need for rigorous correlative biopsy-based investigations, especially at tumor margins.

Implications for Practice

Differentiation of normal, injured, and glioma tissue during FNa-guided resection would be especially helpful in patients with uncertain determination of histology or at the tumor border region. The ability to distinguish among these tissues infused with FNa is particularly vital when it is necessary to identify the presence of normal brain staining due to blood-brain barrier disruption such as that associated with a brain tumor or the

minor mechanical surgical trauma when removing tissue (Belykh et al. 2016). In previous studies that investigated CLE technology, the aim was to make a diagnosis for the whole case, so the conclusion was made based on an analysis of all images acquired during a particular case (Martirosyan, Eschbacher, et al. 2016). In the current study, we performed biopsy-based diagnostic testing analysis so that every biopsy site was treated independently with three possible conclusions being normal, injured, or tumor tissue. In this way, we used CLE to evaluate its use at each region to indicate tissue characteristics for a fluorophore that interacts nonspecifically. Furthermore, we compared diagnostic accuracy with a deep learning-based model for CLE classification. Such computer-aided automatic analysis of CLE images seems to have great potential for improving rapid image-based diagnosis (Aubreville et al. 2017, Jisu, Bo-Yong, and Hyunjin 2017, Kamen et al. 2016).

Current research protocols include administration of FNa at the induction of anesthesia, about 40 minutes prior to resection (Schebesch et al. 2016). This timing allows FNa to accumulate in the brain tumor and FNa clearance from the vessels, thus decreasing the chance for extravasation during actual tumor resection.

In addition, our study suggests that interrogation with CLE may provide additional cellular-level information regarding the tissue architecture and is able to provide high-quality images to differentiate tumor and non-tumor tissues even in the presence of FNa extravasation. Moreover, extravasation of the FNa in the normal brain would create a detectable contrast to visualize more histological cellular features of the normal tissue, potentially resulting in more confidence when differentiating from tumor

tissue. This principle seems to work well in the areas lacking a blood-brain barrier-like structure, such as in the gastrointestinal tract where normal-appearing cellular structure is clearly delineated by CLE in healthy areas.

Wide-field fluorescence cancer imaging systems rely on the ability of the fluorescent probe to be retained specifically in tumor tissue without moving to surrounding normal tissue. The presence of non-selective fluorescence would decrease the diagnostic accuracy of such systems. For example, the presence of non-selective PpIX accumulation in reactive brain tissue after 5-ALA administration (Omoto et al. 2018, Behling et al. 2016) or the presence of high-dose FNa in the surrounding non-tumor tissues present challenging diagnostic situations for wide-field imaging. However, CLE is not an optical instrument technology that detects the presence of the signal per se; rather, it specifically acquires the optical patterns and yields images that reveal different intensities of fluorescent signal.

Whether the use of high concentrations of contrast agent to stain both normal and abnormal tissues will result in clearer or more distinguishable CLE images is a question that remains to be answered for its use in the brain. Therefore, our findings warrant future clinical investigation of CLE interrogation of the tumor bed by acquiring multiple optical CLE biopsies and matched biopsies for histology.

Conclusion

This study is the first to provide evidence that in vivo CLE imaging can distinguish among normal, injured, and tumor brain tissue during FNa-guided surgery

with relatively high specificity and sensitivity. Accurate CLE image interpretation has critical implications for diagnosis and requires specialized training. Decision-making based on the CLE images could be further augmented with computer-aided image interpretation. The operation of CLE technology, generation and appearance of fluorescent images, and associated automated image diagnostic systems are novel for most neurosurgeons and pathologists. Explorations of these problems early to find solutions will help diagnostic yield effect of CLE technology when it soon becomes FDA approved for neurological use.

References

Abdelwahab, M. G., T. Sankar, M. C. Preul, and A. C. Scheck. 2011. "Intracranial implantation with subsequent 3D in vivo bioluminescent imaging of murine gliomas." *J Vis Exp* (57):e3403. doi: 10.3791/3403.

Acerbi, F. 2016. "Fluorescein assistance in neuro-oncological surgery: A trend of the moment or a real technical adjunt?" *Clin Neurol Neurosurg* 144:119-20. doi: 10.1016/j.clineuro.2016.03.011.

Acerbi, F., M. Broggi, G. Broggi, and P. Ferroli. 2015. "What is the best timing for fluorescein injection during surgical removal of high-grade gliomas?" *Acta Neurochir (Wien)* 157 (8):1377-8. doi: 10.1007/s00701-015-2455-z.

Acerbi, F., M. Broggi, M. Eoli, E. Anghileri, C. Cavallo, C. Boffano, R. Cordella, L. Cuppini, B. Pollo, M. Schiariti, S. Visintini, C. Orsi, E. La Corte, G. Broggi, and P. Ferroli. 2014. "Is fluorescein-guided technique able to help in resection of high-grade gliomas?" *Neurosurg Focus* 36 (2):E5. doi: 10.3171/2013.11.FOCUS13487.

Acerbi, F., M. Broggi, K. M. Schebesch, J. Hohne, C. Cavallo, C. De Laurentis, M. Eoli, E. Anghileri, M. Servida, C. Boffano, B. Pollo, M. Schiariti, S. Visintini, C. Montomoli, L. Bosio, E. La Corte, G. Broggi, A. Brawanski, and P. Ferroli. 2018. "Fluorescein-Guided Surgery for Resection of High-Grade Gliomas: A Multicentric Prospective Phase II Study (FLUOGLIO)." *Clin Cancer Res* 24 (1):52-61. doi: 10.1158/1078-0432.CCR-17-1184.

Acerbi, F., C. Cavallo, M. Broggi, R. Cordella, E. Anghileri, M. Eoli, M. Schiariti, G. Broggi, and P. Ferroli. 2014. "Fluorescein-guided surgery for malignant gliomas: a review." *Neurosurg Rev* 37 (4):547-57. doi: 10.1007/s10143-014-0546-6.

Acerbi, F., C. Cavallo, K. M. Schebesch, M. O. Akcakaya, C. de Laurentis, M. K. Hamamcioglu, M. Broggi, A. Brawanski, J. Falco, R. Cordella, P. Ferroli, T. Kiris, and J. Hohne. 2017. "Fluorescein-Guided Resection of Intramedullary Spinal Cord Tumors: Results from a Preliminary, Multicentric, Retrospective Study." *World Neurosurg* 108:603-609. doi: 10.1016/j.wneu.2017.09.061.

Akcakaya, M. O., B. Goker, M. O. Kasimcan, M. K. Hamamcioglu, and T. Kiris. 2017. "Use of Sodium Fluorescein in Meningioma Surgery Performed Under the YELLOW-560 nm Surgical Microscope Filter: Feasibility and Preliminary Results." *World Neurosurg* 107:966-973. doi: 10.1016/j.wneu.2017.07.103.

Aubreville, M., C. Knipfer, N. Oetter, C. Jaremenko, E. Rodner, J. Denzler, C. Bohr, H. Neumann, F. Stelzle, and A. Maier. 2017. "Automatic Classification of Cancerous Tissue in Laserendomicroscopy Images of the Oral Cavity using Deep Learning." *Sci Rep* 7 (1):11979. doi: 10.1038/s41598-017-12320-8.

Banu, M. A., J. H. Kim, B. J. Shin, G. F. Woodworth, V. K. Anand, and T. H. Schwartz. 2014. "Low-dose intrathecal fluorescein and etiology-based graft choice in endoscopic endonasal closure of CSF leaks." *Clin Neurol Neurosurg* 116:28-34. doi: 10.1016/j.clineuro.2013.11.006.

Behling, F., F. Hennersdorf, A. Bornemann, M. Tatagiba, and M. Skardelly. 2016. "5-Aminolevulinic Acid Accumulation in a Cerebral Infarction Mimicking High-Grade Glioma." *World Neurosurg* 92:586 e5-8. doi: 10.1016/j.wneu.2016.05.009.

Belykh, E., N. L. Martirosyan, K. Yagmurlu, E. J. Miller, J. M. Eschbacher, M. Izadyyazdanabadi, L. A. Bardonova, V. A. Byvaltsev, P. Nakaji, and M. C. Preul. 2016. "Intraoperative fluorescence imaging for personalized brain tumor resection: current state and future directions." *Front Surg* 3:55. doi: 10.3389/fsurg.2016.00055.

Bongetta, D., C. Zoia, R. Pugliese, D. Adinolfi, V. Silvani, and P. Gaetani. 2016. "Low-Cost Fluorescein Detection System for High-Grade Glioma Surgery." *World Neurosurg* 88:54-8. doi: 10.1016/j.wneu.2016.01.017.

Bossuyt, P. M., J. B. Reitsma, D. E. Bruns, C. A. Gatsonis, P. P. Glasziou, L. Irwig, J. G. Lijmer, D. Moher, D. Rennie, H. C. de Vet, H. Y. Kressel, N. Rifai, R. M. Golub, D. G. Altman, L. Hooft, D. A. Korevaar, J. F. Cohen, and Stard Group. 2015. "STARD 2015: an updated list of essential items for reporting diagnostic accuracy studies." *Radiology* 277 (3):826-32. doi: 10.1148/radiol.2015151516.

Catapano, G., F. G. Sgulo, V. Seneca, G. Lepore, L. Columbano, and G. di Nuzzo. 2017. "Fluorescein-Guided Surgery for High-Grade Glioma Resection: An Intraoperative "Contrast-Enhancer"." *World Neurosurg* 104:239-247. doi: 10.1016/j.wneu.2017.05.022.

Chan, D. T., S. Y. Hsieh, C. K. Lau, M. K. Kam, H. H. Loong, W. K. Tsang, D. M. Poon, and W. S. Poon. 2017. "Ten-year review of survival and management of malignant glioma in Hong Kong." *Hong Kong Med J* 23 (2):134-9. doi: 10.12809/hkmj164879.

Ciezka, M., M. Acosta, C. Herranz, J. M. Canals, M. Pumarola, A. P. Candiota, and C. Arus. 2016. "Development of a transplantable glioma tumour model from genetically engineered mice: MRI/MRS/MRSI characterisation." *J Neurooncol* 129 (1):67-76. doi: 10.1007/s11060-016-2164-3.

D'Amico, R. S., Z. K. Englander, P. Canoll, and J. N. Bruce. 2017. "Extent of Resection in Glioma-A Review of the Cutting Edge." *World Neurosurg* 103:538-549. doi: 10.1016/j.wneu.2017.04.041.

Diaz, R. J., R. R. Dios, E. M. Hattab, K. Burrell, P. Rakopoulos, N. Sabha, C. Hawkins, G. Zadeh, J. T. Rutka, and A. A. Cohen-Gadol. 2015. "Study of the biodistribution of fluorescein in glioma-infiltrated mouse brain and histopathological correlation of intraoperative findings in high-grade gliomas resected under fluorescein fluorescence guidance." *J Neurosurg* 122 (6):1360-9. doi: 10.3171/2015.2.JNS132507.

Emanuelli, E., L. Milanese, M. Rossetto, D. Cazzador, E. d'Avella, T. Volo, V. Baro, L. Denaro, G. Gioffre, D. Borsetto, and A. Martini. 2015. "The endoscopic endonasal approach for cerebrospinal fluid leak repair in the elderly." *Clin Neurol Neurosurg* 132:21-5. doi: 10.1016/j.clineuro.2015.02.013.

Francaviglia, N., D. G. Iacopino, G. Costantino, A. Villa, P. Impallaria, F. Meli, and R. Maugeri. 2017. "Fluorescein for resection of high-grade gliomas: A safety study control in a single center and review of the literature." *Surg Neurol Int* 8:145. doi: 10.4103/sni.sni_89_17.

Gollapudi, P. R., I. Mohammed, S. R. Pittala, A. Reddy Kotha, N. R. Reddycherla, and D. Rao Ginjupally. 2018. "A simple improvisation to enhance the utility of Fluorescein sodium in the resection of intracranial lesions at routine neurosurgical centres." *World Neurosurg*. doi: 10.1016/j.wneu.2018.01.039.

Hamamcioglu, M. K., M. O. Akcakaya, B. Goker, M. O. Kasimcan, and T. Kiris. 2016. "The use of the YELLOW 560 nm surgical microscope filter for sodium fluorescein-guided resection of brain tumors: Our preliminary results in a series of 28 patients." *Clin Neurol Neurosurg* 143:39-45. doi: 10.1016/j.clineuro.2016.02.006.

Hashimoto, K., H. Kinouchi, H. Yoshioka, K. Kanemaru, M. Ogiwara, T. Yagi, T. Wakai, and Y. Fukumoto. 2017. "Efficacy of Endoscopic Fluorescein Video Angiography in Aneurysm Surgery-Novel and Innovative Assessment of Vascular Blood Flow in the Dead Angles of the Microscope." *Oper Neurosurg (Hagerstown)* 13 (4):471-481. doi: 10.1093/ons/opw042.

Hohne, J., A. Brawanski, and K. M. Schebesch. 2016. "Fluorescein sodium-guided surgery of a brain abscess: A case report." *Surg Neurol Int* 7 (Suppl 39):S955-S957. doi: 10.4103/2152-7806.195234.

Hohne, J., A. Brawanski, and K. M. Schebesch. 2017. "Fluorescence-guided surgery of brain abscesses." *Clin Neurol Neurosurg* 155:36-39. doi: 10.1016/j.clineuro.2017.02.014.

Hohne, J., C. Hohenberger, M. Proescholdt, M. J. Riemenschneider, C. Wendl, A. Brawanski, and K. M. Schebesch. 2017. "Fluorescein sodium-guided resection of cerebral metastases-an update." *Acta Neurochir (Wien)* 159 (2):363-367. doi: 10.1007/s00701-016-3054-3.

Ito, A., T. Endo, T. Inoue, H. Endo, K. Sato, and T. Tominaga. 2017. "Use of Indocyanine Green Fluorescence Endoscopy to Treat Concurrent Perimedullary and Dural Arteriovenous Fistulas in the Cervical Spine." *World Neurosurg* 101:814 e1-814 e6. doi: 10.1016/j.wneu.2017.03.032.

Jisu, Hong, Park Bo-Yong, and Park Hyunjin. 2017. "Convolutional neural network classifier for distinguishing Barrett's esophagus and neoplasia endomicroscopy images." *Conf Proc IEEE Eng Med Biol Soc* 2017:2892-2895. doi: 10.1109/EMBC.2017.8037461.

Kakucs, C., I. A. Florian, G. Ungureanu, and I. S. Florian. 2017. "Fluorescein Angiography in Intracranial Aneurysm Surgery: A Helpful Method to Evaluate the Security of Clipping and Observe Blood Flow." *World Neurosurg* 105:406-411. doi: 10.1016/j.wneu.2017.05.172.

Kamen, A., S. Sun, S. Wan, S. Kluckner, T. Chen, A. M. Gigler, E. Simon, M. Fleischer, M. Javed, S. Daali, A. Igressa, and P. Charalampaki. 2016. "Automatic Tissue Differentiation Based on Confocal Endomicroscopic Images for Intraoperative Guidance in Neurosurgery." *Biomed Res Int* 2016:6183218. doi: 10.1155/2016/6183218.

Kilkenny, C., W. J. Browne, I. C. Cuthill, M. Emerson, and D. G. Altman. 2010. "Improving bioscience research reporting: the ARRIVE guidelines for reporting animal research." *PLoS Biol* 8 (6):e1000412. doi: 10.1371/journal.pbio.1000412.

Lau, D., S. L. Hervey-Jumper, S. Chang, A. M. Molinaro, M. W. McDermott, J. J. Phillips, and M. S. Berger. 2016. "A prospective Phase II clinical trial of 5-

aminolevulinic acid to assess the correlation of intraoperative fluorescence intensity and degree of histologic cellularity during resection of high-grade gliomas." *J Neurosurg* 124 (5):1300-9. doi: 10.3171/2015.5.JNS1577.

Lovato, R. M., J. L. Vitorino Araujo, and J. C. Esteves Veiga. 2017. "Low-Cost Device for Fluorescein-Guided Surgery in Malignant Brain Tumor." *World Neurosurg* 104:61-67. doi: 10.1016/j.wneu.2017.04.169.

Martirosyan, N. L., J. M. Eschbacher, M. Y. Kalani, J. D. Turner, E. Belykh, R. F. Spetzler, P. Nakaji, and M. C. Preul. 2016. "Prospective evaluation of the utility of intraoperative confocal laser endomicroscopy in patients with brain neoplasms using fluorescein sodium: experience with 74 cases." *Neurosurg Focus* 40 (3):E11. doi: 10.3171/2016.1.FOCUS15559.

Martirosyan, N. L., J. Georges, J. M. Eschbacher, D. D. Cavalcanti, A. M. Elhadi, M. G. Abdelwahab, A. C. Scheck, P. Nakaji, R. F. Spetzler, and M. C. Preul. 2014. "Potential application of a handheld confocal endomicroscope imaging system using a variety of fluorophores in experimental gliomas and normal brain." *Neurosurg Focus* 36 (2):E16. doi: 10.3171/2013.11.FOCUS13486.

Minkin, K., E. Naydenov, K. Gabrovski, P. Dimova, M. Penkov, R. Tanova, S. Nachev, and K. Romanski. 2016. "Intraoperative fluorescein staining for benign brain tumors." *Clin Neurol Neurosurg* 149:22-6. doi: 10.1016/j.clineuro.2016.07.016.

Misra, B. K., S. K. Samantray, and O. N. Churi. 2017. "Application of fluorescein sodium videoangiography in surgery for spinal arteriovenous malformation." *J Clin Neurosci* 38:59-62. doi: 10.1016/j.jocn.2016.12.004.

Moore, GE, and WT Peyton. 1948. "The clinical use of fluorescein in neurosurgery; the localization of brain tumors." *Journal of Neurosurgery* 5 (4):6. doi: 10.3171/jns.1948.5.4.0392

Narducci, A., J. Onken, M. Czabanka, N. Hecht, and P. Vajkoczy. 2018. "Fluorescein videoangiography during extracranial-to-intracranial bypass surgery: preliminary results." *Acta Neurochir (Wien)*. doi: 10.1007/s00701-017-3453-0.

Neira, J. A., T. H. Ung, J. S. Sims, H. R. Malone, D. S. Chow, J. L. Samanamud, G. J. Zanazzi, X. Guo, S. G. Bowden, B. Zhao, S. A. Sheth, G. M. McKhann, 2nd, M. B. Sisti, P. Canoll, R. S. D'Amico, and J. N. Bruce. 2017. "Aggressive resection at the infiltrative margins of glioblastoma facilitated by intraoperative fluorescein guidance." *J Neurosurg* 127 (1):111-122. doi: 10.3171/2016.7.JNS16232.

Omoto, K., R. Matsuda, I. Nakagawa, Y. Motoyama, and H. Nakase. 2018. "False-positive inflammatory change mimicking glioblastoma multiforme under 5-aminolevulinic acid-guided surgery: A case report." *Surg Neurol Int* 9:49. doi: 10.4103/sni.sni_473_17.

Roberts, D. W., and J. Olson. 2017. "Fluorescein Guidance in Glioblastoma Resection." *N Engl J Med* 376 (18):e36. doi: 10.1056/NEJMicm1611258.

Sanai, N., and M. S. Berger. 2018. "Surgical oncology for gliomas: the state of the art." *Nat Rev Clin Oncol* 15 (2):112-125. doi: 10.1038/nrclinonc.2017.171.

Sanai, N., J. Eschbacher, G. Hattendorf, S. W. Coons, M. C. Preul, K. A. Smith, P. Nakaji, and R. F. Spetzler. 2011. "Intraoperative confocal microscopy for brain tumors: a feasibility analysis in humans." *Neurosurgery* 68 (2 Suppl Operative):282-90; discussion 290. doi: 10.1227/NEU.0b013e318212464e.

Sankar, T., P. M. Delaney, R. W. Ryan, J. Eschbacher, M. Abdelwahab, P. Nakaji, S. W. Coons, A. C. Scheck, K. A. Smith, R. F. Spetzler, and M. C. Preul. 2010. "Miniaturized handheld confocal microscopy for neurosurgery: results in an experimental glioblastoma model." *Neurosurgery* 66 (2):410-7; discussion 417-8. doi: 10.1227/01.NEU.0000365772.66324.6F.

Schebesch, K. M., A. Brawanski, C. Hohenberger, and J. Hohne. 2016. "Fluorescein Sodium-Guided Surgery of Malignant Brain Tumors: History, Current Concepts, and Future Project." *Turk Neurosurg* 26 (2):185-94. doi: 10.5137/1019-5149.JTN.16952-16.0.

Schindelin, J., I. Arganda-Carreras, E. Frise, V. Kaynig, M. Longair, T. Pietzsch, S. Preibisch, C. Rueden, S. Saalfeld, B. Schmid, J. Y. Tinevez, D. J. White, V. Hartenstein, K. Eliceiri, P. Tomancak, and A. Cardona. 2012. "Fiji: an open-source platform for biological-image analysis." *Nat Methods* 9 (7):676-82. doi: 10.1038/nmeth.2019.

Schwake, M., W. Stummer, E. J. Suero Molina, and J. Wolfer. 2015. "Simultaneous fluorescein sodium and 5-ALA in fluorescence-guided glioma surgery." *Acta Neurochir (Wien)* 157 (5):877-9. doi: 10.1007/s00701-015-2401-0.

Stummer, W. 2017. "Intra-operative tissue diagnosis: isn't it time for some reporting guidelines?" *Acta Neurochir (Wien)* 159 (2):369-370. doi: 10.1007/s00701-016-3057-0.

Suero Molina, E., J. Wolfer, C. Ewelt, A. Ehrhardt, B. Brokinkel, and W. Stummer. 2018. "Dual-labeling with 5-aminolevulinic acid and fluorescein for fluorescence-guided resection of high-grade gliomas: technical note." *J Neurosurg* 128 (2):399-405. doi: 10.3171/2016.11.JNS161072.

Szatmari, T., K. Lumniczky, S. Desaknai, S. Trajcevski, E. J. Hidvegi, H. Hamada, and G. Safrany. 2006. "Detailed characterization of the mouse glioma 261 tumor model for experimental glioblastoma therapy." *Cancer Sci* 97 (6):546-53. doi: 10.1111/j.1349-7006.2006.00208.x.

Szegedy, C , W Liu, Y Jia, P Sermanet, S Reed, D Anguelov, D Erhan, V Vanhoucke, and A Rabinovich. 2015. "Going deeper with convolutions." Proceedings of the IEEE Conference on Computer Vision and Pattern Recognition.

Thien, A., J. P. Rao, W. H. Ng, and N. K. King. 2017. "The Fluoropen: a simple low-cost device to detect intraoperative fluorescein fluorescence in stereotactic needle biopsy of brain tumors." *Acta Neurochir (Wien)* 159 (2):371-375. doi: 10.1007/s00701-016-3041-8.

Xiang, Y., X. P. Zhu, J. N. Zhao, G. H. Huang, J. H. Tang, H. R. Chen, L. Du, D. Zhang, X. F. Tang, H. Yang, and S. Q. Lv. 2018. "Blood-Brain Barrier Disruption, Sodium Fluorescein, And Fluorescence-Guided Surgery Of Gliomas." *Br J Neurosurg*:1-8. doi: 10.1080/02688697.2018.1428731.

Yano, H., N. Nakayama, N. Ohe, K. Miwa, J. Shinoda, and T. Iwama. 2017. "Pathological analysis of the surgical margins of resected glioblastomas excised using photodynamic visualization with both 5-aminolevulinic acid and fluorescein sodium." *J Neurooncol* 133 (2):389-397. doi: 10.1007/s11060-017-2445-5.

Yuana, Z, M IzadyYazdanabadia, D Mokkapatib, R Panvalkarb, JY Shinc, N Tajbakhshc, S Gurudud, and J Liangc. 2017. "Automatic polyp detection in colonoscopy videos." SPIE Medical Imaging.

CHAPTER 4

VISUALIZATION OF BRAIN MICROVASCULATURE AND BLOOD FLOW IN VIVO: FEASIBILITY STUDY USING CONFOCAL LASER ENDOMICROSCOPY

Abstract

Object: Intraoperative techniques for blood flow assessment are essential for neurosurgery. The goal of this study was to perform qualitative and quantitative analyses of blood flow in normal and pathologic brain and spinal cord microvasculature using confocal laser endomicroscopy (CLE).

Methods: Blood flow in cortical, dural, and spinal cord microvasculature was assessed in vivo in swine. We assessed microvasculature in normal conditions and after vessel occlusion, brain injury due to cold or surgical trauma, and cardiac arrest. Tumor-associated microvasculature was also assessed in vivo and ex vivo in 20 patients with gliomas.

Results: We observed erythrocyte flow in blood vessels 5–500 μm in diameter. Various intravascular events were assessed in normal and injured brain tissue: thrombosis, flow arrest and redistribution, flow velocity changes, agglutination, and cells rolling. Microvasculature in in vivo CLE images of gliomas was classified as normal (25/37 vessels, 68%) or abnormal (12/37 vessels, 32%) based on the morphological appearance. Dural lymphatic channels were discriminated from blood vessels. Microvasculature CLE imaging was possible for up to 30 minutes after a single 1 mg/kg intravenous dose of fluorescein.

Conclusions: CLE imaging allows assessment of cerebral and tumor microvasculature and blood flow alterations with subcellular resolution intraoperative imaging demonstrating precise details of real-time ongoing intravascular cell movement. Research and clinical scenarios may benefit from this novel intraoperative in vivo microscopic fluorescence imaging modality.

Introduction

Intraoperative visualization of blood-flow characteristics in vessels is of keen interest during many neurosurgical procedures. Development of cerebral videoangiography with fluorescein sodium (Feindel, Yamamoto, and Hodge 1967) and indocyanine green (ICG) (Raabe et al. 2003, Raabe et al. 2005) as contrast agents provided a simple and useful intraoperative method for neurosurgeons to rapidly assess blood flow in cerebral vessels. Although these wide-field fluorescence imaging techniques are used extensively currently, their main drawbacks are the short temporal imaging resolution that requires several reinjections of the contrast and the inability to resolve the flow of erythrocytes in the microvasculature that comprises the microcirculatory network.

Brain capillary blood flow at the level of cellular resolution has been imaged using fluorescein isothiocyanate-labeled cells and benchtop confocal microscope systems (Seylaz et al. 1999). The development of pen-sized handheld confocal laser endomicroscopy (CLE) has allowed real-time in vivo assessment of tissue microstructure and it has been used to assess brain tumor tissue (Belykh et al. 2019, Martirosyan,

Eschbacher, et al. 2016). However, its application for microvascular imaging has not been thoroughly studied. Building upon the previous findings for murine brain microvasculature obtained with the first-generation CLE (Goetz et al. 2008), we used an FDA-approved new-generation CLE with fluorescein for contrast to assess previously unexplored blood flow variables in cortical and spinal cord microvasculature in a large-animal model and human brain tissue.

The goal of this study was to perform qualitative and quantitative analyses of blood flow in normal and pathologic brain and spinal cord microvasculature. We assessed the feasibility of using CLE to visualize blood cells inside vessels and therefore perform continuous blood flow imaging after the fluorescent contrast injection. We identified variables that can be assessed by this new intraoperative imaging modality for future potential research and clinical use. To our knowledge, this is the first study of cerebral blood flow microimaging in a large animal with a clinical-grade CLE system.

Methods

Experimental Design

To investigate the brain microvasculature within the spectrum of potential conditions, we used several experimental models and performed a retrospective review of clinical CLE images. Normal brain and spinal cord microvasculature of swine were investigated. Microvasculature was assessed in an area of cold injury, cortical injury due to craniotomy trauma, and spinal cord injury, which were all characterized by blood–

brain barrier compromise. Brain tumor microvasculature was assessed in human glioma tissue.

Large-Animal Model for Microvasculature Imaging

All animal experiments were approved by the Institutional Animal Care and Use Committee of the Barrow Neurological Institute and St. Joseph's Hospital and Medical Center and conducted in compliance with the Guide for the Care and Use of Laboratory Animals (Institute of Laboratory Animal Resources, Commission on Life Sciences, National Research Council. Washington, D.C.). Animals were housed and cared for in our institutionally accredited facility operated according to the standards of the Association for Assessment and Accreditation of Laboratory Animal Care International. Experiments were performed on five adult male Yorkshire swine (mean weight ~50 kg). Animals were euthanized immediately at the completion of the procedure while remaining under deep anesthesia state by intravenous KCl injection.

Large-Animal Procedure

The swine were premedicated with intramuscular ketamine and xylazine (11-20 mg/kg and 2-3mg/kg respectively), intubated endotracheally with mechanically assisted ventilation and placed under general anesthesia using 2% isoflurane with constant physiologic monitoring. Intravenous catheters were placed in the femoral veins. Intraarterial catheters were placed through the femoral arterial access, advanced under fluoroscopic angiographic guidance and left in place in the left carotid artery. A craniotomy was then performed to expose the bilateral cerebral hemispheres. The dura

was cut in a curvilinear fashion and reflected toward the superior sagittal sinus to expose the cortical surface. The operative field was draped and imaged with a wide-field operating microscope (KINEVO, Carl Zeiss Meditec, Jena, Germany).

Cold injury was created by placing a stainless steel dissector, cooled in the liquid nitrogen solution, onto the surface of the cortex for one minute, as described elsewhere (Nag 1996). The areas of cortical trauma due to the craniotomy were identified near the edges of the craniotomy as areas of erythematous brain with fluorescein staining on YELLOW 560 mode. Fluorescein was administered with alternating intravenous (1, 2, 5 mg/kg) and intracarotid (0.005, 0.05, 0.1% in 5 mL) injections.

Imaging Spinal Cord Microvasculature

To image spinal cord microvasculature, the swine underwent laminectomy at T3–T8 spinal levels. The dura mater was opened to expose the spinal cord and the CLE probe was placed in contact with the dorsal surface of the spinal cord. After imaging, a mild spinal cord injury was induced using a previously described protocol by delivering a force of 300 g/cm^2 (20 g weight at 15 cm distance) (Martirosyan et al. 2015).

Imaging Dura

To image the cranial dura matter in the swine, a catheter was placed in a lateral sylvian subarachnoid space before opening the dura, and 0.5 mL of ICG (1.25 mg/mL) and 0.42 mL of fluorescein (10 mg/mL) were injected. The dura mater was imaged simultaneously with YELLOW 560 and INFRARED 800 modes of 2 operating microscopes to observe diffusion of the contrast agents in the subarachnoid space. The

surface of the dura was imaged with the CLE probe within 3 hours after contrast injection.

Confocal Endomicroscopy System

The CLE system utilized (CONVIVO, Zeiss Meditec, Germany) is an optical biopsy tool that employs 488-nm laser confocal imaging in a miniaturized 15-cm long, 5-mm thick handheld imaging probe. The probe was encased in a sterile sheath and placed in contact with the brain surface using a freehand-holding technique, or using a semi-rigid retractor to hold the probe in place. Various locations of the brain vasculature were imaged by gently moving the probe, maintaining contact with the brain surface as described previously (Belykh et al. 2019). Two major speeds and resolutions were used: 1920×270, which affords 0.44 seconds/frame, and high-quality imaging at 1920×1080, which affords 1.29 seconds/frame (0.78 frames/second [FPS]). Fluorescein (AK-FLUOR, 10%, Akorn, IL) was used as an imaging contrast agent.

Conditions Investigated

We investigated vessel thickness, vessel diameter, and the maximum vessel diameter amenable to confocal imaging. We also investigated the blood flow patterns in normal and injured brain locations. Duration of CLE blood flow imaging after contrast injection was also assessed in comparison to wide-field fluorescein angiography.

Immunostaining Dural Lymphatic Vessels

Dural excisions were taken from locations that had been marked after detecting candidate lymphatic vessels with the CLE system. The tissue was then formalin-fixed and transported to the department of pathology for paraffin embedding and sectioning at 5-

μm thickness. Tissue sections were deparaffinized in xylenes before rehydrating through decreasing concentrations of ethanol (100%, 95%, 70%, 50%) for 5 minutes each, finishing in 1× phosphate buffered saline (PBS). Antigen retrieval was achieved using either heat-induced epitope retrieval with citric acid buffer (pH 6.0) at 60°C for 20 minutes, or by incubating with formic acid (88% v/v) for 5 minutes at 20°C. Slides were then washed for 5 minutes and incubated with H_2O_2 (3%) for 5 minutes to quell endogenous peroxidases. After a brief rinse in PBS, the slides were then blocked with 1× PBS Tween 20 (0.1%) containing 3% bovine serum albumin, 10% normal goat serum for 30 minutes at 20°C. Tissue sections were then incubated with primary antibody (polyclonal rabbit anti-LYVE-1, Abcam ab33682, Cambridge, UK) diluted at 1:200 in blocking buffer and incubated overnight (~18 hours) at 4°C in a humidified chamber. The slides were washed once again before applying a secondary antibody solution (goat anti-rabbit IgG, Vector Laboratories [Burlingame, CA], PK-6106) for 45 minutes at 20°C. The slides were then incubated with avidin-biotin complex solution (Vector Laboratories, PK-6106) for 30 minutes at 20°C. Chromogenic signal development was then achieved using the IMMpact DAB peroxidase substrate kit (Vector Laboratories, SK-4105) followed by counterstaining with hematoxylin, dehydration, and clearing before mounting. Positive controls used for LYVE-1 included skin and lymph nodes excised from a separate animal. Secondary antibody controls were also performed on experimental and control tissue.

Microvascular Imaging in Human Gliomas

We retrospectively assessed prospectively collected data using a database of in vivo and ex vivo intraoperative digital CLE biopsies of patients with gliomas. All patients whose data were obtained from the database were prospectively enrolled in an original study within a 10-month period, which was approved by the St. Joseph's Hospital and Medical Center Institutional Review Board for Human Research. Patients received 5 mL intravenous 10% fluorescein 5 minutes prior to CLE imaging. The sensitivity and specificity of CLE to provide diagnostic information regarding the brain tumor tissue has been previously reported (Martirosyan, Eschbacher, et al. 2016). Unlike the previous analysis, this study focused on identifying and characterizing normal and abnormal microvasculature. CLE images in this group were obtained with an Optiscan 5.1, which is a previous-generation CLE, equivalent to the new-generation CLE used in this study (Belykh et al. 2019).

Image Analysis

All recordings were analyzed postoperatively in Fiji (NIH). Videos were generated in Fiji by combining single CLE frames in a stack, applying an 8-bit single color type, and saving the file as an AVI or GIF video at 5 FPS speed, with no compression. Statistical analysis was performed in Excel (Microsoft Corp, Redmond, WA). Data are presented as mean ± standard deviation.

RESULTS

In vivo Imaging of Brain Microvasculature in Swine

Vessel Wall Morphology

We were able to visualize brain and spinal cord blood vessels and blood flow in vessels with diameters ranging from 5 to 500 μm in swine (n=5). The thickness of the vessel wall impeded the blood flow imaging in vessels larger than ~200 μm in diameter. Contrast created by fluorescein in the intravascular compartment, in the vessel wall, and in the perivascular parenchyma allowed us to measure vessel wall thickness in multiple vessels (Figure 4.1). The vascular wall cellular structure, including endotheliocytes and pericytes, was visualized (Figure 4.1B). In capillaries (<10 μm), the endothelial cell bodies and pericytes were seen, as these cells were stained by the contrast to varying degrees (Figure 4.1B). In larger vessels, the cellular composition of the vessel walls was observed as tightly interconnected columnar cells in arteries and less tightly packed and stretched cells in veins. Moreover, we could detect the functional state of the vessels—some larger vessels were constricted, as evidenced by the areas of vessel narrowing near the precapillary sphincters (Figure 4.1E) and wrinkled luminal membrane (Figure 4.2). Visualization of the vessel wall was possible during lengthier times after fluorescein injection, with the earliest observance being 8 minutes after fluorescein injection, but more frequently around 30 minutes after injection. Tissue injury, contrast extravasation, and higher dose (subsequent injections of fluorescein) all made visualization of the vessel wall easier at the later times of imaging.

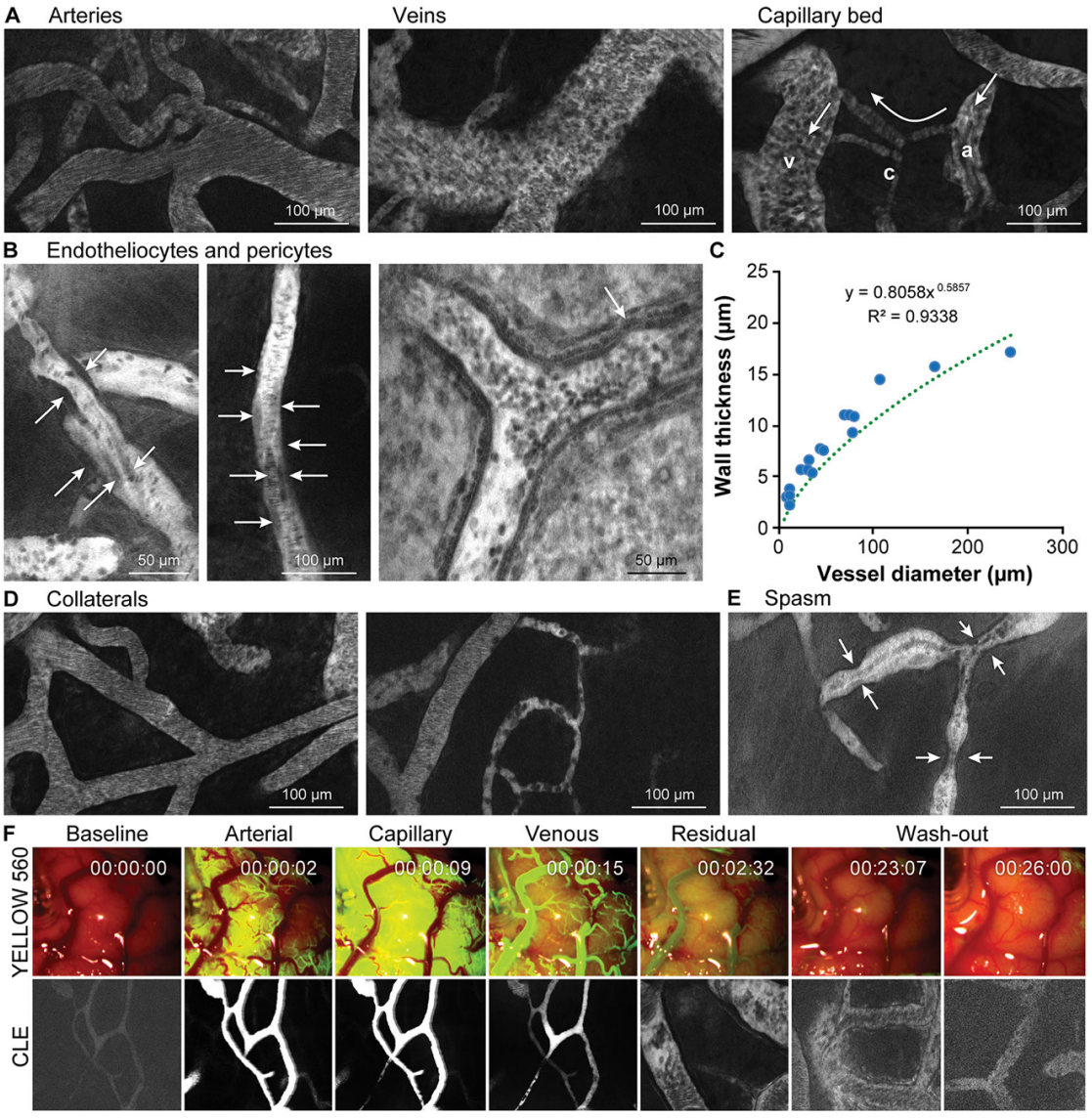

Figure 4.1. Observations of brain microvasculature in swine. (A) Images show the differences in appearance of arterial, venous, and capillary flow in the microvasculature. (B) Visualization of the cellular structure of the vascular wall. Arrows point to endotheliocytes and pericytes. (C) Association between the vessel diameter and wall thickness as measured from 15 microvessels. (D) Abundant collaterals were observed in cortical microvasculature. (E) Example of spasm (arrows) in the small arteriole and its effect on the flow. (F) Visualization of the cortical blood flow during fluorescent

angiography. Change in the fluorescent signal intensity during arterial, capillary, and venous phases (~15 sec) is the basis for flow estimation in wide-field microscopy with a YELLOW 560 filter. Estimation of red blood cell movements in the microvasculature is the basis for flow estimation in confocal endomicroscopy (duration ~26 min after a single 1 mg/kg intravenous fluorescein injection). Abbreviations: a. artery, v. vein, c. capillary. Used with permission from Barrow Neurological Institute, Phoenix, Arizona.

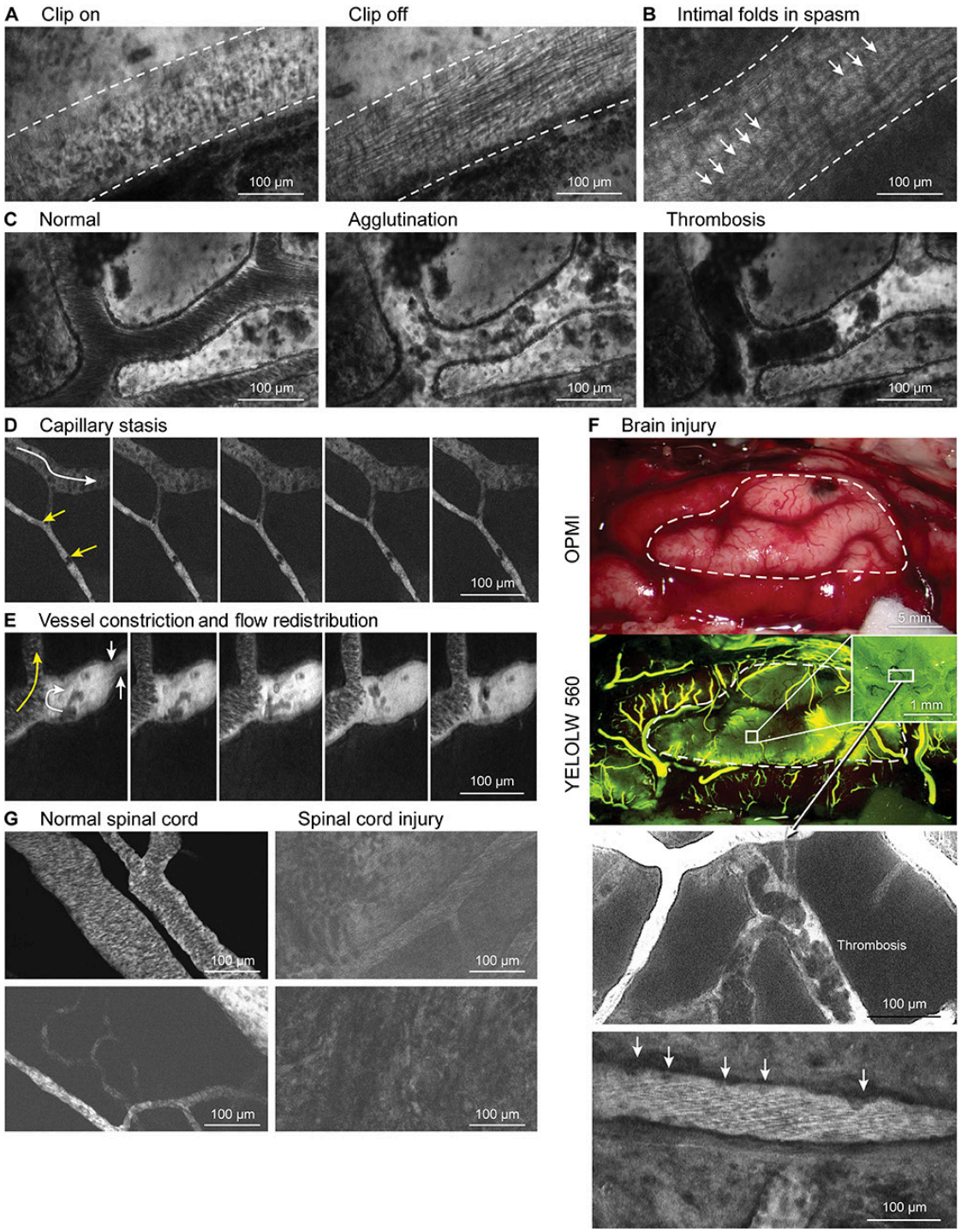

Figure 4.2. Visualization of the functional state of brain microvasculature in swine. (A) During the clipping of proximal artery (clip on), slowing of the blood flow is observed. After the clip was removed (clip off), the restoration of arterial flow pattern was noted.

(B) Spasm of the larger artery creates longitudinal folds on the intimal surface of the vessel observed on the CLE image. (C) Dynamics of the intraluminal thrombi formation in the microvasculature is observed during cardiac arrest. (D) Some collaterals are not functionally active and have stagnant flow (short arrows point to the resting cells in the capillary; long arrow shows direction of the preserved flow). (E) Constriction (short arrows) and partial thrombosis of the vessel. The series of images demonstrate that part of the vessel has a normal flow (curved yellow arrow) while part of a vessel has a turbulent flow (curved white arrow) with agglutinated cells and few blood cells. (F) Imaging of the cortical microvasculature in the area of cortical injury (cold injury). YELLOW 560 fluorescent image during the arterial phase shows gross appearance of fluorescein extravasation into the brain tissue. Confocal endomicroscopy shows intraluminal thrombosis in the venules and cell adhesion to the vascular wall (arrows). The square inset in the right corner enlarges the area depicted on the YELLOW 560 image. The upper confocal endomicroscopy image was taken at the area shown by the rectangle. (G) Normal microvasculature in the spinal cord shows elongated vessels with branches and competent blood-brain barrier preventing contrast extravasation. Multiple extravascular blood cells and extravasation of the contrast are observed at the region of the spinal cord injury. Used with permission from Barrow Neurological Institute, Phoenix, Arizona.

Differentiation of Veins and Arteries

Arteries were differentiated from veins on the basis of several features. Arteries had a more acute branching pattern, while veins tended to show a branching pattern at a right angle. The direction of the flow from a smaller to a larger vessel was also an indicative venous feature. The high-velocity arterial flow created linear intraluminal artefacts, while in vessels with slower venous flow, individual blood cells could be identified (Figure 4.1A). The longer, thinner dark lines represented rapid flow while the shorter, thicker lines represented slower flow. This interpretation of erythrocyte blur can be used as supporting evidence when differentiating between arteries and veins. The capillary network, with a width and vessel wall thickness to accommodate a single blood cell, was easily identified. Capillary flow ranged from stagnant with stationary blood cells to a slow flow with quantifiable velocity to a fast flow that is beyond the ability of the CLE to capture image frames. We identified various branching patterns, including sequential segmental and circular connections of the vessels (Figure 4.1D), as well as the artery–capillary–vein transition.

Blood Flow Alteration

We consistently identified changes in the blood flow pattern in a surface cortical artery after proximal clip application. Interestingly, proximal clipping did not halt the blood flow completely, but rather decreased its speed, likely due to small collaterals and flow redistribution (Figure 4.2A).

Intravascular Events

Various alterations in the blood flow through the brain were investigated. We observed the dynamics of the thrombi formation in the microvasculature during circulatory arrest (Figure 4.2C). In the cortical injury site created with liquid nitrogen-cooled probe, or due to surgical trauma during the craniotomy, the extravasation of the contrast due to blood–brain barrier disruption is evident in the wide-field imaging and CLE imaging (Figure 4.2F). These areas are distinct on CLE images due to perivascular contrast diffusion, stagnation of the flow with intravascular blood cells that are agglutinated and/or attached to the vessel wall, as well as some intravascular thrombi with trapped contrast.

Duration of Confocal Blood Flow Imaging

Although the fluorescence intensity faded over time, it was strong enough for CLE intravascular imaging for at least 20 to 30 minutes after intravenous injection of 1 mg/kg fluorescein and adequate for longer imaging after subsequent fluorescein injections, which were deemed clinically relevant (Table 4.1). This fluorescence lasted significantly longer than the duration of the intravascular contrast visible through a wide-field operating microscope (Figure 4.1F). We were able to continuously visualize blood flow within a total time of more than 3 hours imaging when reinjecting fluorescein.

Table 4.1. Duration of confocal laser endomicroscopy imaging of intravascular blood flow

Order	Route	Dose of Fluorescein	Imaging Duration, min	Comment
1	IV	1 mg/kg	30.0±7.2	Non-useful intravascular fluorescence at the end of time interval
2	IA	0.005% in 5 mL	14.3±3.0	
3	IV	2 mg/kg	30.3±4.9	Useful intravascular fluorescence at the end of time interval
4	IA	0.05% in 5 mL	18.5±4.1	
5	IV	5 mg/kg	43.7±7.0	
6	IA	0.1% in 5 mL	31.5±16.7	

Abbreviations: IV, intravenous; IA, intraarterial

Spinal Cord Microvasculature

The spinal cord microvasculature was also easily visualized. Visualization of the spinal cord vasculature at the injury site revealed diffuse contrast extravasation and extravascular blood cells that obscured the view of the parenchyma (Figure 4.2G).

Lymphatic Vessels in the Dura

Investigation of the dura in animals that received intravenous and intraarterial fluorescein revealed dural cellular architecture and organization (Figure 4.3). The arterial and venous channels were evident and differentiated on the basis of the velocity of the intravascular blood cell flow. Then, we proceeded with subarachnoidal injection of contrast (n=2 animals) to visualize the presumable meningeal lymph vessels as contrast-containing channels. These intradural lymphatic vessels were found in the peritorcular area and near the sagittal sinus. These thin-walled channels had an irregular appearance

and were connected to arachnoidal granulations. Dural tissue sampled at these specific regions showed positive staining for the lymphatic-specific marker LYVE-1.

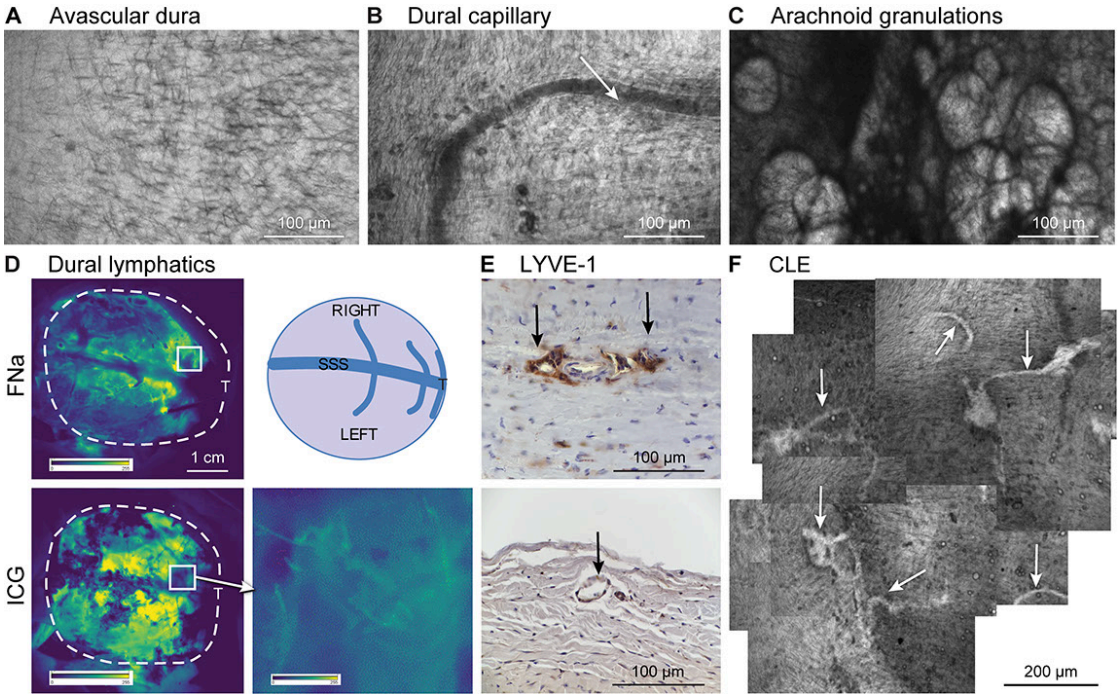

Figure 4.3. In vivo CLE imaging of dura matter in swine. (A) Endomicroscopy appearance of avascular region of the dura. (B) Dural capillary with a detectable flow of intravascular blood cells (arrow). Imaging performed after intravenous fluorescein injection. (C) Lobulated vesicular structures with contrast but without blood cells, presumably arachnoidal granulations, visualized in the dura 30 minutes after subarachnoidal injection of the fluorescein. (D) Wide-field imaging of the dura matter of a pig 30 minutes after simultaneous subarachnoidal injection of fluorescein and indocyanine green shows contrast accumulation in the dura, especially at the regions close to the superior sagittal and transverse sinuses. Top right schematic shows swine brain orientation during imaging. Square insets demonstrate region scanned in E and F. (E) Dura matter immunostained brown for lymphatic vasculature with LYVE-1 (arrows)

shows perivascular lymphatic channels in the upper and superficial lymphatic channel in the lower image. (F) Tiled image of the dura scanned in vivo shows net of small channels (lymphatic vessels) containing fluorescein contrast without blood cells. Abbreviations: ICG, indocyanine green; FNa, fluorescein; SSS, superior sagittal sinus; T, torcula. Used with permission from Barrow Neurological Institute, Phoenix, Arizona.

Microvasculature in Human Glioma and Normal Brain

Human biopsies were read from the conventional H&E sections as grade 2 astrocytomas (n=3), grade 2 oligodendrogliomas (n=4), invasive grade 3 astrocytomas (n=3), grade 3 oligoastrocytomas (n=7), and grade 4 glioblastomas (n=3). On average, 2.7±1.4 in vivo and 1.9±0.9 ex vivo separate CLE biopsies were available per patient yielding 91 optical biopsies for analysis. CLE imaging demonstrated abnormal tissue architecture with profound extravasation of the contrast. Microvessels were encountered in 37/54 (69%) of in vivo and 22/37 (59%) ex vivo biopsies. Identified microvasculature was classified into two general groups: abnormal microvasculature and normal microvasculature. Normal human brain microvasculature was similar to that in a swine brain and was characterized by a competent vascular wall without contrast leakage. These vessels generally had robust flow with arterial and venous patterns in vivo (Figure 4.4). The normal capillary network had a characteristic organized appearance with straight segments interconnected with each other. None of the large vessels (>20 μm) was identified as abnormal, while smaller vessels had either normal or abnormal tumor appearance. All microvessels, identified as abnormal and small (<20 μm), were

characterized by disorganized nonlinear appearance, perivascular crowding of cells, slow or stagnant flow, perivascular leakage of fluorescent contrast, and cells attached to the inner vascular wall. We encountered abnormal vessels in 22% of all glioma digital biopsies. Presence of an abnormal vessel served as an additional diagnostic feature supporting the diagnostic opinion based on the CLE image. However, vessels with normal appearance were also found in the biopsies at invasive glioma margins.

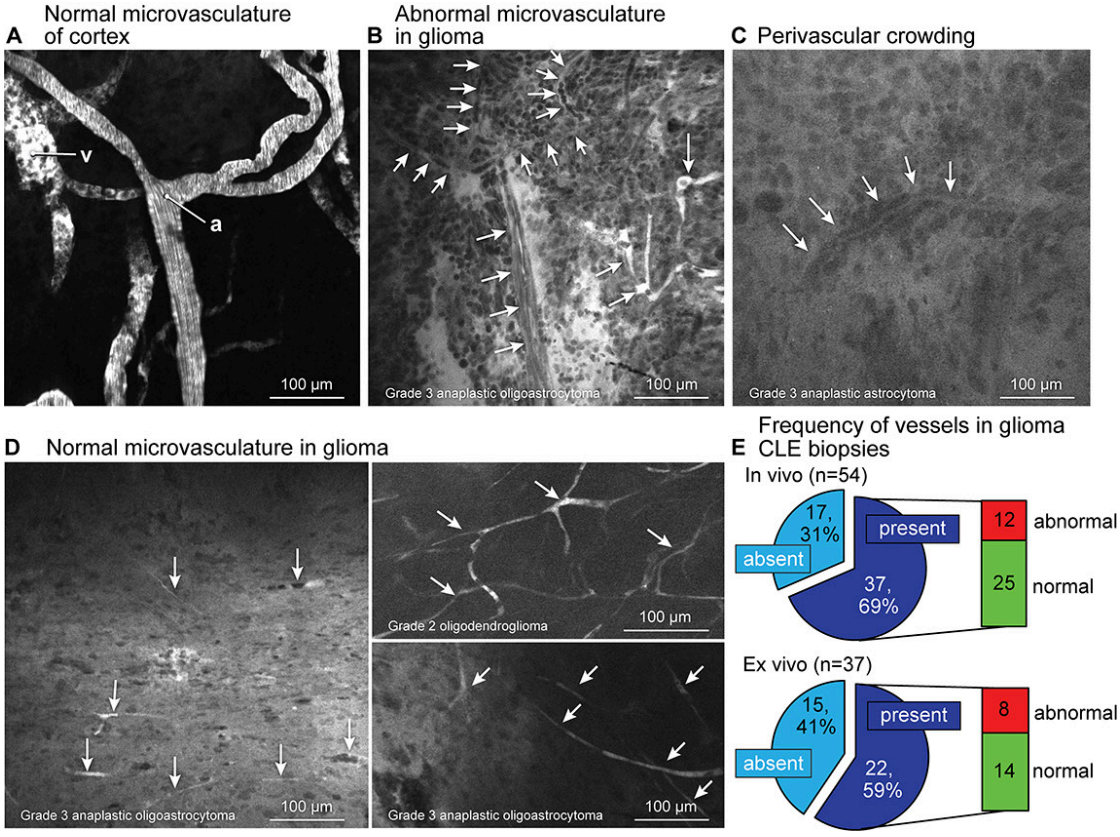

Figure 4.4. Microvasculature in human glioma and normal human brain tissue during in vivo and ex vivo CLE imaging. (A) Normal microvasculature. (B) Abnormal microvasculature (arrows) characterized by torturous appearance, leakage of the contrast, multiple branches, and stagnant flow. Image from grade 3 anaplastic oligoastrocytoma. (C) Micrograph demonstrates perivascular crowding of the heterogeneous (presumably

tumor) cells around the blood vessel. (D) Normal microvasculature. Normal appearing straight thin capillaries (arrows) in the brain tumor parenchyma brightened by the fluorescein contrast (left image of grade 3 anaplastic oligoastrocytoma). Some tumors displayed capillary network (arrows) with preserved barrier function that contained contrast (images of grade 2 oligodendroglioma, Grade III anaplastic oligoastrocytoma on the right) and relatively normal appearance. (E) Quantification of vessels encountered during in vivo and ex vivo CLE imaging of brain gliomas in humans. Abbreviations: a. artery, v. vein. Used with permission from Barrow Neurological Institute, Phoenix, Arizona.

Discussion

This study demonstrates the feasibility of real-time visualization of cerebral microvasculature and blood flow dynamics with subcellular resolution using a handheld, portable CLE in numerous parts of the microcirculation under various physiologic conditions of normal and pathologic brain in a large-animal model, as well as in human normal brain and glioma tissue.

Blood Flow Velocity

Erythrocytes velocity within the cerebrovascular system can be measured using CLE under certain circumstances. The primary limiting factor to measuring erythrocyte velocity is the high velocity of erythrocyte flow relative to the FPS capture rate of the CLE probe. Various investigations have reported objective data regarding normal

erythrocyte velocity within capillaries between 0.4 mm/s and 2 mm/s (Ivanov, Kalinina, and Levkovich Yu 1981, Hudetz, Feher, and Kampine 1996, Unekawa 2008). At its maximum resolution, the CLE probe affords an FPS rate of 0.78, which converts to 1.29 seconds/frame. Even at the slowest normal capillary erythrocyte velocities reported, 0.4 mm/s, a single erythrocyte will transverse at least 516 μm between frame captures. This distance is greater than the CLE field of view (267×475 μm). At the 1920×270 CLE resolution setting used in this investigation (0.44 seconds/frame), a single erythrocyte at 0.4 mm/s velocity will travel 176 μm between frame captures. While this distance falls within the field of view of the CLE probe, it will provide, at maximum, two data points of erythrocyte position. Given these circumstances, measuring erythrocyte velocity with CLE within capillaries remains a challenge.

Within venous flow, thrombosed vessels, or vessels with arrested flow, erythrocyte velocity is reduced to a rate that can accurately be measured by CLE. Previously, erythrocyte velocity within cerebral veins has been reported to be highly variable, measuring slower or faster than capillaries at times (Tomita et al. 2006). At relatively slower speeds, or within in the context of flow-reducing pathology, CLE is capable of estimating erythrocyte velocity. We demonstrated a qualitative way to distinguish arterial and venous erythrocyte flow in the arterioles and venules based on the intravascular appearance of artifacts created by moving cells. Furthermore, velocity in the context of arrested flow, a vessel with thrombosis, and slow venous flow could be visualized with high accuracy and quantified. Faster scanning imaging probe design is required for precise imaging of blood flow velocities (Kim, Hong, and Shin 2018).

Visualization of Dural Lymphatics

We identified lymphatic meningeal channels that were stained with fluorescein. Wide-field imaging after subarachnoid injections of ICG and fluorescein demonstrated accumulation of both tracers in the dura mater, confirming our findings. The safe fluorescein dose for intrathecal administration in humans is considered to be 50 mg (1 mL of 5%), which is substantially higher than the 4.2 mg used in our study (Felisati et al. 2008). We modified a methodology of intrathecal ICG administration for lymphatic imaging in mice (Kwon et al. 2017). Similar to the previous studies in mice (Da Mesquita et al. 2018, Antila et al. 2017) and humans (Absinta et al. 2017, Louveau et al. 2015), we observed meningeal lymphatic vessels near the transverse-sagittal junction area as small vascular channels without erythrocytes. Detecting and imaging these channels with the CLE probe required prolonged scanning of the dural surface. Identification of the interstitium, as well as lymphatic systems in brain and meninges (Louveau et al. 2015), facilitated by the application of intravital endomicroscopy (Benias et al. 2018) has provided additional possible etiological factors for many diseases (Ma et al. 2017, Da Mesquita et al. 2018, Sun et al. 2018). However, the practical implications and clinical significance of such findings, including the visualized meningeal structures in the present study, have yet to be identified.

Potential Clinical Use

Unlike current angiographic imaging modalities, such as wide-field fluorescent angiography with ICG and fluorescein that is of short demonstrable imaging duration, CLE imaging allows for substantially longer observation of the blood flow. CLE is a novel method for in vivo microvasculature imaging than has previously been possible in small-animal models. Future application of this technique is possible for the investigation of brain and spinal cord microvasculature and blood flow during neurosurgical procedures.

Investigating and visualizing microvasculature may be relevant during neurosurgical procedures for traumatic brain injury (Logsdon et al. 2015), cerebrovascular lesions, downstream effects of surgical vessel anastomoses or reconstruction, flow recovery after stroke, perforating vessel competency, moyamoya disease, and revealing tumor blood vessel and flow characteristics. For example, fluorescein-labeled albumin was used to demonstrate the benefits of unfractionated heparin in traumatic brain injury (Nagata et al. 2016). CLE imaging could be used to further investigate this phenomenon. Wide-field fluorescein (Narducci et al. 2019) and ICG (Czabanka et al. 2008) angiography have been used to investigate clinically relevant microcirculatory hemodynamics and blood–brain barrier changes in patients with moyamoya disease (Czabanka et al. 2009). In cerebrovascular bypass procedures, fluorescein angiography is a cost-effective, fast, and safe intraoperative tool to assess patency of the anastomosis (Narducci et al. 2018a). Furthermore, intraoperative fluorescence angiography is used to assess the blood flow state in vascular territories

during bypass procedures (Gruber et al. 2012, Rodriguez-Hernandez and Lawton 2012). Interestingly, fluorescein-based wide-field angiography can provide better resolution of small perforating vessels, as well as afford real-time visualization as an adjunct to ICG videoangiography (Suzuki et al. 2007, Zhao et al. 2019). Further interrogation of the microvasculature and blood flow during fluorescence angiographies with fluorescein using CLE presents a novel opportunity for research to advance our understanding of brain microcirculation at the capillary level during various diseases, conditions, and the course of neurosurgical interventions. The CLE system used in this study received FDA clearance with the intended use for "viewing intraoperative blood flow in the cerebral vascular area, including microvasculature and capillaries." (https://www.accessdata.fda.gov/cdrh_docs/pdf18/K181116.pdf) The clinical benefits of this new intraoperative imaging modality have yet to be investigated.

Limitations

The relatively small field of view and imaging depth limit the potential surface area that could be interrogated at a given time, creating a sampling error that is inherent to any small field-of-view method. The current setup and use of 488-nm fluorophore limit the application of CLE to microvessels with thin vascular walls. Our previous investigations have shown that the maximal imaging depth at which detailed cellular structures could be resolved in the brain is 36 μm (Belykh, Patel, Miller, Bozkurt, Yagmurlu, et al. 2018). This imaging depth is an upper limit of vascular wall thickness, through which the intraluminal flow could be observed. Extravasated blood cells create

significant imaging artefacts that require frequent washing. Overall, CLE presents with a learning curve that must be overcome to develop adequate probe handling technique and to navigate smoothly to desired locations for image acquisition without significant artifacts.

Conclusion

CLE with fluorescein as a contrast agent is a novel tool capable of providing research data on microvasculature, blood flow, and changes in the blood flow in the brain and spinal cord, including differentiation of arterial and venous flow, flow stagnation, and thrombosis. In areas with an altered blood–brain barrier, such as in brain tissue trauma or brain tumors, CLE imaging allows visualization of not only the microvasculature in general, but also of tissue microstructure. These results might be useful for further research about the pathophysiology of stroke and brain perfusion, as well as for better characterization of normal and glioma brain tissues. This study is the first feasibility analysis of CLE as a method for precise assessment of microvasculature of the central nervous system with subcellular resolution. Potential future applications of intraoperative CLE imaging beyond optical biopsy of neoplastic tissue include assessment of blood flow in selected areas of cerebral microvasculature. Research and clinical scenarios may benefit from CLE as a novel intraoperative real-time in vivo microscopic-resolution fluorescence imaging modality.

References

Absinta, M., S. K. Ha, G. Nair, P. Sati, N. J. Luciano, M. Palisoc, A. Louveau, K. A. Zaghloul, S. Pittaluga, J. Kipnis, and D. S. Reich. 2017. "Human and nonhuman primate meninges harbor lymphatic vessels that can be visualized noninvasively by MRI." *Elife* 6. doi: 10.7554/eLife.29738.

Antila, S., S. Karaman, H. Nurmi, M. Airavaara, M. H. Voutilainen, T. Mathivet, D. Chilov, Z. Li, T. Koppinen, J. H. Park, S. Fang, A. Aspelund, M. Saarma, A. Eichmann, J. L. Thomas, and K. Alitalo. 2017. "Development and plasticity of meningeal lymphatic vessels." *J Exp Med* 214 (12):3645-3667. doi: 10.1084/jem.20170391.

Belykh, E., E. J. Miller, A. Carotenuto, A. A. Patel, C. Cavallo, N. L. Martirosyan, D. R. Healey, V. A. Byvaltsev, A. C. Scheck, M. T. Lawton, J. M. Eschbacher, P. Nakaji, and M. C. Preul. 2019. "Progress in Confocal Laser Endomicroscopy for Neurosurgery and Technical Nuances for Brain Tumor Imaging With Fluorescein." *Front Oncol* 9:554. doi: 10.3389/fonc.2019.00554.

Belykh, E., A. A. Patel, E. J. Miller, B. Bozkurt, K. Yagmurlu, E. C. Woolf, A. C. Scheck, J. M. Eschbacher, P. Nakaji, and M. C. Preul. 2018. "Probe-based three-dimensional confocal laser endomicroscopy of brain tumors: technical note." *Cancer Manag Res* 10:3109-3123. doi: 10.2147/CMAR.S165980.

Benias, P. C., R. G. Wells, B. Sackey-Aboagye, H. Klavan, J. Reidy, D. Buonocore, M. Miranda, S. Kornacki, M. Wayne, D. L. Carr-Locke, and N. D. Theise. 2018. "Structure and Distribution of an Unrecognized Interstitium in Human Tissues." *Sci Rep* 8 (1):4947. doi: 10.1038/s41598-018-23062-6.

Czabanka, M., P. Pena-Tapia, G. A. Schubert, J. Woitzik, P. Horn, P. Schmiedek, and P. Vajkoczy. 2009. "Clinical implications of cortical microvasculature in adult Moyamoya disease." *J Cereb Blood Flow Metab* 29 (8):1383-7. doi: 10.1038/jcbfm.2009.69.

Czabanka, M., P. Pena-Tapia, G. A. Schubert, J. Woitzik, P. Vajkoczy, and P. Schmiedek. 2008. "Characterization of cortical microvascularization in adult moyamoya disease." *Stroke* 39 (6):1703-9. doi: 10.1161/STROKEAHA.107.501759.

Da Mesquita, S., A. Louveau, A. Vaccari, I. Smirnov, R. C. Cornelison, K. M. Kingsmore, C. Contarino, S. Onengut-Gumuscu, E. Farber, D. Raper, K. E. Viar, R. D. Powell, W. Baker, N. Dabhi, R. Bai, R. Cao, S. Hu, S. S. Rich, J. M. Munson, M. B. Lopes, C. C. Overall, S. T. Acton, and J. Kipnis. 2018. "Functional aspects of meningeal lymphatics in ageing and Alzheimer's disease." *Nature* 560 (7717):185-191. doi: 10.1038/s41586-018-0368-8.

Feindel, W., Y. L. Yamamoto, and C. P. Hodge. 1967. "Intracarotid fluorescein angiography: a new method for examination of the epicerebral circulation in man." *Can Med Assoc J* 96 (1):1-7.

Felisati, G., A. Bianchi, P. Lozza, and S. Portaleone. 2008. "Italian multicentre study on intrathecal fluorescein for craniosinusal fistulae." *Acta Otorhinolaryngol Ital* 28 (4):159-63.

Goetz, M., S. Thomas, A. Heimann, P. Delaney, C. Schneider, M. Relle, A. Schwarting, P. R. Galle, O. Kempski, M. F. Neurath, and R. Kiesslich. 2008. "Dynamic in vivo imaging of microvasculature and perfusion by miniaturized confocal laser microscopy." *Eur Surg Res* 41 (3):290-7. doi: 10.1159/000148242.

Gruber, A., C. Dorfer, G. Bavinzski, H. Standhardt, H. Ferraz-Leite, and E. Knosp. 2012. "Superselective indocyanine green angiography for selective revascularization in the management of peripheral cerebral aneurysms." *AJNR Am J Neuroradiol* 33 (3):E36-7. doi: 10.3174/ajnr.A2424.

Hudetz, A. G., G. Feher, and J. P. Kampine. 1996. "Heterogeneous autoregulation of cerebrocortical capillary flow: evidence for functional thoroughfare channels?" *Microvasc Res* 51 (1):131-6. doi: 10.1006/mvre.1996.0015.

Ivanov, K. P., M. K. Kalinina, and I. Levkovich Yu. 1981. "Blood flow velocity in capillaries of brain and muscles and its physiological significance." *Microvasc Res* 22 (2):143-55. doi: 10.1016/0026-2862(81)90084-4.

Kim, M., J. Hong, and H. J. Shin. 2018. "Double-pulse laser illumination method for measuring fast cerebral blood flow velocities in the deep brain using a fiber-bundle-based endomicroscopy system." *Biomed Opt Express* 9 (6):2699-2715. doi: 10.1364/BOE.9.002699.

Kwon, S., C. F. Janssen, F. C. Velasquez, and E. M. Sevick-Muraca. 2017. "Fluorescence imaging of lymphatic outflow of cerebrospinal fluid in mice." *J Immunol Methods* 449:37-43. doi: 10.1016/j.jim.2017.06.010.

Logsdon, A. F., B. P. Lucke-Wold, R. C. Turner, J. D. Huber, C. L. Rosen, and J. W. Simpkins. 2015. "Role of Microvascular Disruption in Brain Damage from Traumatic Brain Injury." *Compr Physiol* 5 (3):1147-60. doi: 10.1002/cphy.c140057.

Louveau, A., I. Smirnov, T. J. Keyes, J. D. Eccles, S. J. Rouhani, J. D. Peske, N. C. Derecki, D. Castle, J. W. Mandell, K. S. Lee, T. H. Harris, and J. Kipnis. 2015. "Structural and functional features of central nervous system lymphatic vessels." *Nature* 523 (7560):337-41. doi: 10.1038/nature14432.

Ma, Q., B. V. Ineichen, M. Detmar, and S. T. Proulx. 2017. "Outflow of cerebrospinal fluid is predominantly through lymphatic vessels and is reduced in aged mice." *Nat Commun* 8 (1):1434. doi: 10.1038/s41467-017-01484-6.

Martirosyan, N. L., J. M. Eschbacher, M. Y. Kalani, J. D. Turner, E. Belykh, R. F. Spetzler, P. Nakaji, and M. C. Preul. 2016. "Prospective evaluation of the utility of intraoperative confocal laser endomicroscopy in patients with brain neoplasms using fluorescein sodium: experience with 74 cases." *Neurosurg Focus* 40 (3):E11. doi: 10.3171/2016.1.FOCUS15559.

Martirosyan, N. L., M. Y. Kalani, W. D. Bichard, A. A. Baaj, L. F. Gonzalez, M. C. Preul, and N. Theodore. 2015. "Cerebrospinal fluid drainage and induced hypertension improve spinal cord perfusion after acute spinal cord injury in pigs." *Neurosurgery* 76 (4):461-8; discussion 468-9. doi: 10.1227/NEU.0000000000000638.

Nag, S. 1996. "Cold-injury of the cerebral cortex: immunolocalization of cellular proteins and blood-brain barrier permeability studies." *J Neuropathol Exp Neurol* 55 (8):880-8. doi: 10.1097/00005072-199608000-00003.

Nagata, K., K. Kumasaka, K. D. Browne, S. Li, J. St-Pierre, J. Cognetti, J. Marks, V. E. Johnson, D. H. Smith, and J. L. Pascual. 2016. "Unfractionated heparin after TBI reduces in vivo cerebrovascular inflammation, brain edema and accelerates cognitive recovery." *J Trauma Acute Care Surg* 81 (6):1088-1094. doi: 10.1097/TA.0000000000001215.

Narducci, A., J. Onken, M. Czabanka, N. Hecht, and P. Vajkoczy. 2018. "Fluorescein videoangiography during extracranial-to-intracranial bypass surgery: preliminary results." *Acta Neurochir (Wien)* 160 (4):767-774. doi: 10.1007/s00701-017-3453-0.

Narducci, A., K. Yasuyuki, J. Onken, K. Blecharz, and P. Vajkoczy. 2019. "In vivo demonstration of blood-brain barrier impairment in Moyamoya disease." *Acta Neurochir (Wien)* 161 (2):371-378. doi: 10.1007/s00701-019-03811-w.

Raabe, A., J. Beck, R. Gerlach, M. Zimmermann, and V. Seifert. 2003. "Near-infrared indocyanine green video angiography: a new method for intraoperative assessment of vascular flow." *Neurosurgery* 52 (1):132-9; discussion 139. doi: 10.1097/00006123-200301000-00017.

Raabe, A., P. Nakaji, J. Beck, L. J. Kim, F. P. Hsu, J. D. Kamerman, V. Seifert, and R. F. Spetzler. 2005. "Prospective evaluation of surgical microscope-integrated intraoperative near-infrared indocyanine green videoangiography during aneurysm surgery." *J Neurosurg* 103 (6):982-9. doi: 10.3171/jns.2005.103.6.0982.

Rodriguez-Hernandez, A., and M. T. Lawton. 2012. "Flash fluorescence with indocyanine green videoangiography to identify the recipient artery for bypass with distal middle cerebral artery aneurysms: operative technique." *Neurosurgery* 70 (2 Suppl Operative):209-20. doi: 10.1227/NEU.0b013e31823158f3.

Seylaz, J., R. Charbonne, K. Nanri, D. Von Euw, J. Borredon, K. Kacem, P. Meric, and E. Pinard. 1999. "Dynamic in vivo measurement of erythrocyte velocity and flow in capillaries and of microvessel diameter in the rat brain by confocal laser microscopy." *J Cereb Blood Flow Metab* 19 (8):863-70. doi: 10.1097/00004647-199908000-00005.

Sun, B. L., L. H. Wang, T. Yang, J. Y. Sun, L. L. Mao, M. F. Yang, H. Yuan, R. A. Colvin, and X. Y. Yang. 2018. "Lymphatic drainage system of the brain: A novel target for intervention of neurological diseases." *Prog Neurobiol* 163-164:118-143. doi: 10.1016/j.pneurobio.2017.08.007.

Suzuki, K., N. Kodama, T. Sasaki, M. Matsumoto, T. Ichikawa, R. Munakata, H. Muramatsu, and H. Kasuya. 2007. "Confirmation of blood flow in perforating arteries using fluorescein cerebral angiography during aneurysm surgery." *J Neurosurg* 107 (1):68-73. doi: 10.3171/JNS-07/07/0068.

Tomita, M., N. Tanahashi, H. Takeda, I. Schiszler, T. Osada, M. Unekawa, and N. Suzuki. 2006. "Capillo-venous flow in the brain: significance of intravascular RBC aggregation for venous flow regulation." *Clin Hemorheol Microcirc* 34 (1-2):51-7.

Unekawa, M., Tomita, M., Osada, T., Tomita, Y., Toriumi, H., Tatarishvili, J., Suzuki, N. 2008. "Frequency distribution function of red blood cell velocities in single capillaries of the rat cerebral cortex using intravital laser-scanning confocal microscopy with highspeed camera." *Asian Biomedicine* 2 (3):203-218.

Zhao, X., E. Belykh, C. Cavallo, D. Valli, S. Gandhi, M. C. Preul, P. Vajkoczy, M. T. Lawton, and P. Nakaji. 2019. "Application of Fluorescein Fluorescence in Vascular Neurosurgery." *Front Surg* 6:52. doi: 10.3389/fsurg.2019.00052.

CHAPTER 5

INTRAOPERATIVE CONFOCAL LASER ENDOMICROSCOPY EXAMINATION OF BRAIN TUMOR TISSUE MICROSTRUCTURE DURING FLUORESCENCE-GUIDED SURGERY

Abstract

Object: Noninvasive intraoperative optical biopsy that provides real-time imaging of histoarchitectural (cell resolution) features of brain tumors, especially at the margin of invasive tumors would be of great value. In order to assess the clinical grade confocal laser endomicroscopy (CLE), and to prepare for its use intraoperatively in vivo, an assessment of the ex vivo imaging performance in brain lesions, mostly aimed at invasive brain tumors, was designed.

Methods: Tissue samples from patients undergoing intracranial surgeries with fluorescein sodium (FNa)-based wide-field fluorescence guidance were acquired for immediate intraoperative ex vivo optical biopsies with CLE. H&E-stained frozen section analysis of the same specimens served as a gold standard for blinded neuropathology comparison. FNa was administered at 2-5 mg/kg at the induction of anesthesia and reinjected at 5 mg/kg for CLE contrast improvement. Seventeen histological features were identified and sensitivity, specificity, positive predictive value, and negative predictive value were assessed.

Results: 47 patients were enrolled (122 biopsies), including 32 patients with gliomas and 15 patients with other intracranial lesions. Positive predictive value of CLE optical biopsies was 97% for all specimens and 98% for gliomas. The specificity was

90% for all specimens and 94% for gliomas. FNa reinjection (7 cases, on average 2.6 hours after the first injection) improved image quality increasing percent of accurately diagnosed images from 67% to 93%. Features such as the tissue architecture, cell morphology, atypical cells and hypercellularity were significantly more prevalent in lesional glioma biopsies than in normal and reactive brain ($p<0.001$ for all), or than in glioma biopsies that were labeled as "non-diagnostic" on CLE ($p<0.001$ for all).

Conclusions: The study demonstrated high specificity and positive predictive value of ex vivo intraoperative optical biopsies with CLE and forms the basis for in vivo intraoperative trial. This new non-invasive portable intraoperative imaging provides diagnostic features to discriminate lesional tissue with high specificity and is feasible for incorporation into the fluorescence-guided surgery workflow, particularly in for invasive brain tumors.

Introduction

Complete resection within the bounds of safety is the goal in the treatment of the majority of brain tumors, especially for invasive tumors such high grade gliomas (D'Amico et al. 2017, Sanai and Berger 2008). Therefore, intraoperative tools that aid in identification and differentiation of abnormal brain tissue that should be resected and healthy brain tissue that should be preserved are of particular importance (Barbosa et al. 2015). Here we report an investigation of a relatively new cellular resolution imaging hand-held tool that is poised to become valuable for intraoperative non-invasive optical biopsy.

Previous generations of the confocal laser endomicroscope demonstrated initial feasibility in visualizing brain tumor microstructure with significant diagnostic accuracy (Belykh, Cavallo, Gandhi, et al. 2018b). However, these designs were based largely on the imaging platform directly adapted from those for gastrointestinal use. They were not FDA approved for use in the brain and were used in three limited trials that included in vivo and ex vivo intraoperative use (Sanai, Eschbacher, et al. 2011, Eschbacher et al. 2012, Martirosyan, Eschbacher, et al. 2016). Disadvantages of the early designs included the necessity to sterilize the scanning probe between procedures, the wide 7-mm probe diameter limiting use within narrow surgical corridors, and the straight probe shape profile as it fit in the surgeon's grasp.

The novel generation commercial clinical grade CLE was developed to address these shortcomings. The new CLE system has a 5 mm diameter probe that is curved similar to an aspiration instrument, has increased imaging resolution, and is designed to work with a removable sterile sheet. However, since initial reports on the use of CLE for visualization of brain tumors, wide field fluorescence guidance surgery has gained increased popularity. As such, the fluorescein sodium (FNa) was administered as part of the standard surgical procedure to visualize the bright glow of FNa fluorescence under an operating microscope used in the Yellow560 mode.

In order to assess the clinical grade CLE, and to prepare for its use intraoperatively in vivo, an assessment of the ex vivo imaging performance in brain lesions, mostly aimed at invasive brain tumors, was designed. We studied CLE use during routine fluorescence-guided surgery (FGS) with the operating microscope for

brain tumors to visualize and compare CLE tissue imaging microstructure in ex vivo samples with frozen section biopsies. We assessed feasibility and diagnostic accuracy of these CLE optical biopsies of brain lesions to identify relevant practical and methodological issues for future in vivo use and clinical studies.

Materials and Methods

Study Design

This prospective study was conducted at the St. Joseph's Hospital and Medical Center, with approval from the Institutional Review Board for Human Research (IRB No, 10BN130). All participants gave informed voluntary consent for participation in this study and were recruited from the patients who were operated on from August 2016 to May 2019. Patients eligible for inclusion were adults (>18 years old), scheduled for neurosurgical lesion –removal procedures involving FNa contrast administration at the authors' institution. This was a convenience sample of patients with brain lesions, mostly tumors; the subjects were enrolled when the participating neurosurgeons and CLE were available. Standard intraoperative techniques were used during tumor resection, including neuronavigation, operating microscope, endoscopic assistance, and intraoperative functional mapping in a few patients. Deidentified brain tumor samples were used for this study. Demographic characteristics were thought to be irrelevant to the optical biopsy interpretation and quality assessment for this study.

Fluorescein Sodium Administration

FNa was administered intravenously (IV) at the induction of anesthesia to create a contrast for wide field fluorescence guidance using the Yellow560 mode of the operating microscope. The dose of the FNa was determined by the operating neurosurgeon. FNa was used at a dose of 2 mg/kg in gliomas and meningiomas and 5 mg/kg in metastatic lesions. FNa was re-administered if deemed necessary by the neurosurgeon at a 5 mg/kg dose.

Tissue Collection and Processing

Tissue samples that were to be removed as a part of standard procedure were obtained during the tumor resection. These were samples separate from those obtained for clinical care, i.e. frozen section and permanent section analyses. If possible, multiple biopsies of the tumor core and tumor bed area were acquired. The number of biopsies was determined by the operating neurosurgeon.

The samples were placed on a moisturized nonadherent surgical dressing, transferred to the CLE station (CONVIVO, Carl Zeiss AG, Jena, Germany) in the same operating room, and imaged using the CLE probe affixed in a probe holder in an upright position. Tissue samples were imaged with CLE immediately after acquisition from the brain. The tissue samples were gently moved with microsurgical forceps to find an optimal imaging location. In order to obtain optimally balanced CLE images, we utilized a 488 nm excitation laser and a 517.5–572.5 nm bandpass filter at 1x zoom with automatic gain resulting in 1920×1080 pixels resolution of 267×475 μm field of view.

The neurosurgeon was able to review the CLE images as they were displayed real-time on a large LED screen during the surgery. When the image brightness was not sufficient, the FNa was readministered according to the prescribed dosage upon the request of the neurosurgeon.

After the CLE imaging, the tissue samples were placed on a piece of moisture cottonoid in a plastic container and submitted for histological processing and hematoxylin and eosin (H&E) staining in the neuropathology department.

Image Analysis

The collected CLE images were processed in Fiji by applying the "despeckle" filter and creating short 3-20 frames videos of selected imaging locations. Deidentified CLE optical biopsies and H&E-stained sections were reviewed retrospectively in a blinded fashion by a board certified neuropathologist (J.E.) competent in interpreting CLE images. The neuropathologist had no clinical information except that the biopsy was from an intracranial procedure for a lesion removal.

CLE optical biopsies were presented as multiple still images and video-like image loops per optical biopsy. A CLE optical biopsy was graded as "lesional" when it deemed representative of a tumor or necrotic tissue, as "normal", when it was representative for normal or reactive brain tissue, and as "non-diagnostic", when it was deemed to not represent tumor or necrotic tissue (i.e., "not diagnostic of tumor"). Seventeen histological features were identified and assessed for the CLE optical biopsies as "present" or "absent". The overall quality of CLE images for each optical biopsy were graded

subjectively on a scale from 0 to 5: 0 – not diagnostic or very bad; 1 – bad; 2 – poor; 3 – average; 4 – good; 5 – very good. This quality assessment was based on subjective interpretation of clarity and brightness of tissue microstructure and was performed by a neurosurgeon and neuropathologist experienced in CLE and other fluorescence cell imaging technologies.

H&E slides of biopsies were graded as "lesional" when they were representative of tumor tissue useful for diagnosis or interpretations and "non-lesional" when they were representative of non-tumor tissue, such as normal brain or gliotic reactive brain tissue. All H&E slides were useful for such interpretations. Each H&E slide was also labeled based on the most likely diagnosis for a particular slide or was labeled as "non-diagnostic".

Statistical Analysis

Statistical analysis was performed in Excel (Microsoft, Inc., Redmond, WA). The interpretation of CLE images and H&E histological sections was compared. We also assessed CLE image quality and timing/dose of FNa injection. Exploratory diagnostic accuracy was calculated using 2x2 table and standard formulas for the sensitivity, specificity, positive predictive value and negative predictive value and reported according to the Standards for Reporting Diagnostic accuracy studies guideline (Bossuyt et al. 2015a). For statistical analysis CLE optical biopsies that were not diagnostic of tumor tissue or labeled as normal tissue were used as a negative CLE test result. The inconclusive H&E results were treated as "non-lesional" for the purpose of analysis.

Results

Descriptive Analysis

From the 77 potentially eligible patients consented within the study period, in 13 CLE imaging was not performed due to case cancelation or CLE unavailability, 14 were excluded because they were endoscopic transsphenoidal surgeries, and in 3 patients no biopsy samples were available for analysis resulting in 47 patients and 122 matched optical and histological biopsies available for analysis (Figure 5.1, Table 5.1).

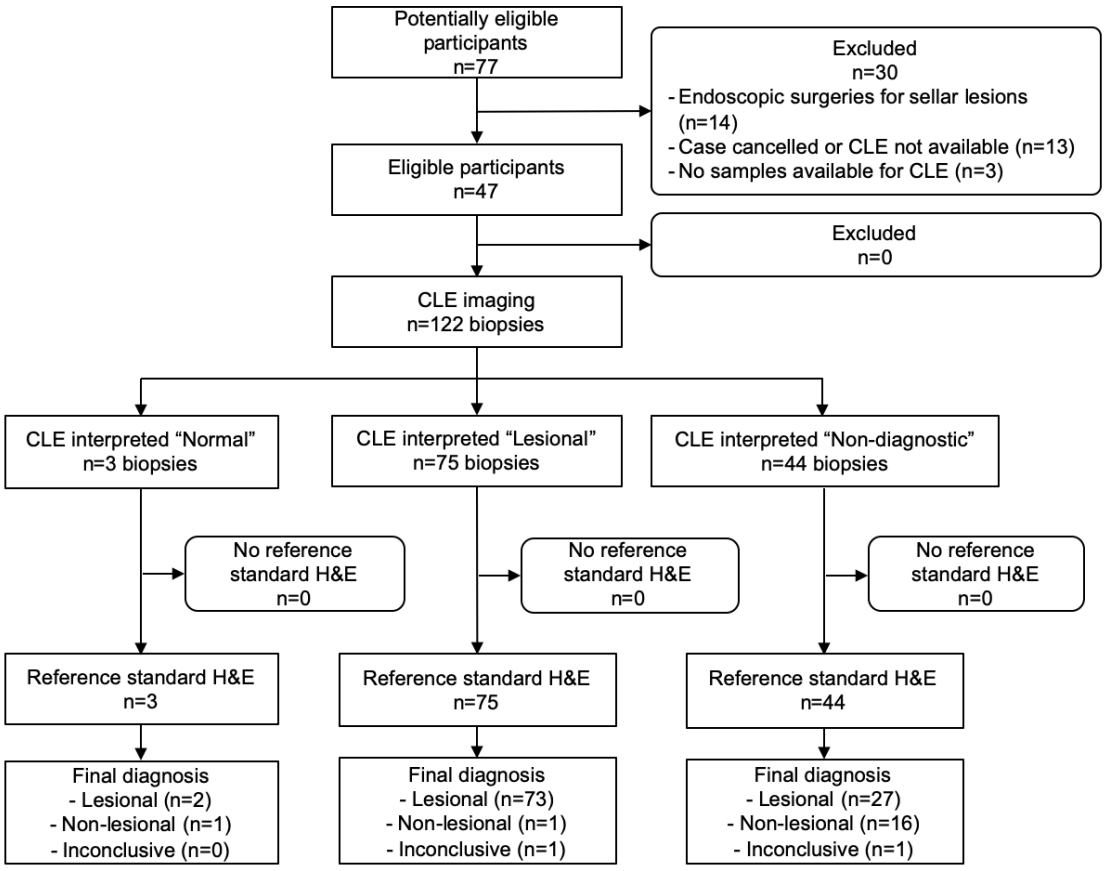

Figure 5.1. Flowchart of the patients.

Table 5.1. General characteristics of the biopsy specimens. GBM, glioblastoma multiforme, HGG, high grade glioma, LGG, low grade glioma, AVM, arteriovenous malformation.

Final diagnosis	N of cases	N of biopsies	Average biopsies per case	H&E diagnoses of biopsies
GBM	19	52	2.7	HGG (30); infiltrating glioma (12); necrosis (1); normal brain (3); reactive gliotic brain (5); inconclusive (1)
Recurrent GBM	5	24	4.8	High grade glioma (11), infiltrating glioma (10); necrosis (1); reactive gliotic brain (1); inconclusive (1)
Infiltrating glioma	5	13	2.6	Infiltrating glioma (11); reactive gliotic brain (1); normal brain (1)
LGG	3	8	2.7	Infiltrating glioma (4); normal brain (4)
Metastasis	4	9	2.3	Metastasis (8); reactive gliotic brain (1)
Meningioma	7	9	1.3	Meningioma (9)
Choroid plexus carcinoma	1	4	4	Choroid plexus carcinoma (4)
Craniopharyngioma	1	1	1	Craniopharyngioma (1)
Schwannoma	1	1	1	Schwannoma (1)
AVM	1	1	1	Reactive gliotic brain (1)
Total	47	122		

Preliminary patient diagnoses per tumor types were: 32 gliomas (19 primary glioblastomas, 4 recurrent glioblastomas, 5 infiltrating gliomas, 5 low-grade gliomas), 7 meningiomas, 4 metastatic brain lesions, 1 choroid plexus carcinoma, 1 craniopharyngioma, 1 schwannoma, 1 arteriovenous malformation (reactive normal

brain). All specimens were successfully analyzed ex vivo with CLE immediately after acquisition.

Re-dosing of Fluorescein Sodium

In all patients resection of the lesion was completed under operating microscope visualization with and without Yellow 560 mode irrespective of regard for ex vivo CLE analysis. In 7 cases (5 gliomas, 1 metastasis and 1 choroid plexus carcinoma), the FNa was re-administered at 5 mg/kg after the initial resection to evaluate the edge with subsequent biopsy acquisition for CLE analysis. Average time of FNa readministration was 157±52 min after the first administration. Analysis of these specimens showed improved brightness and contrast and overall image quality. Among the cases in which the reinjection was performed, the percent of accurately diagnosed images increased from 67% (18/27) to 93% (14/15), and percent of non-diagnostic CLE decreased from 26% (7/27) to 13% (2/15), although our study was not powered to detect differences in these subgroups ($p_{\chi 2}$=.11 and $p_{\chi 2}$=.31 respectively).

Timing of Fluorescein Sodium Injection

In many cases, biopsy acquisition occurs more than 90 minutes after the FNa administration and results in suboptimal contrast in CLE images, when compared to our previous investigation (Martirosyan, Eschbacher, et al. 2016), as well as biopsies at the current study when the FNa was injected 1-5 minutes before imaging. However, the analysis of all biopsies, as well as the glioma-only biopsies obtained after different time periods after FNa injection showed no correlation between the timing of FNa

administration and image quality ($r=-0.14$, $p>0.05$) or the probability of CLE biopsy being diagnosed as either lesional or non-diagnostic images (Logistic regression $p=.93$).

Blinded Review

Overall diagnostic accuracy for all analyzed biopsies was 75%. Lesional CLE biopsies were used as positive CLE test results; and non-lesional CLE, which included non-diagnostic and true negative normal/reactive brain CLE, as negative CLE test results (Table 5.2). In order to elucidate the diagnostic accuracy in various tumor types, subgroup analyses were performed in glioma, metastases and meningioma samples, which confirmed high positive predictive value of the CLE optical biopsies, 98, 91 and 83% respectively (Table 5.3). It should be noted that 2 CLE optical biopsies that were labeled as lesional, but had “non-lesional” H&E reading might have been true positives, that would further improve specificity and positive predictive value to 100% for all specimens and gliomas (see discussion in Figure 5.2).

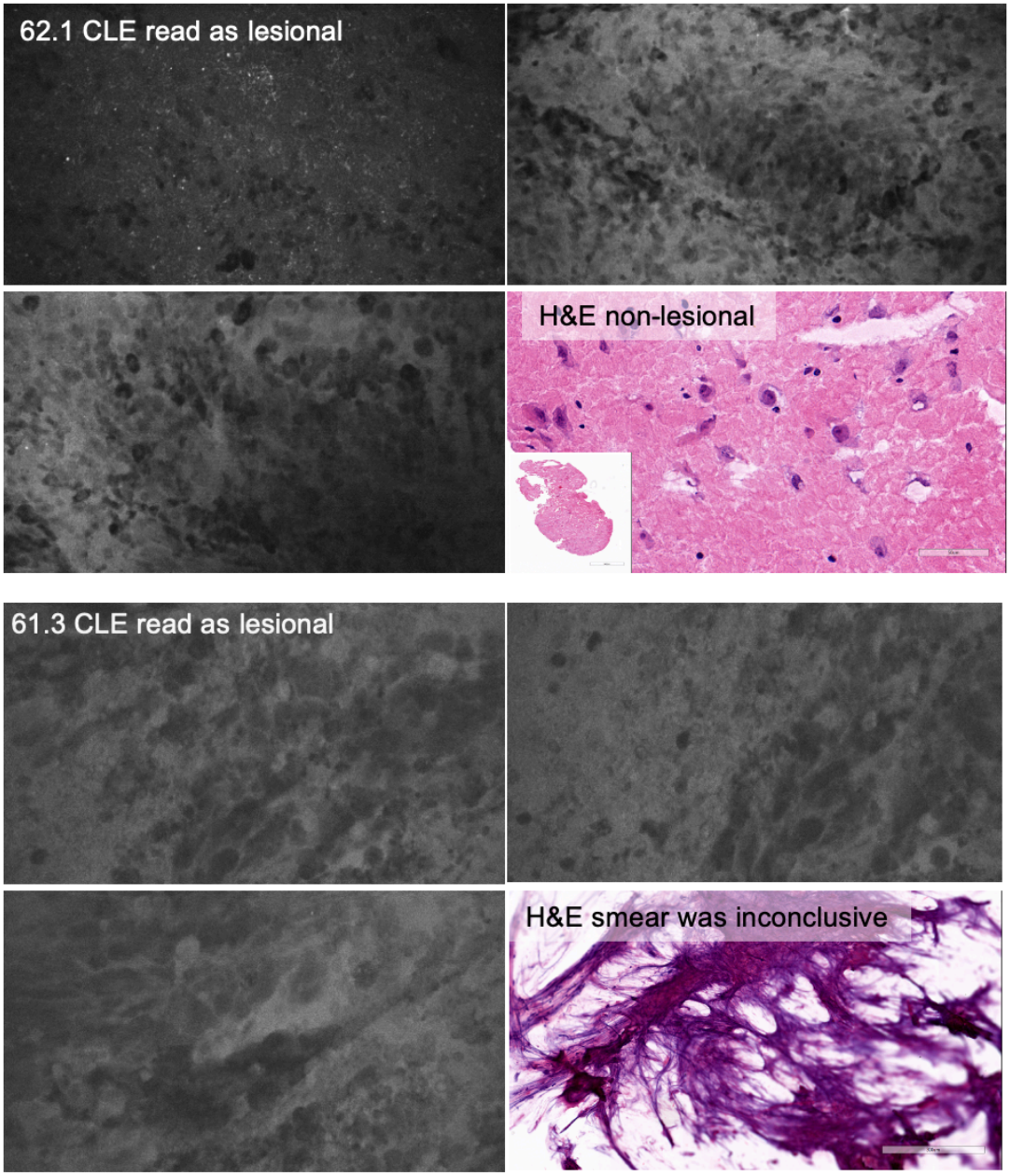

Figure 5.2. Positive CLE optical biopsies that had negative H&E result. A. In one optical biopsy, extravasation of fluorescein that highlighted the background and revealed hypercellular areas of atypical large cells. Overall this CLE optical biopsy was thought to be highly representative of a lesional tissue. However, the H&E was read as a normal cortex without a tumor. We hypothesized that there might be a sampling error, and

specimen contained a tumor area, that was missed during the histological sectioning. B. This optical biopsy demonstrated extravasation of fluorescein sodium contrast with hypercellular areas containing large atypical cells highly suggestive of the cellular tumor. However, due to the scant tissue available for histological processing, smear was performed that turned out to be inconclusive. Both H&E were treated as "non-lesional" for diagnostic accuracy analysis. However, if these two H&E biopsies were to be treated as "lesional", both specificity and positive predictive value will be 100%.

Table 5.2. Confocal laser endomicroscopy interpretation of the biopsy specimens. GBM, glioblastoma multiforme, HGG, high grade glioma, LGG, low grade glioma, AVM, arteriovenous malformation, TP – true positive, FP – false positive, TN – true negative, FN – false negative

H&E Diagnosis	N of specimens	Confocal Laser Endomicroscopy Interpretation				
		Lesional		Non-lesional		
				Normal		Non-diagnostic
		TP lesional	FP lesional	TN normal	FN normal	
Choroid plexus carcinoma	4	3				1
Craniopharyngioma	1	1				
HGG	41	31			1	9
Infiltrating glioma	37	22			1	14
Meningioma	9	6				3
Metastasis	8	7				1
Necrosis	2	2				
Normal brain	8		1			7
Reactive gliotic brain	9			1		8
Schwannoma	1	1				

Inconclusive	2	1		1
Total	122			

Table 5.3. Diagnostic accuracy of ex vivo confocal laser endomicroscopy. Carcinomas include metastatic lesions and choroid plexus carcinoma. Data are given as percentages with lower and upper limits of 95% confidence interval.

	All samples	Gliomas	Carcinomas	Meningiomas
Sensitivity	72% (62-80)	66% (55-76)	83% (51-97)	63% (26-90)
Specificity	90% (67-98)	94% (69-100)	94% (69-100)	94% (69-100)
Positive predictive value	97% (90-100)	98% (89-100)	91% (57-100)	83% (36-99)
Negative predictive value	38% (25-54)	37% (23-53)	89% (64-98)	84% (60-96)

CLE Histological Features

Various histological features were assessed in order to elucidate characteristics of diagnostic and non-diagnostic CLE optical biopsies (Figure 5.3). Frequencies of identifiable histological features on CLE imaging were specifically studied in selected biopsies of glioma, reactive gliosis and normal brain samples (Figure 5.4).

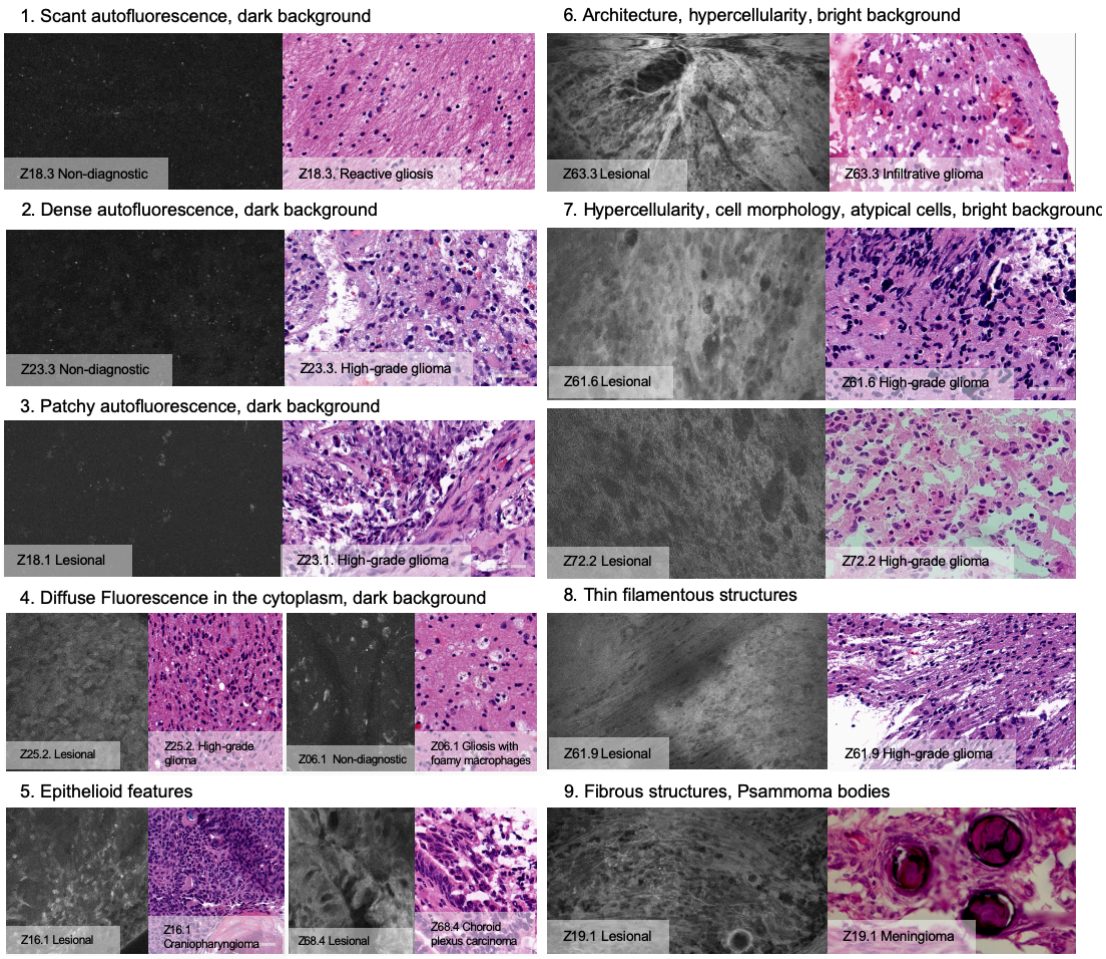

Figure 5.3. Histological features identified on the confocal laser endomicroscopy images of the various brain tumors. Used with permission from Barrow Neurological Institute, Phoenix, Arizona.

Feature		CLE Lesional				CLE non-diagnostic				CLE Normal				P-value	
		Glioma (n=53)		Non-glioma		Glioma (n=23)		Non-glioma (n=15)		Glioma		Non-glioma (n=1)			
		Inf. Glioma (22)	HGG (31)	Gliosis	Normal	Inf. Glioma (14)	HGG (9)	Gliosis (8)	Normal (7)	Inf. Glioma	HGG	Gliosis (1)	Normal	Lesional Glioma vs. Non-diagnostic Glioma	Lesional Glioma vs. Non-diagnostic Non-glioma
Auto-fluorescence	Scant	5%	19%			14%	22%	63%	57%			0%		0.903	0.000
	Dense	27%	26%			43%	44%	25%	14%			0%		0.142	0.866
	Patchy	23%	29%			57%	44%	63%	29%			0%		0.030	0.237
Fluorescence diffusely in cytoplasm		32%	10%			7%	22%	25%	14%			100%		0.538	0.785
Background	Dark	14%	26%			57%	78%	100%	86%			100%		0.000	0.000
	Bright (extravasation)	86%	77%			43%	33%	13%	0%			0%		0.001	0.000
Architecture		95%	77%			36%	22%	38%	14%			100%		0.000	0.000
Cell morphology		73%	74%			0%	0%	38%	14%			100%		0.000	0.000
Atypical cells		38%	48%			0%	0%	0%	0%			0%		0.000	0.004
Hypercellularity		77%	65%			0%	22%	13%	0%			0%		0.000	0.000
Epithelial features		0%	0%			0%	0%	0%	0%			0%		N/A	N/A
Vessels		23%	16%			0%	11%	0%	29%			100%		0.194	0.910
Fibrous structures	Collagen fibers	5%	0%			0%	0%	0%	0%			0%		0.665	0.497
	Thin filamentous structures	0%	3%			7%	0%	0%	0%			100%		0.870	0.497
	Abundant Fibrous structures	14%	6%			7%	22%	0%	14%			0%		0.949	0.856
Psammoma body		0%	0%			0%	0%	0%	0%			0%		N/A	N/A
RBC artifacts prevalent		14%	13%			50%	22%	13%	43%			100%		0.025	0.394

Figure 5.4. Analysis of frequencies of various histological features in gliomas and normal or reactive brain specimens. For the purpose of this analysis, 2 false positives, 2 false negatives CLE optical biopsies and one non-diagnostic H&E sample were excluded. Used with permission from Barrow Neurological Institute, Phoenix, Arizona.

Autofluorescence

Three types of autofluorescence were distinguished: patchy, dense, and scant. Scant autofluorescence was significantly frequent in non-glioma samples that were

deemed “non-diagnostic” by the CLE ($p<0.001$), while there were no significant differences in the frequencies of patchy and dense fluorescence.

Diffuse Intracellular Fluorescence

In some CLE optical biopsies, cells exhibit diffuse accumulation of FNa in the cytoplasm. This was especially noticeable in carcinomas. In gliomas, though, frequency of this pattern was not statistically different among non-tumor and glioma biopsies.

Background Color

The pattern of CLE images in which the extracellular space was dark and usually darker than the cells, was significantly more prevalent in non-glioma specimens ($p<0.001$), or glioma specimens that were rated as “non-diagnostic” ($p<0.001$). On the other hand, bright background was seen in most glioma samples diagnosed as lesional, and was almost absent in biopsies from the normal and reactive brain ($p<0.001$).

Cellular Features

Features such as the tissue architecture, cell morphology, atypical cells and hypercellularity were significantly more prevalent in lesional glioma biopsies than in normal and reactive brain ($p<0.001$ for all), or than in glioma biopsies that were labeled as “non-diagnostic” on CLE ($p<0.001$ for all).

Epithelial Features

The pattern of hypercellular areas with cells contacting each other and having glandular or epithelial arrangement was observed in all 3 metastases, a choroid carcinoma and the epithelial portion of the craniopharyngioma specimen. This feature was not observed in gliomas.

Vessels

Vessels were not frequently identified, most likely because of the lack of blood-flow in ex vivo samples, which hampered their detection. No differences in their frequencies among the diagnostic, non-diagnostic and normal brain samples were seen. However, normal capillaries with stained vessels were thought to be more characteristic of a normal brain or possibly invasive glioma, rather than cellular tumor.

Fibrous Structures

Various acellular fibrous structures were encountered mostly in meningiomas and rarely seen in gliomas. However, some thin filamentous structures representing myelinated cell processes could be seen in gliomas. Psammoma bodies were identified in meningiomas as contrast-impermeable large round structures.

RBC Artifacts

While RBC artifacts are inevitable during the CLE imaging, the abundance of blood was significantly more frequently encountered in CLE biopsies of gliomas that were labeled as “non-diagnostic” compared to “lesional” ($p=.025$).

Adverse Effects

No adverse effects were noted due to biopsy acquisition or FNa administration. One patient has been inadvertently administered 40mg/kg of FNa, and had yellowish skin discoloration that uneventfully resolved within 48 hours.

Discussion

In this study we evaluated CLE for optical biopsies on 122 ex vivo brain samples from 47 patients. The results of this study demonstrated high sensitivity of this diagnostic technology in detecting cellular brain tumor tissue which has significantly informative clinical value. Besides confirming the diagnostic the surgical-pathology workflow during fluorescence-guided brain surgery and for planning of future in vivo CLE studies in various tumor types, discussed below.

Implications for Practice: Incorporation of CLE in the Workflow of Fluorescence-Guided Brain Surgery

In addition to a previous study, where the FNa was administered around 5 minutes before CLE imaging at the set dose (5 ml 10% the FNa IV), this study has demonstrated the feasibility of using CLE during the FGS under Yellow560 mode when the contrast is administered at the anesthesia induction. This timing of FNa injection favors wide-field fluorescence navigation (Acerbi, Broggi, et al. 2014, Acerbi et al. 2015) and has been studied in several clinical trials (Acerbi et al. 2018, Falco et al. 2019). However, in some cases, the contrast of the CLE imaging was insufficient, requiring readministration of the FNa, which resulted in better CLE image quality. The fact that there was no correlation between the time of contrast injection and overall image quality could be explained by heterogeneity of the tumor tissue, blood artefacts, and ex-vivo nature of the study.

The diffusion of FNa at the resection cavity during the reinjection hampered the selectivity of Yellow560 guidance, but improved CLE image quality. Future in vivo

studies should address this problem. It is most likely that CLE will be used at the end of the surgery, after resection under the guidance of Yellow560 has been completed, for inspection of the surgical resection bed, i.e., suspected tumor invasion into eloquent or surrounding cortex. Alternatively, FNa could be used at the completion or during the 5-ALA-guided resection for CLE optical biopsy.

Simultaneous use of 5-ALA and FNa has been previously reported (Schwake et al. 2015). Our experience with the new operating microscope with BLUE400 and YELLOW560 modes demonstrates that both channels could be used alternating without compromise. Concurrent FNa-contrasted CLE could be potentially advantageously used during near-infrared-guided surgeries due to the absence of spectral overlap with FNa for example, with indocyanine green (ICG) (Cho, Salinas, and Lee 2019, Cho, Salinas, et al. 2019). Confocal-assisted fluorescence microscopy with ICG as a contrast for confocal microscopy has been reported (Charalampaki et al. 2019). In view of future incorporation of the CLE in the workflow on FGS, its diagnostic accuracy should also be compared to the wide field imaging with various diagnostic agents such as FNa, 5-ALA and ICG.

It should be noted that other techniques for safe maximal resection, particularly, intraoperative stimulation and awake brain mapping, should be considered (Duffau 2019). These and other functional methods are designed to be highly sensitive for eloquent brain areas that should be preserved, while the goal of FGS and CLE is to specifically detect tumor regions and reveal them for the surgical decision on whether to

resect or preserve. Therefore, these two methods can provide mutually complimentary information.

Diagnostic Accuracy in Different Tumor Types

Because glioma tissue is often challenging to distinguish from normal brain tissue without special or enhanced imaging techniques, application of in vivo CLE for immediate optical biopsy in gliomas is of particular interest. With experience from animal and early clinical studies, we have developed confidence in interpretation of CLE images and in successfully identifying hypercellular high-grade glioma samples based on the characteristic CLE patterns (Sankar et al. 2010, Martirosyan, Georges, et al. 2016, Sanai, Eschbacher, et al. 2011). In contrast to previous reports, here we were able to assess multiple matched biopsies from the same patients, including multiple samples that were read as gliotic brain without tumor.

Coupled with on our previous studies on differentiation of glioma tissue from injured normal brain in the murine model (Belykh, Miller, Patel, et al. 2018), the current work deepens our understanding of the CLE features of the non-tumor normal or gliotic brain in human. Most of the samples of gliotic and normal brain were labeled as non-diagnostic of brain tumor, based on the fact that they lacked the typical cellular features or high cellularity, while most of them had dark extracellular background and some autofluorescence speckles. Normal cells were not clearly visible on these images, making it harder to definitively conclude if the optical biopsy is representative of normal brain tissue. Interestingly, increased speckles on CLE images with a similar device have been

previously seen in low-grade gliomas with 5-ALA use (Sanai, Snyder, et al. 2011), but they most likely represent autofluorescence (Belykh et al. 2019). It is not settled whether this is the normal appearance of brain tissue using CLE imaging with FNa contrast. We believe that future in vivo studies should focus on assessment of marginal tissue in order to provide a confident answer or label of "normal" brain tissue when interpreting a dark CLE optical biopsy with autofluorescence and absence of cellular architecture features.

With respect to metastatic lesions and choroid plexus carcinomas, CLE provides high-contrast, clear, and reliable pictures of cellular features that are highly diagnostic of cellular tumor. The most non-diagnostic optical biopsies are either due to the blood artifacts that hide the actual tissue, or due to the FNa contrast redistribution with time that diminishes contrast among the cells and between the nuclei, cytoplasm and extracellular compartments.

In all available meningioma samples, including one which was composed of 80% dura and 20% invasive meningioma tissue, CLE provided clear high-contrast pictures of hypercellular tissue with fibrous structures and psammoma bodies, if present. Because we lacked normal marginal non-meningioma samples for CLE assessment, we used normal and gliotic brain as a negative control for calculating diagnostic accuracy in meningiomas. However, for future in vivo studies involving meningiomas, it would be important to obtain multiple biopsies of the dura at the edge of the tumor, similar to the tissue acquisition workflow in gliomas. Features of normal dura with FNa has been thoroughly examined in a pig model (Belykh et al. in submission), but its appearance at the marginal tumor regions should be better characterized in future study.

Power Calculation

The prevalence of the lesional samples was 84% (102/122) in all samples and 82% (80/97) in glioma samples in this study. The Buderer formula (Buderer 1996) with accuracy set at 0.05, prevalence of the disease in the tested population set at 84% and the sample size of 122, resulted in z=1.127 and confidence interval (CI) within 0.7-0.75 for sensitivity, and z=1.687 and CI=0.9-0.92 for specificity. For gliomas, the power analysis resulted in z=0.594 with CI<50% for sensitivity, and z=1.307 and CI=0.8-0.85 for specificity. While our study was underpowered for sensitivity, it is the first feasibility study and provides prevalence and diagnostic accuracy values for planning of future diagnostic accuracy studies using the CLE. For example, assuming 82% prevalence of tumor-positive samples, 94% specificity and 66% sensitivity, for CI=95% and 0.05 accuracy, the study size need to be 419 for sensitivity and 103 for specificity.

Study Limitations

Factors such as biopsy location and tumor type, the experience of the CLE user and extent of the scanned region of interest may introduce biases and need to be controlled in future studies. This study is limited to ex vivo analyses due to unavailability of the sterile CLE probe sheaths during the time the study was conducted that would have allowed in vivo use. However, it might be actually viewed as an advantage compared with in vivo acquisition for methodological reasons, as it is more certain that the CLE

images were obtained from the same biopsy region, thereby decreasing the sampling error.

Nevertheless, we acknowledge that sampling error is unavoidable with the small field of view of the imaging probe. H&E slides of multiple samples were inhomogeneous as viewed under the microscope: some had areas of necrosis up to 75% of the whole section, some had only 20% of areas representing infiltrating tumor, while the remaining regions were vessels and hemorrhage. It might also be that CLE can find the tumor cellular areas that are later missed on standard histological examination (Figure 5.2). At the same time, two CLE optical biopsies that were labeled as "normal" (i.e., two false negatives), showed dark background with normal appearing vessels suggestive of normal brain. However, few regions of interest were imaged with CLE for this sort of optical biopsy, therefore the infiltrative tumor areas detected on H&E slide may have been missed. We attempted to move the probe across the specimen to visualize larger areas, find locations with high quality confocal images bearing diagnostic features to minimize the sampling error, however, area of scanning is subject to user bias.

Conclusion

This study demonstrated the feasibility of incorporating CLE assessment of tissue microarchitecture during the FGS and demonstrated high specificity and positive predictive value of ex vivo optical biopsies with CLE in gliomas. This study reinforces the utility of CLE to provide real-time on-the-fly intraoperative cell resolution imaging,

i.e., “optical biopsy”, to the neurosurgeon that is comparable to and certainly quicker than conventional histological analysis from tissue biopsies in the operating room.

References

Acerbi, F., M. Broggi, G. Broggi, and P. Ferroli. 2015. "What is the best timing for fluorescein injection during surgical removal of high-grade gliomas?" *Acta Neurochir (Wien)* 157 (8):1377-8. doi: 10.1007/s00701-015-2455-z.

Acerbi, F., M. Broggi, M. Eoli, E. Anghileri, C. Cavallo, C. Boffano, R. Cordella, L. Cuppini, B. Pollo, M. Schiariti, S. Visintini, C. Orsi, E. La Corte, G. Broggi, and P. Ferroli. 2014. "Is fluorescein-guided technique able to help in resection of high-grade gliomas?" *Neurosurg Focus* 36 (2):E5. doi: 10.3171/2013.11.FOCUS13487.

Acerbi, F., M. Broggi, K. M. Schebesch, J. Hohne, C. Cavallo, C. De Laurentis, M. Eoli, E. Anghileri, M. Servida, C. Boffano, B. Pollo, M. Schiariti, S. Visintini, C. Montomoli, L. Bosio, E. La Corte, G. Broggi, A. Brawanski, and P. Ferroli. 2018. "Fluorescein-Guided Surgery for Resection of High-Grade Gliomas: A Multicentric Prospective Phase II Study (FLUOGLIO)." *Clin Cancer Res* 24 (1):52-61. doi: 10.1158/1078-0432.CCR-17-1184.

Barbosa, B. J., E. D. Mariano, C. M. Batista, S. K. Marie, M. J. Teixeira, C. U. Pereira, M. S. Tatagiba, and G. A. Lepski. 2015. "Intraoperative assistive technologies and extent of resection in glioma surgery: a systematic review of prospective controlled studies." *Neurosurg Rev* 38 (2):217-26; discussion 226-7. doi: 10.1007/s10143-014-0592-0.

Belykh, E., C. Cavallo, S. Gandhi, X. Zhao, D. Veljanoski, M. Izady Yazdanabadi, N. L. Martirosyan, V. A. Byvaltsev, J. Eschbacher, M. C. Preul, and P. Nakaji. 2018. "Utilization of intraoperative confocal laser endomicroscopy in brain tumor surgery." *J Neurosurg Sci* 62 (6):704-717. doi: 10.23736/S0390-5616.18.04553-8.

Belykh, E., E. J. Miller, A. Carotenuto, A. A. Patel, C. Cavallo, N. L. Martirosyan, D. R. Healey, V. A. Byvaltsev, A. C. Scheck, M. T. Lawton, J. M. Eschbacher, P. Nakaji, and M. C. Preul. 2019. "Progress in Confocal Laser Endomicroscopy for Neurosurgery and Technical Nuances for Brain Tumor Imaging With Fluorescein." *Front Oncol* 9:554. doi: 10.3389/fonc.2019.00554.

Belykh, E., E. J. Miller, A. A. Patel, M. I. Yazdanabadi, N. L. Martirosyan, K. Yagmurlu, B. Bozkurt, V. A. Byvaltsev, J. M. Eschbacher, P. Nakaji, and M. C. Preul. 2018. "Diagnostic Accuracy of a Confocal Laser Endomicroscope for In Vivo Differentiation Between Normal Injured And Tumor Tissue During Fluorescein-

Guided Glioma Resection: Laboratory Investigation." *World Neurosurg* 115:e337-e348. doi: 10.1016/j.wneu.2018.04.048.

Bossuyt, P. M., J. B. Reitsma, D. E. Bruns, C. A. Gatsonis, P. P. Glasziou, L. Irwig, J. G. Lijmer, D. Moher, D. Rennie, H. C. de Vet, H. Y. Kressel, N. Rifai, R. M. Golub, D. G. Altman, L. Hooft, D. A. Korevaar, J. F. Cohen, and Stard Group. 2015. "STARD 2015: an updated list of essential items for reporting diagnostic accuracy studies." *BMJ* 351:h5527. doi: 10.1136/bmj.h5527.

Buderer, N. M. 1996. "Statistical methodology: I. Incorporating the prevalence of disease into the sample size calculation for sensitivity and specificity." *Acad Emerg Med* 3 (9):895-900. doi: 10.1111/j.1553-2712.1996.tb03538.x.

Charalampaki, P., M. Nakamura, D. Athanasopoulos, and A. Heimann. 2019. "Confocal-Assisted Multispectral Fluorescent Microscopy for Brain Tumor Surgery." *Front Oncol* 9:583. doi: 10.3389/fonc.2019.00583.

Cho, S. S., R. Salinas, E. De Ravin, C. W. Teng, C. Li, K. G. Abdullah, L. Buch, J. Hussain, F. Ahmed, J. Dorsey, S. Mohan, S. Brem, S. Singhal, and J. Y. K. Lee. 2019. "Near-Infrared Imaging with Second-Window Indocyanine Green in Newly Diagnosed High-Grade Gliomas Predicts Gadolinium Enhancement on Postoperative Magnetic Resonance Imaging." *Mol Imaging Biol*. doi: 10.1007/s11307-019-01455-x.

Cho, S. S., R. Salinas, and J. Y. K. Lee. 2019. "Indocyanine-Green for Fluorescence-Guided Surgery of Brain Tumors: Evidence, Techniques, and Practical Experience." *Front Surg* 6:11. doi: 10.3389/fsurg.2019.00011.

D'Amico, R. S., Z. K. Englander, P. Canoll, and J. N. Bruce. 2017. "Extent of Resection in Glioma-A Review of the Cutting Edge." *World Neurosurg* 103:538-549. doi: 10.1016/j.wneu.2017.04.041.

Duffau, H. 2019. "Surgery for Malignant Brain Gliomas: Fluorescence-Guided Resection or Functional-Based Resection?" *Front Surg* 6:21. doi: 10.3389/fsurg.2019.00021.

Eschbacher, J., N. L. Martirosyan, P. Nakaji, N. Sanai, M. C. Preul, K. A. Smith, S. W. Coons, and R. F. Spetzler. 2012. "In vivo intraoperative confocal microscopy for real-time histopathological imaging of brain tumors." *J Neurosurg* 116 (4):854-60. doi: 10.3171/2011.12.JNS11696.

Falco, J., C. Cavallo, I. G. Vetrano, C. de Laurentis, L. Siozos, M. Schiariti, M. Broggi, P. Ferroli, and F. Acerbi. 2019. "Fluorescein Application in Cranial and Spinal Tumors Enhancing at Preoperative MRI and Operated With a Dedicated Filter on the Surgical Microscope: Preliminary Results in 279 Patients Enrolled in the

FLUOCERTUM Prospective Study." *Front Surg* 6:49. doi: 10.3389/fsurg.2019.00049.

Martirosyan, N. L., J. M. Eschbacher, M. Y. Kalani, J. D. Turner, E. Belykh, R. F. Spetzler, P. Nakaji, and M. C. Preul. 2016. "Prospective evaluation of the utility of intraoperative confocal laser endomicroscopy in patients with brain neoplasms using fluorescein sodium: experience with 74 cases." *Neurosurg Focus* 40 (3):E11. doi: 10.3171/2016.1.FOCUS15559.

Martirosyan, N. L., J. Georges, M. Y. Kalani, P. Nakaji, R. F. Spetzler, B. G. Feuerstein, and M. C. Preul. 2016. "Handheld confocal laser endomicroscopic imaging utilizing tumor-specific fluorescent labeling to identify experimental glioma cells in vivo." *Surg Neurol Int* 7 (Suppl 40):S995-S1003. doi: 10.4103/2152-7806.195577.

Sanai, N., and M. S. Berger. 2008. "Glioma extent of resection and its impact on patient outcome." *Neurosurgery* 62 (4):753-64; discussion 264-6. doi: 10.1227/01.neu.0000318159.21731.cf.

Sanai, N., J. Eschbacher, G. Hattendorf, S. W. Coons, M. C. Preul, K. A. Smith, P. Nakaji, and R. F. Spetzler. 2011. "Intraoperative confocal microscopy for brain tumors: a feasibility analysis in humans." *Neurosurgery* 68 (2 Suppl Operative):282-90; discussion 290. doi: 10.1227/NEU.0b013e318212464e.

Sanai, N., L. A. Snyder, N. J. Honea, S. W. Coons, J. M. Eschbacher, K. A. Smith, and R. F. Spetzler. 2011. "Intraoperative confocal microscopy in the visualization of 5-aminolevulinic acid fluorescence in low-grade gliomas." *J Neurosurg* 115 (4):740-8. doi: 10.3171/2011.6.JNS11252.

Sankar, T., P. M. Delaney, R. W. Ryan, J. Eschbacher, M. Abdelwahab, P. Nakaji, S. W. Coons, A. C. Scheck, K. A. Smith, R. F. Spetzler, and M. C. Preul. 2010. "Miniaturized handheld confocal microscopy for neurosurgery: results in an experimental glioblastoma model." *Neurosurgery* 66 (2):410-7; discussion 417-8. doi: 10.1227/01.NEU.0000365772.66324.6F.

Schwake, M., W. Stummer, E. J. Suero Molina, and J. Wolfer. 2015. "Simultaneous fluorescein sodium and 5-ALA in fluorescence-guided glioma surgery." *Acta Neurochir (Wien)* 157 (5):877-9. doi: 10.1007/s00701-015-2401-0.

CHAPTER 6

CONFOCAL LASER ENDOMICROSCOPY ASSESSMENT OF PITUITARY TUMOR MICROSTRUCTURE: FEASIBILITY STUDY

Abstract

Purpose: We investigated the feasibility of diagnosing unprocessed pituitary adenoma tissue using intraoperative digital optical biopsy with confocal laser endomicroscopy (CLE)

Methods: CLE probe positioning in the endonasal corridor was assessed. Biopsies from 9 patients who underwent transsphenoidal surgery for pituitary adenomas after intravenous fluorescein injection (2 mg/kg) were imaged with CLE in the operating room to obtain real-time cell-resolution histological images. CLE images and corresponding histopathology slides were randomized and assessed by a blinded board-certified neuropathologist. Image quality and timing of fluorescein injection were assessed.

Results: Using frozen sections as the standard, 13 of 16 (81%) samples were diagnosed as definitive pituitary adenomas. Of those 13 samples, 8 (62%) were CLE-diagnosed as pituitary adenoma, while 5 (38%) showed no identifiable histologic features of tumor and were graded as non-diagnostic, likely due to too late (>10 min, n=3) or too early (<1 min, n=1) biopsy acquisition after fluorescein injection or to blood artifacts (n=1). Another 3 of 16 (19%) frozen sections were diagnosed as “favoring pituitary adenoma.” Of those 3, 2 (66%) were CLE-diagnosed as pituitary adenomas and 1 was non-diagnostic due to too early biopsy acquisition.

Conclusions: This is the first study to assess CLE probe use within the transsphenoidal approach and to show feasibility of obtaining diagnostic digital biopsies of pituitary tumor tissue. Fluorescein provided sufficient contrast for CLE imaging at a dose of 2 mg/kg, optimally 1 to 10 minutes after injection. This results provide a basis for in vivo studies using CLE in transsphenoidal surgery.

Introduction

The standard method for rapid intraoperative diagnosis in pituitary surgery is frozen section histopathological analysis. This technique relies on evaluation of limited amounts of tissue to help guide surgical decision-making. Despite its role in intraoperative diagnosis, frozen section analysis has marked limitations, including processing, preparation time, artifacts, and decreased availability of tissues for permanent sample analysis (Tilgner et al. 2005, Uematsu et al. 2007). Although permanent sections offer higher diagnostic accuracy, permanent section analysis requires even longer processing times than frozen sections (Plesec and Prayson 2007). Real-time guidance of pituitary adenoma resection requires more rapid tissue analysis than classic histologic interpretation provides.

Fluorescence imaging, such as confocal laser endomicroscopy (CLE), yielding real-time on-the-fly imaging, is a faster modality of data acquisition, compared with frozen or permanent section analysis, and it can be used intraoperatively to improve surgical decision-making. CLE is advantageous because it allows for rapid image analysis from numerous observational perspectives (Behbahaninia et al. 2013, Zehri et al.

2014). The effectiveness of this technique has been demonstrated in gastrointestinal and gynecological surgeries (Tan et al. 2009, van den Broek et al. 2011). CLE practicability has been examined in a murine malignant glioma model and its real-time diagnostic application in human brain tumor resection has been assessed (Eschbacher et al. 2012, Fenton et al. 2014, Martirosyan et al. 2011, Sankar et al. 2010). Furthermore, the diagnostic specificities and sensitives of CLE for gliomas and meningiomas were on par with those of frozen sections (Martirosyan, Eschbacher, et al. 2016). However, feasibility of pituitary tissue assessment with CLE has not been previously examined.

In this study, for the first time, we examined the feasibility of CLE, with fluorescein used as a contrast agent, for rapid intraoperative assessment of tissue microstructure of human pituitary adenomas.

Materials and Methods

Feasibility of CLE Positioning for Endonasal Procedures

Three cadaveric heads with arterial and venous systems injected with colored silicone were used to assess the endonasal placement of the scanning probe in the pituitary gland. Using the standard endoscopic instruments and straight endoscope, an endonasal transsphenoidal approach to the pituitary gland was established.

Biopsy Specimens

This prospective study was approved by the St. Joseph's Hospital and Medical Center Institutional Review Board for Human Research. A total of 9 patients undergoing

endonasal transsphenoidal surgery for pituitary adenoma within a 3-month period were included. Fluorescein was administered intravenously (IV) at a dose of 2 mg/kg before biopsy collection. Tissue samples that were suspected to contain pituitary tumor and were to be removed as a usual part of the standard procedure were collected for this study. These biopsies were not used for patient care decision-making and were acquired when sufficient tissue was available after permanent and frozen section biopsy were acquired for patient care. Immediately after resection, samples were put on moisturized nonadherent surgical dressing and examined ex vivo in the same operating room but away from the patient. A confocal laser endomicroscope (CONVIVO, Carl Zeiss AG, Jena, Germany) was used to obtain confocal digital images. Time to imaging the tissue sample following fluorescein injection ranged from 1 to 45 minutes.

Imaging Protocol

CLE uses data acquisition parameters comparable to those presented in our previous work (Eschbacher et al. 2012, Martirosyan et al. 2014). The CLE system includes a 15-cm long scanner probe shaft that is covered by a sterile outer sheath (5-mm outer diameter). This probe is rigidly connected to a scanner unit using a 3.8-m long cable. The scanner unit itself is attached to a mobile workstation. The scanning depth and recording functions are controlled through a touchscreen display or controlled remotely to vary imaging from the surface to a depth of 0 to 500 μm. Incident excitation light is generated by a 488-nm laser. A single optical fiber serves as both the excitation and detection pinholes for confocal isolation of the focal plane. The detector signal and

scanning are digitally synchronized to produce en face optical sections creating images parallel to the tissue surface. Aside from the IV fluorescein, no additional fluorophore was used for ex vivo imaging.

To create optimal quality images, we set the system to use a green bandpass filter (517.5–572.5 nm) to detect emitted fluorescence. Generally, the laser power setting was set at 0.5–0.9 mW during the scanning, with a maximum power limit of 1 mW. Utilizing 1× zoom, a field of view of 267×475 μm was scanned at 1920×1080 pixels (full high definition) with a speed of 0.75 frames per second and with a lateral and axial resolution of approximately 0.7 μm and 4.5 μm, respectively. The static images produced were saved and used to create a time-lapse series that functioned as a digital looping video.

Trained team members performed the CLE scanning (E.B., X.Z.). Digital optical biopsies were primarily acquired with the CLE probe affixed in the upright position to a retractor arm that was tightened to stabilize probe position. Small tissue samples (2–5 mm^3) were placed on the surface of the probe and, while maintaining contact with the probe, gently moved with microsurgical forceps to scan the larger sample surface. Multiple images were acquired for every biopsy location.

Tissue Sampling, Histology, and Processing

After CLE imaging, each biopsy sample was divided in half for frozen section and permanent section preparation and sent to the pathology department. Histologic analysis was conducted using standard light microscopic evaluation of 10-μm–thick hematoxylin and eosin (H&E)–stained sections. Both frozen and permanent histologic sections were

used to validate the CLE images. The reasoning for using the H&E staining as a reference standard rather than other specific stains was that, similarly to fluorescein, H&E provides non-specific staining of both normal and abnormal tissue. Furthermore, CLE is seen as an in vivo tool for preliminary histological evaluation of the tissue, which is complimentary or alternative to frozen section analysis.

A neuropathologist with experience interpreting CLE images, but not involved in the surgeries, reviewed the CLE digital images (several images and video-loops from one sample), as well as frozen and permanent section slides. An educational set of CLE images was reviewed before examining the study CLE images. Histology slides and CLE images were presented in random order. Histopathologic features of the CLE images and H&E–stained frozen and permanent sections were assessed and rated by a neuropathologist. CLE images were categorized as diagnostic if they showed identifiable histologic features.

Results

Feasibility of CLE Positioning for Transsphenoidal Surgery

The scanning probe was successfully used in a transsphenoidal approach in all 3 cadaveric specimens. The size of the probe was adequate for en face imaging of the pituitary gland tissue within the sella turcica (Figure 6.1).

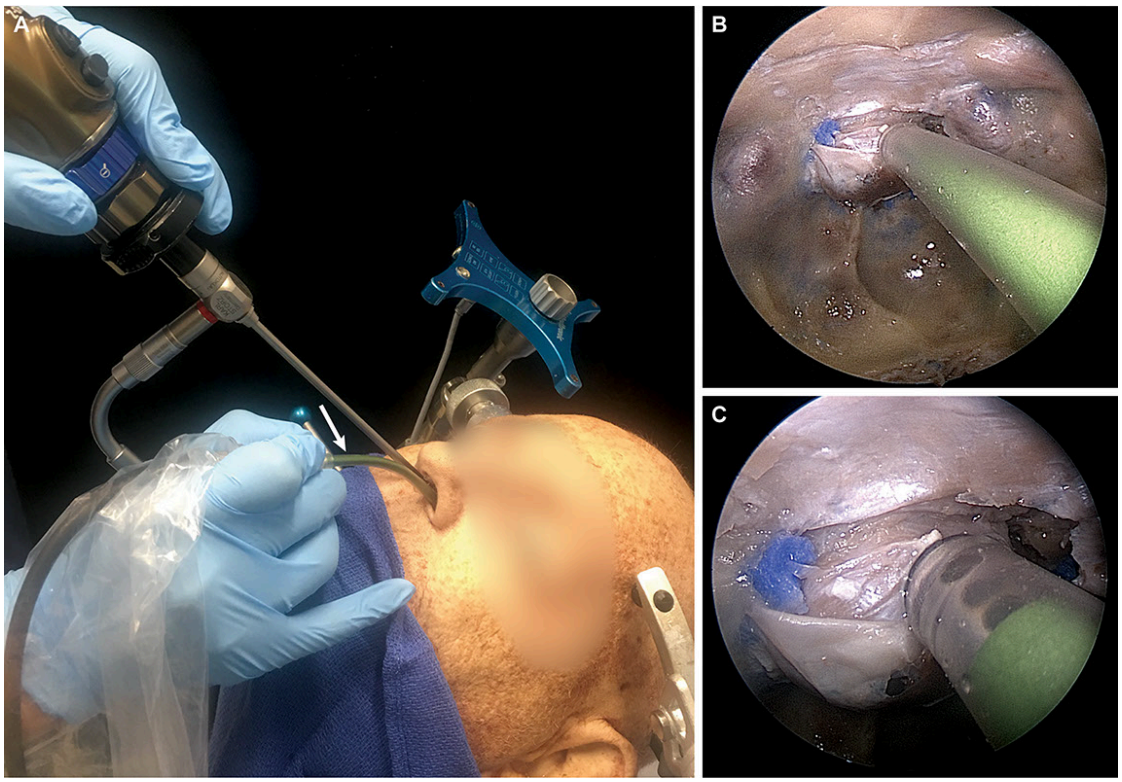

Figure 6.1. Position of confocal laser endomicroscopy (CLE) scanning probe in the endonasal transsphenoidal approach. (A) Overall position (arrow points to the CLE probe). (B and C) Endoscopic view of tip of the probe in the sellar region.

Descriptive Analysis

The CLE images of pituitary adenomas demonstrated appropriate characteristic features: sheets of cells with prominent nuclei, increased cellularity, nonorganized tissue architecture, vascularity, and stroma (Figure 6.2). We observed heterogenous uptake of fluorescein by cells creating a nuclear-cytoplasmic contrast, as well as contrast between neighboring cells.

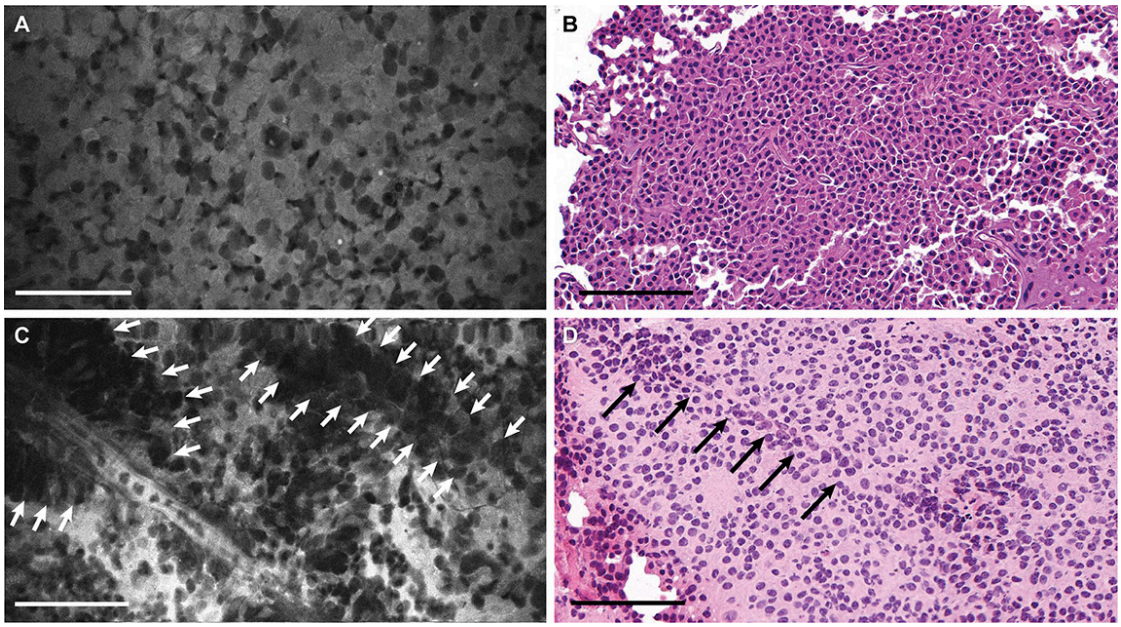

Figure 6.2. Photomicrographs of a pituitary adenoma. (A) Confocal laser endomicroscopy (CLE) image (also see Video 1) and (B) hematoxylin and eosin (H&E) stain of the same tumor from subject 19.3 demonstrate sheets of uniform non-lobulated cells with prominent nuclei. (C) CLE image (also see Video 2) and (D) H&E image from subject 24.3 demonstrate perivascular sheets of the cells (arrows). Bar = 100 μm.

Blinded Review

The study included 9 patients with pituitary adenomas that resulted in 19 samples scanned with CLE. Results of the blinded review are presented in Figure 6.3. A neuropathologist and pathologist correctly identified 62% (8/13) of pituitary adenomas imaged with CLE, using frozen sections as the comparative diagnostic standard, while the remaining 5 CLE samples correlating with frozen section-identified adenomas were considered non-diagnostic (Figure 6.4). Also, among the 7 sections identified as pituitary adenomas using permanent sections as the standard, 4 (57%) were also identified as

pituitary adenomas using CLE while the other samples were deemed non-diagnostic. Non-diagnostic CLE images were attributed to timing of fluorescein injection, and erythrocytes in the field obscuring useful interpretation. Most non-diagnostic CLE images resulted when biopsies were acquired after fluorescein was injected very early (<1 min) or very late (>10 min) (Figure 6.5). Additionally, very small biopsy samples made it difficult to find optimal imaging locations. Blood present in one sample was characterized by the neuropathologist as non-diagnostic.

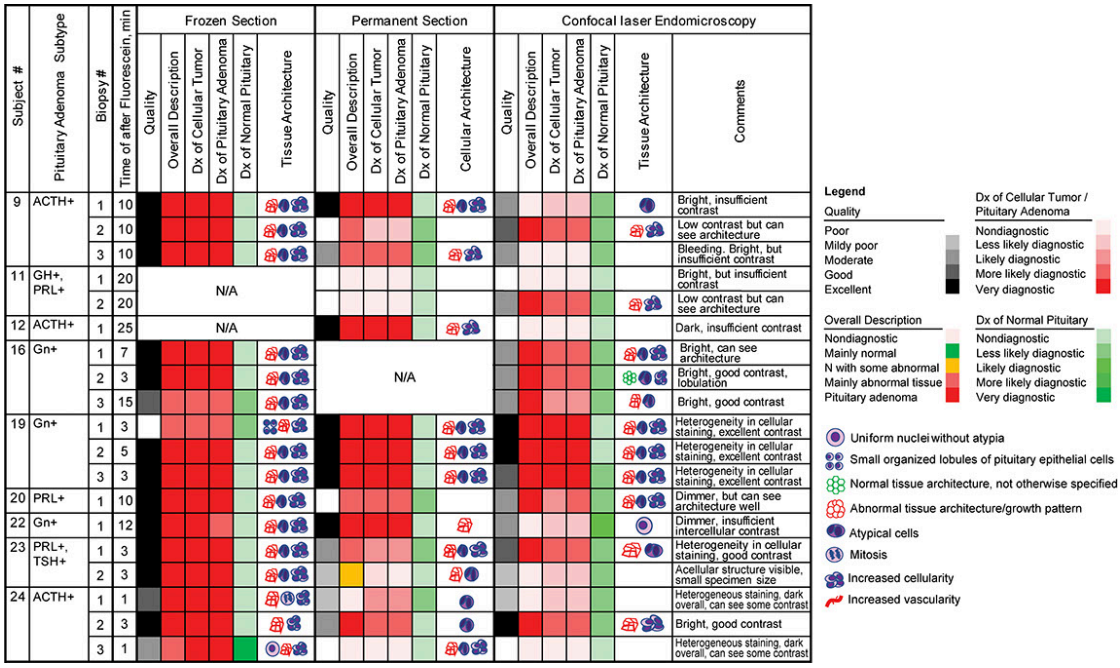

Figure 6.3. Results of the qualitative comparative assessment of the frozen sections, fixed permanent sections, and confocal laser endomicroscopy images of pituitary adenomas by a neuropathologist blinded to patient data. Abbreviations: ACTH, adrenocorticotropic hormone; Dx, diagnosis; GH, growth hormone; Gn, gonadotroph; N, normal; PRL, prolactin; TSH, thyroid stimulating hormone.

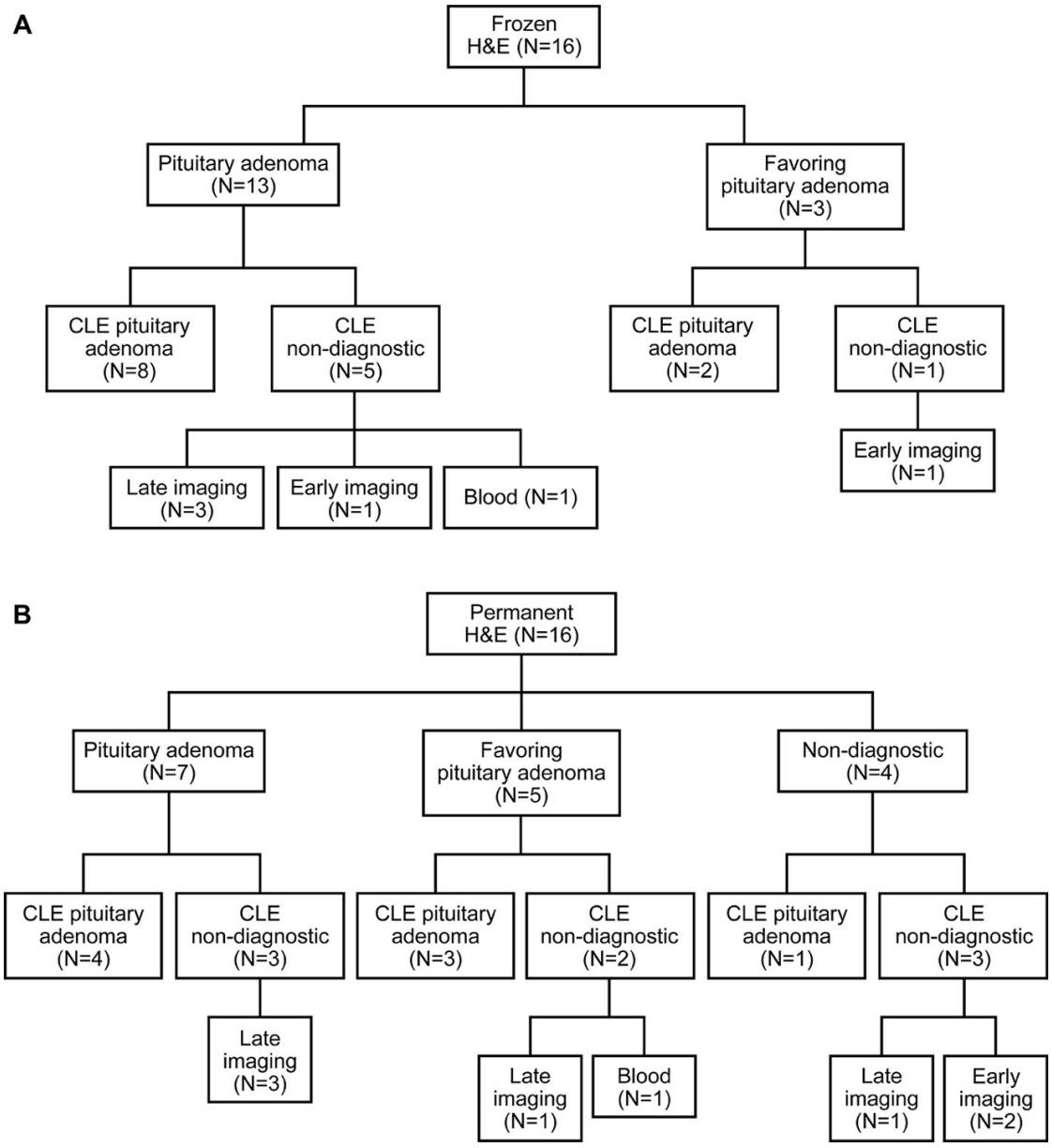

Figure 6.4. Study design flowchart demonstrating confocal laser endomicroscopy (CLE) accuracy with (A) frozen hematoxylin and eosin (H&E) sections and (B) fixed permanent H&E sections, as the standard.

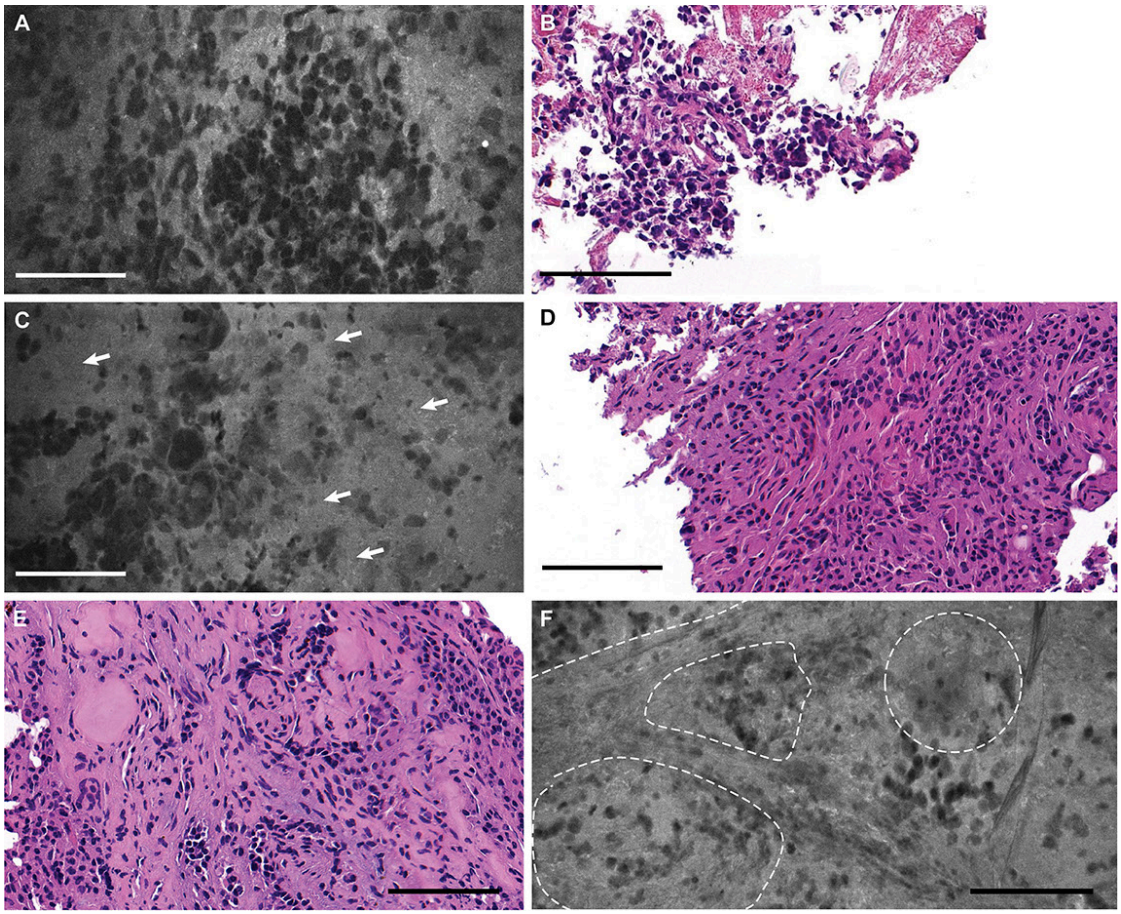

Figure 6.5. CLE images that were non-diagnostic due to (A) too early (<1 min) biopsy acquisition after fluorescein injection, (C) too late (>10 min) biopsy acquisition, and (F) images demonstrating more uniform lobules of pituitary epithelial cells suggestive of normal pituitary. Arrows point to the hypercellular areas of tissue with suboptimal contrasting of the cellular outlines, dotted lies outline lobules. (B, D, and E) H&E stained sections are from the same specimens as A, C and E, respectively. Bars = 100 μm. *Used with permission from Barrow Neurological Institute, Phoenix, Arizona.*

Discussion

Confocal Endomicroscopy Technology

Although frozen sections and imprint cytology (Brommeland et al. 2003) are routine techniques used for intraoperative diagnosis, they are not infallible. These histologic analyses are subject to preparation and processing time delay, freezing and sectioning artifacts, as well as the potential for tissue loss and degradation. Furthermore, diagnostic discrepancies exist between frozen and permanent sections (Plesec and Prayson 2007). Studies have suggested confocal reflectance microscopy as an effective alternative to using standard histology for intraoperative diagnosis and evaluation of tumor margins (Mooney et al. 2018, Eschbacher et al. 2017, Georges et al. 2014, Forest et al. 2015). Another reflectance microscopy technology based on stimulated Raman scattering was shown to be effective for digital biopsies of ex vivo samples of lesional brain samples (Orringer et al. 2017).

Unlike the above-mentioned technologies, CLE is intended for handheld, portable, in vivo digital optical interrogation of tissues without the need for tissue removal. A previous generation of the CLE device was determined to be an effective diagnostic imaging modality in a study of multiple intracranial tumors, including gliomas and meningiomas (Martirosyan, Eschbacher, et al. 2016). CLE technology has also been successfully used to visualize internal tissue microstructures such as fiber bundles in multiple brain tumor types (Charalampaki et al. 2019, Charalampaki et al. 2015, Belykh, Patel, Miller, Bozkurt, Yagmurlu, et al. 2018).

In this study, we performed a proof-of-principle assessment of pituitary adenoma tissue with the first clinical-grade and FDA–approved CLE device. CLE imaging allows for the spatial resolution of biopsy samples without physical disturbance. When combined with the appropriate fluorescent dye, CLE can be effective in visualizing characteristic tissue architecture and morphology for histopathologic analysis. Moreover, the CLE probe is similar in size to a standard neurosurgical suction device, thus finding a comfortable and accustomed manual application in real-time on-the-fly intraoperative visualization of brain tumors and normal tissue at the cellular level (Martirosyan et al. 2018b).

This proof-of-principle study has demonstrated the potential use of CLE in detecting pituitary adenomas tissue microstructure. A neuropathologist with no prior knowledge of the biopsied specimens was able to correctly identify 8 of 13 CLE images (62%) as pituitary adenomas using frozen sections as the standard. The remaining 5 images were labeled non-diagnostic for the following reasons: 3 were imaged very late (>10 min), 1 was imaged very early (<1 min), and 1 showed too much blood artifact. Future studies should use tissue acquisition with fluorescein injection times between 1 and 10 minutes to minimize non-diagnostic image collection. In vivo imaging should allow for better CLE quality due to a larger area available for scanning that would permit diagnostic frame detection. Nevertheless, bleeding artifacts would still remain.

Biopsy Acquisition

The small size of some pituitary biopsies presented an obstacle for adequate histological assessment, which should be noted for future study planning. On a patient level, all permanent diagnoses agreed with the frozen section diagnosis. On the biopsy level, all but one frozen sections were diagnosed as “very likely” pituitary adenomas, and one as “mainly abnormal tissue”. Two permanent section were inconclusive, and 1 permanent to section contained both normal and abnormal tissue. Although we believe that some CLE biopsies contained the lobulated appearance characteristic of normal pituitary architecture (Figure 5 E, F), none of histological slides were composed completely of a normal gland. Therefore, future in vivo CLE assessment will need to confirm the histological appearance of normal pituitary.

Optimal Dosing and Timing of Fluorescein Injection

The optimal timing for CLE imaging was determined as >1 min, but <10 min. For these timings, 2 mg/kg IV fluorescein was a sufficient dosing regimen, but other doses have yet to be evaluated for pituitary adenomas. In another study, a 5 mL 10% fluorescein IV dose was used to visualize gliomas and meningiomas (Martirosyan, Eschbacher, et al. 2016). The success with higher dosing in other brain neoplasms applied to pituitary masses for improved CLE imaging warrants further investigation.

Feasibility for Endonasal Procedures

Both microscopic and endoscopic transsphenoidal approaches are viable methods for pituitary adenoma resection, with the endoscopic technique offering some benefits (Strychowsky et al. 2011). The goals of these procedures are complete surgical resection with minimal recurrence rates and preservation of normal pituitary function. Therefore, precise spatial visualization of microadenomas and residual tumor is crucial. CLE offers a potential imaging modality for minimally invasive, transnasal assessment of pituitary tissue microstructure. Previously, the CLE probe design was too wide and did not allow for transnasal access; however, a miniaturized CLE probe affords imaging through transnasal transsphenoidal corridors (Figure 6.1). A proof-of-concept study of intraoperative, transnasal CLE could be conducted, modeling the study we have conducted here, and would seem to provide an advantageous means to verify remaining microscopic pathologic tissue remnants within the sella turcica. Such CLE application may be especially relevant in assessing invasion of tumors from the sella turcica as they are approached more widely in association with endoscopic procedures of the cavernous sinus.

Although this is a feasibility study, several potential future aspects merit discussion. The potential cost of CLE use would include a disposable sterile drape, capital equipment cost for the CLE system, and potential procedural fee for interpretation. Although we did not assess the time added to the case in this study, our previous assessment demonstrated that the first diagnostic frame appeared on average within 17 seconds after initiation of imaging in vivo.

Other Fluorophores

Although this study used fluorescein as the fluorescent dye for CLE, other fluorophores have the potential to aid in visualization of pituitary adenomas. Other studies have assessed the efficacy of two near-infrared (700–850 nm) fluorophores in pituitary adenoma resections: indocyanine green (ICG) and OTL38 (On Target Laboratories, West Lafayette, Indiana) (Cho et al. 2018, Cho, Zeh, et al. 2019, Lee et al. 2018). ICG, a dye frequently used in neurosurgery, can be applied in a technique known as second-window ICG, which can use the enhanced vascular permeability of pituitary adenomas to allow for intraoperative imaging. Additionally, this second-window technique has shown higher sensitivity for all pituitary adenomas than visible-light spectrum visualization alone. OTL38 is a folate ligand combined with an ICG analog that has shown promise in visualizing tumors that overexpress folate receptors, such as nonfunctional pituitary adenomas (Evans et al. 2003, Evans et al. 2008). Both of these dyes have demonstrated increased tissue penetration and considerably lower background signal when compared to 5-aminolevulinic acid (5-ALA) and fluorescein (Frangioni 2003, Padalkar and Pleshko 2015). OTL38 has exhibited both higher sensitivity and specificity for nonfunctional pituitary adenomas in comparison to white light (Cho and Lee 2019). Unlike, a specific folate dye, fluorescein penetrates the tissue non-specifically, creating a contrast for better visualization of the contours of all cells and nuclei, as well as extracellular fibers. Therefore, unlike other specific dyes, the interpretation is based not solely on the presence of the fluorescent signal, but mainly on the evaluation of cytoarchitecture and histological features. Because fluorescein does not

interfere with near-infrared ICG and 5-ALA, fluorescein-based CLE is compatible with other wide-field fluorescence-guided surgery techniques used in operating microscopes. Further development of CLE technology with other fluorophores, such as ICG (Charalampaki et al. 2019, Martirosyan et al. 2011) and 5-ALA (Meza et al. 2015) is possible.

Limitations

In our study, the precise diagnosis could not be determined by CLE for every case. Pituitary adenomas that exhibited apparent characteristic features, such as sheets of cells with prominent nuclei, brightly reflective cytoplasm, and increased cellularity could be identified. However, various factors rendered some samples non-diagnostic in the neuropathologist's evaluation. A significant limiting factor creating difficulty in interpreting some of the CLE images, as well as some of the permanent H&E-stained sections, was the small size of biopsy samples for ex vivo imaging. This factor should be taken in consideration for future study planning.

We have not compared various pituitary adenoma subtypes (subtypes are shown in Figure 6.3), however because fluorescein is a non-specific contrast, we do not expect differences. The goal for the CLE assessment is to complement, and perhaps replace the conventional intraoperative frozen section analysis performed with non-specific H&E staining. Another challenge to be investigated is differentiation of non-tumorous gland hyperplasia.

CLE imaging timing was also a significant factor in diagnostic capability. Some images acquired later than10 min after fluorescein injection or less than 1 min after injection were non-diagnostic. There certainly were diagnostic images 10 minutes after injection, but it appeared that the rate of non-diagnostic images increased with time. This may be due to fluorescein distribution evenly throughout the cells and diminished the contrast between the intracellular, intranuclear and extracellular compartments. When imaging was obtained too early, the fluorescein contrast was not optimally diffused, thus cytoplasmic-nuclear contrast was not apparent. Other inconclusive CLE images were obtained from suboptimal locations with the presence of blood artifacts, impairing proper image appraisal.

This study did not assess diagnostic accuracy. Here we assessed optimal timing and feasibility of the fluorescein dose, as well as feasibility of the CLE probe to be used in the transsphenoidal approach. The probe was not approved for in vivo use at the time this study was conducted. Investigation of in vivo CLE use is the subject of studies comparing CLE and frozen sectioning for assessing pituitary adenomas, with careful consideration of CLE imaging timing, sample location, and sample numbers.

Conclusion

CLE imaging is feasible for the rapid evaluation of pituitary adenoma biopsies. CLE can visualize histopathologic characteristics of pituitary adenomas, with the added benefit of preserving specimens for permanent section analysis. Fluorescein provided sufficient contrast for CLE imaging of pituitary adenomas at a dose of 2 mg/kg IV. The

optimal imaging interval was 1 to 10 minutes after fluorescein injection. Non-diagnostic CLE images were mostly due to limited tissue availability, suboptimal timing, and blood artifacts; these limitations should be taken into account for in vivo use. Further studies will evaluate the potential advantageous use of in vivo CLE for endoscopic transsphenoidal surgeries.

References

Behbahaninia, M., N. L. Martirosyan, J. Georges, J. A. Udovich, M. Y. Kalani, B. G. Feuerstein, P. Nakaji, R. F. Spetzler, and M. C. Preul. 2013. "Intraoperative fluorescent imaging of intracranial tumors: a review." *Clin Neurol Neurosurg* 115 (5):517-28. doi: 10.1016/j.clineuro.2013.02.019.

Belykh, E., A. A. Patel, E. J. Miller, B. Bozkurt, K. Yagmurlu, E. C. Woolf, A. C. Scheck, J. M. Eschbacher, P. Nakaji, and M. C. Preul. 2018. "Probe-based three-dimensional confocal laser endomicroscopy of brain tumors: technical note." *Cancer Manag Res* 10:3109-3123. doi: 10.2147/CMAR.S165980.

Brommeland, T., S. Lindal, B. Straume, I. L. Dahl, and R. Hennig. 2003. "Does imprint cytology of brain tumours improve intraoperative diagnoses?" *Acta Neurol Scand* 108 (3):153-6. doi: 10.1034/j.1600-0404.2003.00115.x.

Charalampaki, P., M. Javed, S. Daali, H. J. Heiroth, A. Igressa, and F. Weber. 2015. "Confocal Laser Endomicroscopy for Real-time Histomorphological Diagnosis: Our Clinical Experience With 150 Brain and Spinal Tumor Cases." *Neurosurgery* 62 Suppl 1:171-6. doi: 10.1227/NEU.0000000000000805.

Charalampaki, P., M. Nakamura, D. Athanasopoulos, and A. Heimann. 2019. "Confocal-Assisted Multispectral Fluorescent Microscopy for Brain Tumor Surgery." *Front Oncol* 9:583. doi: 10.3389/fonc.2019.00583.

Cho, S. S., J. Jeon, L. Buch, S. Nag, M. Nasrallah, P. S. Low, M. S. Grady, S. Singhal, and J. Y. K. Lee. 2018. "Intraoperative near-infrared imaging with receptor-specific versus passive delivery of fluorescent agents in pituitary adenomas." *J Neurosurg*:1-11. doi: 10.3171/2018.7.jns181642.

Cho, S. S., and J. Y. K. Lee. 2019. "Intraoperative Fluorescent Visualization of Pituitary Adenomas." *Neurosurg Clin N Am* 30 (4):401-412. doi: 10.1016/j.nec.2019.05.002.

Cho, S. S., R. Zeh, J. T. Pierce, J. Jeon, M. Nasrallah, N. D. Adappa, J. N. Palmer, J. G. Newman, C. White, J. Kharlip, P. Snyder, P. Low, S. Singhal, M. S. Grady, and J. Y. K. Lee. 2019. "Folate Receptor Near-Infrared Optical Imaging Provides Sensitive and Specific Intraoperative Visualization of Nonfunctional Pituitary Adenomas." *Oper Neurosurg (Hagerstown)* 16 (1):59-70. doi: 10.1093/ons/opy034.

Eschbacher, J. M., J. F. Georges, E. Belykh, M. I. Yazdanabadi, N. L. Martirosyan, E. Szeto, C. Y. Seiler, M. A. Mooney, J. K. Daniels, K. Y. Goehring, K. R. Van Keuren-Jensen, M. C. Preul, S. W. Coons, S. Mehta, and P. Nakaji. 2017. "Immediate Label-Free Ex Vivo Evaluation of Human Brain Tumor Biopsies With Confocal Reflectance Microscopy." *J Neuropathol Exp Neurol* 76 (12):1008-1022. doi: 10.1093/jnen/nlx089.

Eschbacher, J., N. L. Martirosyan, P. Nakaji, N. Sanai, M. C. Preul, K. A. Smith, S. W. Coons, and R. F. Spetzler. 2012. "In vivo intraoperative confocal microscopy for real-time histopathological imaging of brain tumors." *J Neurosurg* 116 (4):854-60. doi: 10.3171/2011.12.JNS11696.

Evans, C. O., P. Reddy, D. J. Brat, E. B. O'Neill, B. Craige, V. L. Stevens, and N. M. Oyesiku. 2003. "Differential expression of folate receptor in pituitary adenomas." *Cancer Res* 63 (14):4218-24.

Evans, C. O., C. Yao, D. Laborde, and N. M. Oyesiku. 2008. "Folate receptor expression in pituitary adenomas cellular and molecular analysis." *Vitam Horm* 79:235-66. doi: 10.1016/s0083-6729(08)00408-1.

Fenton, K. E., N. L. Martirosyan, M. G. Abdelwahab, S. W. Coons, M. C. Preul, and A. C. Scheck. 2014. "In vivo visualization of GL261-luc2 mouse glioma cells by use of Alexa Fluor-labeled TRP-2 antibodies." *Neurosurg Focus* 36 (2):E12. doi: 10.3171/2013.12.focus13488.

Forest, F., E. Cinotti, V. Yvorel, C. Habougit, F. Vassal, C. Nuti, J. L. Perrot, B. Labeille, and M. Peoc'h. 2015. "Ex vivo confocal microscopy imaging to identify tumor tissue on freshly removed brain sample." *J Neurooncol* 124 (2):157-64. doi: 10.1007/s11060-015-1832-z.

Frangioni, J. V. 2003. "In vivo near-infrared fluorescence imaging." *Curr Opin Chem Biol* 7 (5):626-34.

Georges, J., A. Zehri, E. Carlson, J. Nichols, M. A. Mooney, N. L. Martirosyan, L. Ghaffari, M. Y. Kalani, J. Eschbacher, B. Feuerstein, T. Anderson, M. C. Preul, K. Van Keuren-Jensen, and P. Nakaji. 2014. "Label-free microscopic assessment of glioblastoma biopsy specimens prior to biobanking [corrected]." *Neurosurg Focus* 36 (2):E8. doi: 10.3171/2013.11.FOCUS13478.

Lee, J. Y. K., S. S. Cho, R. Zeh, J. T. Pierce, M. Martinez-Lage, N. D. Adappa, J. N. Palmer, J. G. Newman, K. O. Learned, C. White, J. Kharlip, P. Snyder, P. S. Low, S. Singhal, and M. S. Grady. 2018. "Folate receptor overexpression can be visualized in real time during pituitary adenoma endoscopic transsphenoidal surgery with near-infrared imaging." *J Neurosurg* 129 (2):390-403. doi: 10.3171/2017.2.jns163191.

Martirosyan, N. L., D. D. Cavalcanti, J. M. Eschbacher, P. M. Delaney, A. C. Scheck, M. G. Abdelwahab, P. Nakaji, R. F. Spetzler, and M. C. Preul. 2011. "Use of in vivo near-infrared laser confocal endomicroscopy with indocyanine green to detect the boundary of infiltrative tumor." *J Neurosurg* 115 (6):1131-8. doi: 10.3171/2011.8.JNS11559.

Martirosyan, N. L., J. M. Eschbacher, M. Y. Kalani, J. D. Turner, E. Belykh, R. F. Spetzler, P. Nakaji, and M. C. Preul. 2016. "Prospective evaluation of the utility of intraoperative confocal laser endomicroscopy in patients with brain neoplasms using fluorescein sodium: experience with 74 cases." *Neurosurg Focus* 40 (3):E11. doi: 10.3171/2016.1.FOCUS15559.

Martirosyan, N. L., J. Georges, J. M. Eschbacher, D. D. Cavalcanti, A. M. Elhadi, M. G. Abdelwahab, A. C. Scheck, P. Nakaji, R. F. Spetzler, and M. C. Preul. 2014. "Potential application of a handheld confocal endomicroscope imaging system using a variety of fluorophores in experimental gliomas and normal brain." *Neurosurg Focus* 36 (2):E16. doi: 10.3171/2013.11.focus13486.

Martirosyan, Nikolay L., Joseph Georges, Jennifer M. Eschbacher, Evgenii Belykh, Alessandro Carotenuto, Robert F. Spetzler, Peter Nakaji, and Mark C. Preul. 2018. "Confocal scanning microscopy provides rapid, detailed intraoperative histological assessment of brain neoplasms: Experience with 106 cases." *Clinical Neurology and Neurosurgery* 169:21-28. doi: 10.1016/j.clineuro.2018.03.015.

Meza, D., D. Wang, Y. Wang, S. Borwege, N. Sanai, and J. T. Liu. 2015. "Comparing high-resolution microscopy techniques for potential intraoperative use in guiding low-grade glioma resections." *Lasers Surg Med* 47 (4):289-95. doi: 10.1002/lsm.22347.

Mooney, M. A., J. Georges, M. I. Yazdanabadi, K. Y. Goehring, W. L. White, A. S. Little, M. C. Preul, S. W. Coons, P. Nakaji, and J. M. Eschbacher. 2018. "Immediate ex-vivo diagnosis of pituitary adenomas using confocal reflectance microscopy: a proof-of-principle study." *J Neurosurg* 128 (4):1072-1075. doi: 10.3171/2016.11.JNS161651.

Orringer, D. A., B. Pandian, Y. S. Niknafs, T. C. Hollon, J. Boyle, S. Lewis, M. Garrard, S. L. Hervey-Jumper, H. J. L. Garton, C. O. Maher, J. A. Heth, O. Sagher, D. A. Wilkinson, M. Snuderl, S. Venneti, S. H. Ramkissoon, K. A. McFadden, A.

Fisher-Hubbard, A. P. Lieberman, T. D. Johnson, X. S. Xie, J. K. Trautman, C. W. Freudiger, and S. Camelo-Piragua. 2017. "Rapid intraoperative histology of unprocessed surgical specimens via fibre-laser-based stimulated Raman scattering microscopy." *Nat Biomed Eng* 1. doi: 10.1038/s41551-016-0027.

Padalkar, M. V., and N. Pleshko. 2015. "Wavelength-dependent penetration depth of near infrared radiation into cartilage." *Analyst* 140 (7):2093-100. doi: 10.1039/c4an01987c.

Plesec, T. P., and R. A. Prayson. 2007. "Frozen section discrepancy in the evaluation of central nervous system tumors." *Arch Pathol Lab Med* 131 (10):1532-40. doi: 10.1043/1543-2165(2007)131[1532:fsdite]2.0.co;2.

Sankar, T., P. M. Delaney, R. W. Ryan, J. Eschbacher, M. Abdelwahab, P. Nakaji, S. W. Coons, A. C. Scheck, K. A. Smith, R. F. Spetzler, and M. C. Preul. 2010. "Miniaturized handheld confocal microscopy for neurosurgery: results in an experimental glioblastoma model." *Neurosurgery* 66 (2):410-7; discussion 417-8. doi: 10.1227/01.NEU.0000365772.66324.6F.

Strychowsky, J., S. Nayan, K. Reddy, F. Farrokhyar, and D. Sommer. 2011. "Purely endoscopic transsphenoidal surgery versus traditional microsurgery for resection of pituitary adenomas: systematic review." *J Otolaryngol Head Neck Surg* 40 (2):175-85.

Tan, J., M. A. Quinn, J. M. Pyman, P. M. Delaney, and W. J. McLaren. 2009. "Detection of cervical intraepithelial neoplasia in vivo using confocal endomicroscopy." *Bjog* 116 (12):1663-70. doi: 10.1111/j.1471-0528.2009.02261.x.

Tilgner, J., M. Herr, C. Ostertag, and B. Volk. 2005. "Validation of intraoperative diagnoses using smear preparations from stereotactic brain biopsies: intraoperative versus final diagnosis--influence of clinical factors." *Neurosurgery* 56 (2):257-65; discussion 257-65. doi: 10.1227/01.neu.0000148899.39020.87.

Uematsu, Y., Y. Owai, R. Okita, Y. Tanaka, and T. Itakura. 2007. "The usefulness and problem of intraoperative rapid diagnosis in surgical neuropathology." *Brain Tumor Pathol* 24 (2):47-52. doi: 10.1007/s10014-007-0219-z.

van den Broek, F. J., J. A. van Es, S. van Eeden, P. C. Stokkers, C. Y. Ponsioen, J. B. Reitsma, P. Fockens, and E. Dekker. 2011. "Pilot study of probe-based confocal laser endomicroscopy during colonoscopic surveillance of patients with longstanding ulcerative colitis." *Endoscopy* 43 (2):116-22. doi: 10.1055/s-0030-1255954.

Zehri, A. H., W. Ramey, J. F. Georges, M. A. Mooney, N. L. Martirosyan, M. C. Preul, and P. Nakaji. 2014. "Neurosurgical confocal endomicroscopy: A review of

contrast agents, confocal systems, and future imaging modalities." *Surg Neurol Int* 5:60. doi: 10.4103/2152-7806.131638.

CHAPTER 7

The following chapter has been published in the Journal World Neurosurgery

(DOI: 10.1016/j.wneu.2018.01.151)

CHAPTER 7

SCANNING FIBER ENDOSCOPE IMPROVES DETECTION OF 5-ALA INDUCED PPIX FLUORESCENCE AT THE BOUNDARY OF INFILTRATIVE GLIOMA

Abstract

Objective: Fluorescence-guided surgery with protoporphyrin IX (PpIX) as a photodiagnostic marker is gaining acceptance for resection of malignant gliomas. Current wide-field imaging technologies do not have sufficient sensitivity to detect low PpIX concentrations. We evaluated a scanning fiber endoscope (SFE) for detection of PpIX fluorescence in gliomas and compared it with an operating microscope (OPMI) equipped with fluorescence module and a benchtop confocal laser scanning microscope (CLSM).

Methods: 5-aminolevulinic acid (5-ALA)-induced PpIX fluorescence was assessed in GL261-Luc2 cells in vitro and in vivo after implantation in mouse brains, at an invading glioma growth stage, simulating residual tumor. Intraoperative fluorescence of high and low PpIX concentrations in normal brain and tumor regions with SFE, OPMI, CLSM, and histopathology were compared.

Results: SFE imaging of PpIX correlated to CLSM at the cellular level. PpIX accumulated in normal brain cells but significantly less than in glioma cells. SFE was more sensitive to accumulated PpIX in fluorescent brain areas than OPMI ($P<.01$) and dramatically increased imaging time (>6×) before tumor-to-background contrast was diminished because of photobleaching.

Conclusions: SFE provides new endoscopic capabilities to view PpIX-fluorescing tumor regions at cellular resolution. SFE may allow accurate 5-ALA application to

gliomas and other tumor types when current detection techniques have failed to provide reliable visualization. SFE was significantly more sensitive than OPMI to low PpIX concentrations, which is relevant to identifying the leading edge or metastasizing cells of malignant glioma or to treating low-grade gliomas. This new application has the potential to benefit surgical outcomes.

Introduction

Surgical removal is the first-line treatment for brain gliomas, and increasing the extent of resection correlates with better survival and quality of life (Hervey-Jumper and Berger 2016). The theranostic implications of fluorescence-guided neurosurgery—increased surgical precision and improved completeness of resection during brain tumor surgery—have been reviewed (Belykh et al. 2016). Specifically, the extent of glioblastoma multiforme resection has substantially improved under aminolevulinic acid (5-ALA)–induced protoporphyrin IX (PpIX) fluorescence guidance (Lau et al. 2016, Nabavi et al. 2009). When administered orally before surgery, 5-ALA metabolizes and accumulates as the photodiagnostic biomarker PpIX within neoplastic tissue. Although high-grade gliomas are usually highly fluorescent, low-grade gliomas show significantly lower PpIX fluorescence, which is detectable in only 9%–15.9% of cases (Widhalm et al. 2013, Jaber et al. 2016). Fluorescence in detectable low-grade diffuse infiltrative gliomas is not observed throughout the tumor mass, but rather mostly in the anaplastic foci, which correlates to increased cell proliferation and malignant potential (Widhalm et al. 2013). Similarly, several studies suggest that PpIX detection using current operating

microscopes is suboptimal and that PpIX accumulates in low-grade gliomas at levels below the detection limit of current systems (Valdes et al. 2015, Valdes et al. 2012, Meza et al. 2015, Kitai et al. 2014). Therefore, improved PpIX detection offers considerable promise for PpIX-guided surgery.

In this study, we assess a scanning fiber endoscope (SFE) for PpIX-guided glioma removal in an animal model of malignant glioma. We also describe the features of in vivo PpIX cellular-level imaging in tumor using SFE technology to identify the leading margin and metastasizing cells in a malignant glioma, and its imaging of tissue in normal brain.

Materials and Methods

SFE Probe

We used an SFE imaging platform integrated with low-power 405-nm diode laser for illumination (Figure 7.1) (Yang et al. 2014, Lee et al. 2010). A piezoelectric actuator sweeps the laser-delivery fiberoptic element in a spiral pattern resulting in a 50°–80° field of view. A concentric ring of 6 light-collection fiberoptics (0.5-mm diameter) relays reflected and fluoresce light to a 3-channel (red, green, and blue [RGB]), wavelength separation, light-detection system. The SFE probe has a 30-Hz imaging frame rate and 20–35 μm optical resolution for probe-to-target distances of 3–8 mm. A real-time image processing algorithm mitigated the autofluorescence level in the red fluorescence channel (Yang et al. 2014). Images were recorded as a single frame of the red channel or as a

color image (8-bit RGB, 608×608 pixels). RGB images with exposure times of 0.2–2.0 seconds were collected using a Canon EOS camera focused on the SFE display screen.

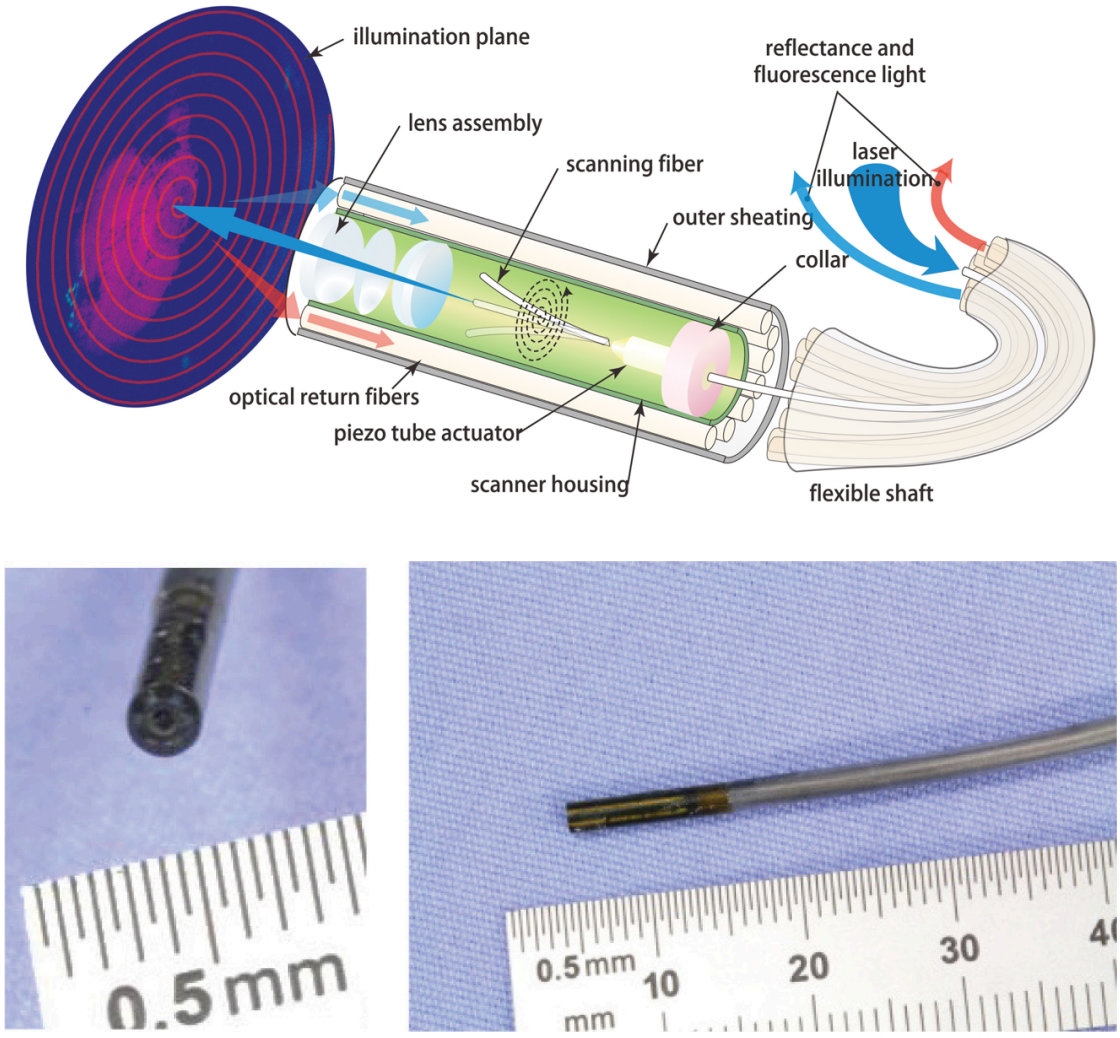

Figure 7.1. Functional diagram (top) and tip (bottom) of the scanning fiber endoscope. (Top) Functional diagram of the scanning fiber endoscope (SFE). The multimodal SFE simultaneously records reflectance and fluorescence images using low-power laser diode illumination sources. The forward-viewing SFE imaging probe consists of a rigid tip on the end of a long flexible shaft (2-3 meters). This rigid tip contains a laser-delivery fiberoptic scanning element sealed with a lens assembly as the central 1-mm diameter

core. A ring of 6 or 12 light collecting optical fibers (for SFE models with an outer diameter of 1.6 and 2.1 mm, respectively) surrounds the scanning element of the SFE. Reflecting and fluorescing light is separated using dichroic filters into 3 channels (red, green, and blue) and is collected by individual photomultiplier tubes. The overall SFE frame rate of 30 Hz is achieved by scanning the 405-nm focused illumination beam at 11-12 kHz in a spiral pattern to a maximum field of view of 50-80 degrees. Although video-frame averaging can be used to enhance signal-to-noise ratio of lower-grade or residual tumors with protoporphyrin IX (PpIX) imaging, no averaging was used in this study. (Bottom) Scanning fiber endoscope (SFE) probe tip. This SFE probe used in this study had a rigid scanning tip with an outer diameter of 2.1 mm and a length of 9 mm. A 405-nm diode laser at 1-6 mW (Model S3FC405, Thorlabs, Inc., Newton, New Jersey) was coupled to the probe's single-scanning illumination fiber, which vibrates at 11.5 kHz. Because transmission losses in illumination fiber and associated optics are about 50%, 0.5-3.0 mW of laser power was scanned over the tissue, with an illumination spot size of 30-50 microns. The desired field of view and fluorescence signal level determined the separation distance between probe tip and tissue, which was typically 3-8 mm for quantitative fluorescence imaging, and up to 30 mm to generate a full view of the mouse brain. The co-registered red-green-blue (RGB) video images were displayed on a 15-inch diagonal color monitor (Dell USA LP, Round Rock, Texas). The optical resolution of the SFE probe used in these experiments was 20, 25, or 35 □m for a probe-to-target distance of 3, 4, or 8 mm, respectively, determined by high-contrast test targets (1951 USAF Contrast Resolution Target, Edmund Optics, Inc., Barrington, New Jersey, USA).

Supplemental top Figure is used with permission from Eric J Seibel, PhD. Supplemental Bottom Figure is used with permission from Barrow Neurological Institute, Phoenix, Arizona.

Operating Microscope

OPMI Pentero 900 (Carl Zeiss Meditec, AG, Oberkochen, Germany) with a BLUE-400 mode was used for imaging (8-bit RGB, 1920×1080 pixels) at a 20-cm distance from the target.

Cell Culture

GL261-Luc2 cells were rendered bioluminescent as described previously (Abdelwahab et al. 2011). Cells were grown in Dulbecco's modified Eagle's medium, containing 10% fetal calf serum, and maintained at 37°C with 5% CO_2. Cells were harvested by trypsinization, washed, and resuspended at a concentration of $1–2\times10^7$ cells/mL in medium without fetal calf serum before implantation in mice.

Animal Tumor Model

C57BL/6 mice (The Jackson Laboratory, Bar Harbor, Maine) were used in accordance with the National Institutes of Health's *Guide for Care and Use of Laboratory Animals* and with approval from the Institutional Animal Care and Use Committee of St. Joseph's Hospital and Medical Center. Intracranial implantation was performed by intraperitoneal injection of xylazine (80 mg/kg) and ketamine (10 mg/kg)

in anesthetized 10-week-old female mice (n=15) following a previously established protocol (Martirosyan et al. 2014), and 2 mice were left without tumors for controls. A GL261-Luc2 cell solution (2 µl of 2.11×10^7 cells/mL) was injected 3 mm below the brain surface. Confirmatory in vivo tumor growth imaging was performed 14 days later with an IVIS Spectrum System (PerkinElmer, Inc., Waltham, MA) (Abdelwahab et al. 2011) (see Figure 7.2 showing IVIS imaging results).

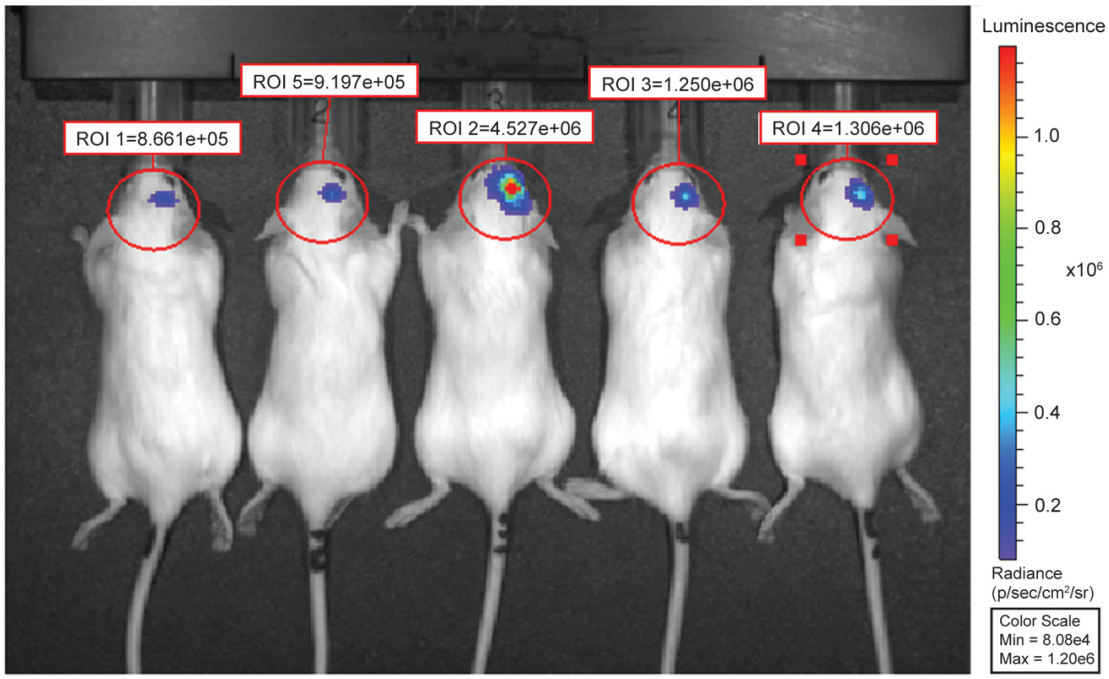

Figure 7.2. Bioluminescence imaging of GL261-Luc2 brain tumors. Representative image shows results of IVIS imaging (IVIS Spectrum; PerkinElmer, Inc., Waltham, MA) confirming the presence of small brain tumors in the mice. Mean signal intensity is calculated for outlined regions of interest (ROI). Used with permission from Barrow Neurological Institute, Phoenix, Arizona.

Animal Surgeries

Animals underwent surgery under anesthesia (80 g/kg xylazine and 10 g/kg ketamine) on days 16–20 post-injection during invading-growth tumor stage as shown on IVIS imaging. Craniotomy, in vivo, and rapid ex vivo imaging with OPMI Pentero and SFE was performed at 2 hours (n=9 implanted, n=2 controls), 3 hours (n=2), 8 hours (n=2), and 24 hours (n=2) after 5-ALA administration (2.5-mg intraperitoneally). The 2-hour post–5-ALA injection start time corresponded to the 2- to 4-hour window used clinically (Ewelt et al. 2011). After surgery, the animals were euthanized according to institutional guidelines. Brains were rapidly removed, sliced in the coronal plane, then imaged ex vivo and further processed.

Brain Specimen Preparation and Histopathologic Imaging

Brains were fixed in 10% formalin, embedded in paraffin, sliced, stained (hematoxylin and eosin [H&E] and Luxol fast blue for myelin) and imaged with an upright Aperio microscopy system (Leica Biosystems, Nussloch, Germany).

For confocal imaging, the brains were fixed in 4% paraformaldehyde and processed using CUBIC protocol (Susaki et al. 2015). All reagents were from Sigma-Aldrich Co., LLC (St. Louis, Missouri).

Confocal Laser Scanning Microscopy (CLSM)

Live-cell imaging was performed in 35-mm glass-bottom dishes (MatTek Corp., Ashland, Massachusetts) in 5% CO_2 at 37°C after 4 mM 5-ALA (NIOPIK, Moscow,

Russia) treatment in culture medium. A 405-nm laser was used for PpIX excitation, along with a 598- to 740-nm detection window. Next, cells were fixed in 4% paraformaldehyde, permeabilized with Triton X-100, and stained with Alexa Fluor 633 Phalloidin (Thermo Fischer Scientific, Waltham, Massachusetts) and 4′,6-diamidino-2-phenylindole (DAPI) following manufacturer recommendations.

Coronal mouse brain slices were stained with acridine orange (AO) and imaged on glass-bottom dishes using 405-nm laser and 635-750-nm detection for PpIX, and 488-nm laser with 493- to 593-nm detection for AO (Martirosyan et al. 2014).

Confocal imaging was performed on an LSM 710 DUO (Carl Zeiss AG, Oberkochen, Germany) using a Plan-Apochromat 20×/0.8 M27 objective and on a Nikon A1+ (Nikon Instruments Inc., NY) using Apo 40×/1.25 water immersion objective (CFI Apo Lambda S 40X WI).

Image Analysis

Image analysis was performed with Fiji software (Schindelin et al. 2012). The fluorescence tumor-to-background and tumor-to-normal brain ratios were calculated from the red channel. Heat-map histograms were displayed using a 16-color linear look-up table of the red channel. Specular reflections in SFE images were removed by subtracting coregistered regions in the green channel from the red channel to avoid false-positive visual interpretation of the PpIX signal. Quantification and analysis of 3-dimensional CLSM images were performed using Imaris (Bitplane, Inc., Belfast, Northern Ireland).

Statistical Analysis

Statistical analysis was performed using Statistica (Dell, Round Rock, Texas). $P<.05$ was selected as a minimal significance value.

Results

SFE is Capable of Visualizing PpIX in Individual Tumor Cells in a Monolayer Culture

After 1 hour of incubation with 5-ALA, SFE imaging detected PpIX fluorescence from individual glioma cells in a monolayer GL261-Luc2 culture (Figure 7.3). Measured PpIX fluorescence intensity was 202.1±23.4 arbitrary units (AU) from the cells and 66.0±17.5 AU from the background region ($P<.01$, Mann-Whitney 2-sided test). Tumor-to-background (T/B) ratio was calculated as 3.1 and matched reported T/B ratio using automatic detection in SFE images (Hu et al. 2017). Background fluorescence intensity was higher with SFE than with the CLSM. However, background noise in SFE images can be further reduced by applying a median filter and integrating multiple frames. Correlative CLSM of live cells incubated with 5-ALA and fixed cells stained for nuclei and cytoskeleton suggested that individual groups of cells and separate single cells were visualized with SFE. Live-cell CLSM showed a rapid increase of PpIX fluorescence intensity within 20-40 minutes after incubation with 5-ALA and a subsequent linear increase in values within 8 hours of observation. PpIX fluorescence from a single layer of glioma cells was not visible in OPMI Pentero (Figure 7.4).

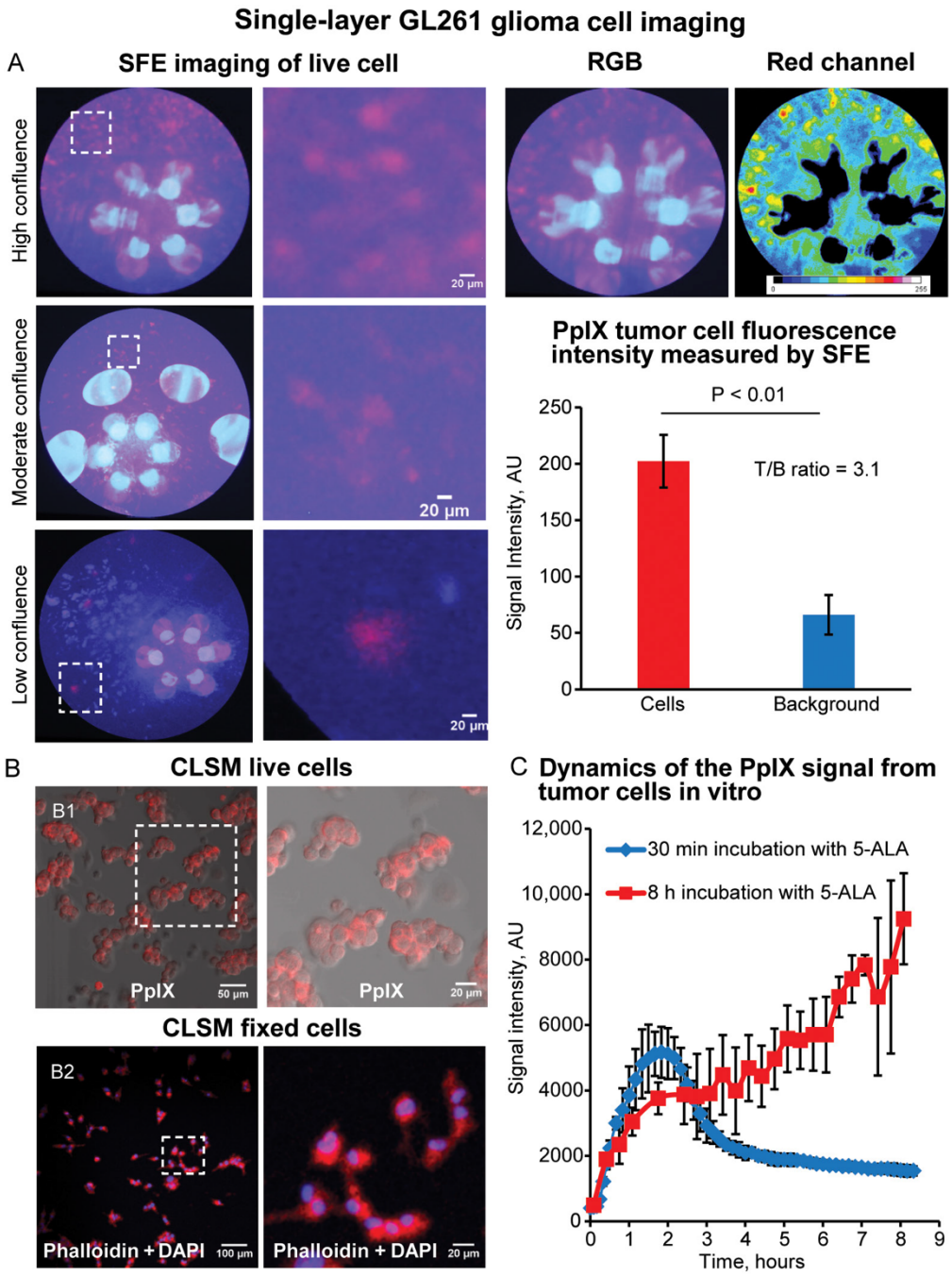

Figure 7.3. In vivo protoporphyrin IX (PpIX) imaging of monolayer GL261 cell culture. (A) Scanning fiber endoscope (SFE) images of individual tumor cells in high-, moderate-, and low-cell-density cell cultures. (B) Confocal laser scanning microscope (CLSM) image of the same culture. Live cells (B1) and cells stained with 4′,6-diamidino-2-

phenylindole (DAPI) and Alexa Fluor 633 Phalloidin (B2). (C) Graph of PpIX fluorescence measured during time-series live-cell imaging of GL261 cells incubated with 5-aminolevulinic acid (5-ALA). Group one was imaged continuously after treatment with 5-ALA. The second group was treated for 30 minutes, washed with phosphate-buffered saline 3 times, and incubated in media for 8 hours. N=3 for each time point at each group. Data are presented as mean and standard deviation. Used with permission from Barrow Neurological Institute, Phoenix, Arizona.

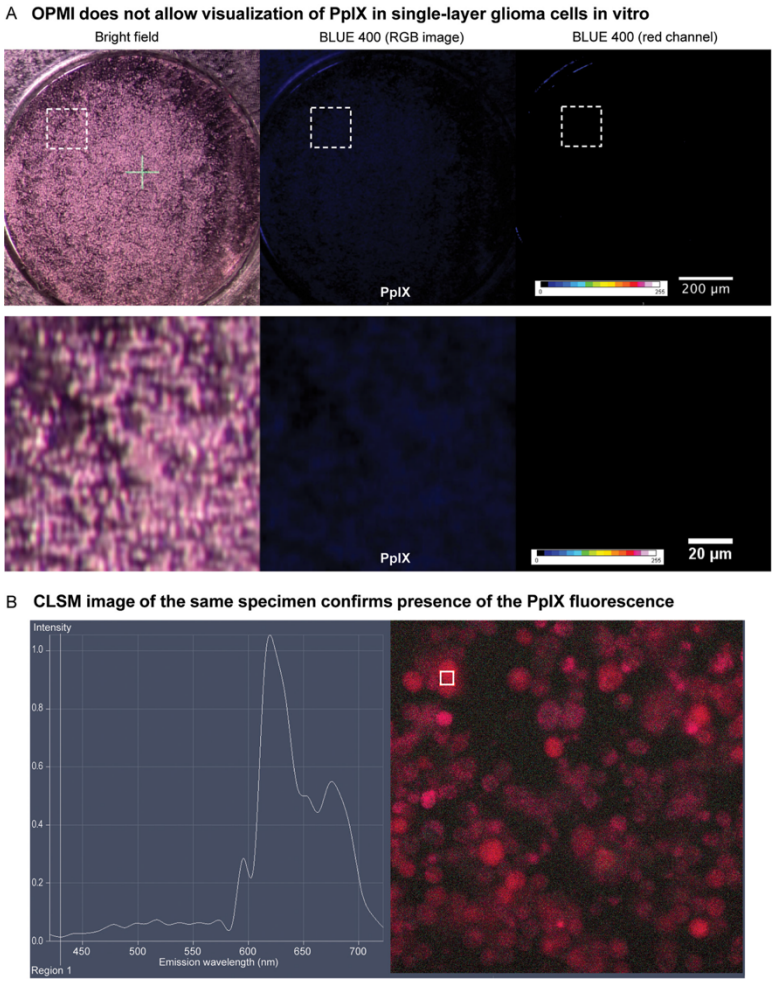

Figure 7.4. The OPMI Pentero did not show protoporphyrin IX (PpIX) fluorescence from a monolayer glioma cell culture (GL261) incubated with 5-aminolevulinic acid (5-ALA).

(A) Representative images taken with the OPMI Pentero in a bright-field and BLUE-400 mode, and a single red channel from the BLUE-400 mode presented in a 16-color look-up table. (B) Confocal laser-scanning microscopy (CLSM) taken in the lambda mode (right) confirms PpIX fluorescence in cells with emission spectra (left). Used with permission from Barrow Neurological Institute, Phoenix, Arizona.

SFE Imaging of PpIX Fluorescence in Normal Brain

SFE imaging of fresh brain slices and correlative histology showed that nuclei of the medulla, pons, cerebellar peduncles, thalamus, and to a lesser degree the hypothalamic nuclei produced increased PpIX signal. Significant fluorescence signal was also detected from the fimbria of the hippocampus and anterior commissure (Figure 7.5). OPMI Pentero showed minimal red signal from the same structures, which was barely distinguishable through oculars. PpIX signal intensities obtained by SFE and the OPMI Pentero from the same areas were correlated (Spearman $\rho = .82$, $P<.05$). The relative PpIX fluorescence intensities from the cerebellar and cerebral cortex areas were low in readings from both SFE and the OPMI Pentero. Overall, SFE showed appreciably higher sensitivity to PpIX in the fluorescent brain areas (30.4±8.8%) compared to the OPMI Pentero (13.3±2.7%), $P<.01$.

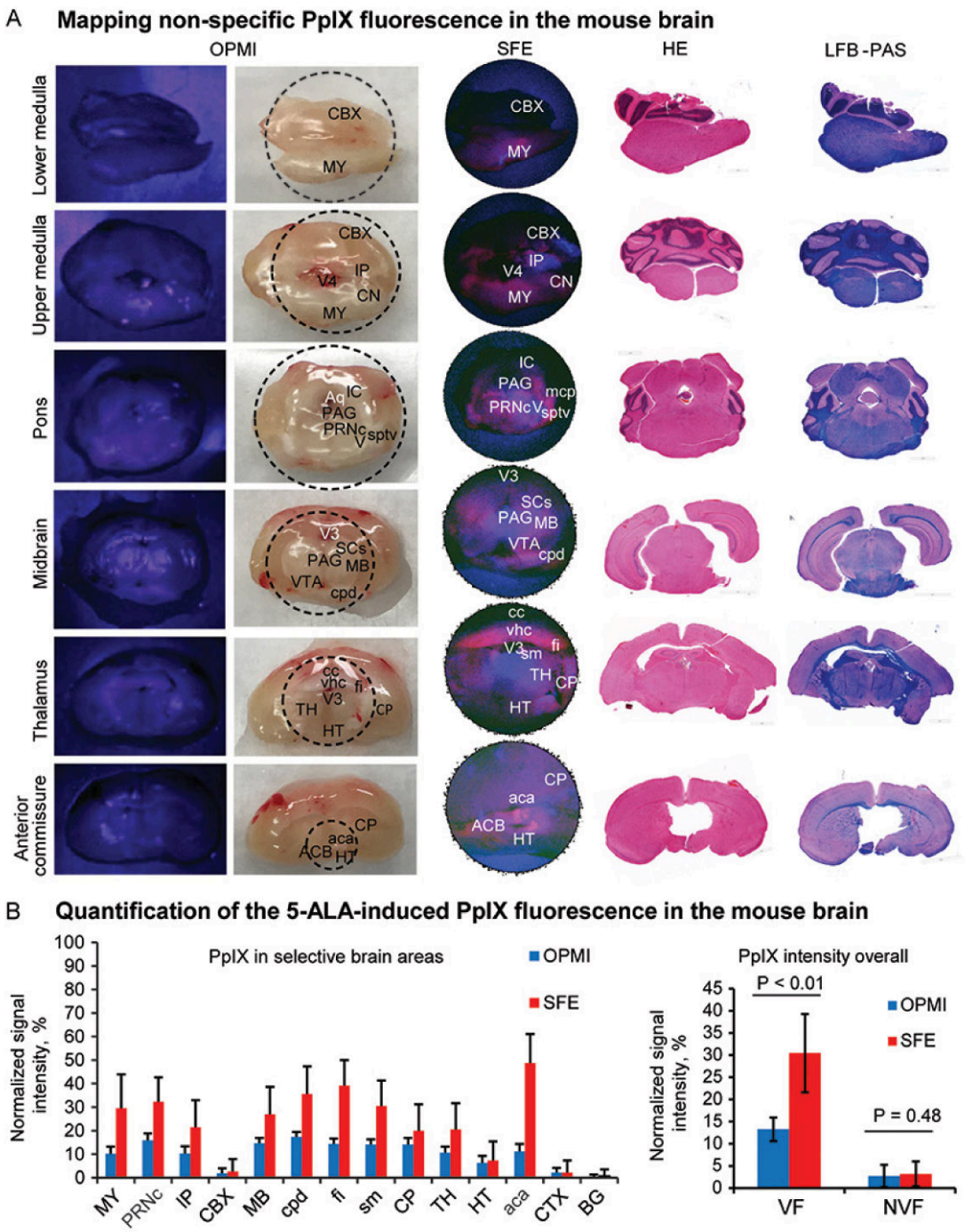

Figure 7.5. Rapid protoporphyrin IX (PpIX) fluorescence mapping in fresh coronal slices of normal mouse brain. (A) Correlative images obtained with the OPMI Pentero BLUE-400 and the scanning fiber endoscope (SFE), with the same sections shown after staining

with hematoxylin and eosin and luxol fast blue–periodic acid-Schiff (LFB-PAS). (B) Quantification of the PpIX signal in various brain regions and comparison (Mann-Whitney U test) of the PpIX signal from areas with no visible fluorescence (NVF) (CBX, TH, CTX, BG areas selected for analysis) and areas with visible fluorescence (VF). Abbreviations: aca, anterior commissure; ACB, nucleus accumbens; Aq, cerebral aqueduct; BG, basal ganglia; CBX, cerebellar cortex; cc, corpus callosum; CN, cochlear nuclei; CP, caudoputamen; cpd, cerebral peduncle; CTX, cerebral cortex; fi, fimbria; HT, hypothalamus; IC, inferior colliculus; IP, interposed nucleus; MB, midbrain; mcp, middle cerebellar peduncle; MY, medulla; PAG, periaqueductal gray; PRNc, pontine reticular nucleus, caudal part; SCs, superior colliculus, sensory related; sm, stria medullaris; sptv, spinal tract of the trigeminal; TH, thalamus; V, nucleus of cranial nerve five; vhc, ventral hippocampal commissure; VTA, ventral tegmental area; V3, third ventricle; V4, fourth ventricle. Used with permission from Barrow Neurological Institute, Phoenix, Arizona.

SFE Imaging of PpIX in Brain Tumors In Vivo

The optimal SFE imaging time period—when the tumor produced the brightest signal and a higher T/B ratio—was within 2-3 hours after 5-ALA administration (Figure 7.6) (Martirosyan et al. 2014, Sroka et al. 1996). Tumor fluorescence was significantly weaker at 8 and 12 hours, with suboptimal T/B ratio (T/B=2). Visible tumor fluorescence bleached faster when it was weak, especially at 8 and 12 hours after 5-ALA administration (see Figure 7.7 demonstrating rapid bleaching of low PpIX signal).

Bleaching was most pronounced at the peripheral tumor areas and occurred gradually over the entire tumor.

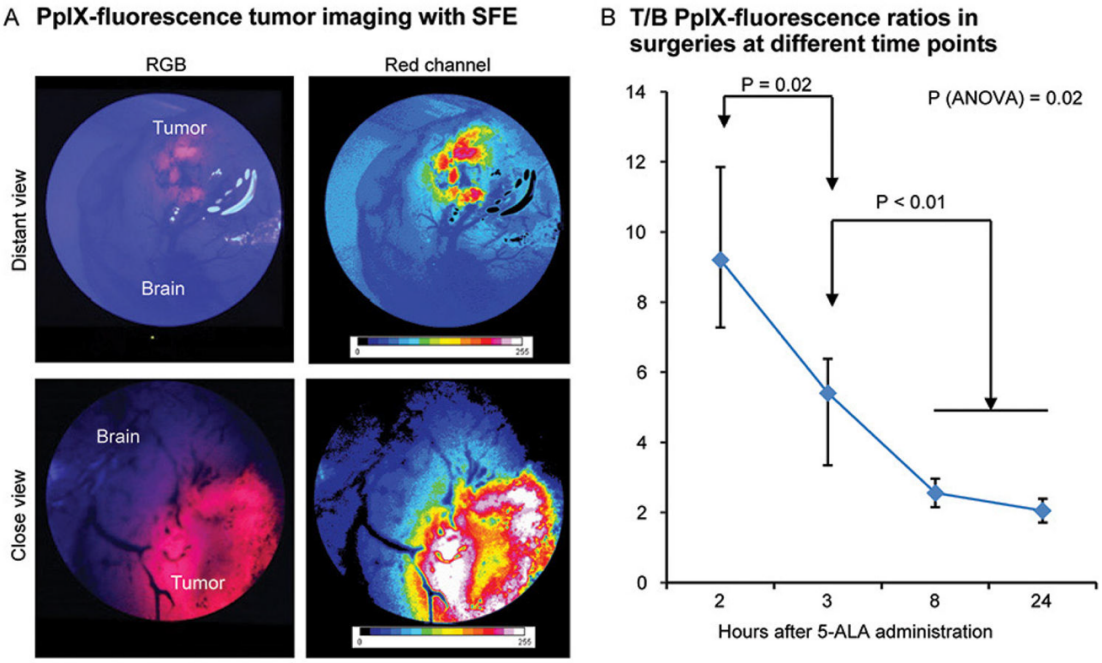

Figure 7.6. Protoporphyrin IX (PpIX) detection in tumor with scanning fiber endoscope (SFE). **(A)** SFE image of mouse brain with tumor visible below cortex. **(B)** Quantification of tumor PpIX fluorescence at different times after 5-aminolevulinic acid injection (n=3 at 2 h, n=6 at 3 h, n=2 at 8 h, and n=2 at 24 h). Kruskal-Wallis analysis of variance (ANOVA) and Mann-Whitney U tests used for comparisons. Data presented as mean and range. RGB, red, green, blue; T/B, tumor-to-brain. *Used with permission from Barrow Neurological Institute, Phoenix, Arizona.*

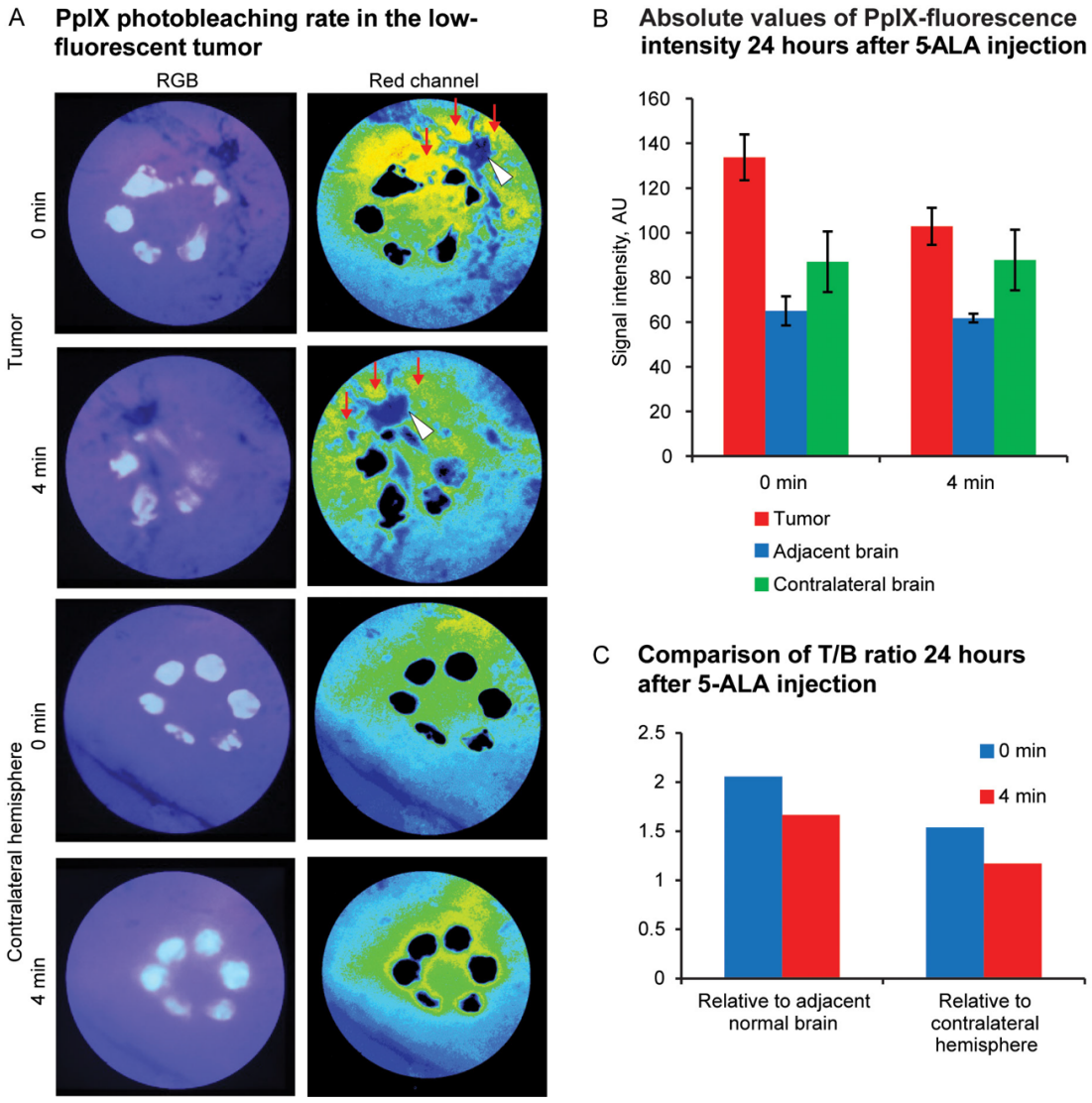

Figure 7.7. Assessment of PpIX tumor fluorescence 24 h after 5-ALA injection. **(A)** Visual investigation using scanning fiber endoscope (SFE) of fresh slice of brain with tumor shows vague low-intensity protoporphyrin IX (PpIX) signal that significantly diminishes within 4 minutes. (Arrowheads *indicate same* abnormally dilated vessel and possible bleeding point within tumor. Red arrows indicate same tumor areas at 0 and 4 minutes.) The 6 bright circles in the left images and the 6 dark circles in the right images are retroreflections from the 6 concentric light-collection fibers. **(B)** Quantification of

fluorescence intensities from tumor core at 0 and 4 minutes of imaging compared to 2 normal brain areas: adjacent brain and contralateral hemisphere. Normal brain shows relatively stable fluorescence, whereas tumor has significantly decreased fluorescence within 4 minutes. **(C)** Tumor-to-normal brain (T/B) ratio significantly decreases after 4 minutes of constant imaging because of PpIX photobleaching in the tumor. A T/B ratio of 2 is suboptimal and a T/B of 1.5 after photobleaching does not allow reliable visual tumor identification. RGB, red-green-blue; 5-ALA, 5-aminolevulenic acid, AU, arbitrary units. Used with permission from Barrow Neurological Institute, Phoenix, Arizona.

SFE Detected Invasive Tumor Areas and Tumor Border

SFE imaging at the higher magnifications permitted visualization of the tumor core and various tumor border patterns (Figure 7.8A-B). Groups of cells, and some individual cells, were identifiable. Dark spots on the fluorescence images corresponded to bleeding points near injured vessels (Figure 7.8C). Necrotic areas exhibited diminished PpIX fluorescence (Figure 7.8D).

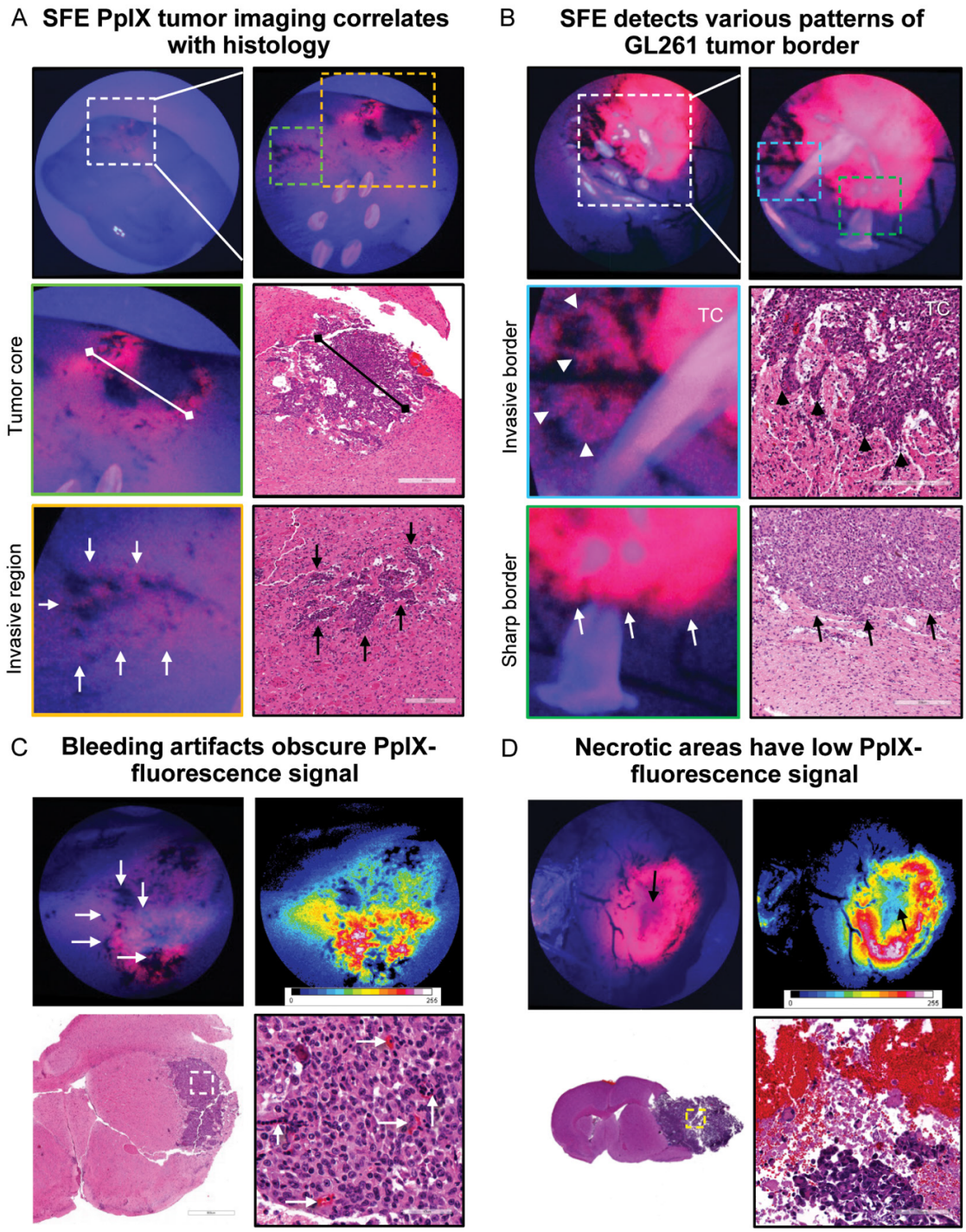

Figure 7.8. Tumor border visualized with scanning fiber endoscope (SFE). **(A)** Representative SFE images of coronal brain cut through tumor core (TC) and correlative hematoxylin-and-eosin (HE)–stained sections. TC size measured on SFE and histological

sections matched. Regions of invasion (*arrows*) are visible as patches of increased protoporphyrin IX (PpIX) signal close to areas of bleeding from abnormal vasculature. The 6 bright circles on the top right-side image are retroreflections from SFE light-collection fibers. **(B)** Invasive border regions with flames of glioma cells penetrating normal brain (*arrowheads*) and noninvasive tumor border regions (*arrows*). **(C)** HE-stained section demonstrates bleeding points associated with tumor microvasculature (*arrows*) corresponding to dark spots on SFE. **(D)** Correlative images illustrate diminished PpIX signal (*arrow*) at necrotic TC. *Used with permission from Barrow Neurological Institute, Phoenix, Arizona.*

Quantification of PpIX Fluorescence at the Tumor Border

We further studied PpIX distribution at the tumor border on fresh and stained mouse brain tissue (Figure 7.9). Most of the strong PpIX fluorescence was detected inside tumor cells. PpIX was also detected extracellularly near the tumor border. Particularly, single-channel CLSM imaging confirmed the presence of the PpIX diffusion gradient from the tumor about 200 μm into the normal brain. This may be accounted for by the gradual signal decrease observed with SFE at the tumor border. Normal brain cells, especially pyramidal-shaped neurons, had accumulated PpIX, but to a significantly lesser degree than tumor cells (Figure 7.9D-E). Further CLSM investigation of cleared specimens stained with AO and imaged up to 400 μm deep confirmed the complex tumor shape associated with invasive tumor fronts and perivascular spread, similar to in vivo SFE imaging.

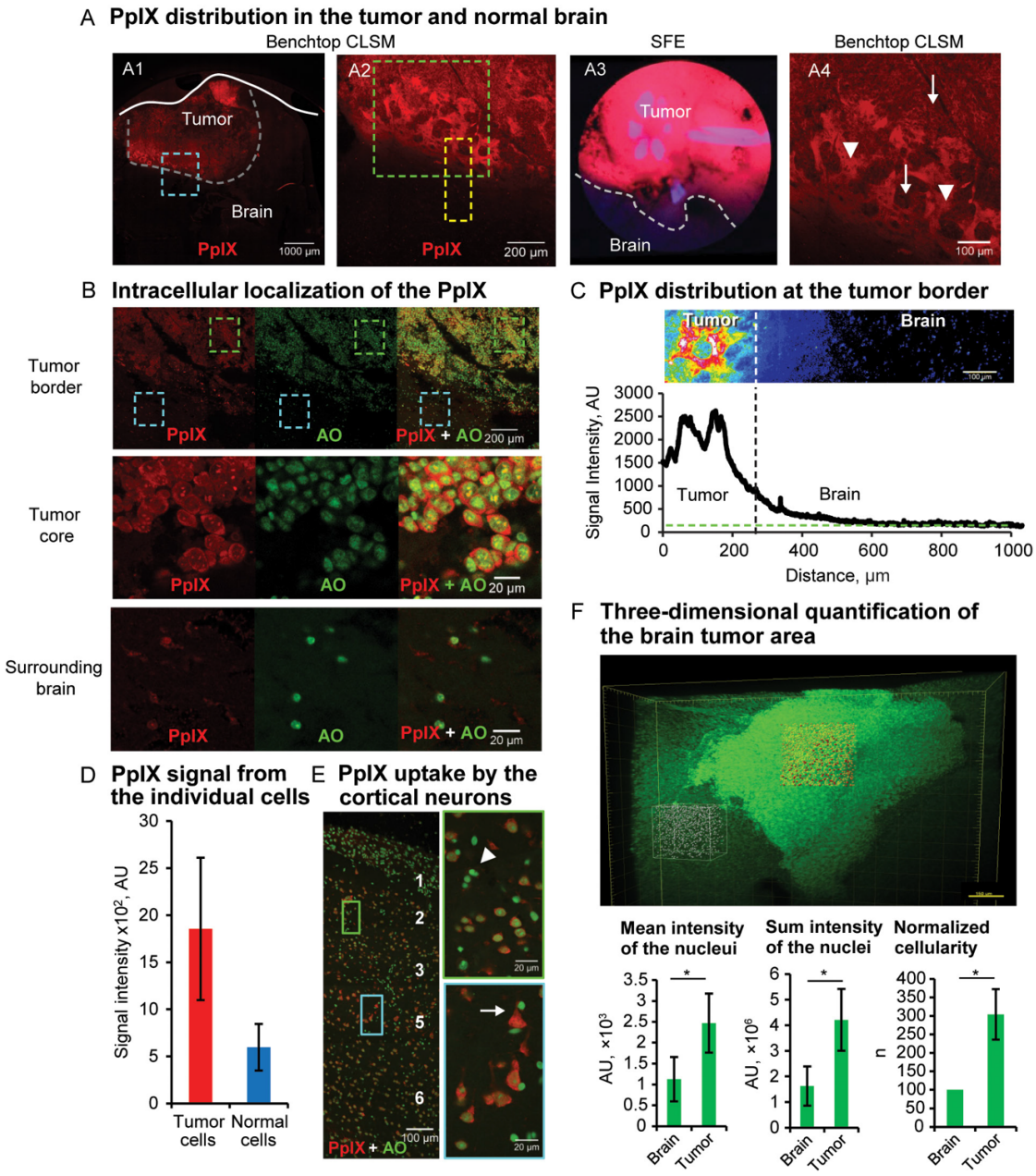

Figure 7.9. Protoporphyrin IX (PpIX) distribution at tumor border. (A) Confocal laser scanning microscope (CLSM) findings for fresh samples correlate to SFE findings. The image in A1 shows PpIX in tumor Blue box denotes tumor border area shown at higher magnification on A2. Comparison of tumor border visualized by the SFE (A3) and CLSM (A4). Green box in A2 denotes area shown in A4; yellow box denotes area used

for quantification in part C. Increased PpIX accumulation is shown in A4 in tumor cells (arrows) and in extracellular regions at border (arrowheads). (B) CLSM images of fresh sample counterstained with acridine orange (AO) confirm intracellular localization of PpIX and significantly lower but detectable accumulation of PpIX in surrounding normal brain cells. Boxes denote areas shown at a higher magnification (green box = tumor core; blue box = surrounding brain). (C) Quantification of the PpIX at tumor border. Green line indicates level of the noise; vertical line delineates tumor border. (D) Quantification of PpIX fluorescence intensity in tumor and normal cells (P<.01 Mann-Whitney U test, n=10 per group). (E) CSLM image of brain cortex 2 hours after 5-aminolevulinic acid administration. Boxes denote cortical layers 2 (green box) and 5 (blue box) shown at higher magnification on right. Neurons, especially large pyramidal cells in layer 5, show a higher PpIX signal than glial cells (arrowhead). (F) Volume image of cleared and AO-stained brain tumor. Boxes denote examples of volumes outlined for quantification shown in graphs (n=3, *P<.01 with Mann-Whitney U test). AU, arbitrary units. Used with permission from Barrow Neurological Institute, Phoenix, Arizona.

Comparison of SFE and Operating Microscope for PpIX Detection

In the small tumors modeling lower-grade tumors, the OPMI Pentero photobleached PpIX before the tumor could be located and brought into focus (~30 seconds to 1 minute) in 3 trial animals. Doubling the 5-ALA dose to 5 mg produced bright lava-like red fluorescence detectable and localizable by both SFE and the OPMI Pentero. To investigate the quantitative difference in PpIX detection, we separately

analyzed time-series images of mouse brain tumors with SFE and the OPMI Pentero. In this experiment, initially highly fluorescent tumors, as well as initially red-pink "average" and low-fluorescent tumors, had significantly longer imaging time (Table 7.1) without noticeable photobleaching under SFE illumination than with OPMI Pentero light exposure (see Figure 7.10 showing dynamic PpIX bleaching).

Table 7.1. Imaging time before loss of PpIX tumor-to-brain contrast.*

Technique	Signal Intensity		
	Low	Moderate	High
OPMI Pentero	<3 min	No data	10-15 min
SFE	20 min	50-60 min	>60 min

Abbreviations: PpIX, protoporphyrin IX; SFE, scanning fiber endoscope.

*Data extrapolated from graphical results of time imaging experiments (see Figure 7.10, showing changes of PpIX signal intensity during imaging).

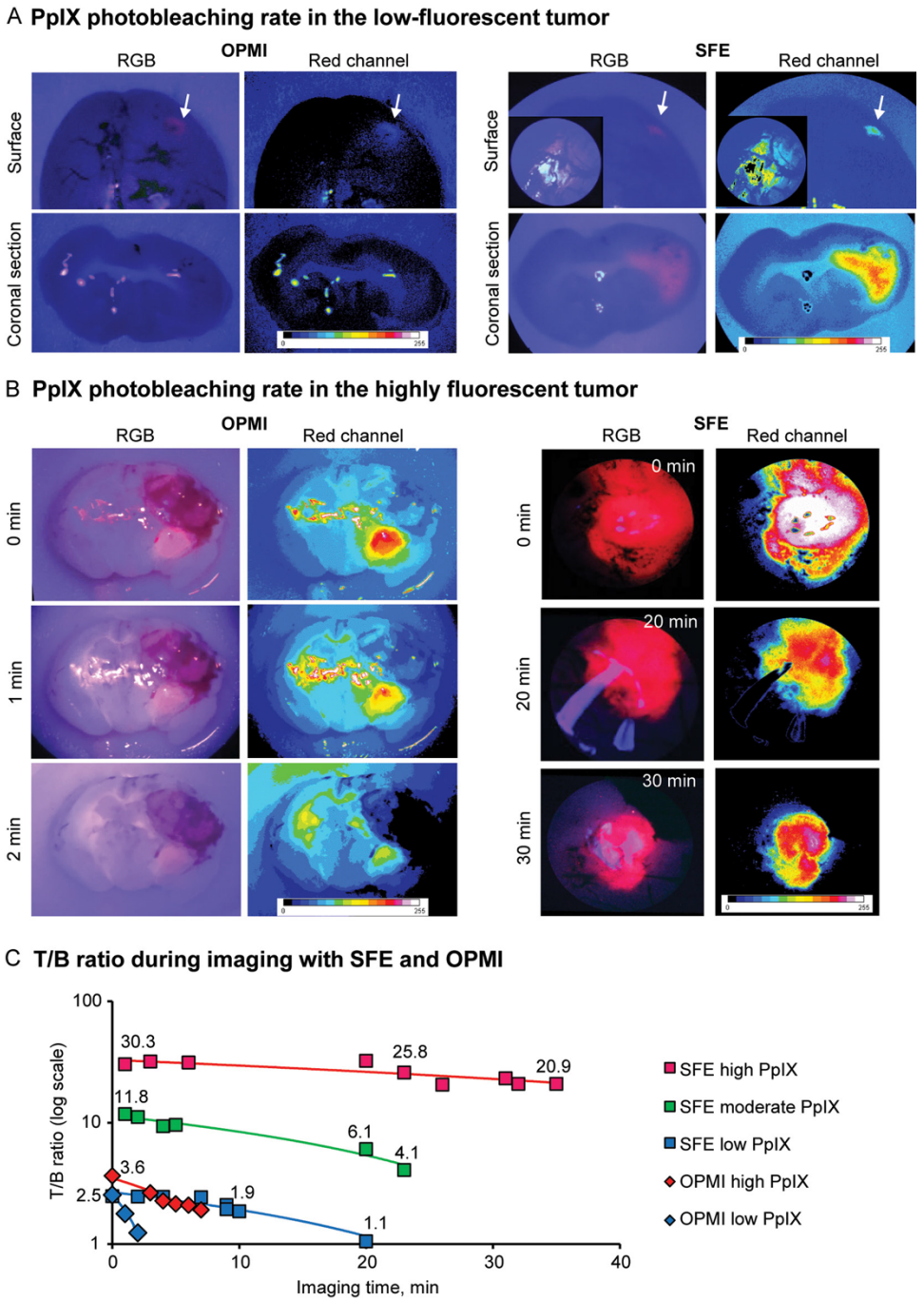

Figure 7.10. Comparison of protoporphyrin IX (PpIX) imaging in experimental gliomas using the OPMI Pentero and scanning fiber endoscope (SFE). (A) Representative images of brain surface obtained for the same fresh brain sample were obtained first with the

OPMI Pentero BLUE-400, then with SFE (arrows indicate tumor signal visible through cortex). Insets at right show magnified view with SFE probe positioned closer to the specimen. Coronal section of same fresh specimen shows low PpIX signal from tumor detectable with SFE but not with the OPMI Pentero. (B) Representative images of highly fluorescent brain tumors (high PpIX) taken at various times during imaging. (C) Quantification of tumor-to-brain (T/B) ratio in samples with varying during continuous imaging with the OPMI Pentero and SFE. Regions for T/B ratio calculation were chosen from tumor core and surrounding non-fluorescent normal brain. High PpIX = double 5-ALA dose (5 mg) 2h post-injection; moderate PpIX = 2.5 mg 5-ALA, 2h post-injection; low PpIX = 2.5 mg 5-ALA 8h and longer post-injection. RGB, red-green-blue. Used with permission from Barrow Neurological Institute, Phoenix, Arizona.

SFE as a Tool for Surgical Visualization

We performed brain tumor removal under PpIX fluorescence guidance with SFE in 2 mice. The SFE probe was fixed in a constant position with a Greenberg retractor and provided sufficient working distance to perform manipulations with microsurgical instruments and a suction device. Surgical access to the main mass, and to border regions of the tumor, was well visualized and guided using SFE imaging of the PpIX signal. Histologic investigation of the samples confirmed complete tumor removal (see Figure 7.11 demonstrating brain histology after tumor removal). SFE provided visualization for microsurgical manipulations comparable to that of other endoscopes used in clinical neurosurgery (Rapp et al. 2014). Decreasing the SFE imaging distance from about 2 cm

to 3 mm provided wide-field to magnified views for efficient detection of areas harboring only a few tumor cells with low PpIX signal for relatively long durations.

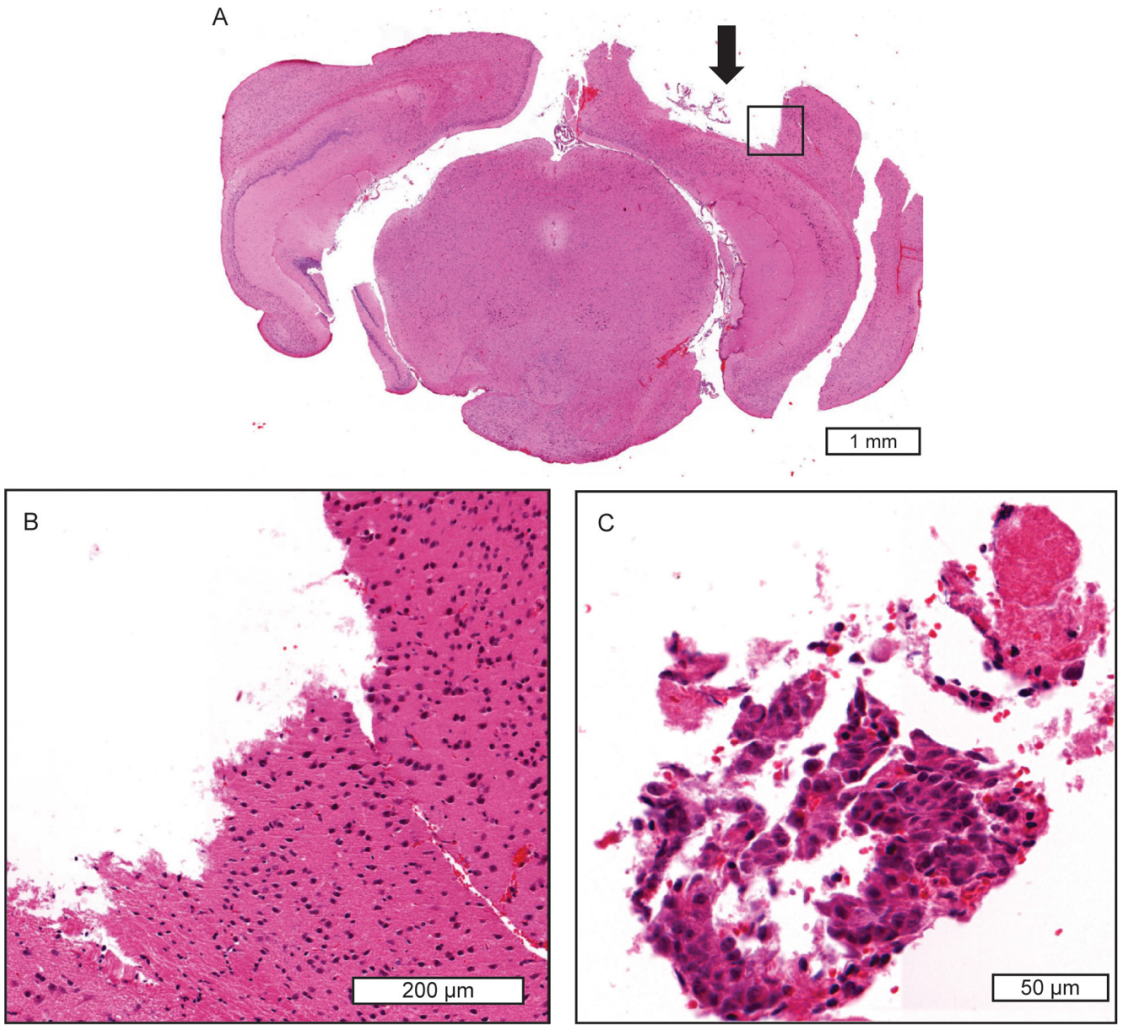

Figure 7.11. Hematoxylin-and-eosin (H&E) staining of mouse brain after surgery shows complete tumor removal. (A) Coronal slice of whole brain at tumor level (*arrow indicates resection cavity*). (B) Resection cavity. (C) H&E stain shows fragment of excised GL261 tumor. *Used with permission from Barrow Neurological Institute, Phoenix, Arizona.*

Discussion

PpIX in the Normal Brain

PpIX distribution in normal rabbit brain was previously mapped with a benchtop CLSM (Olivo and Wilson 2004); however, the study provided only small field images that do not characterize PpIX signal gradient across large brain areas. Here, we mapped PpIX signal distribution in a whole mouse brain using a clinical tool. We observed that PpIX is produced by normal brain cells in the mouse model, but to a lesser extent than by tumor cells. Previous clinical trials found that weak PpIX signal may be visible in non-tumor reactive tissue (Lau et al. 2016, Utsuki et al. 2007, Stummer et al. 2000). Additionally, the operating microscope was limited in detecting low PpIX signal. Moreover, we demonstrated that SFE overcame such limitations and offered a surgically useful visualization tool capable of detecting significantly lower concentrations of PpIX from non-tumor normal brain areas and of successfully differentiating them from PpIX signal obtained from an experimental glioma.

Timing of Imaging Relative to 5-ALA Administration

Although a maximum T/B PpIX fluorescence ratio of 85 was reportedly observed 24 hours after 5-ALA injection (Olivo and Wilson 2004), our study showed that the absolute values of tumor fluorescence intensity are much lower at 24 hours than at the earlier time points. Our in vivo observations demonstrated that tumor fluorescence was maximal at 2 hours post 5-ALA injection, while at 8 and 24 hours it was too low. In the humans the practically useful time for oral 5-ALA administration was define as 3-4 hours

before anesthesia (Potapov et al. 2015, Lau et al. 2016). This may vary in animal models because of the differences in metabolism and pharmacokinetics of 5-ALA. In humans, after oral administration, plasma concentrations of 5-ALA start to rise after 3 hours, peak at 7 hours and slowly decrease to about ½ peak at 12 hours (Webber, Kessel, and Fromm 1997). Concerns about variability in time of peak fluorescence were previously reported for non-brain malignancies (Regula et al. 1995, Webber, Kessel, and Fromm 1997). It should also be noted that dosages of 5-ALA used in the experimental studies are usually higher (100 mg/kg used in this study; 100 mg/kg (Swanson et al. 2015); 20, 100 and 200 mg/kg (Cho et al. 2014); 62.5–125 mg/kg (Fisher et al. 2017)) than that used in humans (20mg/kg). Our observations showed that dosages above 100mg/kg result in bright animal tumor fluorescence subjectively similar to those observed in humans, while higher dosages result in even brighter red fluorescence.

PpIX Detection Sensitivity

We demonstrated that SFE clearly detected PpIX signal from a single layer of tumor cells, which was not possible with the OPMI Pentero, a wide-field surgical visualization. SFE allowed visualization of the tumor border and detection of invading glioma fronts on the cellular level with a low PpIX signal. This unique capability of SFE may be practical for low-concentration 5-ALA clinical protocols (5 mg/kg) (Haj-Hosseini et al. 2015) used for high-grade tumors, as well as for the regular protocol (20 mg/kg) used for low-grade tumors, when detection sensitivity of operating microscopes is not sufficient.

Surgical Tools that Improve PpIX Detection

Several surgical tools have been studied to improve PpIX detection. The optical fiber spectrophotometer showed promise in detecting PpIX spectral signature in tumors, correlating to the OPMI Pentero visual PpIX signal intensity (Stummer et al. 2014, Potapov et al. 2013). Confocal endomicroscopy was reported to provide real-time diagnostic imaging at the cellular level (Foersch et al. 2012, Sankar et al. 2010). However, clinical-grade endomicroscopy systems, designed to work with 488-nm excitable fluorophores (Martirosyan, Eschbacher, et al. 2016), have not proven optimal for PpIX detection (Martirosyan et al. 2014). A common drawback of both spectrophotometer and endomicroscope is their limited field of view. These systems allow for intraoperative "optical biopsy" of a limited number of sites, but are impractical for examining a large resection cavity or an expansive tumor border region. In comparison, non-contact SFE is better for interrogation of large tissue surfaces with a viewing field in a 50 to 80-degree–range cone angle and increased probe-tissue separation distance. Furthermore, real-time quantitative spectral analysis is possible with the SFE platform (Zhang et al. 2013). SFE is a flexible endoscope that allows interrogation of brain areas behind in resection cavities—areas that are inaccessible to operating microscopes and current confocal endomicroscopy systems (Liu, Meza, and Sanai 2014). In this situation, the shorter working distance is practical to guide surgeries that are blocked from straight line-of-sight imaging with surgical microscopes. However, SFE is still an unsophisticated prototype. Large specular reflections can obscure much of

the field of view and require adjustment of the SFE imaging angle or some additional optical filtering.

Photobleaching of PpIX

High-optical power density of the exciting light may result in a loss of fluorescence, which is relevant for PpIX-guided surgery. Our finding of rapid photobleaching of the weak PpIX signal from the low-grade tumor models that were illuminated by the OPMI Pentero BLUE-400 may provide an important clinical insight and explanation of why, besides their lower detection sensitivity, PpIX is rarely visible under operating microscopes in low-grade glial tumors (Jaber et al. 2016). Indeed, improvements in the operating microscopes' signal detection increased the diagnostic accuracy (Valdes et al. 2015). Future clinical applications of SFE may benefit from the >6 times longer imaging without noticeable photobleaching, especially near the tumor border, where fluorescence is weak. This increased duration of imaging is attributed to the shorter time interval and smaller dose of light exposure and may be critical for interrogation of the resection cavity for residual tumor along the margins at the end of the surgical procedure. In the future, the procedure for residual tumor resection can be semiautomated under the surgeon's supervision using a surgical robot with optical guidance from SFE (see Figure 7.12).

SFE had a significantly lower photobleaching rate and longer imaging time suitable for surgical guidance. Photobleaching of PpIX depends on the dose rate (J/cm^2) of the light source, which is substantially higher for the Pentero BLUE-400 than for SFE.

Increased imaging time was especially useful for a low-PpIX fluorescence signal, which is bleached completely under the OPMI Pentero within the first seconds to minutes, whereas SFE visualization was diagnostic for more than 10 minutes. The rapid OPMI Pentero BLUE-400 photobleaching of the PpIX fluorescence fits well with prior measurements taken at equivalent dose rates (Konig et al. 1993, Moan et al. 1997). For example, Moan et al. (Moan et al. 1997) found that the PpIX bleaching dose for 70% destruction in live cancer cell lines is 40 J/cm^2 using a 630-nm light source. The power density of the OPMI is 20 mW/cm^2, or for every minute of exposure, the dose rate was 1.2 J/cm^2 at the 405-nm wavelength. The PpIX absorption coefficient at 630 nm is a factor 33 times less than at 405 nm. Hence, the OPMI Pentero BLUE reaches an equivalent 630 nm dose of 40 J/cm^2 within only 60 seconds. Thus, we expect a majority of cancer cells to go dark in less than a minute.

Photoexcited PpIX not only produces red fluorescence but also transfers energy to produce reactive oxygen. The oxygen singlet state is omnivorous and reacts with both tumor tissue and PpIX. Reaction of the singlet oxygen with tumor tissue is beneficial and is used in photodynamic therapy. Photobleaching of PpIX is predominantly dependent on its reaction with excited singlet-state oxygen (Ericson et al. 2003). The quantity of reactive oxygen depends upon diffusion of ground-state oxygen within the tumor tissue and its energy transfer with photoexcited PpIX. The continuous Pentero BLUE illumination power density is about 10 times greater than the average 405-nm illumination power density of the 30-Hz SFE probe at the shortest working distance.

Hence, the improved lifetime of PpIX fluorescence under SFE illumination is attributed to the shorter time interval (smaller dose) of light exposure.

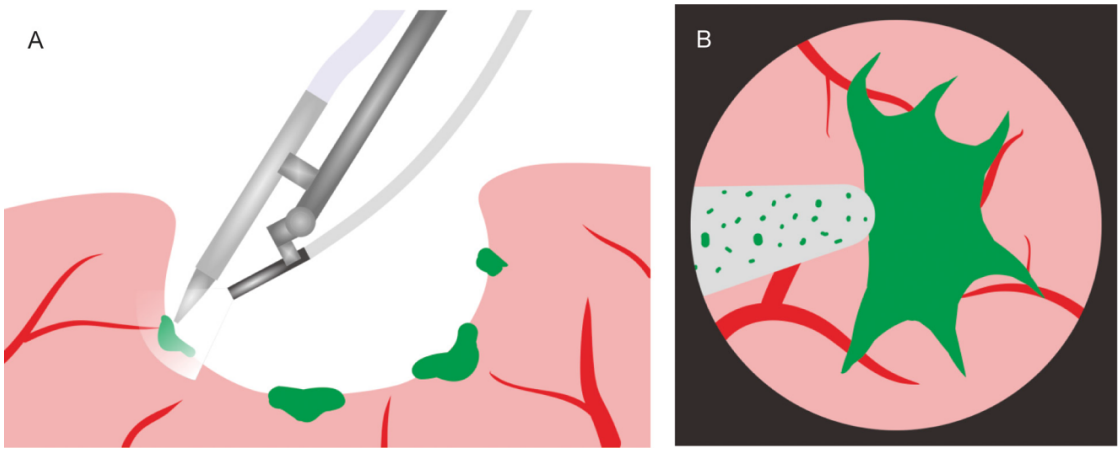

Figure 7.12. Illustration depicting fluorescence-guided robotic–assistance for residual tumor clean-up using the scanning focal endoscope (SFE). (A) Robotic assembly of the SFE and an ultrasonic microsurgical aspirator currently being developed. (B) SFE view of brain tumor and simulated tip of microsurgical aspirator tool. Used with permission from Barrow Neurological Institute, Phoenix, Arizona.

Study Limitations

Although the GL261 tumor model is an invasive syngeneic malignant glial tumor type, the extent of the tumor border observed in this study is less than that usually observed in human invasive gliomas, where the spread is more diffuse. However, no better larger models exist for investigating the PpIX signal in large-scale diffusive borders, except in clinical trials. Further clinical study is warranted to test the diagnostic utility of SFE in human brain tumor surgeries.

A cautionary note is that false-positive PpIX fluorescence in non-tumor abnormal reactive tissue has been reported, which is related to the intrinsic properties of 5-ALA, although healthy normal brain tissue visualized with the OPMI Pentero did not have visible fluorescence (Lau et al. 2016). This is an expected limitation for any wide-field imaging system, including both SFE and the OPMI Pentero. Particularly, our findings demonstrate increased nonspecific PpIX fluorescence in brain areas characterized by increased cellularity, as observed with SFE and CLSM. Therefore, increased tumor cellularity and metabolic activity compared to that in the normal brain are two major factors contributing to the detectable high PpIX signal.

Conclusion

SFE has unique qualities compared to other tools intended to improve the overall efficiency of fluorescence-guided surgery. The significant aspects of this study are the high sensitivity and reduced photobleaching of PpIX with SFE compared to those of the OPMI Pentero operating microscope, which explains the lower effectiveness of fluorescence-guided resection of low-grade gliomas, and problems with using intraoperative guidance for full resection of residual tumor. SFE is the first wide-field surgical imaging tool capable of detecting PpIX fluorescence in individual cells. With SFE, we mapped PpIX fluorescence in the normal brain and identified tumor margins with low PpIX concentrations, not visible with current surgical microscope systems. Finally, SFE provides wide-field visualization that can be used to interrogate large areas of the resection cavity, including the hidden side-wall regions.

References

Abdelwahab, M. G., T. Sankar, M. C. Preul, and A. C. Scheck. 2011. "Intracranial implantation with subsequent 3D in vivo bioluminescent imaging of murine gliomas." *J Vis Exp* (57):e3403. doi: 10.3791/3403.

Belykh, E., N. L. Martirosyan, K. Yagmurlu, E. J. Miller, J. M. Eschbacher, M. Izadyyazdanabadi, L. A. Bardonova, V. A. Byvaltsev, P. Nakaji, and M. C. Preul. 2016. "Intraoperative Fluorescence Imaging for Personalized Brain Tumor Resection: Current State and Future Directions." *Front Surg* 3:55. doi: 10.3389/fsurg.2016.00055.

Cho, H. R., D. H. Kim, D. Kim, P. Doble, D. Bishop, D. Hare, C. K. Park, W. K. Moon, M. H. Han, and S. H. Choi. 2014. "Malignant glioma: MR imaging by using 5-aminolevulinic acid in an animal model." *Radiology* 272 (3):720-30. doi: 10.1148/radiol.14131459.

Ericson, M. B., S. Grapengiesser, F. Gudmundson, A. M. Wennberg, O. Larko, J. Moan, and A. Rosen. 2003. "A spectroscopic study of the photobleaching of protoporphyrin IX in solution." *Lasers Med Sci* 18 (1):56-62. doi: 10.1007/s10103-002-0254-2.

Ewelt, C., F. W. Floeth, J. Felsberg, H. J. Steiger, M. Sabel, K. J. Langen, G. Stoffels, and W. Stummer. 2011. "Finding the anaplastic focus in diffuse gliomas: the value of Gd-DTPA enhanced MRI, FET-PET, and intraoperative, ALA-derived tissue fluorescence." *Clin Neurol Neurosurg* 113 (7):541-7. doi: 10.1016/j.clineuro.2011.03.008.

Fisher, C. J., C. Niu, W. Foltz, Y. Chen, E. Sidorova-Darmos, J. H. Eubanks, and L. Lilge. 2017. "ALA-PpIX mediated photodynamic therapy of malignant gliomas augmented by hypothermia." *PLoS One* 12 (7):e0181654. doi: 10.1371/journal.pone.0181654.

Foersch, S., A. Heimann, A. Ayyad, G. A. Spoden, L. Florin, K. Mpoukouvalas, R. Kiesslich, O. Kempski, M. Goetz, and P. Charalampaki. 2012. "Confocal laser endomicroscopy for diagnosis and histomorphologic imaging of brain tumors in vivo." *PLoS One* 7 (7):e41760. doi: 10.1371/journal.pone.0041760.

Haj-Hosseini, N., J. C. Richter, M. Hallbeck, and K. Wardell. 2015. "Low dose 5-aminolevulinic acid: Implications in spectroscopic measurements during brain tumor surgery." *Photodiagnosis Photodyn Ther* 12 (2):209-14. doi: 10.1016/j.pdpdt.2015.03.004.

Hervey-Jumper, S. L., and M. S. Berger. 2016. "Maximizing safe resection of low- and high-grade glioma." *J Neurooncol* 130 (2):269-282. doi: 10.1007/s11060-016-2110-4.

Hu, D., Y. Jiang, E. Belykh, Y. Gong, M. C. Preul, B. Hannaford, and E. J. Seibel. 2017. "Toward real-time tumor margin identification in image-guided robotic brain tumor resection." *Proc. SPIE 10135, Medical Imaging 2017: Image-Guided Procedures, Robotic Interventions, and Modeling, 101350D (March 3, 2017)*:101350D. doi: 10.1117/12.2255417.

Jaber, M., J. Wolfer, C. Ewelt, M. Holling, M. Hasselblatt, T. Niederstadt, T. Zoubi, M. Weckesser, and W. Stummer. 2016. "The Value of 5-Aminolevulinic Acid in Low-grade Gliomas and High-grade Gliomas Lacking Glioblastoma Imaging Features: An Analysis Based on Fluorescence, Magnetic Resonance Imaging, 18F-Fluoroethyl Tyrosine Positron Emission Tomography, and Tumor Molecular Factors." *Neurosurgery* 78 (3):401-11; discussion 411. doi: 10.1227/NEU.0000000000001020.

Kitai, R., H. Takeuchi, N. Miyoshi, B. Andriana, H. Neishi, N. Hashimoto, and K. Kikuta. 2014. "[Determining the tumor-cell density required for macroscopic observation of 5-ALA-induced fluorescence of protoporphyrin IX in cultured glioma cells and clinical cases]." *No Shinkei Geka* 42 (6):531-6.

Konig, K., H. Schneckenburger, A. Ruck, and R. Steiner. 1993. "In vivo photoproduct formation during PDT with ALA-induced endogenous porphyrins." *J Photochem Photobiol B* 18 (2-3):287-90.

Lau, D., S. L. Hervey-Jumper, S. Chang, A. M. Molinaro, M. W. McDermott, J. J. Phillips, and M. S. Berger. 2016. "A prospective Phase II clinical trial of 5-aminolevulinic acid to assess the correlation of intraoperative fluorescence intensity and degree of histologic cellularity during resection of high-grade gliomas." *J Neurosurg* 124 (5):1300-9. doi: 10.3171/2015.5.JNS1577.

Lee, C. M., C. J. Engelbrecht, T. D. Soper, F. Helmchen, and E. J. Seibel. 2010. "Scanning fiber endoscopy with highly flexible, 1 mm catheterscopes for wide-field, full-color imaging." *J Biophotonics* 3 (5-6):385-407. doi: 10.1002/jbio.200900087.

Liu, J. T., D. Meza, and N. Sanai. 2014. "Trends in fluorescence image-guided surgery for gliomas." *Neurosurgery* 75 (1):61-71. doi: 10.1227/NEU.0000000000000344.

Martirosyan, N. L., J. M. Eschbacher, M. Y. Kalani, J. D. Turner, E. Belykh, R. F. Spetzler, P. Nakaji, and M. C. Preul. 2016. "Prospective evaluation of the utility of intraoperative confocal laser endomicroscopy in patients with brain neoplasms using fluorescein sodium: experience with 74 cases." *Neurosurg Focus* 40 (3):E11. doi: 10.3171/2016.1.FOCUS15559.

Martirosyan, N. L., J. Georges, J. M. Eschbacher, D. D. Cavalcanti, A. M. Elhadi, M. G. Abdelwahab, A. C. Scheck, P. Nakaji, R. F. Spetzler, and M. C. Preul. 2014. "Potential application of a handheld confocal endomicroscope imaging system

using a variety of fluorophores in experimental gliomas and normal brain." *Neurosurg Focus* 36 (2):E16. doi: 10.3171/2013.11.FOCUS13486.

Meza, D., D. Wang, Y. Wang, S. Borwege, N. Sanai, and J. T. Liu. 2015. "Comparing high-resolution microscopy techniques for potential intraoperative use in guiding low-grade glioma resections." *Lasers Surg Med* 47 (4):289-95. doi: 10.1002/lsm.22347.

Moan, J., G. Streckyte, S. Bagdonas, O. Bech, and K. Berg. 1997. "Photobleaching of protoporphyrin IX in cells incubated with 5-aminolevulinic acid." *Int J Cancer* 70 (1):90-7.

Nabavi, A., H. Thurm, B. Zountsas, T. Pietsch, H. Lanfermann, U. Pichlmeier, M. Mehdorn, and A. L. A. Recurrent Glioma Study Group. 2009. "Five-aminolevulinic acid for fluorescence-guided resection of recurrent malignant gliomas: a phase ii study." *Neurosurgery* 65 (6):1070-6; discussion 1076-7. doi: 10.1227/01.NEU.0000360128.03597.C7.

Olivo, M., and B. C. Wilson. 2004. "Mapping ALA-induced PPIX fluorescence in normal brain and brain tumour using confocal fluorescence microscopy." *Int J Oncol* 25 (1):37-45.

Potapov, A. A., S. A. Goriainov, V. B. Loshchenov, T. A. Savel'eva, A. G. Gavrilov, V. A. Okhlopkov, VIu Zhukov, P. V. Zelenkov, D. A. Gol'bin, V. A. Shurkhai, L. V. Shishkina, P. V. Grachev, M. N. Kholodtsova, S. G. Kuz'min, G. N. Vorozhtsov, and A. P. Chumakova. 2013. "[Intraoperative combined spectroscopy (optical biopsy) of cerebral gliomas]." *Zh Vopr Neirokhir Im N N Burdenko* 77 (2):3-10.

Potapov, A. A., S. A. Goryaynov, V. A. Okhlopkov, D. I. Pitskhelauri, G. L. Kobyakov, V. Y. Zhukov, D. A. Gol'bin, D. V. Svistov, B. V. Martynov, A. L. Krivoshapkin, A. S. Gaytan, Y. E. Anokhina, M. D. Varyukhina, M. F. Gol'dberg, A. V. Kondrashov, and A. P. Chumakova. 2015. "[Clinical guidelines for the use of intraoperative fluorescence diagnosis in brain tumor surgery]." *Zh Vopr Neirokhir Im N N Burdenko* 79 (5):91-101. doi: 10.17116/neiro201579591-101.

Rapp, M., M. Kamp, H. J. Steiger, and M. Sabel. 2014. "Endoscopic-assisted visualization of 5-aminolevulinic acid-induced fluorescence in malignant glioma surgery: a technical note." *World Neurosurg* 82 (1-2):e277-9. doi: 10.1016/j.wneu.2013.07.002.

Regula, J., A. J. MacRobert, A. Gorchein, G. A. Buonaccorsi, S. M. Thorpe, G. M. Spencer, A. R. Hatfield, and S. G. Bown. 1995. "Photosensitisation and photodynamic therapy of oesophageal, duodenal, and colorectal tumours using 5 aminolaevulinic acid induced protoporphyrin IX--a pilot study." *Gut* 36 (1):67-75.

Sankar, T., P. M. Delaney, R. W. Ryan, J. Eschbacher, M. Abdelwahab, P. Nakaji, S. W. Coons, A. C. Scheck, K. A. Smith, R. F. Spetzler, and M. C. Preul. 2010. "Miniaturized handheld confocal microscopy for neurosurgery: results in an experimental glioblastoma model." *Neurosurgery* 66 (2):410-7; discussion 417-8. doi: 10.1227/01.NEU.0000365772.66324.6F.

Schindelin, J., I. Arganda-Carreras, E. Frise, V. Kaynig, M. Longair, T. Pietzsch, S. Preibisch, C. Rueden, S. Saalfeld, B. Schmid, J. Y. Tinevez, D. J. White, V. Hartenstein, K. Eliceiri, P. Tomancak, and A. Cardona. 2012. "Fiji: an open-source platform for biological-image analysis." *Nat Methods* 9 (7):676-82. doi: 10.1038/nmeth.2019.

Sroka, R., W. Beyer, L. Gossner, T. Sassy, S. Stocker, and R. Baumgartner. 1996. "Pharmacokinetics of 5-aminolevulinic-acid-induced porphyrins in tumour-bearing mice." *J Photochem Photobiol B* 34 (1):13-9.

Stummer, W., A. Novotny, H. Stepp, C. Goetz, K. Bise, and H. J. Reulen. 2000. "Fluorescence-guided resection of glioblastoma multiforme by using 5-aminolevulinic acid-induced porphyrins: a prospective study in 52 consecutive patients." *J Neurosurg* 93 (6):1003-13. doi: 10.3171/jns.2000.93.6.1003.

Stummer, W., J. C. Tonn, C. Goetz, W. Ullrich, H. Stepp, A. Bink, T. Pietsch, and U. Pichlmeier. 2014. "5-Aminolevulinic acid-derived tumor fluorescence: the diagnostic accuracy of visible fluorescence qualities as corroborated by spectrometry and histology and postoperative imaging." *Neurosurgery* 74 (3):310-9; discussion 319-20. doi: 10.1227/NEU.0000000000000267.

Susaki, E. A., K. Tainaka, D. Perrin, H. Yukinaga, A. Kuno, and H. R. Ueda. 2015. "Advanced CUBIC protocols for whole-brain and whole-body clearing and imaging." *Nat Protoc* 10 (11):1709-27. doi: 10.1038/nprot.2015.085.

Swanson, K. I., P. A. Clark, R. R. Zhang, I. K. Kandela, M. Farhoud, J. P. Weichert, and J. S. Kuo. 2015. "Fluorescent cancer-selective alkylphosphocholine analogs for intraoperative glioma detection." *Neurosurgery* 76 (2):115-23; discussion 123-4. doi: 10.1227/NEU.0000000000000622.

Utsuki, S., H. Oka, S. Sato, S. Shimizu, S. Suzuki, Y. Tanizaki, K. Kondo, Y. Miyajima, and K. Fujii. 2007. "Histological examination of false positive tissue resection using 5-aminolevulinic acid-induced fluorescence guidance." *Neurol Med Chir (Tokyo)* 47 (5):210-3; discussion 213-4.

Valdes, P. A., V. Jacobs, B. T. Harris, B. C. Wilson, F. Leblond, K. D. Paulsen, and D. W. Roberts. 2015. "Quantitative fluorescence using 5-aminolevulinic acid-induced protoporphyrin IX biomarker as a surgical adjunct in low-grade glioma surgery." *J Neurosurg* 123 (3):771-80. doi: 10.3171/2014.12.JNS14391.

Valdes, P. A., F. Leblond, V. L. Jacobs, B. C. Wilson, K. D. Paulsen, and D. W. Roberts. 2012. "Quantitative, spectrally-resolved intraoperative fluorescence imaging." *Sci Rep* 2:798. doi: 10.1038/srep00798.

Webber, J., D. Kessel, and D. Fromm. 1997. "On-line fluorescence of human tissues after oral administration of 5-aminolevulinic acid." *J Photochem Photobiol B* 38 (2-3):209-14.

Widhalm, G., B. Kiesel, A. Woehrer, T. Traub-Weidinger, M. Preusser, C. Marosi, D. Prayer, J. A. Hainfellner, E. Knosp, and S. Wolfsberger. 2013. "5-Aminolevulinic acid induced fluorescence is a powerful intraoperative marker for precise histopathological grading of gliomas with non-significant contrast-enhancement." *PLoS One* 8 (10):e76988. doi: 10.1371/journal.pone.0076988.

Yang, C., V. W. Hou, E. J. Girard, L. Y. Nelson, and E. J. Seibel. 2014. "Target-to-background enhancement in multispectral endoscopy with background autofluorescence mitigation for quantitative molecular imaging." *J Biomed Opt* 19 (7):76014. doi: 10.1117/1.JBO.19.7.076014.

Zhang, L., A. S. Kim, J. S. Ridge, L. Y. Nelson, J. H. Berg, and E. J. Seibel. 2013. "Trimodal detection of early childhood caries using laser light scanning and fluorescence spectroscopy: clinical prototype." *J Biomed Opt* 18 (11):111412. doi: 10.1117/1.JBO.18.11.111412.

CHAPTER 8

DISCUSSION

Recommendations for CLE Use

CLE use requires training for optimal probe operation during surgery and image acquisition. Such training can be performed on what are relatively crude gels impregnated with fluorescent materials or drugs, or is preferably accomplished with *in vivo* models; for example, on experimental brain tumor models in mice. Imaging of *in vivo* models provides cellular structure, the critical information for the neurosurgeon and neuropathologist when making surgical and clinical decisions. While *ex vivo* imaging also demonstrates cellular architecture, these images do not provide information about living tissue—the goal for use of CLE system. Such *ex vivo* imaging has nevertheless been accomplished on large brain slices from swine, and *in vivo* in craniotomy exposures in anesthetized swine (without brain tissue pathological analysis). However, the ideal utility of the CLE system is *in vivo* use.

CLE images are able to provide information on internal tissue microstructure, especially in hypercellular tumor regions, demonstrate microvasculature and blood flow, and many additional histological features that are typically observed in conventional histological slides. However, it must be noted that CLE images show histoarchitectural features slightly differently than they would normally appear on conventional histological slides, and an adjustment period for optimal reading of such images may be required. Furthermore, intravital (e.g., *in vivo* and also very rapid harvest of *ex vivo* tissue) CLE imaging provides additional information regarding cellular movements—a novel imaging

method not previously achievable with conventional histological techniques. Clinicians that use CLE require special training for CLE image interpretation to most beneficially and advantageously use the data provided by *in vivo* confocal microscopy.

When used with fluorescein sodium as a contrast agent, CLE imaging can produce both continuous images and Z-stacks of images. Viewing data sets in a cine-like movie format provides additional information regarding the cellular movements that can better support image interpretation, especially the differentiation of blood cells from the surrounding tissue.

The timing of fluorescent contrast injection is important as the gradient of contrast diffusion across the tissue and through the cellular and nuclear membranes is what creates visible histological features around the extracellular and intracellular structures. Fluorescein sodium leaks through the incompetent blood-brain barrier at the tumor region to create a contrast signal. Fluorescein sodium provides sufficient contrast at about 1-10 minutes after injection when dosed at 2-5 mg/kg. Longer delay after injection is potentially feasible when fluorescein sodium is given at the start of a procedure for wide-field fluorescence navigation, however the fluorescence intensity may not be always sufficient for high quality CLE images.

CLE optical biopsies should be primarily graded as lesional versus non-lesional to provide preliminary information similar to a frozen section analysis and in order to support intraoperative decision making regarding tumor resection. Detailed final histopathological diagnosis is not the goal of the CLE optical biopsies at this point in

time and should continue to be performed with conventional histological techniques to maintain current standards in diagnostic accuracy.

Limitations

The ability of the CLE system to identify histological features of normal human brain tissue requires further study. Unfortunately, there is rarely an appropriate indication to biopsy normal tissue; however, sometimes in functional or epilepsy cases, small resections of cortex are required, and thus CLE imaging could potentially be performed in these areas prior to resection and then correlated to conventional histology afterward. Importantly, there is currently no evidence on the impact of intraoperative CLE on patient care, although its positive impact does seem intuitive; the faster histopathological analysis provided by real-time, high resolution, on-the-fly cellular imaging versus waiting for preparation of a frozen section and consequent analysis would clearly benefit the surgery-pathology operating room work flow. This study provides the premise and necessary information to plan and conduct a clinical study of CLE to address future clinical benefit questions. In the *ex vivo* clinical study, a critical goal was to assess the feasibility of the CLE imaging in this context. Feasibility of CLE during pituitary surgery was analyzed separately from the other intracranial surgeries due to the inherent differences in blood-brain barrier properties of pituitary tissue; as pituitary tissue lacks a blood-brain barrier, differences in how fluorescein contrast highlights the pituitary versus other brain tissues are expected. Future *in vivo* studies on the utility of the CLE system for imaging the pituitary are necessary to demonstrate statistically (with the appropriate

study power) if the diagnostic accuracy is sufficient enough to make this tool clinically useful for transsphenoidal pituitary surgery.

Innovation

This project investigated the utility of the cutting-edge CLE technology, which has already improved workflow in the field of gastrointestinal surgery, for brain pathology (Akarsu and Akarsu 2018).

This project is the first to establish the feasibility of *in vivo* microscopic visualization of brain tumor tissue in the neurosurgical-pathological operating room workflow and especially during the fluorescence-guided procedures.

Based on the results of early animal and human studies, CLE technology has already received 510k clearance for clinical use to visualize internal tissue microstructure during intracranial surgery.

Preclinical experiments confirmed that enhanced optical visualization of the PpIX using the CLE system improves both the duration of useful PpIX imaging and the accuracy in detecting the border of infiltrative tumor.

Overall, a conceptually new approach for pathological imaging and resection planning in neurosurgery was established: obtaining “optical” biopsy of the tissue and analyzing and interpreting the histological image upfront to optimize the following tissue resection.

Future Work

Results of the clinical project demonstrated the high diagnostic accuracy of CLE for identification of the brain tumor tissue, which, on its own, has significant value during surgery. Immediate future work should focus on the assessment of clinical benefits of *in vivo* CLE in terms of improving surgical workflow, extent of lesion resection, integration with other neurosurgical operative visualization technologies, and overall patient outcomes. Specifically, future studies should include not only digital biopsies from the core tumor areas, but also from the areas of normal brain tissue where possible. Assessing the diagnostic features of normal brain tissue with the CLE system is of critical importance to optimizing the sensitivity and negative predictive values of the CLE digital biopsy overall. Such biopsies could potentially be obtained during surgical resection for epilepsy, for example.

After using the generation 2 CLE probe for *in vivo* digital biopsies in animals and in *ex vivo* biopsies in humans, several areas for improvement in probe design have been recognized. First, the probe cable is relatively heavy in comparison to the weight of the handheld probe itself, which creates constant traction on the probe. When holding the probe, some relatively significant effort is necessary to counteract the dragging force of the cable, which freely hangs down from the proximal end of the probe. The probe could be better balanced to improve probe ergonomics and optimize smooth manipulation of the distal probe end. Alternatively, it would be ideal if the probe could be made wireless or if the cable itself could be lighter. Second, the probe tip could be made malleable to allow for easier imaging of less accessible areas at the side of the resection cavity.

Additional practical improvements of CLE could include introduction of digital telepathology; CLE images could theoretically be instantly transferred to a pathologist's workstation or mobile device at any time. This way, pathologist would be able to analyze the CLE data in real-time and provide immediate intraoperative consultation to a surgeon. Another technological advance that could enhance the power an utility of CLE data would be the development and refinement of computer-aided image interpretation using convolutional neural networks on accumulated large clinical CLE image data sets.

Lastly, anticipating the rapid development of new targeted fluorescent probes (Orbay et al. 2013, Chi et al. 2014), the CLE could become a clinical platform for *in vivo* nondestructive visualization and spatial localization of such molecular probes directly in tumor and surrounding brain tissue with cellular resolution. Furthermore, highly sensitive near-view visualization endomicroscopes, like the scanning fiber endoscope, would be particularly advantageous for the detection of fluorescent probes at tumor margins towards the end of surgical resection. The enormous impact that confocal microscopy made on the preclinical biological sciences could be translated into clinical human research *in vivo* and, ultimately, into improvements of patient care.

Abdelwahab, M. G., T. Sankar, M. C. Preul, and A. C. Scheck. 2011. "Intracranial implantation with subsequent 3D in vivo bioluminescent imaging of murine gliomas." *J Vis Exp* (57):e3403. doi: 10.3791/3403.

Absinta, M., S. K. Ha, G. Nair, P. Sati, N. J. Luciano, M. Palisoc, A. Louveau, K. A. Zaghloul, S. Pittaluga, J. Kipnis, and D. S. Reich. 2017. "Human and nonhuman primate meninges harbor lymphatic vessels that can be visualized noninvasively by MRI." *Elife* 6. doi: 10.7554/eLife.29738.

Acerbi, F. 2016. "Fluorescein assistance in neuro-oncological surgery: A trend of the moment or a real technical adjunt?" *Clin Neurol Neurosurg* 144:119-20. doi: 10.1016/j.clineuro.2016.03.011.

Acerbi, F., M. Broggi, G. Broggi, and P. Ferroli. 2015. "What is the best timing for fluorescein injection during surgical removal of high-grade gliomas?" *Acta Neurochir (Wien)* 157 (8):1377-8. doi: 10.1007/s00701-015-2455-z.

Acerbi, F., M. Broggi, M. Eoli, E. Anghileri, C. Cavallo, C. Boffano, R. Cordella, L. Cuppini, B. Pollo, M. Schiariti, S. Visintini, C. Orsi, E. La Corte, G. Broggi, and P. Ferroli. 2014. "Is fluorescein-guided technique able to help in resection of high-grade gliomas?" *Neurosurg Focus* 36 (2):E5. doi: 10.3171/2013.11.FOCUS13487.

Acerbi, F., M. Broggi, K. M. Schebesch, J. Hohne, C. Cavallo, C. De Laurentis, M. Eoli, E. Anghileri, M. Servida, C. Boffano, B. Pollo, M. Schiariti, S. Visintini, C. Montomoli, L. Bosio, E. La Corte, G. Broggi, A. Brawanski, and P. Ferroli. 2018. "Fluorescein-Guided Surgery for Resection of High-Grade Gliomas: A Multicentric Prospective Phase II Study (FLUOGLIO)." *Clin Cancer Res* 24 (1):52-61. doi: 10.1158/1078-0432.CCR-17-1184.

Acerbi, F., C. Cavallo, M. Broggi, R. Cordella, E. Anghileri, M. Eoli, M. Schiariti, G. Broggi, and P. Ferroli. 2014. "Fluorescein-guided surgery for malignant gliomas: a review." *Neurosurg Rev* 37 (4):547-57. doi: 10.1007/s10143-014-0546-6.

Acerbi, F., C. Cavallo, K. M. Schebesch, M. O. Akcakaya, C. de Laurentis, M. K. Hamamcioglu, M. Broggi, A. Brawanski, J. Falco, R. Cordella, P. Ferroli, T. Kiris, and J. Hohne. 2017. "Fluorescein-Guided Resection of Intramedullary

Spinal Cord Tumors: Results from a Preliminary, Multicentric, Retrospective Study." *World Neurosurg* 108:603-609. doi: 10.1016/j.wneu.2017.09.061.

Ackerman, L. V., and G. A. Ramirez. 1959. "The indications for and limitations of frozen section diagnosis; a review of 1269 consecutive frozen section diagnoses." *Br J Surg* 46 (198):336-50.

Akarsu, M., and C. Akarsu. 2018. "Evaluation of New Technologies in Gastrointestinal Endoscopy." *JSLS* 22 (1). doi: 10.4293/JSLS.2017.00053.

Akcakaya, M. O., B. Goker, M. O. Kasimcan, M. K. Hamamcioglu, and T. Kiris. 2017. "Use of Sodium Fluorescein in Meningioma Surgery Performed Under the YELLOW-560 nm Surgical Microscope Filter: Feasibility and Preliminary Results." *World Neurosurg* 107:966-973. doi: 10.1016/j.wneu.2017.07.103.

Ammirati, M., N. Vick, Y. L. Liao, I. Ciric, and M. Mikhael. 1987. "Effect of the extent of surgical resection on survival and quality of life in patients with supratentorial glioblastomas and anaplastic astrocytomas." *Neurosurgery* 21 (2):201-6.

Antila, S., S. Karaman, H. Nurmi, M. Airavaara, M. H. Voutilainen, T. Mathivet, D. Chilov, Z. Li, T. Koppinen, J. H. Park, S. Fang, A. Aspelund, M. Saarma, A. Eichmann, J. L. Thomas, and K. Alitalo. 2017. "Development and plasticity of meningeal lymphatic vessels." *J Exp Med* 214 (12):3645-3667. doi: 10.1084/jem.20170391.

Aubreville, M., C. Knipfer, N. Oetter, C. Jaremenko, E. Rodner, J. Denzler, C. Bohr, H. Neumann, F. Stelzle, and A. Maier. 2017. "Automatic Classification of Cancerous Tissue in Laserendomicroscopy Images of the Oral Cavity using Deep Learning." *Sci Rep* 7 (1):11979. doi: 10.1038/s41598-017-12320-8.

Banu, M. A., J. H. Kim, B. J. Shin, G. F. Woodworth, V. K. Anand, and T. H. Schwartz. 2014. "Low-dose intrathecal fluorescein and etiology-based graft choice in endoscopic endonasal closure of CSF leaks." *Clin Neurol Neurosurg* 116:28-34. doi: 10.1016/j.clineuro.2013.11.006.

Barbosa, B. J., E. D. Mariano, C. M. Batista, S. K. Marie, M. J. Teixeira, C. U. Pereira, M. S. Tatagiba, and G. A. Lepski. 2015. "Intraoperative assistive technologies and extent of resection in glioma surgery: a systematic review of prospective

controlled studies." *Neurosurg Rev* 38 (2):217-26; discussion 226-7. doi: 10.1007/s10143-014-0592-0.

Becker, V., T. Vercauteren, C. H. von Weyhern, C. Prinz, R. M. Schmid, and A. Meining. 2007. "High-resolution miniprobe-based confocal microscopy in combination with video mosaicing (with video)." *Gastrointest Endosc* 66 (5):1001-7. doi: 10.1016/j.gie.2007.04.015.

Behbahaninia, M., N. L. Martirosyan, J. Georges, J. A. Udovich, M. Y. Kalani, B. G. Feuerstein, P. Nakaji, R. F. Spetzler, and M. C. Preul. 2013. "Intraoperative fluorescent imaging of intracranial tumors: a review." *Clin Neurol Neurosurg* 115 (5):517-28. doi: 10.1016/j.clineuro.2013.02.019.

Behling, F., F. Hennersdorf, A. Bornemann, M. Tatagiba, and M. Skardelly. 2016. "5-Aminolevulinic Acid Accumulation in a Cerebral Infarction Mimicking High-Grade Glioma." *World Neurosurg* 92:586 e5-8. doi: 10.1016/j.wneu.2016.05.009.

Belykh, E., C. Cavallo, S. Gandhi, X. Zhao, D. Veljanoski, M. Izady Yazdanabadi, N. L. Martirosyan, V. A. Byvaltsev, J. Eschbacher, M. C. Preul, and P. Nakaji. 2018a. "Utilization of intraoperative confocal laser endomicroscopy in brain tumor surgery." *J Neurosurg Sci*. doi: 10.23736/S0390-5616.18.04553-8.

Belykh, E., C. Cavallo, S. Gandhi, X. Zhao, D. Veljanoski, M. Izady Yazdanabadi, N. L. Martirosyan, V. A. Byvaltsev, J. Eschbacher, M. C. Preul, and P. Nakaji. 2018b. "Utilization of intraoperative confocal laser endomicroscopy in brain tumor surgery." *J Neurosurg Sci* 62 (6):704-717. doi: 10.23736/S0390-5616.18.04553-8.

Belykh, E., N. L. Martirosyan, K. Yagmurlu, E. J. Miller, J. M. Eschbacher, M. Izadyyazdanabadi, L. A. Bardonova, V. A. Byvaltsev, P. Nakaji, and M. C. Preul. 2016. "Intraoperative Fluorescence Imaging for Personalized Brain Tumor Resection: Current State and Future Directions." *Front Surg* 3:55. doi: 10.3389/fsurg.2016.00055.

Belykh, E., E. J. Miller, A. Carotenuto, A. A. Patel, C. Cavallo, N. L. Martirosyan, D. R. Healey, V. A. Byvaltsev, A. C. Scheck, M. T. Lawton, J. M. Eschbacher, P. Nakaji, and M. C. Preul. 2019. "Progress in Confocal Laser Endomicroscopy for Neurosurgery and Technical Nuances for Brain Tumor Imaging With Fluorescein." *Front Oncol* 9:554. doi: 10.3389/fonc.2019.00554.

Belykh, E., E. J. Miller, D. Hu, N. L. Martirosyan, E. C. Woolf, A. C. Scheck, V. A. Byvaltsev, P. Nakaji, L. Y. Nelson, E. J. Seibel, and M. C. Preul. 2018. "Scanning Fiber Endoscope Improves Detection of 5-Aminolevulinic Acid-Induced Protoporphyrin IX Fluorescence at the Boundary of Infiltrative Glioma." *World Neurosurg* 113:e51-e69. doi: 10.1016/j.wneu.2018.01.151.

Belykh, E., E. J. Miller, A. A. Patel, M. I. Yazdanabadi, N. L. Martirosyan, K. Yagmurlu, B. Bozkurt, V. A. Byvaltsev, J. M. Eschbacher, P. Nakaji, and M. C. Preul. 2018. "Diagnostic Accuracy of a Confocal Laser Endomicroscope for In Vivo Differentiation Between Normal Injured And Tumor Tissue During Fluorescein-Guided Glioma Resection: Laboratory Investigation." *World Neurosurg* 115:e337-e348. doi: 10.1016/j.wneu.2018.04.048.

Belykh, E., A. A. Patel, E. J. Miller, B. Bozkurt, K. Yagmurlu, E. C. Woolf, A. C. Scheck, J. M. Eschbacher, P. Nakaji, and M. C. Preul. 2018. "Probe-based three-dimensional confocal laser endomicroscopy of brain tumors: technical note." *Cancer Manag Res* 10:3109-3123. doi: 10.2147/CMAR.S165980.

Belykh, Evgenii, Claudio Cavallo, Xiaochun Zhao, Michael T. Lawton, Peter Nakaji, and Mark C. Preul. 2018. "312 Intraoperative Imaging of Cerebral Vasculature and Blood Flow Using Confocal Laser Endomicroscopy: New Perspectives in Precise Real-Time Brain Fluorescence Microimaging." *Neurosurgery* 65 (CN_suppl_1):126-127. doi: 10.1093/neuros/nyy303.312.

Belykh, Evgenii G., Xiaochun Zhao, Claudio Cavallo, Michael A. Bohl, Kaan Yagmurlu, Joseph L. Aklinski, Vadim A. Byvaltsev, Nader Sanai, Robert F. Spetzler, Michael T. Lawton, Peter Nakaji, and Mark C. Preul. 2018. "Laboratory Evaluation of a Robotic Operative Microscope - Visualization Platform for Neurosurgery." *Cureus*. doi: 10.7759/cureus.3072.

Belykh, Evgenii, Arpan A. Patel, Eric J. Miller, Baran Bozkurt, Kaan Yağmurlu, Eric C. Woolf, Adrienne C. Scheck, Jennifer M. Eschbacher, Peter Nakaji, and Mark C. Preul. 2018. "Probe-based three-dimensional confocal laser endomicroscopy of brain tumors: technical note." *Cancer Management and Research* Volume 10:3109-3123. doi: 10.2147/cmar.s165980.

Benias, P. C., R. G. Wells, B. Sackey-Aboagye, H. Klavan, J. Reidy, D. Buonocore, M. Miranda, S. Kornacki, M. Wayne, D. L. Carr-Locke, and N. D. Theise. 2018. "Structure and Distribution of an Unrecognized Interstitium in Human Tissues." *Sci Rep* 8 (1):4947. doi: 10.1038/s41598-018-23062-6.

Bongetta, D., C. Zoia, R. Pugliese, D. Adinolfi, V. Silvani, and P. Gaetani. 2016. "Low-Cost Fluorescein Detection System for High-Grade Glioma Surgery." *World Neurosurg* 88:54-8. doi: 10.1016/j.wneu.2016.01.017.

Bossuyt, P. M., J. B. Reitsma, D. E. Bruns, C. A. Gatsonis, P. P. Glasziou, L. Irwig, J. G. Lijmer, D. Moher, D. Rennie, H. C. de Vet, H. Y. Kressel, N. Rifai, R. M. Golub, D. G. Altman, L. Hooft, D. A. Korevaar, J. F. Cohen, and Stard Group. 2015a. "STARD 2015: an updated list of essential items for reporting diagnostic accuracy studies." *BMJ* 351:h5527. doi: 10.1136/bmj.h5527.

Bossuyt, P. M., J. B. Reitsma, D. E. Bruns, C. A. Gatsonis, P. P. Glasziou, L. Irwig, J. G. Lijmer, D. Moher, D. Rennie, H. C. de Vet, H. Y. Kressel, N. Rifai, R. M. Golub, D. G. Altman, L. Hooft, D. A. Korevaar, J. F. Cohen, and Stard Group. 2015b. "STARD 2015: an updated list of essential items for reporting diagnostic accuracy studies." *Radiology* 277 (3):826-32. doi: 10.1148/radiol.2015151516.

Brommeland, T., S. Lindal, B. Straume, I. L. Dahl, and R. Hennig. 2003. "Does imprint cytology of brain tumours improve intraoperative diagnoses?" *Acta Neurol Scand* 108 (3):153-6. doi: 10.1034/j.1600-0404.2003.00115.x.

Buderer, N. M. 1996. "Statistical methodology: I. Incorporating the prevalence of disease into the sample size calculation for sensitivity and specificity." *Acad Emerg Med* 3 (9):895-900. doi: 10.1111/j.1553-2712.1996.tb03538.x.

Catapano, G., F. G. Sgulo, V. Seneca, G. Lepore, L. Columbano, and G. di Nuzzo. 2017. "Fluorescein-Guided Surgery for High-Grade Glioma Resection: An Intraoperative "Contrast-Enhancer"." *World Neurosurg* 104:239-247. doi: 10.1016/j.wneu.2017.05.022.

Chan, D. T., S. Y. Hsieh, C. K. Lau, M. K. Kam, H. H. Loong, W. K. Tsang, D. M. Poon, and W. S. Poon. 2017. "Ten-year review of survival and management of malignant glioma in Hong Kong." *Hong Kong Med J* 23 (2):134-9. doi: 10.12809/hkmj164879.

Charalampaki, P., M. Javed, S. Daali, H. J. Heiroth, A. Igressa, and F. Weber. 2015. "Confocal Laser Endomicroscopy for Real-time Histomorphological Diagnosis: Our Clinical Experience With 150 Brain and Spinal Tumor Cases." *Neurosurgery* 62 Suppl 1:171-6. doi: 10.1227/NEU.0000000000000805.

Charalampaki, P., M. Nakamura, D. Athanasopoulos, and A. Heimann. 2019. "Confocal-Assisted Multispectral Fluorescent Microscopy for Brain Tumor Surgery." *Front Oncol* 9:583. doi: 10.3389/fonc.2019.00583.

Chen, B., H. Wang, P. Ge, J. Zhao, W. Li, H. Gu, G. Wang, Y. Luo, and D. Chen. 2012. "Gross total resection of glioma with the intraoperative fluorescence-guidance of fluorescein sodium." *Int J Med Sci* 9 (8):708-14. doi: 10.7150/ijms.4843.

Chi, C., Y. Du, J. Ye, D. Kou, J. Qiu, J. Wang, J. Tian, and X. Chen. 2014. "Intraoperative imaging-guided cancer surgery: from current fluorescence molecular imaging methods to future multi-modality imaging technology." *Theranostics* 4 (11):1072-84. doi: 10.7150/thno.9899.

Cho, H. R., D. H. Kim, D. Kim, P. Doble, D. Bishop, D. Hare, C. K. Park, W. K. Moon, M. H. Han, and S. H. Choi. 2014. "Malignant glioma: MR imaging by using 5-aminolevulinic acid in an animal model." *Radiology* 272 (3):720-30. doi: 10.1148/radiol.14131459.

Cho, S. S., J. Jeon, L. Buch, S. Nag, M. Nasrallah, P. S. Low, M. S. Grady, S. Singhal, and J. Y. K. Lee. 2018. "Intraoperative near-infrared imaging with receptor-specific versus passive delivery of fluorescent agents in pituitary adenomas." *J Neurosurg*:1-11. doi: 10.3171/2018.7.jns181642.

Cho, S. S., and J. Y. K. Lee. 2019. "Intraoperative Fluorescent Visualization of Pituitary Adenomas." *Neurosurg Clin N Am* 30 (4):401-412. doi: 10.1016/j.nec.2019.05.002.

Cho, S. S., R. Salinas, E. De Ravin, C. W. Teng, C. Li, K. G. Abdullah, L. Buch, J. Hussain, F. Ahmed, J. Dorsey, S. Mohan, S. Brem, S. Singhal, and J. Y. K. Lee. 2019. "Near-Infrared Imaging with Second-Window Indocyanine Green in Newly Diagnosed High-Grade Gliomas Predicts Gadolinium Enhancement on Postoperative Magnetic Resonance Imaging." *Mol Imaging Biol*. doi: 10.1007/s11307-019-01455-x.

Cho, S. S., R. Salinas, and J. Y. K. Lee. 2019. "Indocyanine-Green for Fluorescence-Guided Surgery of Brain Tumors: Evidence, Techniques, and Practical Experience." *Front Surg* 6:11. doi: 10.3389/fsurg.2019.00011.

Cho, S. S., R. Zeh, J. T. Pierce, J. Jeon, M. Nasrallah, N. D. Adappa, J. N. Palmer, J. G. Newman, C. White, J. Kharlip, P. Snyder, P. Low, S. Singhal, M. S. Grady, and J. Y. K. Lee. 2019. "Folate Receptor Near-Infrared Optical Imaging Provides Sensitive and Specific Intraoperative Visualization of Nonfunctional Pituitary Adenomas." *Oper Neurosurg (Hagerstown)* 16 (1):59-70. doi: 10.1093/ons/opy034.

Ciezka, M., M. Acosta, C. Herranz, J. M. Canals, M. Pumarola, A. P. Candiota, and C. Arus. 2016. "Development of a transplantable glioma tumour model from genetically engineered mice: MRI/MRS/MRSI characterisation." *J Neurooncol* 129 (1):67-76. doi: 10.1007/s11060-016-2164-3.

Croce, A. C., and G. Bottiroli. 2014. "Autofluorescence spectroscopy and imaging: a tool for biomedical research and diagnosis." *Eur J Histochem* 58 (4):2461. doi: 10.4081/ejh.2014.2461.

Czabanka, M., P. Pena-Tapia, G. A. Schubert, J. Woitzik, P. Horn, P. Schmiedek, and P. Vajkoczy. 2009. "Clinical implications of cortical microvasculature in adult Moyamoya disease." *J Cereb Blood Flow Metab* 29 (8):1383-7. doi: 10.1038/jcbfm.2009.69.

Czabanka, M., P. Pena-Tapia, G. A. Schubert, J. Woitzik, P. Vajkoczy, and P. Schmiedek. 2008. "Characterization of cortical microvascularization in adult moyamoya disease." *Stroke* 39 (6):1703-9. doi: 10.1161/STROKEAHA.107.501759.

D'Amico, R. S., Z. K. Englander, P. Canoll, and J. N. Bruce. 2017. "Extent of Resection in Glioma-A Review of the Cutting Edge." *World Neurosurg* 103:538-549. doi: 10.1016/j.wneu.2017.04.041.

Da Mesquita, S., A. Louveau, A. Vaccari, I. Smirnov, R. C. Cornelison, K. M. Kingsmore, C. Contarino, S. Onengut-Gumuscu, E. Farber, D. Raper, K. E. Viar, R. D. Powell, W. Baker, N. Dabhi, R. Bai, R. Cao, S. Hu, S. S. Rich, J. M. Munson, M. B. Lopes, C. C. Overall, S. T. Acton, and J. Kipnis. 2018. "Functional aspects of meningeal lymphatics in ageing and Alzheimer's disease." *Nature* 560 (7717):185-191. doi: 10.1038/s41586-018-0368-8.

Devaux, B. C., J. R. O'Fallon, and P. J. Kelly. 1993. "Resection, biopsy, and survival in malignant glial neoplasms. A retrospective study of clinical parameters, therapy, and outcome." *J Neurosurg* 78 (5):767-75. doi: 10.3171/jns.1993.78.5.0767.

Diaz, R. J., R. R. Dios, E. M. Hattab, K. Burrell, P. Rakopoulos, N. Sabha, C. Hawkins, G. Zadeh, J. T. Rutka, and A. A. Cohen-Gadol. 2015. "Study of the biodistribution of fluorescein in glioma-infiltrated mouse brain and histopathological correlation of intraoperative findings in high-grade gliomas resected under fluorescein fluorescence guidance." *J Neurosurg* 122 (6):1360-9. doi: 10.3171/2015.2.JNS132507.

Duffau, H. 2019. "Surgery for Malignant Brain Gliomas: Fluorescence-Guided Resection or Functional-Based Resection?" *Front Surg* 6:21. doi: 10.3389/fsurg.2019.00021.

Emanuelli, E., L. Milanese, M. Rossetto, D. Cazzador, E. d'Avella, T. Volo, V. Baro, L. Denaro, G. Gioffre, D. Borsetto, and A. Martini. 2015. "The endoscopic endonasal approach for cerebrospinal fluid leak repair in the elderly." *Clin Neurol Neurosurg* 132:21-5. doi: 10.1016/j.clineuro.2015.02.013.

Ericson, M. B., S. Grapengiesser, F. Gudmundson, A. M. Wennberg, O. Larko, J. Moan, and A. Rosen. 2003. "A spectroscopic study of the photobleaching of protoporphyrin IX in solution." *Lasers Med Sci* 18 (1):56-62. doi: 10.1007/s10103-002-0254-2.

Eschbacher, J. M., J. F. Georges, E. Belykh, M. I. Yazdanabadi, N. L. Martirosyan, E. Szeto, C. Y. Seiler, M. A. Mooney, J. K. Daniels, K. Y. Goehring, K. R. Van Keuren-Jensen, M. C. Preul, S. W. Coons, S. Mehta, and P. Nakaji. 2017. "Immediate Label-Free Ex Vivo Evaluation of Human Brain Tumor Biopsies With Confocal Reflectance Microscopy." *J Neuropathol Exp Neurol* 76 (12):1008-1022. doi: 10.1093/jnen/nlx089.

Eschbacher, J., N. L. Martirosyan, P. Nakaji, N. Sanai, M. C. Preul, K. A. Smith, S. W. Coons, and R. F. Spetzler. 2012. "In vivo intraoperative confocal microscopy for real-time histopathological imaging of brain tumors." *J Neurosurg* 116 (4):854-60. doi: 10.3171/2011.12.JNS11696.

Evans, C. O., P. Reddy, D. J. Brat, E. B. O'Neill, B. Craige, V. L. Stevens, and N. M. Oyesiku. 2003. "Differential expression of folate receptor in pituitary adenomas." *Cancer Res* 63 (14):4218-24.

Evans, C. O., C. Yao, D. Laborde, and N. M. Oyesiku. 2008. "Folate receptor expression in pituitary adenomas cellular and molecular analysis." *Vitam Horm* 79:235-66. doi: 10.1016/s0083-6729(08)00408-1.

Ewelt, C., F. W. Floeth, J. Felsberg, H. J. Steiger, M. Sabel, K. J. Langen, G. Stoffels, and W. Stummer. 2011. "Finding the anaplastic focus in diffuse gliomas: the value of Gd-DTPA enhanced MRI, FET-PET, and intraoperative, ALA-derived tissue fluorescence." *Clin Neurol Neurosurg* 113 (7):541-7. doi: 10.1016/j.clineuro.2011.03.008.

Falco, J., C. Cavallo, I. G. Vetrano, C. de Laurentis, L. Siozos, M. Schiariti, M. Broggi, P. Ferroli, and F. Acerbi. 2019. "Fluorescein Application in Cranial and Spinal Tumors Enhancing at Preoperative MRI and Operated With a Dedicated Filter on the Surgical Microscope: Preliminary Results in 279 Patients Enrolled in the FLUOCERTUM Prospective Study." *Front Surg* 6:49. doi: 10.3389/fsurg.2019.00049.

Feindel, W., Y. L. Yamamoto, and C. P. Hodge. 1967. "Intracarotid fluorescein angiography: a new method for examination of the epicerebral circulation in man." *Can Med Assoc J* 96 (1):1-7.

Felisati, G., A. Bianchi, P. Lozza, and S. Portaleone. 2008. "Italian multicentre study on intrathecal fluorescein for craniosinusal fistulae." *Acta Otorhinolaryngol Ital* 28 (4):159-63.

Fenton, K. E., N. L. Martirosyan, M. G. Abdelwahab, S. W. Coons, M. C. Preul, and A. C. Scheck. 2014. "In vivo visualization of GL261-luc2 mouse glioma cells by use of Alexa Fluor-labeled TRP-2 antibodies." *Neurosurg Focus* 36 (2):E12. doi: 10.3171/2013.12.focus13488.

Fisher, C. J., C. Niu, W. Foltz, Y. Chen, E. Sidorova-Darmos, J. H. Eubanks, and L. Lilge. 2017. "ALA-PpIX mediated photodynamic therapy of malignant gliomas augmented by hypothermia." *PLoS One* 12 (7):e0181654. doi: 10.1371/journal.pone.0181654.

Foersch, S., A. Heimann, A. Ayyad, G. A. Spoden, L. Florin, K. Mpoukouvalas, R. Kiesslich, O. Kempski, M. Goetz, and P. Charalampaki. 2012. "Confocal laser endomicroscopy for diagnosis and histomorphologic imaging of brain tumors in vivo." *PLoS One* 7 (7):e41760. doi: 10.1371/journal.pone.0041760.

Folaron, M., R. Strawbridge, K. S. Samkoe, C. Filan, D. W. Roberts, and S. C. Davis. 2018a. "Elucidating the kinetics of sodium fluorescein for fluorescence-guided surgery of glioma." *J Neurosurg*:1-11. doi: 10.3171/2018.4.JNS172644.

Folaron, Margaret, Rendall Strawbridge, Kimberley S. Samkoe, Caroline Filan, David W. Roberts, and Scott C. Davis. 2018b. "Elucidating the kinetics of sodium fluorescein for fluorescence-guided surgery of glioma." *Journal of Neurosurgery*:1-11. doi: 10.3171/2018.4.jns172644.

Forest, F., E. Cinotti, V. Yvorel, C. Habougit, F. Vassal, C. Nuti, J. L. Perrot, B. Labeille, and M. Peoc'h. 2015. "Ex vivo confocal microscopy imaging to identify tumor tissue on freshly removed brain sample." *J Neurooncol* 124 (2):157-64. doi: 10.1007/s11060-015-1832-z.

Francaviglia, N., D. G. Iacopino, G. Costantino, A. Villa, P. Impallaria, F. Meli, and R. Maugeri. 2017. "Fluorescein for resection of high-grade gliomas: A safety study control in a single center and review of the literature." *Surg Neurol Int* 8:145. doi: 10.4103/sni.sni_89_17.

Frangioni, J. V. 2003. "In vivo near-infrared fluorescence imaging." *Curr Opin Chem Biol* 7 (5):626-34.

Georges, J., A. Zehri, E. Carlson, J. Nichols, M. A. Mooney, N. L. Martirosyan, L. Ghaffari, M. Y. Kalani, J. Eschbacher, B. Feuerstein, T. Anderson, M. C. Preul, K. Van Keuren-Jensen, and P. Nakaji. 2014. "Label-free microscopic assessment of glioblastoma biopsy specimens prior to biobanking [corrected]." *Neurosurg Focus* 36 (2):E8. doi: 10.3171/2013.11.FOCUS13478.

Goetz, M., S. Thomas, A. Heimann, P. Delaney, C. Schneider, M. Relle, A. Schwarting, P. R. Galle, O. Kempski, M. F. Neurath, and R. Kiesslich. 2008. "Dynamic in vivo imaging of microvasculature and perfusion by miniaturized confocal laser microscopy." *Eur Surg Res* 41 (3):290-7. doi: 10.1159/000148242.

Gollapudi, P. R., I. Mohammed, S. R. Pittala, A. Reddy Kotha, N. R. Reddycherla, and D. Rao Ginjupally. 2018. "A simple improvisation to enhance the utility of Fluorescein sodium in the resection of intracranial lesions at routine neurosurgical centres." *World Neurosurg*. doi: 10.1016/j.wneu.2018.01.039.

Gruber, A., C. Dorfer, G. Bavinzski, H. Standhardt, H. Ferraz-Leite, and E. Knosp. 2012. "Superselective indocyanine green angiography for selective revascularization in the management of peripheral cerebral aneurysms." *AJNR Am J Neuroradiol* 33 (3):E36-7. doi: 10.3174/ajnr.A2424.

Haj-Hosseini, N., J. C. Richter, M. Hallbeck, and K. Wardell. 2015. "Low dose 5-aminolevulinic acid: Implications in spectroscopic measurements during brain tumor surgery." *Photodiagnosis Photodyn Ther* 12 (2):209-14. doi: 10.1016/j.pdpdt.2015.03.004.

Hamamcioglu, M. K., M. O. Akcakaya, B. Goker, M. O. Kasimcan, and T. Kiris. 2016. "The use of the YELLOW 560 nm surgical microscope filter for sodium fluorescein-guided resection of brain tumors: Our preliminary results in a series of 28 patients." *Clin Neurol Neurosurg* 143:39-45. doi: 10.1016/j.clineuro.2016.02.006.

Hashimoto, K., H. Kinouchi, H. Yoshioka, K. Kanemaru, M. Ogiwara, T. Yagi, T. Wakai, and Y. Fukumoto. 2017. "Efficacy of Endoscopic Fluorescein Video Angiography in Aneurysm Surgery-Novel and Innovative Assessment of Vascular Blood Flow in the Dead Angles of the Microscope." *Oper Neurosurg (Hagerstown)* 13 (4):471-481. doi: 10.1093/ons/opw042.

Hervey-Jumper, S. L., and M. S. Berger. 2016. "Maximizing safe resection of low- and high-grade glioma." *J Neurooncol* 130 (2):269-282. doi: 10.1007/s11060-016-2110-4.

Hohne, J., A. Brawanski, and K. M. Schebesch. 2016. "Fluorescein sodium-guided surgery of a brain abscess: A case report." *Surg Neurol Int* 7 (Suppl 39):S955-S957. doi: 10.4103/2152-7806.195234.

Hohne, J., A. Brawanski, and K. M. Schebesch. 2017. "Fluorescence-guided surgery of brain abscesses." *Clin Neurol Neurosurg* 155:36-39. doi: 10.1016/j.clineuro.2017.02.014.

Hohne, J., C. Hohenberger, M. Proescholdt, M. J. Riemenschneider, C. Wendl, A. Brawanski, and K. M. Schebesch. 2017. "Fluorescein sodium-guided resection of cerebral metastases-an update." *Acta Neurochir (Wien)* 159 (2):363-367. doi: 10.1007/s00701-016-3054-3.

Hu, D., Y. Jiang, E. Belykh, Y. Gong, M. C. Preul, B. Hannaford, and E. J. Seibel. 2017. "Toward real-time tumor margin identification in image-guided robotic brain tumor resection." *Proc. SPIE 10135, Medical Imaging 2017: Image-Guided Procedures, Robotic Interventions, and Modeling, 101350D (March 3, 2017)*:101350D. doi: 10.1117/12.2255417.

Hudetz, A. G., G. Feher, and J. P. Kampine. 1996. "Heterogeneous autoregulation of cerebrocortical capillary flow: evidence for functional thoroughfare channels?" *Microvasc Res* 51 (1):131-6. doi: 10.1006/mvre.1996.0015.

Ito, A., T. Endo, T. Inoue, H. Endo, K. Sato, and T. Tominaga. 2017. "Use of Indocyanine Green Fluorescence Endoscopy to Treat Concurrent Perimedullary and Dural Arteriovenous Fistulas in the Cervical Spine." *World Neurosurg* 101:814 e1-814 e6. doi: 10.1016/j.wneu.2017.03.032.

Ivanov, K. P., M. K. Kalinina, and I. Levkovich Yu. 1981. "Blood flow velocity in capillaries of brain and muscles and its physiological significance." *Microvasc Res* 22 (2):143-55. doi: 10.1016/0026-2862(81)90084-4.

Izadyyazdanabadi, M., E. Belykh, M. A. Mooney, J. M. Eschbacher, P. Nakaji, Y. Yang, and M. C. Preul. 2018. "Prospects for Theranostics in Neurosurgical Imaging: Empowering Confocal Laser Endomicroscopy Diagnostics via Deep Learning." *Front Oncol* 8:240. doi: 10.3389/fonc.2018.00240.

Izadyyazdanabadi, Mohammadhassan, Evgenii Belykh, Claudio Cavallo, Xiaochun Zhao, Sirin Gandhi, Leandro Borba Moreira, Jennifer Eschbacher, Peter Nakaji, Mark C. Preul, and Yezhou Yang. 2018. "Weakly-Supervised Learning-Based Feature Localization for Confocal Laser Endomicroscopy Glioma Images." 11071:300-308. doi: 10.1007/978-3-030-00934-2_34.

Jaber, M., J. Wolfer, C. Ewelt, M. Holling, M. Hasselblatt, T. Niederstadt, T. Zoubi, M. Weckesser, and W. Stummer. 2016. "The Value of 5-Aminolevulinic Acid in Low-grade Gliomas and High-grade Gliomas Lacking Glioblastoma Imaging Features: An Analysis Based on Fluorescence, Magnetic Resonance Imaging,

18F-Fluoroethyl Tyrosine Positron Emission Tomography, and Tumor Molecular Factors." *Neurosurgery* 78 (3):401-11; discussion 411. doi: 10.1227/NEU.0000000000001020.

Jisu, Hong, Park Bo-Yong, and Park Hyunjin. 2017. "Convolutional neural network classifier for distinguishing Barrett's esophagus and neoplasia endomicroscopy images." *Conf Proc IEEE Eng Med Biol Soc* 2017:2892-2895. doi: 10.1109/EMBC.2017.8037461.

Kakucs, C., I. A. Florian, G. Ungureanu, and I. S. Florian. 2017. "Fluorescein Angiography in Intracranial Aneurysm Surgery: A Helpful Method to Evaluate the Security of Clipping and Observe Blood Flow." *World Neurosurg* 105:406-411. doi: 10.1016/j.wneu.2017.05.172.

Kamen, A., S. Sun, S. Wan, S. Kluckner, T. Chen, A. M. Gigler, E. Simon, M. Fleischer, M. Javed, S. Daali, A. Igressa, and P. Charalampaki. 2016. "Automatic Tissue Differentiation Based on Confocal Endomicroscopic Images for Intraoperative Guidance in Neurosurgery." *Biomed Res Int* 2016:6183218. doi: 10.1155/2016/6183218.

Kilkenny, C., W. J. Browne, I. C. Cuthill, M. Emerson, and D. G. Altman. 2010. "Improving bioscience research reporting: the ARRIVE guidelines for reporting animal research." *PLoS Biol* 8 (6):e1000412. doi: 10.1371/journal.pbio.1000412.

Kim, M., J. Hong, and H. J. Shin. 2018. "Double-pulse laser illumination method for measuring fast cerebral blood flow velocities in the deep brain using a fiber-bundle-based endomicroscopy system." *Biomed Opt Express* 9 (6):2699-2715. doi: 10.1364/BOE.9.002699.

Kitai, R., H. Takeuchi, N. Miyoshi, B. Andriana, H. Neishi, N. Hashimoto, and K. Kikuta. 2014. "[Determining the tumor-cell density required for macroscopic observation of 5-ALA-induced fluorescence of protoporphyrin IX in cultured glioma cells and clinical cases]." *No Shinkei Geka* 42 (6):531-6.

Koc, K., I. Anik, B. Cabuk, and S. Ceylan. 2008. "Fluorescein sodium-guided surgery in glioblastoma multiforme: a prospective evaluation." *Br J Neurosurg* 22 (1):99-103. doi: 10.1080/02688690701765524.

Konig, K., H. Schneckenburger, A. Ruck, and R. Steiner. 1993. "In vivo photoproduct formation during PDT with ALA-induced endogenous porphyrins." *J Photochem Photobiol B* 18 (2-3):287-90.

Kwon, S., C. F. Janssen, F. C. Velasquez, and E. M. Sevick-Muraca. 2017. "Fluorescence imaging of lymphatic outflow of cerebrospinal fluid in mice." *J Immunol Methods* 449:37-43. doi: 10.1016/j.jim.2017.06.010.

Lacroix, M., D. Abi-Said, D. R. Fourney, Z. L. Gokaslan, W. Shi, F. DeMonte, F. F. Lang, I. E. McCutcheon, S. J. Hassenbusch, E. Holland, K. Hess, C. Michael, D. Miller, and R. Sawaya. 2001. "A multivariate analysis of 416 patients with glioblastoma multiforme: prognosis, extent of resection, and survival." *J Neurosurg* 95 (2):190-8. doi: 10.3171/jns.2001.95.2.0190.

Lau, D., S. L. Hervey-Jumper, S. Chang, A. M. Molinaro, M. W. McDermott, J. J. Phillips, and M. S. Berger. 2016. "A prospective Phase II clinical trial of 5-aminolevulinic acid to assess the correlation of intraoperative fluorescence intensity and degree of histologic cellularity during resection of high-grade gliomas." *J Neurosurg* 124 (5):1300-9. doi: 10.3171/2015.5.JNS1577.

Lee, C. M., C. J. Engelbrecht, T. D. Soper, F. Helmchen, and E. J. Seibel. 2010. "Scanning fiber endoscopy with highly flexible, 1 mm catheterscopes for wide-field, full-color imaging." *J Biophotonics* 3 (5-6):385-407. doi: 10.1002/jbio.200900087.

Lee, J. Y. K., S. S. Cho, R. Zeh, J. T. Pierce, M. Martinez-Lage, N. D. Adappa, J. N. Palmer, J. G. Newman, K. O. Learned, C. White, J. Kharlip, P. Snyder, P. S. Low, S. Singhal, and M. S. Grady. 2018. "Folate receptor overexpression can be visualized in real time during pituitary adenoma endoscopic transsphenoidal surgery with near-infrared imaging." *J Neurosurg* 129 (2):390-403. doi: 10.3171/2017.2.jns163191.

Liu, J. T., D. Meza, and N. Sanai. 2014. "Trends in fluorescence image-guided surgery for gliomas." *Neurosurgery* 75 (1):61-71. doi: 10.1227/NEU.0000000000000344.

Logsdon, A. F., B. P. Lucke-Wold, R. C. Turner, J. D. Huber, C. L. Rosen, and J. W. Simpkins. 2015. "Role of Microvascular Disruption in Brain Damage from Traumatic Brain Injury." *Compr Physiol* 5 (3):1147-60. doi: 10.1002/cphy.c140057.

Louveau, A., I. Smirnov, T. J. Keyes, J. D. Eccles, S. J. Rouhani, J. D. Peske, N. C. Derecki, D. Castle, J. W. Mandell, K. S. Lee, T. H. Harris, and J. Kipnis. 2015. "Structural and functional features of central nervous system lymphatic vessels." *Nature* 523 (7560):337-41. doi: 10.1038/nature14432.

Lovato, R. M., J. L. Vitorino Araujo, and J. C. Esteves Veiga. 2017. "Low-Cost Device for Fluorescein-Guided Surgery in Malignant Brain Tumor." *World Neurosurg* 104:61-67. doi: 10.1016/j.wneu.2017.04.169.

Ma, Q., B. V. Ineichen, M. Detmar, and S. T. Proulx. 2017. "Outflow of cerebrospinal fluid is predominantly through lymphatic vessels and is reduced in aged mice." *Nat Commun* 8 (1):1434. doi: 10.1038/s41467-017-01484-6.

Martirosyan, N. L., D. D. Cavalcanti, J. M. Eschbacher, P. M. Delaney, A. C. Scheck, M. G. Abdelwahab, P. Nakaji, R. F. Spetzler, and M. C. Preul. 2011. "Use of in vivo near-infrared laser confocal endomicroscopy with indocyanine green to detect the boundary of infiltrative tumor." *J Neurosurg* 115 (6):1131-8. doi: 10.3171/2011.8.JNS11559.

Martirosyan, N. L., J. M. Eschbacher, M. Y. Kalani, J. D. Turner, E. Belykh, R. F. Spetzler, P. Nakaji, and M. C. Preul. 2016. "Prospective evaluation of the utility of intraoperative confocal laser endomicroscopy in patients with brain neoplasms using fluorescein sodium: experience with 74 cases." *Neurosurg Focus* 40 (3):E11. doi: 10.3171/2016.1.FOCUS15559.

Martirosyan, N. L., J. Georges, J. M. Eschbacher, E. Belykh, A. Carotenuto, R. F. Spetzler, P. Nakaji, and M. C. Preul. 2018a. "Confocal scanning microscopy provides rapid, detailed intraoperative histological assessment of brain neoplasms: Experience with 106 cases." *Clin Neurol Neurosurg* 169:21-28. doi: 10.1016/j.clineuro.2018.03.015.

Martirosyan, N. L., J. Georges, J. M. Eschbacher, D. D. Cavalcanti, A. M. Elhadi, M. G. Abdelwahab, A. C. Scheck, P. Nakaji, R. F. Spetzler, and M. C. Preul. 2014. "Potential application of a handheld confocal endomicroscope imaging system using a variety of fluorophores in experimental gliomas and normal brain." *Neurosurg Focus* 36 (2):E16. doi: 10.3171/2013.11.focus13486.

Martirosyan, N. L., J. Georges, M. Y. Kalani, P. Nakaji, R. F. Spetzler, B. G. Feuerstein, and M. C. Preul. 2016. "Handheld confocal laser endomicroscopic imaging

utilizing tumor-specific fluorescent labeling to identify experimental glioma cells in vivo." *Surg Neurol Int* 7 (Suppl 40):S995-S1003. doi: 10.4103/2152-7806.195577.

Martirosyan, N. L., M. Y. Kalani, W. D. Bichard, A. A. Baaj, L. F. Gonzalez, M. C. Preul, and N. Theodore. 2015. "Cerebrospinal fluid drainage and induced hypertension improve spinal cord perfusion after acute spinal cord injury in pigs." *Neurosurgery* 76 (4):461-8; discussion 468-9. doi: 10.1227/NEU.0000000000000638.

Martirosyan, Nikolay L., Joseph Georges, Jennifer M. Eschbacher, Evgenii Belykh, Alessandro Carotenuto, Robert F. Spetzler, Peter Nakaji, and Mark C. Preul. 2018b. "Confocal scanning microscopy provides rapid, detailed intraoperative histological assessment of brain neoplasms: Experience with 106 cases." *Clinical Neurology and Neurosurgery* 169:21-28. doi: 10.1016/j.clineuro.2018.03.015.

Meza, D., D. Wang, Y. Wang, S. Borwege, N. Sanai, and J. T. Liu. 2015. "Comparing high-resolution microscopy techniques for potential intraoperative use in guiding low-grade glioma resections." *Lasers Surg Med* 47 (4):289-95. doi: 10.1002/lsm.22347.

Minkin, K., E. Naydenov, K. Gabrovski, P. Dimova, M. Penkov, R. Tanova, S. Nachev, and K. Romanski. 2016. "Intraoperative fluorescein staining for benign brain tumors." *Clin Neurol Neurosurg* 149:22-6. doi: 10.1016/j.clineuro.2016.07.016.

Misra, B. K., S. K. Samantray, and O. N. Churi. 2017. "Application of fluorescein sodium videoangiography in surgery for spinal arteriovenous malformation." *J Clin Neurosci* 38:59-62. doi: 10.1016/j.jocn.2016.12.004.

Moan, J., G. Streckyte, S. Bagdonas, O. Bech, and K. Berg. 1997. "Photobleaching of protoporphyrin IX in cells incubated with 5-aminolevulinic acid." *Int J Cancer* 70 (1):90-7.

Mooney, M. A., J. Georges, M. I. Yazdanabadi, K. Y. Goehring, W. L. White, A. S. Little, M. C. Preul, S. W. Coons, P. Nakaji, and J. M. Eschbacher. 2018. "Immediate ex-vivo diagnosis of pituitary adenomas using confocal reflectance microscopy: a proof-of-principle study." *J Neurosurg* 128 (4):1072-1075. doi: 10.3171/2016.11.JNS161651.

Moore, G. E., W. T. Peyton, and et al. 1948. "The clinical use of fluorescein in neurosurgery; the localization of brain tumors." *J Neurosurg* 5 (4):392-8. doi: 10.3171/jns.1948.5.4.0392.

Moore, GE, and WT Peyton. 1948. "The clinical use of fluorescein in neurosurgery; the localization of brain tumors." *Journal of Neurosurgery* 5 (4):6. doi: 10.3171/jns.1948.5.4.0392

Nabavi, A., H. Thurm, B. Zountsas, T. Pietsch, H. Lanfermann, U. Pichlmeier, M. Mehdorn, and A. L. A. Recurrent Glioma Study Group. 2009. "Five-aminolevulinic acid for fluorescence-guided resection of recurrent malignant gliomas: a phase ii study." *Neurosurgery* 65 (6):1070-6; discussion 1076-7. doi: 10.1227/01.NEU.0000360128.03597.C7.

Nag, S. 1996. "Cold-injury of the cerebral cortex: immunolocalization of cellular proteins and blood-brain barrier permeability studies." *J Neuropathol Exp Neurol* 55 (8):880-8. doi: 10.1097/00005072-199608000-00003.

Nagata, K., K. Kumasaka, K. D. Browne, S. Li, J. St-Pierre, J. Cognetti, J. Marks, V. E. Johnson, D. H. Smith, and J. L. Pascual. 2016. "Unfractionated heparin after TBI reduces in vivo cerebrovascular inflammation, brain edema and accelerates cognitive recovery." *J Trauma Acute Care Surg* 81 (6):1088-1094. doi: 10.1097/TA.0000000000001215.

Narducci, A., J. Onken, M. Czabanka, N. Hecht, and P. Vajkoczy. 2018a. "Fluorescein videoangiography during extracranial-to-intracranial bypass surgery: preliminary results." *Acta Neurochir (Wien)* 160 (4):767-774. doi: 10.1007/s00701-017-3453-0.

Narducci, A., J. Onken, M. Czabanka, N. Hecht, and P. Vajkoczy. 2018b. "Fluorescein videoangiography during extracranial-to-intracranial bypass surgery: preliminary results." *Acta Neurochir (Wien)*. doi: 10.1007/s00701-017-3453-0.

Narducci, A., K. Yasuyuki, J. Onken, K. Blecharz, and P. Vajkoczy. 2019. "In vivo demonstration of blood-brain barrier impairment in Moyamoya disease." *Acta Neurochir (Wien)* 161 (2):371-378. doi: 10.1007/s00701-019-03811-w.

Neira, J. A., T. H. Ung, J. S. Sims, H. R. Malone, D. S. Chow, J. L. Samanamud, G. J. Zanazzi, X. Guo, S. G. Bowden, B. Zhao, S. A. Sheth, G. M. McKhann, 2nd, M.

B. Sisti, P. Canoll, R. S. D'Amico, and J. N. Bruce. 2017. "Aggressive resection at the infiltrative margins of glioblastoma facilitated by intraoperative fluorescein guidance." *J Neurosurg* 127 (1):111-122. doi: 10.3171/2016.7.JNS16232.

Nitta, T., and K. Sato. 1995. "Prognostic implications of the extent of surgical resection in patients with intracranial malignant gliomas." *Cancer* 75 (11):2727-31.

Norman, M. U., S. Hulliger, P. Colarusso, and P. Kubes. 2008. "Multichannel fluorescence spinning disk microscopy reveals early endogenous CD4 T cell recruitment in contact sensitivity via complement." *J Immunol* 180 (1):510-21.

Novis, D. A., and R. J. Zarbo. 1997. "Interinstitutional comparison of frozen section turnaround time. A College of American Pathologists Q-Probes study of 32868 frozen sections in 700 hospitals." *Arch Pathol Lab Med* 121 (6):559-67.

Okuda, T., H. Yoshioka, and A. Kato. 2012. "Fluorescence-guided surgery for glioblastoma multiforme using high-dose fluorescein sodium with excitation and barrier filters." *J Clin Neurosci* 19 (12):1719-22. doi: 10.1016/j.jocn.2011.12.034.

Olivo, M., and B. C. Wilson. 2004. "Mapping ALA-induced PPIX fluorescence in normal brain and brain tumour using confocal fluorescence microscopy." *Int J Oncol* 25 (1):37-45.

Omoto, K., R. Matsuda, I. Nakagawa, Y. Motoyama, and H. Nakase. 2018. "False-positive inflammatory change mimicking glioblastoma multiforme under 5-aminolevulinic acid-guided surgery: A case report." *Surg Neurol Int* 9:49. doi: 10.4103/sni.sni_473_17.

Orbay, H., J. Bean, Y. Zhang, and W. Cai. 2013. "Intraoperative targeted optical imaging: a guide towards tumor-free margins in cancer surgery." *Curr Pharm Biotechnol* 14 (8):733-42.

Orringer, D. A., B. Pandian, Y. S. Niknafs, T. C. Hollon, J. Boyle, S. Lewis, M. Garrard, S. L. Hervey-Jumper, H. J. L. Garton, C. O. Maher, J. A. Heth, O. Sagher, D. A. Wilkinson, M. Snuderl, S. Venneti, S. H. Ramkissoon, K. A. McFadden, A. Fisher-Hubbard, A. P. Lieberman, T. D. Johnson, X. S. Xie, J. K. Trautman, C. W. Freudiger, and S. Camelo-Piragua. 2017. "Rapid intraoperative histology of

unprocessed surgical specimens via fibre-laser-based stimulated Raman scattering microscopy." *Nat Biomed Eng* 1. doi: 10.1038/s41551-016-0027.

Osman, H., J. Georges, D. Elsahy, E. M. Hattab, S. Yocom, and A. A. Cohen-Gadol. 2018. "In Vivo Microscopy in Neurosurgical Oncology." *World Neurosurg* 115:110-127. doi: 10.1016/j.wneu.2018.03.218.

Padalkar, M. V., and N. Pleshko. 2015. "Wavelength-dependent penetration depth of near infrared radiation into cartilage." *Analyst* 140 (7):2093-100. doi: 10.1039/c4an01987c.

Park, J. C., Y. Park, H. K. Kim, J. H. Jo, C. H. Park, E. H. Kim, D. H. Jung, H. Chung, S. K. Shin, S. K. Lee, and Y. C. Lee. 2017. "Probe-based confocal laser endomicroscopy in the margin delineation of early gastric cancer for endoscopic submucosal dissection." *J Gastroenterol Hepatol* 32 (5):1046-1054. doi: 10.1111/jgh.13635.

Pavlov, V., D. Meyronet, V. Meyer-Bisch, X. Armoiry, B. Pikul, C. Dumot, P. A. Beuriat, F. Signorelli, and J. Guyotat. 2016. "Intraoperative Probe-Based Confocal Laser Endomicroscopy in Surgery and Stereotactic Biopsy of Low-Grade and High-Grade Gliomas: A Feasibility Study in Humans." *Neurosurgery* 79 (4):604-12. doi: 10.1227/NEU.0000000000001365.

Plesec, T. P., and R. A. Prayson. 2007. "Frozen section discrepancy in the evaluation of central nervous system tumors." *Arch Pathol Lab Med* 131 (10):1532-40. doi: 10.1043/1543-2165(2007)131[1532:fsdite]2.0.co;2.

Potapov, A. A., S. A. Goriainov, V. B. Loshchenov, T. A. Savel'eva, A. G. Gavrilov, V. A. Okhlopkov, VIu Zhukov, P. V. Zelenkov, D. A. Gol'bin, V. A. Shurkhai, L. V. Shishkina, P. V. Grachev, M. N. Kholodtsova, S. G. Kuz'min, G. N. Vorozhtsov, and A. P. Chumakova. 2013. "[Intraoperative combined spectroscopy (optical biopsy) of cerebral gliomas]." *Zh Vopr Neirokhir Im N N Burdenko* 77 (2):3-10.

Potapov, A. A., S. A. Goryaynov, V. A. Okhlopkov, D. I. Pitskhelauri, G. L. Kobyakov, V. Y. Zhukov, D. A. Gol'bin, D. V. Svistov, B. V. Martynov, A. L. Krivoshapkin, A. S. Gaytan, Y. E. Anokhina, M. D. Varyukhina, M. F. Gol'dberg, A. V. Kondrashov, and A. P. Chumakova. 2015. "[Clinical guidelines for the use of intraoperative fluorescence diagnosis in brain tumor surgery]." *Zh Vopr Neirokhir Im N N Burdenko* 79 (5):91-101. doi: 10.17116/neiro201579591-101.

Potapov, A. A., S. A. Goryaynov, V. A. Okhlopkov, L. V. Shishkina, V. B. Loschenov, T. A. Savelieva, D. A. Golbin, A. P. Chumakova, M. F. Goldberg, M. D. Varyukhina, and A. Spallone. 2016. "Laser biospectroscopy and 5-ALA fluorescence navigation as a helpful tool in the meningioma resection." *Neurosurg Rev* 39 (3):437-47. doi: 10.1007/s10143-015-0697-0.

Raabe, A., J. Beck, R. Gerlach, M. Zimmermann, and V. Seifert. 2003. "Near-infrared indocyanine green video angiography: a new method for intraoperative assessment of vascular flow." *Neurosurgery* 52 (1):132-9; discussion 139. doi: 10.1097/00006123-200301000-00017.

Raabe, A., P. Nakaji, J. Beck, L. J. Kim, F. P. Hsu, J. D. Kamerman, V. Seifert, and R. F. Spetzler. 2005. "Prospective evaluation of surgical microscope-integrated intraoperative near-infrared indocyanine green videoangiography during aneurysm surgery." *J Neurosurg* 103 (6):982-9. doi: 10.3171/jns.2005.103.6.0982.

Rao, S., A. Rajkumar, M. D. Ehtesham, and P. Duvuru. 2009. "Challenges in neurosurgical intraoperative consultation." *Neurol India* 57 (4):464-8. doi: 10.4103/0028-3886.55598.

Rapp, M., M. Kamp, H. J. Steiger, and M. Sabel. 2014. "Endoscopic-assisted visualization of 5-aminolevulinic acid-induced fluorescence in malignant glioma surgery: a technical note." *World Neurosurg* 82 (1-2):e277-9. doi: 10.1016/j.wneu.2013.07.002.

Regula, J., A. J. MacRobert, A. Gorchein, G. A. Buonaccorsi, S. M. Thorpe, G. M. Spencer, A. R. Hatfield, and S. G. Bown. 1995. "Photosensitisation and photodynamic therapy of oesophageal, duodenal, and colorectal tumours using 5 aminolaevulinic acid induced protoporphyrin IX--a pilot study." *Gut* 36 (1):67-75.

Roberts, D. W., and J. Olson. 2017. "Fluorescein Guidance in Glioblastoma Resection." *N Engl J Med* 376 (18):e36. doi: 10.1056/NEJMicm1611258.

Rodriguez-Hernandez, A., and M. T. Lawton. 2012. "Flash fluorescence with indocyanine green videoangiography to identify the recipient artery for bypass with distal middle cerebral artery aneurysms: operative technique." *Neurosurgery* 70 (2 Suppl Operative):209-20. doi: 10.1227/NEU.0b013e31823158f3.

Roessler, K., W. Dietrich, and K. Kitz. 2002. "High diagnostic accuracy of cytologic smears of central nervous system tumors. A 15-year experience based on 4,172 patients." *Acta Cytol* 46 (4):667-74.

Rostomily, R. C., A. M. Spence, D. Duong, K. McCormick, M. Bland, and M. S. Berger. 1994. "Multimodality management of recurrent adult malignant gliomas: results of a phase II multiagent chemotherapy study and analysis of cytoreductive surgery." *Neurosurgery* 35 (3):378-88; discussion 388.

Sanai, N., and M. S. Berger. 2008. "Glioma extent of resection and its impact on patient outcome." *Neurosurgery* 62 (4):753-64; discussion 264-6. doi: 10.1227/01.neu.0000318159.21731.cf.

Sanai, N., and M. S. Berger. 2018. "Surgical oncology for gliomas: the state of the art." *Nat Rev Clin Oncol* 15 (2):112-125. doi: 10.1038/nrclinonc.2017.171.

Sanai, N., J. Eschbacher, G. Hattendorf, S. W. Coons, M. C. Preul, K. A. Smith, P. Nakaji, and R. F. Spetzler. 2011. "Intraoperative confocal microscopy for brain tumors: a feasibility analysis in humans." *Neurosurgery* 68 (2 Suppl Operative):282-90; discussion 290. doi: 10.1227/NEU.0b013e318212464e.

Sanai, N., L. A. Snyder, N. J. Honea, S. W. Coons, J. M. Eschbacher, K. A. Smith, and R. F. Spetzler. 2011. "Intraoperative confocal microscopy in the visualization of 5-aminolevulinic acid fluorescence in low-grade gliomas." *J Neurosurg* 115 (4):740-8. doi: 10.3171/2011.6.JNS11252.

Sankar, T., P. M. Delaney, R. W. Ryan, J. Eschbacher, M. Abdelwahab, P. Nakaji, S. W. Coons, A. C. Scheck, K. A. Smith, R. F. Spetzler, and M. C. Preul. 2010. "Miniaturized handheld confocal microscopy for neurosurgery: results in an experimental glioblastoma model." *Neurosurgery* 66 (2):410-7; discussion 417-8. doi: 10.1227/01.NEU.0000365772.66324.6F.

Schebesch, K. M., A. Brawanski, C. Hohenberger, and J. Hohne. 2016. "Fluorescein Sodium-Guided Surgery of Malignant Brain Tumors: History, Current Concepts, and Future Project." *Turk Neurosurg* 26 (2):185-94. doi: 10.5137/1019-5149.JTN.16952-16.0.

Schindelin, J., I. Arganda-Carreras, E. Frise, V. Kaynig, M. Longair, T. Pietzsch, S. Preibisch, C. Rueden, S. Saalfeld, B. Schmid, J. Y. Tinevez, D. J. White, V.

Hartenstein, K. Eliceiri, P. Tomancak, and A. Cardona. 2012. "Fiji: an open-source platform for biological-image analysis." *Nat Methods* 9 (7):676-82. doi: 10.1038/nmeth.2019.

Schwake, M., W. Stummer, E. J. Suero Molina, and J. Wolfer. 2015. "Simultaneous fluorescein sodium and 5-ALA in fluorescence-guided glioma surgery." *Acta Neurochir (Wien)* 157 (5):877-9. doi: 10.1007/s00701-015-2401-0.

Seylaz, J., R. Charbonne, K. Nanri, D. Von Euw, J. Borredon, K. Kacem, P. Meric, and E. Pinard. 1999. "Dynamic in vivo measurement of erythrocyte velocity and flow in capillaries and of microvessel diameter in the rat brain by confocal laser microscopy." *J Cereb Blood Flow Metab* 19 (8):863-70. doi: 10.1097/00004647-199908000-00005.

Shinoda, J., H. Yano, S. Yoshimura, A. Okumura, Y. Kaku, T. Iwama, and N. Sakai. 2003. "Fluorescence-guided resection of glioblastoma multiforme by using high-dose fluorescein sodium. Technical note." *J Neurosurg* 99 (3):597-603. doi: 10.3171/jns.2003.99.3.0597.

Sroka, R., W. Beyer, L. Gossner, T. Sassy, S. Stocker, and R. Baumgartner. 1996. "Pharmacokinetics of 5-aminolevulinic-acid-induced porphyrins in tumour-bearing mice." *J Photochem Photobiol B* 34 (1):13-9.

Strychowsky, J., S. Nayan, K. Reddy, F. Farrokhyar, and D. Sommer. 2011. "Purely endoscopic transsphenoidal surgery versus traditional microsurgery for resection of pituitary adenomas: systematic review." *J Otolaryngol Head Neck Surg* 40 (2):175-85.

Stummer, W. 2017. "Intra-operative tissue diagnosis: isn't it time for some reporting guidelines?" *Acta Neurochir (Wien)* 159 (2):369-370. doi: 10.1007/s00701-016-3057-0.

Stummer, W., A. Novotny, H. Stepp, C. Goetz, K. Bise, and H. J. Reulen. 2000. "Fluorescence-guided resection of glioblastoma multiforme by using 5-aminolevulinic acid-induced porphyrins: a prospective study in 52 consecutive patients." *J Neurosurg* 93 (6):1003-13. doi: 10.3171/jns.2000.93.6.1003.

Stummer, W., U. Pichlmeier, T. Meinel, O. D. Wiestler, F. Zanella, H. J. Reulen, and A. LA-Glioma Study Group. 2006. "Fluorescence-guided surgery with 5-

aminolevulinic acid for resection of malignant glioma: a randomised controlled multicentre phase III trial." *Lancet Oncol* 7 (5):392-401. doi: 10.1016/S1470-2045(06)70665-9.

Stummer, W., S. Stocker, S. Wagner, H. Stepp, C. Fritsch, C. Goetz, A. E. Goetz, R. Kiefmann, and H. J. Reulen. 1998. "Intraoperative detection of malignant gliomas by 5-aminolevulinic acid-induced porphyrin fluorescence." *Neurosurgery* 42 (3):518-25; discussion 525-6.

Stummer, W., J. C. Tonn, C. Goetz, W. Ullrich, H. Stepp, A. Bink, T. Pietsch, and U. Pichlmeier. 2014. "5-Aminolevulinic acid-derived tumor fluorescence: the diagnostic accuracy of visible fluorescence qualities as corroborated by spectrometry and histology and postoperative imaging." *Neurosurgery* 74 (3):310-9; discussion 319-20. doi: 10.1227/NEU.0000000000000267.

Suero Molina, E., J. Wolfer, C. Ewelt, A. Ehrhardt, B. Brokinkel, and W. Stummer. 2018. "Dual-labeling with 5-aminolevulinic acid and fluorescein for fluorescence-guided resection of high-grade gliomas: technical note." *J Neurosurg* 128 (2):399-405. doi: 10.3171/2016.11.JNS161072.

Sun, B. L., L. H. Wang, T. Yang, J. Y. Sun, L. L. Mao, M. F. Yang, H. Yuan, R. A. Colvin, and X. Y. Yang. 2018. "Lymphatic drainage system of the brain: A novel target for intervention of neurological diseases." *Prog Neurobiol* 163-164:118-143. doi: 10.1016/j.pneurobio.2017.08.007.

Susaki, E. A., K. Tainaka, D. Perrin, H. Yukinaga, A. Kuno, and H. R. Ueda. 2015. "Advanced CUBIC protocols for whole-brain and whole-body clearing and imaging." *Nat Protoc* 10 (11):1709-27. doi: 10.1038/nprot.2015.085.

Suzuki, K., N. Kodama, T. Sasaki, M. Matsumoto, T. Ichikawa, R. Munakata, H. Muramatsu, and H. Kasuya. 2007. "Confirmation of blood flow in perforating arteries using fluorescein cerebral angiography during aneurysm surgery." *J Neurosurg* 107 (1):68-73. doi: 10.3171/JNS-07/07/0068.

Swanson, K. I., P. A. Clark, R. R. Zhang, I. K. Kandela, M. Farhoud, J. P. Weichert, and J. S. Kuo. 2015. "Fluorescent cancer-selective alkylphosphocholine analogs for intraoperative glioma detection." *Neurosurgery* 76 (2):115-23; discussion 123-4. doi: 10.1227/NEU.0000000000000622.

Szatmari, T., K. Lumniczky, S. Desaknai, S. Trajcevski, E. J. Hidvegi, H. Hamada, and G. Safrany. 2006. "Detailed characterization of the mouse glioma 261 tumor model for experimental glioblastoma therapy." *Cancer Sci* 97 (6):546-53. doi: 10.1111/j.1349-7006.2006.00208.x.

Szegedy, C , W Liu, Y Jia, P Sermanet, S Reed, D Anguelov, D Erhan, V Vanhoucke, and A Rabinovich. 2015. "Going deeper with convolutions." Proceedings of the IEEE Conference on Computer Vision and Pattern Recognition.

Tan, J., M. A. Quinn, J. M. Pyman, P. M. Delaney, and W. J. McLaren. 2009. "Detection of cervical intraepithelial neoplasia in vivo using confocal endomicroscopy." *Bjog* 116 (12):1663-70. doi: 10.1111/j.1471-0528.2009.02261.x.

Thien, A., J. P. Rao, W. H. Ng, and N. K. King. 2017. "The Fluoropen: a simple low-cost device to detect intraoperative fluorescein fluorescence in stereotactic needle biopsy of brain tumors." *Acta Neurochir (Wien)* 159 (2):371-375. doi: 10.1007/s00701-016-3041-8.

Tilgner, J., M. Herr, C. Ostertag, and B. Volk. 2005. "Validation of intraoperative diagnoses using smear preparations from stereotactic brain biopsies: intraoperative versus final diagnosis--influence of clinical factors." *Neurosurgery* 56 (2):257-65; discussion 257-65. doi: 10.1227/01.neu.0000148899.39020.87.

Tomita, M., N. Tanahashi, H. Takeda, I. Schiszler, T. Osada, M. Unekawa, and N. Suzuki. 2006. "Capillo-venous flow in the brain: significance of intravascular RBC aggregation for venous flow regulation." *Clin Hemorheol Microcirc* 34 (1-2):51-7.

Uematsu, Y., Y. Owai, R. Okita, Y. Tanaka, and T. Itakura. 2007. "The usefulness and problem of intraoperative rapid diagnosis in surgical neuropathology." *Brain Tumor Pathol* 24 (2):47-52. doi: 10.1007/s10014-007-0219-z.

Unekawa, M., Tomita, M., Osada, T., Tomita, Y., Toriumi, H., Tatarishvili, J., Suzuki, N. 2008. "Frequency distribution function of red blood cell velocities in single capillaries of the rat cerebral cortex using intravital laser-scanning confocal microscopy with highspeed camera." *Asian Biomedicine* 2 (3):203-218.

Utsuki, S., H. Oka, S. Sato, S. Shimizu, S. Suzuki, Y. Tanizaki, K. Kondo, Y. Miyajima, and K. Fujii. 2007. "Histological examination of false positive tissue resection

using 5-aminolevulinic acid-induced fluorescence guidance." *Neurol Med Chir (Tokyo)* 47 (5):210-3; discussion 213-4.

Valdes, P. A., V. Jacobs, B. T. Harris, B. C. Wilson, F. Leblond, K. D. Paulsen, and D. W. Roberts. 2015. "Quantitative fluorescence using 5-aminolevulinic acid-induced protoporphyrin IX biomarker as a surgical adjunct in low-grade glioma surgery." *J Neurosurg* 123 (3):771-80. doi: 10.3171/2014.12.JNS14391.

Valdes, P. A., F. Leblond, V. L. Jacobs, B. C. Wilson, K. D. Paulsen, and D. W. Roberts. 2012. "Quantitative, spectrally-resolved intraoperative fluorescence imaging." *Sci Rep* 2:798. doi: 10.1038/srep00798.

van den Broek, F. J., J. A. van Es, S. van Eeden, P. C. Stokkers, C. Y. Ponsioen, J. B. Reitsma, P. Fockens, and E. Dekker. 2011. "Pilot study of probe-based confocal laser endomicroscopy during colonoscopic surveillance of patients with longstanding ulcerative colitis." *Endoscopy* 43 (2):116-22. doi: 10.1055/s-0030-1255954.

Webber, J., D. Kessel, and D. Fromm. 1997. "On-line fluorescence of human tissues after oral administration of 5-aminolevulinic acid." *J Photochem Photobiol B* 38 (2-3):209-14.

Wei, L., Y. Chen, C. Yin, S. Borwege, N. Sanai, and J. T. C. Liu. 2017. "Optical-sectioning microscopy of protoporphyrin IX fluorescence in human gliomas: standardization and quantitative comparison with histology." *J Biomed Opt* 22 (4):46005. doi: 10.1117/1.JBO.22.4.046005.

Widhalm, G., B. Kiesel, A. Woehrer, T. Traub-Weidinger, M. Preusser, C. Marosi, D. Prayer, J. A. Hainfellner, E. Knosp, and S. Wolfsberger. 2013. "5-Aminolevulinic acid induced fluorescence is a powerful intraoperative marker for precise histopathological grading of gliomas with non-significant contrast-enhancement." *PLoS One* 8 (10):e76988. doi: 10.1371/journal.pone.0076988.

Wood, J. R., S. B. Green, and W. R. Shapiro. 1988. "The prognostic importance of tumor size in malignant gliomas: a computed tomographic scan study by the Brain Tumor Cooperative Group." *J Clin Oncol* 6 (2):338-43. doi: 10.1200/jco.1988.6.2.338.

Xiang, Y., X. P. Zhu, J. N. Zhao, G. H. Huang, J. H. Tang, H. R. Chen, L. Du, D. Zhang, X. F. Tang, H. Yang, and S. Q. Lv. 2018. "Blood-Brain Barrier Disruption, Sodium Fluorescein, And Fluorescence-Guided Surgery Of Gliomas." *Br J Neurosurg*:1-8. doi: 10.1080/02688697.2018.1428731.

Yang, C., V. W. Hou, E. J. Girard, L. Y. Nelson, and E. J. Seibel. 2014. "Target-to-background enhancement in multispectral endoscopy with background autofluorescence mitigation for quantitative molecular imaging." *J Biomed Opt* 19 (7):76014. doi: 10.1117/1.JBO.19.7.076014.

Yano, H., N. Nakayama, N. Ohe, K. Miwa, J. Shinoda, and T. Iwama. 2017. "Pathological analysis of the surgical margins of resected glioblastomas excised using photodynamic visualization with both 5-aminolevulinic acid and fluorescein sodium." *J Neurooncol* 133 (2):389-397. doi: 10.1007/s11060-017-2445-5.

Yuana, Z, M IzadyYazdanabadia, D Mokkapatib, R Panvalkarb, JY Shinc, N Tajbakhshc, S Gurudud, and J Liangc. 2017. "Automatic polyp detection in colonoscopy videos." SPIE Medical Imaging.

Zehri, A. H., W. Ramey, J. F. Georges, M. A. Mooney, N. L. Martirosyan, M. C. Preul, and P. Nakaji. 2014. "Neurosurgical confocal endomicroscopy: A review of contrast agents, confocal systems, and future imaging modalities." *Surg Neurol Int* 5:60. doi: 10.4103/2152-7806.131638.

Zhang, L., A. S. Kim, J. S. Ridge, L. Y. Nelson, J. H. Berg, and E. J. Seibel. 2013. "Trimodal detection of early childhood caries using laser light scanning and fluorescence spectroscopy: clinical prototype." *J Biomed Opt* 18 (11):111412. doi: 10.1117/1.JBO.18.11.111412.

Zhao, S., J. Wu, C. Wang, H. Liu, X. Dong, C. Shi, C. Shi, Y. Liu, L. Teng, D. Han, X. Chen, G. Yang, L. Wang, C. Shen, and H. Li. 2013. "Intraoperative fluorescence-guided resection of high-grade malignant gliomas using 5-aminolevulinic acid-induced porphyrins: a systematic review and meta-analysis of prospective studies." *PLoS One* 8 (5):e63682. doi: 10.1371/journal.pone.0063682.

Zhao, X., E. Belykh, C. Cavallo, D. Valli, S. Gandhi, M. C. Preul, P. Vajkoczy, M. T. Lawton, and P. Nakaji. 2019. "Application of Fluorescein Fluorescence in Vascular Neurosurgery." *Front Surg* 6:52. doi: 10.3389/fsurg.2019.00052.

APPENDIX A

LIST OF PUBLICATIONS

LIST OF PUBLICATIONS

Below is a list of papers and coauthors who worked on these projects. Some of these works related to the studies of the intraoperative optical biopsies of brain tumors with confocal laser endomicroscopy and near view scanning fiber endoscopy, marked with (*), are included in this thesis.

Reviews

Review of the advanced optical fluorescence imaging technologies and the place of CLE in neurosurgery

1. Belykh E, Martirosyan NL, Yagmurlu K, Miller EJ, Eschbacher JM, Izadyyazdanabadi M, et al. Intraoperative Fluorescence Imaging for personalized Brain Tumor Resection: Current State and Future Directions. *Frontiers in Surgery* (2016) 3:27. doi: 10.3389/fsurg.2016.00055. PubMed PMID: WOS:000410268400001.

Review of all CLE techniques and topics related specifically to in vivo CLE imaging in neurosurgery.

2. Belykh E, Cavallo C, Gandhi S, Zhao X, Veljanoski D, Izady Yazdanabadi M, et al. Utilization of intraoperative confocal laser endomicroscopy in brain tumor surgery. J Neurosurg Sci (2018) 62(6):704-17. Epub 2018/08/28. doi: 10.23736/S0390-5616.18.04553-8. PubMed PMID: 30160080.

Review of drug delivery for fluorescence guided brain tumor surgery.

3. (under review in Frontiers in Oncology) Belykh E., Shaffer K.V., Lin C., Preul M.C., Chen L. Blood Brain Barrier, Blood-Brain Tumor Barrier and Fluorescence-Guided Surgical Oncology: How Optical Labels are Delivered to the Brain Tumors

Wide-field and near-view fluorescence microscopy for neurosurgery

In this paper we (1) assessed the optical excitation profile of common operating microscopes (2) assessed PpIX photobleaching rate in experimental gliomas, and (3) described a novel method for ratiometric quantitative fluorescence imaging.

4. Belykh E, Miller EJ, Patel AA, Bozkurt B, Yağmurlu K, Robinson TR, et al. Optical Characterization of Neurosurgical Operating Microscopes: Quantitative Fluorescence and Assessment of PpIX Photobleaching. *Sci Rep* (2018) 8(1):12543. Epub 2018/08/22. doi: 10.1038/s41598-018-30247-6. PubMed PMID: 30135440; PubMed Central PMCID: PMCPMC6105612.

In this paper a new method of improved 5-ALA induced PpIX fluorescnnce is described and evaluated.

5. *Belykh E, Miller EJ, Hu D, Martirosyan NL, Woolf EC, Scheck AC, et al. Scanning Fiber Endoscope Improves Detection of 5-Aminolevulinic Acid-Induced Protoporphyrin IX Fluorescence at the Boundary of Infiltrative Glioma. *World Neurosurg* (2018) 113:e51-e69. Epub 2018/02/02. doi: 10.1016/j.wneu.2018.01.151. PubMed PMID: 29408716; PubMed Central PMCID: PMCPMC5924630.

In this paper we evaluated novel robotic microscope with three fluorescent modes for fluorescnce-guided surgery

6. Belykh EG, Zhao X, Cavallo C, Bohl MA, Yagmurlu K, Aklinski JL, et al. Laboratory Evaluation of a Robotic Operative Microscope - Visualization Platform for Neurosurgery. *Cureus* (2018) 10(7):e3072. Epub 2018/10/04. doi: 10.7759/cureus.3072. PubMed PMID: 30280067; PubMed Central PMCID: PMCPMC6166902.

In this paper a simulation model for fluorescence-guided surgery is developed and evaluated.

7. Valli D[&], Belykh E.[&], Zhao X, Gandhi S, Cavallo C, Martirosyan NL, et al. Development of a Simulation Model for Fluorescence-Guided Brain Tumor Surgery. *Front Oncol* (2019) 9:748. Epub 2019/09/03. doi: 10.3389/fonc.2019.00748. PubMed PMID: 31475107; PubMed Central PMCID: PMCPMC6706957. (& - co-first authors)

In this paper the direct comparison of 5-ALA and fluorescien sodium for fluorescence guidence in performed on various mouse models using advanced microscopy techniques.

8. (in submission) Belykh E., Shaffer K.V., Zhao X., Bardonova L., Carotenuto A., Eric Miller E., Abramov I., Healey D.R., Luna-Melendez E., Quarles C., Yu K., Deneen B., Mehta S., Preul M.C. Direct Microscopic Comparison of 5-ALA and Fluorescein Sodium for Detection of Malignant Glioma Border: Laboratory Investigation

Confocal fluorescence microscopy for neurosurgery

In this paper, generational comparison of CLE was described along with detailed technical assessment of optimal parameters for brain tumor imaiging

9. *Belykh E, Miller EJ, Carotenuto A, Patel AA, Cavallo C, Martirosyan NL, et al. Progress in Confocal Laser Endomicroscopy for Neurosurgery and Technical Nuances for Brain Tumor Imaging With Fluorescein. *Front Oncol* (2019) 9:554. Epub 2019/07/03. doi: 10.3389/fonc.2019.00554. PubMed PMID: 31334106; PubMed Central PMCID: PMCPMC6616132.

   In this paper the possibility to differentiate normal injured and tumor brain tissue with fluorescein CLE was established.

10. *Belykh E, Miller EJ, Patel AA, Yazdanabadi MI, Martirosyan NL, Yagmurlu K, et al. Diagnostic Accuracy of a Confocal Laser Endomicroscope for In Vivo Differentiation Between Normal Injured And Tumor Tissue During Fluorescein-Guided Glioma Resection: Laboratory Investigation. World Neurosurg (2018) 115:e337-e48. Epub 2018/04/21. doi: 10.1016/j.wneu.2018.04.048. PubMed PMID: 29673821.

    In this paper we described novel 3D imaging microscopy with CLE

11. Belykh E, Patel AA, Miller EJ, Bozkurt B, Yagmurlu K, Woolf EC, et al. Probe-based three-dimensional confocal laser endomicroscopy of brain tumors: technical note. *Cancer Manag Res* (2018) 10:3109-23. Epub 2018/09/15. doi:

10.2147/CMAR.S165980. PubMed PMID: 30214304; PubMed Central PMCID: PMCPMC6124793.

Below are the papers that describe clinical experience of confocal laser endomicroscopy

12. *(In submission)Belykh E., Zhao X., Nakaji P., Eschbacher J.M., Preul M.C. Intraoperative confocal laser endomicroscopy examination of tissue microstructure during fluorescence-guided brain tumor surgery.
13. *(In submission) Belykh E., Ngo B., Farhadi D.S., Zhao X., Mooney M.A., White W.L., Daniels J.K., Little A.S., Eschbacher J.M.,. Preul M.C. Confocal laser endomicroscopy assessment of pituitary tumor microstructure: feasibility study.
14. *(In submission) Belykh E., Zhao X., Ngo B., Farhadi D.S., Kindelin A., Ahmad S., Martirosyan N.L., Lawton M.T., Preul M.C. Visualization of brain microvasculature and blood flow in vivo: feasibility study using confocal laser endomicroscopy

APPENDIX B

TABLE 2.1

Table 2.1. Confocal laser endomicroscopy (CLE) imaging parameters

Parameter	Gen1	Gen2	Comment
Laser wavelength	488 nm	488 nm	Always the same
Laser power	Range: 0–1000 mW	Range: 0–100%	Percentages correlate to the actual laser power. 50% results in ~500 mW laser power; 10%, 100 mW. TIFF image metadata records actual laser power in mW, which may be used for further analysis.
Depth	Displayed only relative value showing the arrow position on the horizontal scale; not recorded	Range: -50–200 μm; also displayed as relative value on the vertical scale	Knowledge of depth position is crucial for understanding of imaging location and adjustment of depth on the fly for optimal image quality. Awareness of depth helps to avoid low-quality images by not imaging too deep into a tissue. The axial imaging resolution is <4.5 μm.
Brightness	Range: 0–100%	Range: 0–100%	The brightness is the built-in adjustable proprietary setting parameter used during CLE imaging. Unlike the gain and laser power, the brightness could be adjusted during the imaging. Knowledge of brightness is important to assess the true brightness of the fluorescent staining.
Gain	Options: low, normal, high, max	Range: 1800–3000	Gain is an important parameter to consider, as it influences the image brightness. We mostly used the system with gain at the midlevel (normal or 2400). We found it useful to increase or reduce the gain for imaging of very bright and dark fluorescent samples respectively.

Speed (resolution)	Options: 1024 × 1024 μm 475 × 475 μm	Options: 1080 540 270 135	Numbers represent the number of horizontal lines that the laser travels during image acquisition. Acquisition speed 1080 results in a 1920 × 1080 pixel scan at <0.5 μm axial resolution; speed 540 results in a 1920 × 540 pixel scan, etc. Scan area–aspect ratio is kept the same as 16 × 9. Most images are taken in the "high-image quality low-speed" mode (1080). Higher speeds (270 and 135) are rarely used and do not produce diagnostic-quality images. Higher speed might be adjusted for an initial search of an optimal imaging position to quickly verify the presence of fluorescence. At the settings window, the user can select two speeds that would be rapidly available to choose from on the primary screen.
Zoom	Constant; changes not available	Options: 1× 1.4× 2×	Zoom is usually set at 1× giving a FOV size of 475 × 267 μm (width/height). This FOV size is 2× less compared to Gen1 system; however, with FNa Gen2 provides subjectively similar appearing images to Gen1. We almost never use 2× zoom with FNa, as we feel that a larger field of view is favorable for imaging with FNa. However, 1.4× and 2× zoom are useful with other fluorophores like acridine orange or acriflavine, which bind to the cellular structures and therefore result in more contrasted images.
Filter	Options: Green fluoro (505–585 nm) Green-red fluoro (505–750 nm)	Options: Gray filter Green bandpass Green longpass Red filter	Our experience with FNa is that the green longpass filter provides overall brighter images than the green bandpass filter. The red bandpass filter may be unnecessary for the work with FNa. We are not able to detect reliable PpIX (peak emission~630nm) signal with red or green longpass filters, which we believe is mostly due to the absence of an appropriate excitation laser source (405 nm for PpIX).

Z-stack	Not available	Start position offset, range: -50–+47 µm End position offset, range: -47–+50 µm Step size, range: 3–20 µm	We find that for most cases +10 µm and -15 µm offsets (total depth 25 µm) with the minimally possible (3 µm) Z-step are the most optimal for 3-dimensional reconstruction of the Z-stack.
Time stamp	Not available on the image	2017-04-14_12-39-20-34	Time stamp is critical for matching individual CLE images with the time on microscope and navigation in order to track the optical biopsy location.

Abbreviations: FOV, field of view; FNa, fluorescein sodium; Gen1, first generation; Gen2, second generation; PpIX, protoporphyrin; TIFF, tagged image file format

APPENDIX C

PERMISSIONS

PERMISSIONS

All articles in this dissertation were used with permission from all co-authors.